

AD-A182 713

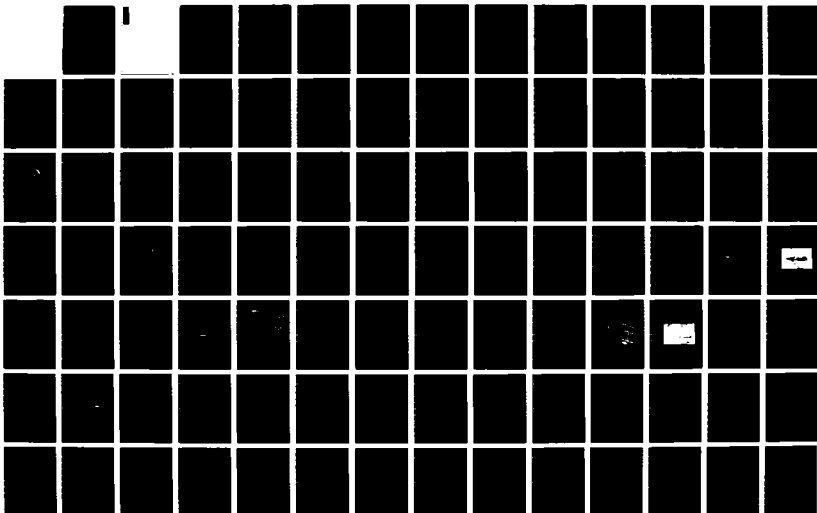
DYNAMICS AND AEROELASTICITY OF COMPOSITE STRUCTURES(U)
MASSACHUSETTS INST OF TECH CAMBRIDGE TECHNOLOGY LAB FOR
ADVAN. G CHEN ET AL. 22 APR 87 TELAC-86-14A

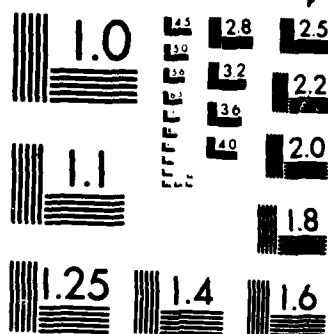
1/3

UNCLASSIFIED

AFOSR-TR-87-0845 F49620-84-C-0099

F/G 1/3. 12 NL





MICROCOPY RESOLUTION TEST CHART
NATIONAL BUREAU OF STANDARDS 1963-A

UNCLASSIFIED

SECURITY CLASSIFICATION OF THIS PAGE

ADA182713

REPORT DOCUMENTATION PAGE

1a. REPORT SECURITY CLASSIFICATION UNCLASSIFIED			1b. RESTRICTIVE MARKINGS		
2a. SECURITY CLASSIFICATION AUTHORITY			3. DISTRIBUTION/AVAILABILITY OF REPORT Approved for public release; distribution unlimited.		
2b. DECLASSIFICATION/DOWNGRADING SCHEDULE			5. MONITORING ORGANIZATION REPORT NUMBER(S) AFOSR-TR. 87-0845		
4. PERFORMING ORGANIZATION REPORT NUMBER(S) TELAC REPORT 86-14A			7a. NAME OF MONITORING ORGANIZATION AFOSR/NA		
6a. NAME OF PERFORMING ORGANIZATION Technology Laboratory for Advanced Composites		6b. OFFICE SYMBOL (If applicable)		7b. ADDRESS (City, State and ZIP Code) Bldg 410 Bolling AFB DC 20332-6448	
6c. ADDRESS (City, State and ZIP Code) M.I.T.; Room 33-309 77 Massachusetts Ave. Cambridge, MA 02139		8a. NAME OF FUNDING/SPONSORING ORGANIZATION AFOSR		8b. OFFICE SYMBOL (If applicable) NA	
8c. ADDRESS (City, State and ZIP Code) Bolling Air Force Base DC 20332-6448		9. PROCUREMENT INSTRUMENT IDENTIFICATION NUMBER F49620-87-C-0099			
11. TITLE (Include Security Classification) DYNAMICS AND AERO- ELASTICITY OF COMPOSITE STRUCTURES		10. SOURCE OF FUNDING NOS.			
		PROGRAM ELEMENT NO. 61102		PROJECT NO. 2302	
				TASK NO. B1	
				WORK UNIT NO.	
12. PERSONAL AUTHOR(S) Gun-Shing Chen & John Dugundji					
13a. TYPE OF REPORT Final Report		13b. TIME COVERED FROM 7/1/85 TO 6/30/86		14. DATE OF REPORT (Yr., Mo., Day) 1987 April 22	
15. PAGE COUNT 212					
16. SUPPLEMENTARY NOTATION					
17. COSATI CODES			18. SUBJECT TERMS (Continue on reverse if necessary and identify by block number)		
FIELD	GROUP	SUB. GR.	Aeroelasticity, Composites, Forwarded swept wings, Body freedom flutter		
19. ABSTRACT (Continue on reverse if necessary and identify by block number)					
<p>An analytical and experimental investigation was made of the aeroelastic flutter and divergence behavior of a forward swept graphite/epoxy wing aircraft with rigid body freedoms in free flight.</p> <p>Analytically, a transient aeroelastic analysis, using a Rayleigh-Ritz formulation, modified strip theory and measured aircraft aerodynamic derivatives, was developed to predict and interpret the aeroelastic behavior and instability mechanism. The transient aerodynamics approximated the Theodorsen function by Pade approximants and used augmented state variables to investigate stability by standard linear eigenvalue analysis. Some effects of aeroelastic tailoring, wing frequencies, rigid body modes, static stability margins, and inertia coupling effects were explored.</p> <p>Experimentally, a generic, full-span, 30° forward swept wing aircraft model allowing both rigid body pitch and plunge was constructed and tested in MIT's low speed wind tunnel. The effect of aeroelastic tailoring was demonstrated by using wings with different ply</p>					
20. DISTRIBUTION/AVAILABILITY OF ABSTRACT UNCLASSIFIED/UNLIMITED <input checked="" type="checkbox"/> SAME AS RPT <input type="checkbox"/> DTIC USERS <input type="checkbox"/>			21. ABSTRACT SECURITY CLASSIFICATION UNCLASSIFIED		
22a. NAME OF RESPONSIBLE INDIVIDUAL ANTHONY K AMOS			22b. TELEPHONE NUMBER (Include Area Code) (202) 767-4937		22c. OFFICE SYMBOL AFOSR/NA

layups, namely $[0_2/90]_s$, $[15_2/0]_s$, $[30_2/0]_s$, and $[-15_2/0]_s$, which covered a range of bending-twisting coupling. The wind tunnel tests on these softly restrained "free flying" models revealed body freedom flutter, bending-torsion wing flutter, and a tunnel support related dynamic instability which could be eliminated by proper adjustment of the support stiffness. Good agreement with linear theory was found for all observed instabilities and transient responses. The body freedom flutter boundary followed the same aeroelastic tailoring trends as the cantilever divergence boundary but at a lower speed. Additional tests with only rigid body pitch present showed still lower flutter speeds. The model with $[15_2/0]_s$ wing showed the best tailored aeroelastic behavior of all wings tested.

DYNAMICS AND AEROELASTICITY OF
COMPOSITE STRUCTURES

Gun-Shing Chen
John Dugundji

Technology Laboratory for Advanced Composites
Department of Aeronautics and Astronautics
Massachusetts Institute of Technology
Cambridge, Massachusetts 02139



April 1987

Accession For	
NTIS CRA&I	<input checked="" type="checkbox"/>
DTIC TAB	<input type="checkbox"/>
Unannounced	<input type="checkbox"/>
Justification	
By	
Distribution/	
Availability Codes	
Dist	Avail and/or Special
A1	

Final Report for Period: 1 July 1985 - 30 June 1986

AFOSR No. F49620-84-C-0099

ABSTRACT

An analytical and experimental investigation was made of the aeroelastic flutter and divergence behavior of a forward swept graphite/epoxy wing aircraft with rigid body freedoms in free flight.

Analytically, a transient aeroelastic analysis, using a Rayleigh-Ritz formulation, modified strip theory and measured aircraft aerodynamic derivatives, was developed to predict and interpret the aeroelastic behavior and instability mechanisms. The transient aerodynamics approximated the Theodoresen function by Pade approximants and used augmented state variables to investigate stability by standard linear eigenvalue analysis. Some effects of aerelastic tailoring, wing frequencies, rigid body modes, static stability margins, and inertia coupling effects were explored.

Experimentally, a generic, full-span, 30° forward swept wing aircraft model allowing both rigid body pitch and plunge was constructed and tested in MIT's low speed wind tunnel. The effects of aeroelastic tailoring were demonstrated by using wings with different ply layups, namely $[0_2/90]_s$, $[15_2/0]_s$, $[30_2/0]_s$, and $[-15_2/0]_s$, which covered a range of bending-twisting coupling. The wind tunnel tests on these softly restrained "free flying" models revealed body freedom flutter, bending-torsion wing flutter, and a tunnel support related dynamic instability which could be eliminated by proper adjustment of the support stiffness. Good agreement with linear theory was found for all observed instabilities and transient responses. The body freedom flutter boundary followed the same aeroelastic tailoring trends as the cantilever divergence boundary but at a lower speed. Additional tests with only rigid body pitch present showed still lower flutter speeds. The model with $[15_2/0]_s$ wing showed the best tailored aeroelastic behavior of all wings tested.

FOREWARD

This report describes work done at the Technology Laboratory for Advanced Composites (TELAC) of the Massachusetts Institute of Technology for the Air Force Office of Scientific Research under Contract No. AFOSR F49620-85-C-0099. Dr. Anthony K. Amos was the technical monitor.

The work reported here was performed during the period 1 July 1985 through 30 June 1986, and represents an Sc.D. thesis by Gun-Shing Chen entitled, "Aeroelastic Behavior of Forward Swept Graphite/Epoxy Wing Aircraft with Rigid Body Freedoms", May 1986. The work was done under the supervision of John Dugundji, the Principal Investigator, and included the assistance of an undergraduate student, Karen Needels, and the supporting laboratory staff.

A brief paper based on some of this work entitled, "Experimental Aeroelastic Behavior of Forward Swept Graphite/Epoxy Wings with Rigid Body Freedoms", was presented at the 27th AIAA/ASME/ASCE/AHS Structures, Structural Dynamics and Materials Conference, San Antonio, Texas, May 19-21, 1986, AIAA Paper No. 86-0971, and will be published shortly as an article in the Journal of Aircraft.

TABLE OF CONTENTS

Chapter 1	Introduction	15
Chapter 2	Theory	21
	2.1 Overview	21
	2.2 Aeroelastic Formulation and Analysis	24
	(a) Structural modeling	24
	(b) Transient aerodynamic modeling	30
	(c) Aeroelastic analysis	38
	2.3 Wind Tunnel Support Stability Analysis	40
Chapter 3	Experiment	50
	3.1 Wind Tunnel Model, Support System, and Instrumentation	50
	3.2 Vibration Tests	70
	3.3 Aerodynamic Tests	71
	3.4 Cantilever Wing Flutter Tests	73
	3.5 Body Freedom Flutter Tests	74
Chapter 4	Results	77
	4.1 Model Structural and Aerodynamic Characteristics	77
	4.2 Cantilever Wing Divergence and Flutter	89
	4.3 Body Freedom Flutter	93
	(a) Support instability	93
	(b) Body freedom flutter	99

Chapter 5 Discussion	118
5.1 Summary of Results	118
(a) Aeroelastic tailoring effect	118
(b) Body freedom flutter vs. wing divergence	122
(c) Pitch-plunge testing vs. pitch only testing	124
(d) Analytical correlation	126
5.2 Body Freedom Flutter of Completely Unrestrained Vehicle	135
5.3 Effect of Some Parameters on Body Freedom Flutter	150
(a) Influence of wing frequencies	152
(b) Effect of "rigid" aircraft static margin	154
(c) Inertia coupling effect	157
5.4 Aeroelastic Effect on Support Instability	159
 Chapter 6 Conclusions and Recommendations	 166
 References	 171
 Appendix A Structural Inertia and Stiffness Coefficients	 176
 Appendix B Transient Aerodynamic Coefficients	 183
 Appendix C ω-V Plots	 192

LIST OF FIGURES

<u>FIGURE</u>		<u>PAGE</u>
2.1	Aeroelastic Tailoring Mechanism	23
2.2	Mathematical Model and Axis System	25
2.3	Spanwise Lift-Curve-Slope Distribution	32
2.4	Theodorsen Function Approximation	36
2.5	Simplified Longitudinal Stability Model	41
2.6	Plunge Damping Effect on Support Instability (Root Locus Plot, Rigid Aircraft Model)	48
2.7	ω -V Plot, Original Support, Rigid Aircraft Model	49
3.1	Aircraft Model Layout	51
3.2	Forward Swept Wing Aircraft Model	52
3.3	Forward Swept Graphite/Epoxy Wing	53
3.4	Schematic of Curing Assembly Cross-Section	56
3.5	AS4/3501-6 Graphite/Epoxy Cure Cycle	57
3.6	Wind Tunnel Setup	63
3.7	Wind Tunnel Setup (Picture)	64
3.8	Wing Root Strain Gages Arrangement	67
3.9	Model Pitch Angle Measurement	68
3.10	Model Plunge Height Measurement	69
4.1	Cantilever Wing Vibration Modes, $[0_2/90]_s$ Wing	80
4.2	Cantilever wing Vibration Modes, $[15_2/0]_s$ Wing	81
4.3	Cantilever wing Vibration Modes, $[30_2/0]_s$ Wing	82
4.4	Cantilever wing Vibration Modes, $[-15_2/0]_s$ Wing	83
4.5	Cantilever Load Deflection Curve, $[0_2/90]_s$ Wing	85
4.6	Lift Coefficient for Aircraft Model	87
4.7	Moment Coefficient for Aircraft Model	88

4.8	Cantilever Wing Flutter and Divergence Boundaries	90
4.9	Support Instability, $[0_2/90]_s$ Wing (V= 10 m/sec)	96
4.10	Support Instabilities, $[0_2/90]_s$ Wing	97
4.11	Body Freedom Flutter Onset, $[0_2/90]_s$ Wing	101
4.12	Transient Decay Rate	102
4.13	Body Freedom Flutter, $[0_2/90]_s$ Wing (V= 20 m/sec)	107
4.14	Bending-Torsion Flutter, $[15_2/0]_s$ Wing (V= 29 m/sec)	110
4.15	Body Freedom Flutter, $[30_2/0]_s$ Wing (V= 27 m/sec)	112
4.16	Body Freedom Flutter, $[-15_2/0]_s$ Wing (V= 13 m/sec)	115
5.1	Body Freedom Flutter Boundaries, Model on Modified Support System	121
5.2	Body Freedom Flutter Boundary, Model Free in Pitch-Plunge vs. Pitch Only	125
5.3	ω -V Plot, Modified Support, $[0_2/90]_s$ Wing	129
5.4	ω -V Plot, Modified Support, $[15_2/0]_s$ Wing	131
5.5	ω -V Plot, Modified Support, $[30_2/0]_s$ Wing	133
5.6	ω -V Plot, Modified Support, $[-15_2/0]_s$ Wing	134
5.7	Root Locus Plot, Completely Unrestrained Model with $[0_2/90]_s$ Wing	137
5.8	Root Locus Plot, Completely Unrestrained Model with $[15_2/0]_s$ Wing	139
5.9	Root Locus Plot, Completely Unrestrained Model with $[30_2/0]_s$ Wing	141
5.10	Root Locus Plot, Completely Unrestrained Model with $[-15_2/0]_s$ Wing	143
5.11	Root Locus Comparison, $[0_2/90]_s$ Wing, Completely Unrestrained Model vs. Model on Modified Support	146
5.12	Root Locus Comparison, $[15_2/0]_s$ Wing, Completely	147

Unrestrained Model vs. Model on Modified Support

5.13	Root Locus Comparison, $[30_2/0]_s$ Wing, Completely Unrestrained Model vs. Model on Modified Support	148
5.14	Root Locus Comparison, $[-15_2/0]_s$ Wing, Completely Unrestrained Model vs. Model on Modified Support	149
5.15	Influence of Wing Frequencies on Body Freedom Flutter, $([0_2/90]_s \text{ wing})$	153
5.16	Static Margin Effect on Body Freedom Flutter	156
5.17	Influence of Wing Root Position on Body Freedom Flutter	158
5.18	Pitch Inertia Coupling Effect on Body Freedom Flutter	160
5.19	Plunge Inertia Coupling Effect on Body Freedom Flutter	161
5.20	Aeroelastic Effect on Support Instability	163
A.1	k_{1t} and k_{2t} vs. Effective Aspect Ratio, β	182
C.1	ω -V Plot, Original Support, $[0_2/90]_s$ Wing ($\delta_c = 0^\circ$)	193
C.2	ω -V Plot, Original Support, $[0_2/90]_s$ Wing ($\delta_c = 2.5^\circ$)	194
C.3	ω -V Plot, Original Support, $[0_2/90]_s$ Wing ($\delta_c = 5^\circ$)	195
C.4	ω -V Plot, Model Free in Pitch Only, $[0_2/90]_s$ Wing ($\delta_c = 0^\circ$)	196
C.5	ω -V Plot, Model Free in Pitch Only, $[0_2/90]_s$ Wing ($\delta_c = 2.5^\circ$)	197
C.6	ω -V Plot, Original Support, $[15_2/0]_s$ Wing ($\delta_c = 2.5^\circ$)	198
C.7	ω -V Plot, Original Support, $[15_2/0]_s$ Wing ($\delta_c = 5^\circ$)	199
C.8	ω -V Plot, Model Free in Pitch Only, $[15_2/0]_s$ Wing ($\delta_c = 0^\circ$)	200
C.9	ω -V Plot, Model Free in Pitch Only, $[15_2/0]_s$ Wing ($\delta_c = 2.5^\circ$)	201

C.10	ω -V Plot, Model Free in Pitch Only, $[15_2/0]_s$ Wing ($\delta_c = -2.5^\circ$)	202
C.11	ω -V Plot, Original Support, $[30_2/0]_s$ Wing ($\delta_c = 0^\circ$)	203
C.12	ω -V Plot, Original Support, $[30_2/0]_s$ Wing ($\delta_c = 2.5^\circ$)	204
C.13	ω -V Plot, Model Free in Pitch Only, $[30_2/0]_s$ Wing ($\delta_c = 0^\circ$)	205
C.14	ω -V Plot, Model Free in Pitch Only, $[30_2/0]_s$ Wing ($\delta_c = 2.5^\circ$)	206
C.15	ω -V Plot, Model Free in Pitch Only, $[30_2/0]_s$ Wing ($\delta_c = -2.5^\circ$)	207
C.16	ω -V Plot, Original Support, $[-15_2/0]_s$ Wing ($\delta_c = 0^\circ$)	208
C.17	ω -V Plot, Original Support, $[-15_2/0]_s$ Wing ($\delta_c = 2.5^\circ$)	209
C.18	ω -V Plot, Model Free in Pitch Only, $[-15_2/0]_s$ Wing ($\delta_c = 0^\circ$)	210
C.19	ω -V Plot, Model Free in Pitch Only, $[-15_2/0]_s$ Wing ($\delta_c = 2.5^\circ$)	211
C.20	ω -V Plot, Model Free in Pitch Only, $[-15_2/0]_s$ Wing ($\delta_c = -2.5^\circ$)	212

LIST OF TABLES

<u>TABLE</u>		<u>PAGE</u>
3.1	Graphite/Epoxy Material Properties	54
3.2	Coupling Stiffness and Bending/Torsion Stiffness Ratios of Composite Wings	59
3.3	Aircraft Model and Support Properties	65
4.1	Vibration Frequencies of Cantilever Wings	79
4.2	Calculated Fundamental Frequency and Vibration Mode of Free-Free Wings	86
4.3	Support Instability Boundaries	95
4.4	Calculated Body Freedom Flutter Modes (with modified support system)	104
4.5	Calculated Body Freedom Flutter Modes (model free in pitch only)	106
4.6	Body Freedom Flutter Boundary, $[0_2/90]_s$ Wing	109
4.7	Body Freedom Flutter Boundary, $[15_2/0]_s$ Wing	111
4.8	Body Freedom Flutter Boundary, $[30_2/0]_s$ Wing	113
4.9	Body Freedom Flutter Boundary, $[-15_2/0]_s$ Wing	116
5.1	Summary of Divergence and Flutter Boundaries	119
5.2	Comparison of Body Freedom Flutter Boundaries of Two Different Finite Span Corrections	128
A.1	Mode Shape Integrals	179

NOMENCLATURE

AR	Wing aspect ratio
a_0	Theoretical two-dimensional lift-curve-slope, 2π
b	Streamwise semi-chord length
$C(\bar{p})$	Generalized Theodorsen function
c	Streamwise chord length
C_L, C_M	Lift and moment coefficients of aircraft model
$C_{L_\alpha}, C_{M_\alpha}$ C_{M_α}	Aerodynamic derivatives
C_{l_α}	Sectional lift-curve-slope
D_{ij}	Laminate bending stiffness terms
g_n	Pole locations of approximated airloads
h	sectional mid-chord deflection (+: upward)
I	Aircraft pitch inertia
j	$\sqrt{-1}$
\underline{K}	Stiffness matrix
K_1, K_2	Support plunging and pitching stiffness
k	Reduced frequency, $b\omega/V$

\hat{L}	Transformed sectional lift
L_A	Total lift of rigid aircraft
	Semi-span length
M	Aircraft mass
\bar{M}	Inertia matrix
\hat{M}	Transformed sectional aerodynamic moment
M_A	Total aerodynamic moment of rigid aircraft
M_x, M_y, M_{xy}	Moments per unit length
\hat{N}	Transformed sectional cambering forces
p	Laplace variables, $s+jw$
\bar{p}	Dimensionless Laplace variables, pb/V
$\{Q\}$	Generalized loading vector
q	Dynamic pressure
q_i	Generalized coordinates of assumed modes
S_w	Total wing area includes exposed fuselage area
T	Kinetic energy
U	Potential energy
V	Airspeed

w	Vertical displacement of aircraft
$x-y-z$	Aircraft coordinate system
$\bar{x}-\bar{y}$	Laminated wing coordinate system
y_i	Augmented state variables
α	Sectional rotation (+: leading edge up rotation)
β	Effective wing aspect ratio
$\kappa_x, \kappa_y, \kappa_{xy}$	Curvatures
σ	Real part of Laplace variables
ω	Circular frequency (rad/sec)
ρ	Atmospheric density
Δp	Pressure disturbance
δW_e	Virtual work
δw	Virtual displacement
ξ	Sectional cambering deformation (+: mid-chord downward)
Λ	Wing swept angle (+: aft swept wing)
μ	Mass ratio, $M/\rho S_w c$
ζ_1, ζ_2	Equivalent viscous damping ratios in plunge and pitch freedoms

CHAPTER ONE

INTRODUCTION

In the early history of forward swept wing (FSW) design, e.g., Ju-287 bomber, HFB-320 corporate jet and XFG-1 fuel transport glider, the wing was swept forward moderately for non-performance related purposes and no serious aeroelastic problem arose within their designated flight envelope. For the high speed performance FSW aircraft, the adverse aeroelastic behavior, presumed aeroelastic wing divergence, became critical and virtually impossible to improve without incurring a significant structural weight penalty. Since then, this seemingly insurmountable aeroelastic problem excluded the FSW concept from practical aircraft design. It was not until the 1970's that the FSW concept was revived by the successful development and application of advanced composite materials to conventional aircraft. Its application to the aeroelastic problem of FSW design was first studied by Krone in the mid 1970's [1]. His work turned the key to unlock the FSW's inherent aeroelastic problem. Since then, renewed interests in FSW design have inspired many studies and tests concerning the aeroelastic behavior, aeroelastic tailoring [2-12], and active aeroelastic instability control technology [13,14] for such wing configuration. The X-29 experimental aircraft demonstrates the most visible revisit of the FSW design concept.

Because of the inherent aeroelastic destiffening characteristics of FSW configuration, it is natural to assume that this design would be divergence critical. However, when the fuselage is allowed to participate in the motion, the situation can be markedly different. An aeroelastic/flight dynamic interaction becomes strongly possible due to the attendant aerodynamic stiffening phenomenon of the aircraft short period mode. Such interaction may modify the presumed cantilever wing aeroelastic behavior or even cause additional aeroelastic problems. Therefore, the effect of rigid body freedoms on the aeroelastic behavior of a FSW aircraft is more critical than it is for conventional aircraft.

One of the earliest reports on the subject of rigid body freedom effects was due to Frazer and Duncan in 1929 [15]. Their study showed that fuselage mobility had a negligible effect on the symmetric wing flutter speeds, but significantly increased the antisymmetric wing flutter speed. No flight dynamics involved instability was mentioned in their report.

In the mid 1950s, Gaukroger [16,17] conducted a series of wind tunnel investigations concerning the effect of wing root boundary conditions. His investigations showed that the rigid body effect exists only for the "flying wing" type aircraft with a low value of the fuselage pitching moment of inertia, but rarely exists for a practical, conventional aircraft. These investigations of aft swept and delta wing configurations were summarized in Ref. 18. The term "body freedom flutter" was then commonly used to characterize the instability resulting

from wing bending coupling with rigid body pitching and plunging freedoms. It was also mentioned that symmetric wing flutter is barely influenced by the presence of rigid body freedoms.

In 1954, McLaughlin performed a theoretical investigation of short period dynamic instability with an aft swept elastic wing [19]. He found no dynamic instability due to wing flexibility. In 1955, Cunningham and Lundstrom also described the flutter testing of a rocket mounted straight wing [20]. Their observations revealed a low frequency type instability, involving rigid body motions and wing deformation, in addition to the wing flutter. For the antisymmetric oblique wing aircraft [21], Jones and Nisbet had demonstrated that rigid body freedoms, including roll freedom, are essential to aeroelastic analysis. With the proper ratio of wing roll inertia to fuselage inertia, a low frequency body freedom flutter occurred at a speed greater than the wing divergence speed.

Due to the presumed static aeroelastic wing divergence, the aircraft rigid body freedoms were usually ignored in many of the renewed FSW studies prior to 1980. Recently, however, several authors pointed out significant effects of rigid body freedoms in modifying the cantilever aeroelastic behavior of FSW design. While performing studies for a Rockwell design of an FSW demonstrator, Miller and Wykes discovered a low frequency type instability involving a coupling between the wing divergence mode and the aircraft short period mode [22].

Their analysis showed that the rigid body/wing bending flutter depends on the distance between the wing center of mass and the aircraft center of mass for a typical FSW aircraft. In Ref. 23 this effect was explored on a limited basis by a simple half-plane model without rigid body plunging motion present. Further work on a large, half-plane aircraft model was performed by Chipman et al [24,25] at NASA Langley. Generally, however, the aeroelastic behavior of a free flying FSW aircraft is not yet well understood, and experimental data on this effect is limited.

The mechanism by which cantilever wing divergence could be eliminated or delayed through the use of advanced composite materials is based on the inherent property of advanced composite materials, namely directional stiffness. The application of directional stiffness in structural design for deformation control under aerodynamic loading, or aeroelastic tailoring, is not totally new in aeronautical history. This concept was applied as early as 1949 by Munk in a wooden propeller design [26]. The intended fixed pitch in Munk's design was accomplished by properly orienting the grain of the wood. The other early example was a novel wing design, known as the aero-isoclinic wing, incorporated in the design of Short Sherpa prototype [27]. Aeroelastic tailoring in this case was achieved in part, by placing the torsion-box well back in the wing.

For the past three decades, however, the concept of aeroelastic tailoring was not fully realizable until the

development of advanced composite materials, which have the advantage of easily orienting the stiffness properties, as well as high strength and stiffness to weight ratios. Following the successful application of advanced composite materials to the primary structure of conventional aircraft, such as AV-8B and F-18, the concept of aeroelastic tailoring using advanced composite materials was first applied to a remotely piloted research vehicle [28], HiMAT, in 1978. As in the previous example, the purpose of the aeroelastic tailoring in HiMAT is to maintain the desired aerodynamic shape and aerodynamic performance at varied flight regimes. It is only in the case of a forward swept wing, that aeroelastic tailoring is not only designed for aerodynamic shape control but also aiming at a control of aeroelastic instability

In previous investigations at MIT, the aeroelastic behavior of unswept and forward swept graphite/epoxy cantilever wings was studied experimentally [9,10]. The present investigation extends these investigations to include the effect of rigid body freedoms on the aeroelastic behavior of FSW aircraft. The principal objectives in this investigation are to study the aeroelastic behavior of FSW aircraft and aeroelastic tailoring with advanced composite materials. The research effort consists of extensive "free flying" wind tunnel experiments and analytical investigation. A linear aeroelastic analysis using modified strip theory and measured aircraft aerodynamic derivatives is developed to predict and interpret the experimental aeroelastic behavior. The aeroelastic behavior

of the FSW aircraft is then carefully examined through parametric studies of the verified analytical model. The graphite/epoxy wings, with various degree of bending-twisting coupling, are formulated by a Rayleigh-Ritz approximation. The transient aeroelastic analysis is accomplished by a rational polynomial fit of the Theodorsen function in the Laplace domain. Stability of the wind tunnel support system is carefully analyzed for the "rigid" model. Descriptions of the aforementioned analytical formulation are contained in Chapter 2.

In Chapter 3, details are given of the experimental design, setup and procedure used to detect the aeroelastic behavior of the FSW aircraft model. The results of the experiments are given in Chapter 4. A discussion concerning the correlation of observed aeroelastic behavior and predicted results are included in Chapter 5. Also in Chapter 5, the criticality of body freedom flutter instability is compared with the cantilever wing divergence instability. The effect of aeroelastic tailoring on body freedom flutter is examined for all wings tested. The mutual effect of support instability and body freedom flutter is examined analytically and experimentally. Lastly, parametric trends are predicted for aircraft static margin, ratio of wing pitch inertia to fuselage inertia, and wing frequency. Chapter 6 summarizes the conclusions and recommendations of this investigation. Appendices are given which detail the analytical formulation and wind tunnel experimental results.

CHAPTER TWO

THEORY

2.1 Overview

In the present study, the aeroelastic tailoring concerns the application of advanced composite materials to the control of aeroelastic behavior. From the underlying classical laminated plate theory [29], the out of plane behavior of a symmetric laminate can be analytically described by the laminate constitutive relation as

$$\begin{Bmatrix} M_x \\ M_y \\ M_{xy} \end{Bmatrix} = \begin{bmatrix} D_{11} & D_{12} & D_{16} \\ D_{12} & D_{22} & D_{26} \\ D_{16} & D_{26} & D_{66} \end{bmatrix} \begin{Bmatrix} \kappa_x \\ \kappa_y \\ \kappa_{xy} \end{Bmatrix} \quad (2.1)$$

For the moderate to high aspect ratio wing, the chordwise rigidity is usually assumed. In this case, the most important parameter in the aeroelastic tailoring analysis is the D_{16} term which dictates the bending-twisting coupling, i.e., M_x to κ_{xy} and M_{xy} to κ_x behavior, of a laminated wing structure. Usually this D_{16} term is normalized by the bending stiffness, D_{11} , and torsional stiffness, D_{66} , as $D_{16}/\sqrt{D_{11} D_{66}}$ to indicate the effect of elastic coupling on aeroelastic tailoring [8]. Physically, this coupling stiffness ratio is bounded in between -1 and 1 which can be easily proved from the positiveness

condition of the bending stiffness matrix in Eq. (2.1). For wings with plate-like deformation, e.g., low aspect ratio or highly elastically coupled wing, it should be noted that the D_{26} term will play an increasingly important role in the aeroelastic tailoring mechanism.

A simple example of elastic bending-twisting coupling is given in Figure 2.1. The degree of tailoring, or bending-twisting coupling, is considered to be dominated by the designated major ply orientation as shown in Figure 2.1. In comparing with the wing structural axis, (laminate axis), Figure 2.1.a has the major ply orientation coinciding with the laminate axis, and leads to a vanishing or negligible D_{16} term. Figure 2.1.b and 2.1.c have the major ply orientation rotate toward and away from the wing leading edge respectively, and will consequently have favorable and adverse D_{16} contributions. The deformation coupling will be illustrated by the streamwise sectional twisting as the wing statically bends up. Figure 2.1.a shows a parallel displacement of wing section. Figure 2.1.b has an induced negative angle of attack which tends to restore the wing deformation in the air flow to the original position. Figure 2.1.c shows the induced positive angle of attack and its divergence tendency with airflow. As a result, the ply orientation of Figure 2.1.b will undo the aeroelastic deformation and consequently eliminate or delay the aeroelastic instability. It should be noted that the dynamic type behavior, such as wing flutter, is much more complicated than the simple static mechanism illustrated above. This

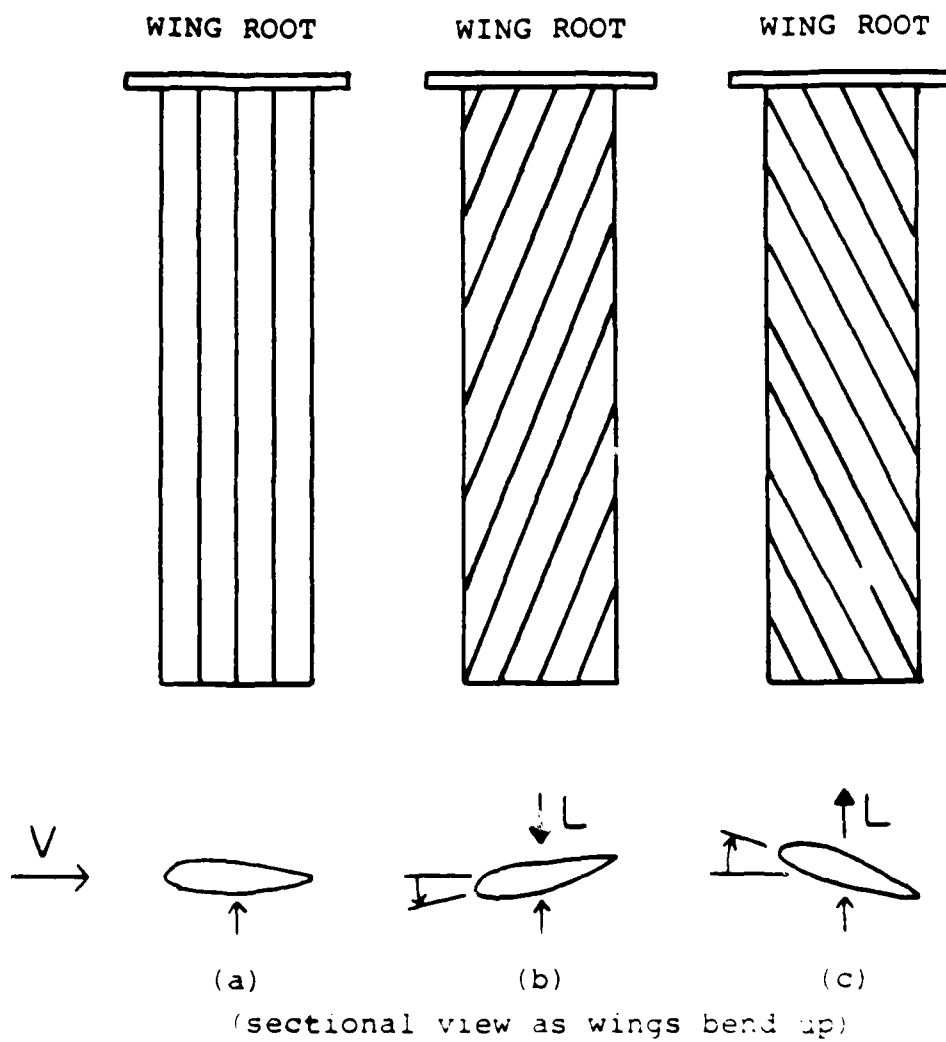


Fig. 2.1 Aeroelastic Tailoring Mechanism

simple static example, however, should provide understanding of the underlying mechanism and initial trends of the aeroelastic tailoring.

2.2 Aeroelastic Formulation and Analysis

The flutter analysis of an aircraft in steady flight is formulated by the Rayleigh-Ritz approximation. The development of the mathematical model governing the uncoupled longitudinal motions considers small disturbances from a steady rectilinear flight. The small disturbances include the vehicle rigid body motions and elastic deformations, and are described in an axis system moving steadily with the vehicle in still air. For steady level flight, the axis system can be considered fixed in space while the air is flowing in the opposite direction at constant speed, and is identical to the tunnel support axis system as shown in Figure 2.2. To isolate and emphasize the effect of wing aeroelastic behavior, the analysis hypothesizes a rigid aircraft with the only flexible component being the wing. The governing equation of the aeroelastic system is derived by the energy method, i.e., a Rayleigh-Ritz type formulation. This method has the advantage of using an axis system which does not coincide with the center of mass of the deformed configuration.

(a) Structural Modeling

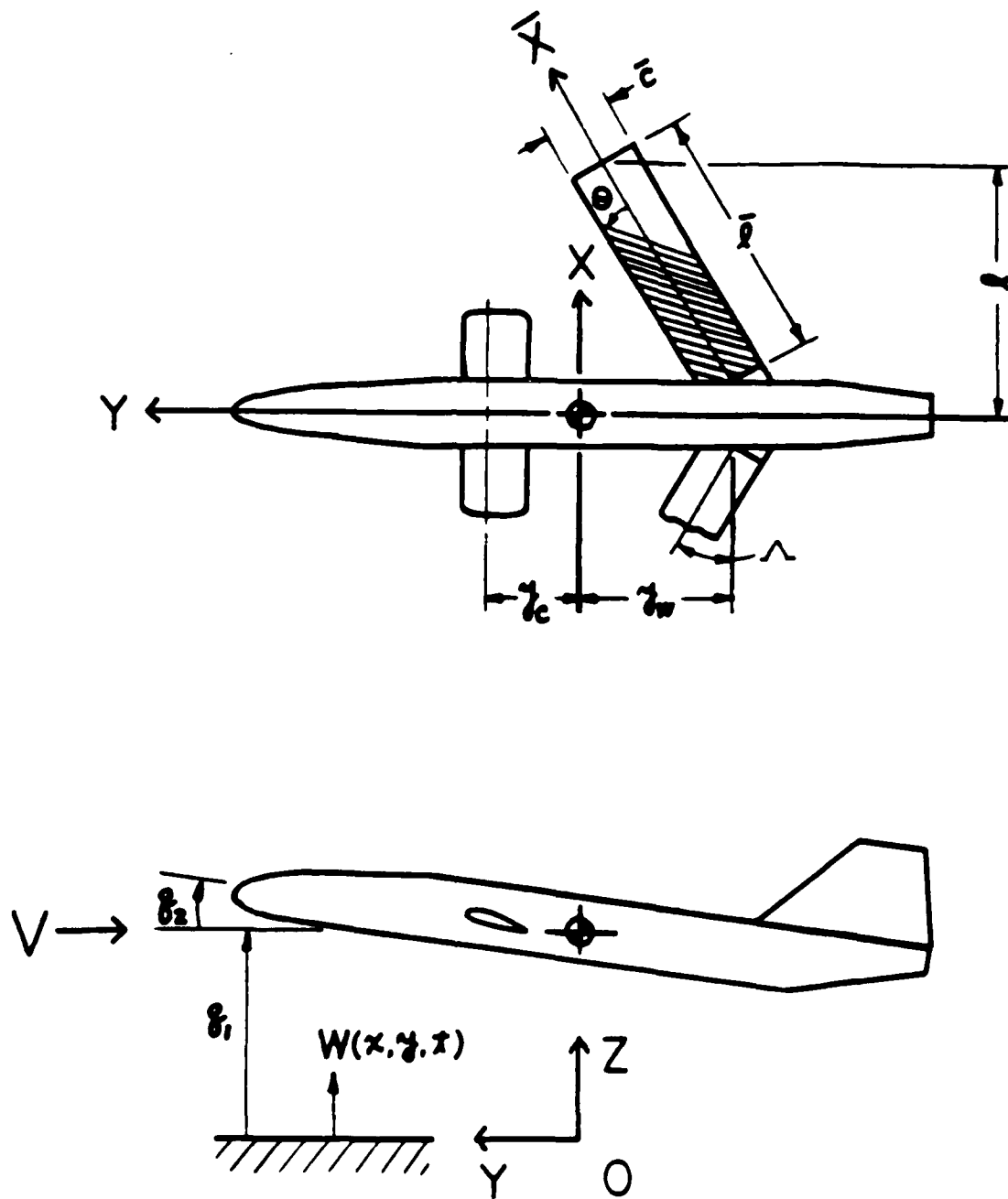


Fig. 2.2 Mathematical Model and Axis System

Any vertical displacement of the vehicle with respect to a space-fixed horizontal plane is approximated by a superposition of finite number of assumed modes, i.e.,

$$\begin{aligned}w(x,y,t) &= \sum_{i=1}^N r_i(x,y) q_i(t) \\ &= \sum_{i=1}^N \phi_i(x) \psi_i(y) q_i(t)\end{aligned}\tag{2.2}$$

where N is the number of assumed modes. The assumed modes, $r_i(x,y)$, include aircraft vertical translation (plunging) and pitching displacement about the undeformed aircraft center of gravity, and elastic wing component modes. The elastic wing component modes, conveniently expressed in the wing coordinate system, represent wing deformations relative to the wing root position for the rigid fuselage assumption. The degree of accuracy provided by the Rayleigh-Ritz type analysis depends entirely upon the choice and number of modes. For example, the use of unrestrained normal modes will give more accurate results and fast convergence. It is, however, structurally and aerodynamically convenient to use the uncoupled beam-type bending and torsional modes for the equivalent plate model. In addition, Ref. 30 has revealed the importance of the additional chordwise mode in modeling vibration analysis of an anisotropic plate. Using the same assumed wing component modes in Refs. 9 and 10, the seven assumed modes are

$$\begin{aligned}
 \phi_1(x) &= 1 & \psi_1(y) &= 1 \\
 \phi_2(x) &= 1 & \psi_2(y) &= y \\
 \phi_3(\bar{x}) &= \cosh(\epsilon_1 \bar{x}/\bar{\ell}) - \cos(\epsilon_1 \bar{x}/\bar{\ell}) & \psi_3(\bar{y}) &= 1 \\
 & - \alpha_1 [\sinh(\epsilon_1 \bar{x}/\bar{\ell}) - \sin(\epsilon_1 \bar{x}/\bar{\ell})] \\
 \phi_4(\bar{x}) &= \sin(\pi \bar{x}/2\bar{\ell}) & \psi_4(\bar{y}) &= \bar{y}/\bar{c} \\
 \phi_5(\bar{x}) &= \cosh(\epsilon_2 \bar{x}/\bar{\ell}) - \cos(\epsilon_2 \bar{x}/\bar{\ell}) & \psi_5(\bar{y}) &= 1 \\
 & - \alpha_2 [\sinh(\epsilon_2 \bar{x}/\bar{\ell}) - \sin(\epsilon_2 \bar{x}/\bar{\ell})] \\
 \phi_6(\bar{x}) &= \sin(3\pi \bar{x}/2\bar{\ell}) & \psi_6(\bar{y}) &= \bar{y}/\bar{c} \\
 \phi_7(\bar{x}) &= \bar{x}/\bar{\ell}(1-\bar{x}/\bar{\ell}) & \psi_7(\bar{y}) &= 4(\bar{y}/\bar{c})^2 - \frac{1}{3}
 \end{aligned} \tag{2.3}$$

where $\epsilon_1 = 1.8751$, $\alpha_1 = 0.7341$, $\epsilon_2 = 4.6941$ and $\alpha_2 = 1.0185$.

The derivation of governing differential equations involves the evaluation of kinetic energy, T , and potential energy, U , and the use of Lagrange's equation, i.e.,

$$\frac{d}{dt} \left(\frac{\partial L}{\partial \dot{q}_i} \right) - \frac{\partial L}{\partial q_i} = Q_i \quad \text{for } i=1 \text{ to } 7 \tag{2.4}$$

where $L = T - U$ and Q_i 's are the generalized forces obtained via the virtual work expression. The kinetic energy of an unrestrained aircraft is

$$T = \frac{1}{2} \iint_{A/C} m_A \dot{w}^2 dx dy \tag{2.5}$$

where $(\dot{}) = d/dt$ and m_A is the mass per area in x - y plane.

Because of the zero potential energy associated with the aircraft rigid body motions, the total potential energy contains only the strain energy of the elastic wing. In practice, only the out of plane deformation is relevant to the aerodynamic operator. Therefore, only the bending strain energy will be evaluated for a symmetric laminate plate wing, i.e.,

$$U = \frac{1}{2} \iint_{\text{wing}} \left[D_{11} w_{,\bar{x}\bar{x}}^2 + 2D_{12} w_{,\bar{x}\bar{x}} w_{,\bar{y}\bar{y}} + D_{22} w_{,\bar{y}\bar{y}}^2 + 4D_{16} w_{,\bar{x}\bar{x}} w_{,\bar{x}\bar{y}} + 4D_{26} w_{,\bar{y}\bar{y}} w_{,\bar{x}\bar{y}} + 4D_{66} w_{,\bar{x}\bar{y}}^2 \right] d\bar{x} d\bar{y} \quad (2.6)$$

where $w_{,\bar{x}}$ denotes $\partial w / \partial \bar{x}$ and so on, and the D_{ij} 's are laminate bending stiffness terms derived from classical laminate plate theory [29]. Substituting Eq. (2.2) into (2.5) and (2.6), one obtains the kinetic and potential energy in terms of generalized coordinates as

$$T = \frac{1}{2} \sum_{i=1}^7 \sum_{j=1}^7 m_{ij} \dot{q}_i \dot{q}_j$$

$$U = \frac{1}{2} \sum_{i=1}^7 \sum_{j=1}^7 k_{ij} q_i q_j \quad (2.7)$$

where

$$\begin{aligned}
 m_{ij} &= \iint_{A/C} m_A \gamma_i \gamma_j dx dy \\
 k_{ij} &= \iint_{\text{wing}} \left[D_{11} \gamma_{i, \bar{x}\bar{x}} \gamma_{j, \bar{x}\bar{x}} + D_{22} \gamma_{i, \bar{y}\bar{y}} \gamma_{j, \bar{y}\bar{y}} \right. \\
 &\quad + 4D_{66} \gamma_{i, \bar{x}\bar{y}} \gamma_{j, \bar{x}\bar{y}} \\
 &\quad + D_{12} (\gamma_{i, \bar{x}\bar{x}} \gamma_{j, \bar{y}\bar{y}} + \gamma_{j, \bar{x}\bar{x}} \gamma_{i, \bar{y}\bar{y}}) \\
 &\quad + 2D_{16} (\gamma_{i, \bar{x}\bar{x}} \gamma_{j, \bar{x}\bar{y}} + \gamma_{j, \bar{x}\bar{x}} \gamma_{i, \bar{x}\bar{y}}) \\
 &\quad \left. + 2D_{26} (\gamma_{i, \bar{y}\bar{y}} \gamma_{j, \bar{x}\bar{y}} + \gamma_{j, \bar{y}\bar{y}} \gamma_{i, \bar{x}\bar{y}}) \right] d\bar{x} d\bar{y} \quad (2.8)
 \end{aligned}$$

Appendix A details the inertia and stiffness coefficients. In analyzing the tunnel restrained configuration, the additional potential energy terms are added as

$$U = \frac{1}{2} K_1 q_1^2 + \frac{1}{2} K_2 q_2^2 \quad (2.9)$$

where K_1 and K_2 are the support plunge and pitch spring constants. Placing Eq. (2.7) and (2.9) into Eq. (2.4) results in a set of differential equations of motion of the flexible aircraft as

$$\underline{M} \{\ddot{q}\} + \underline{K} \{q\} = \{Q\} \quad (2.10)$$

where $\{q\} = [q_1, q_2, q_3, q_4, q_5, q_6, q_7]^T$.

(b) Transient Aerodynamic Modeling

For the purposes of the present study, it is intended to develop an accurate and relatively easy flutter analysis tool to interpret and correlate the experimental aeroelastic behavior of a three-dimensional vehicle configuration. The two-dimensional incompressible aerodynamic theory, including camber oscillation [31], is hence chosen even though there exists advanced but computationally complicated unsteady aerodynamic theory. To compensate the shortcoming of using two-dimensional aerodynamic tool for a complicated vehicle configuration, two modifications are made to the proposed aerodynamic tool. One is the so-called "modified strip theory" [32] which accounts for finite span effect by using the spanwise lift-curve-slope distribution. The static lift-curve-slope distribution is obtained by Weissinger L-method with constant angle of attack across the span [33]. This approximate procedure uses a lifting-line type of representation of vortex sheet, but satisfies downwash boundary condition at the three-quarter chord point of each spanwise station. This implies a lift-curve-slope of 2π in the specializing case of a two-dimensional airfoil. In Ref. 33, charts of the necessary influence coefficients, which facilitate wing loading calculation, are presented. Although the procedure in Ref. 33 involves the evaluation of wing loading at only seven spanwise stations, Multhopp integration points, the resulting accuracy is considered adequate for the

present purpose, and the method is used because of its simplicity.

For the present aircraft model, 30° forward swept wing with aspect ratio of seven, the symmetric lift-curve-slope are given at four Multhopp integration station (semi-span) as

$$\begin{aligned}C_{l_{\alpha}} &= 2.20 \text{ at } 92\% \text{ semi-span} \\C_{l_{\alpha}} &= 3.63 \text{ at } 70\% \text{ semi-span} \\C_{l_{\alpha}} &= 4.54 \text{ at } 38\% \text{ semi-span} \\C_{l_{\alpha}} &= 5.74 \text{ at fuselage centerline}\end{aligned}$$

The spanwise lift-curve-slope distribution used in the flutter analysis is then interpolated at ten equally divided wing spans as shown in Figure 2.3 which gives an average value of 4.07 across the full-span.

The spanwise distributions of the lift and moment on the deformed wing are then found by using the aforementioned values of static sectional lift-curve-slope in conjunction with the effective angle of attack distribution resulting from wing oscillation. As suggested in Ref. 32, the proposed modification should be applied only to cases involving low to moderate reduced frequencies. The examination of the results of flutter analysis is necessary to validate the assumption.

The other modification is intended to account for the canard/wing/fuselage interaction by using the "rigid" aircraft lift and moment characteristics measured experimentally. The total lift and moment associated with the rigid body motions are then evaluated by using measured aerodynamic derivatives,

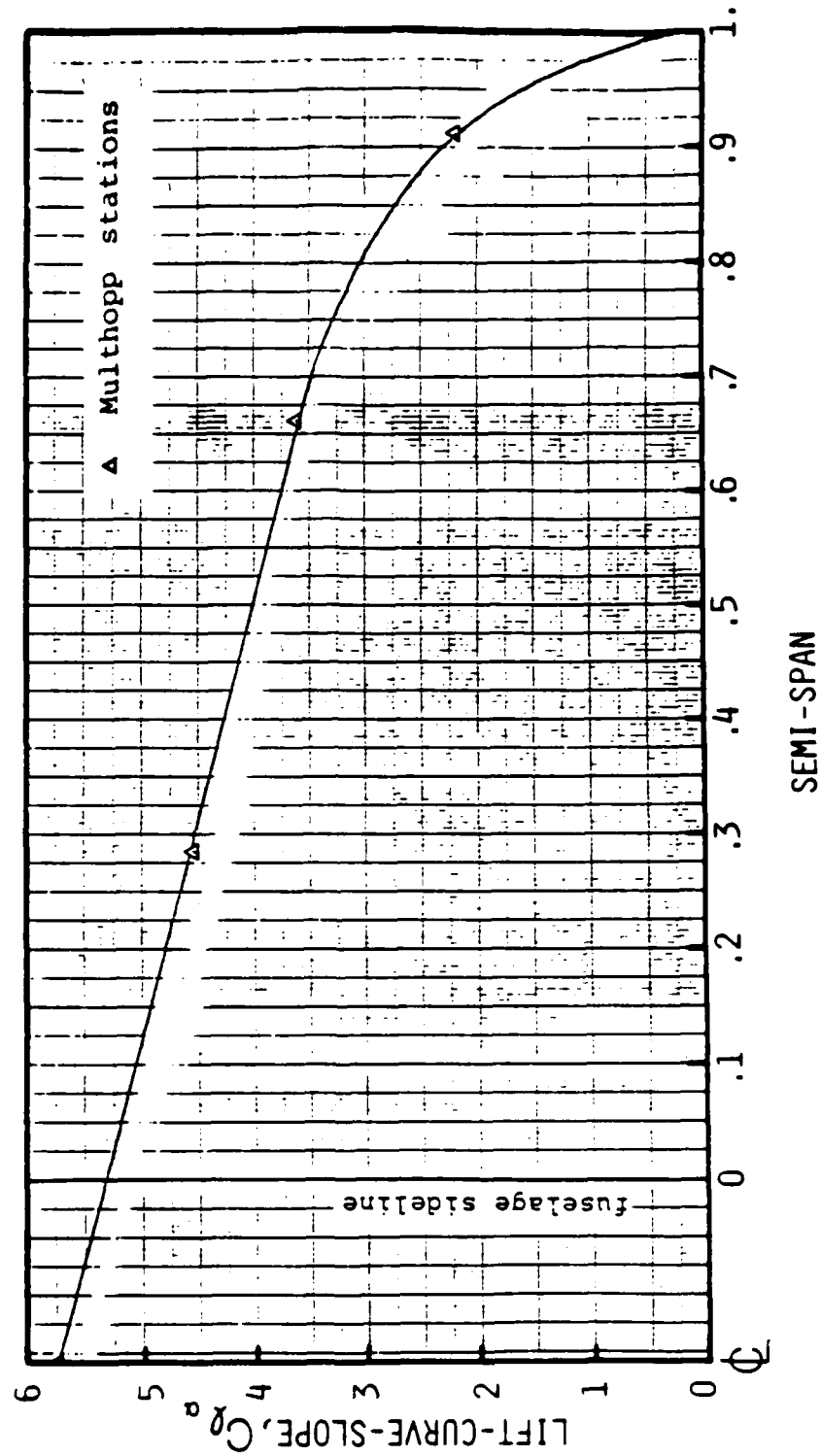


Fig. 2.3 Spanwise Lift-Curve-Slope Distribution

C_{L_α} , C_{M_α} , and C_{M_α} , as

$$\begin{aligned} L_A &= q S_w C_{L_\alpha} (q_2 - \dot{q}_1/V) - q S_w c C_{M_\alpha} \dot{q}_2/V \\ M_A &= q S_w c C_{M_\alpha} (q_2 - \dot{q}_1/V) + q S_w c^2 C_{M_\alpha} \dot{q}_2/V \end{aligned} \quad (2.11)$$

where q is the dynamic pressure, S_w and c are the total wing area and mean aerodynamic chord length respectively.

The transient aerodynamic coefficients are then derived from the expression of virtual work due to pressure disturbance as

$$\delta W_e = \iint_{A/C} \Delta p \delta w(x,y) dx dy \quad (2.12)$$

In light of the proposed semi-analytical aerodynamic tool, it is convenient to decompose the virtual work contribution into "body" and "wing" parts as

$$\begin{aligned} \delta W_e &= \int_{A/C} \Delta p \delta w dx dy \\ &= L_{body} \delta q_1 + M_{body} \delta q_2 + \int_{wing} \Delta P \delta w dx dy \end{aligned} \quad (2.13)$$

where "body" denotes contributions from canard/fuselage contribution. Incorporating wing airloads described by the modified streamwise-strip theory, the virtual work expression

is then

$$\begin{aligned}\delta W_e &= L_{\text{body}} \delta q_1 + M_{\text{body}} \delta q_2 + \int_{\text{wing}} (L \delta h + M \delta \alpha + N \delta \xi) dx \\ &= \sum_{i=1}^7 Q_i \delta q_i\end{aligned}\quad (2.14)$$

where L , M and N are sectional forces and moments, and h , α , and ξ represent sectional deformations defined at sectional mid-chord position. For a Rayleigh-Ritz type analysis, the spanwise variation of sectional deformations are defined and expressed in terms of the assumed modes q_i as,

$$\begin{aligned}h &= q_1 + (y_w - \bar{x} \sin \Lambda) q_2 + \phi_3 q_3 + \phi_5 q_5 = \sum_{i=1}^7 \eta_i q_i \\ \alpha &= q_2 - (\phi_3' \bar{x} q_3 + \phi_5' \bar{x} q_5) \sin \Lambda + \frac{1}{c} (\phi_4 q_4 + \phi_6 q_6) \cos \Lambda \\ &= \sum_{i=1}^7 \theta_i q_i \\ \xi &= \phi_7 q_7 = \sum_{i=1}^7 \zeta_i q_i\end{aligned}\quad (2.15)$$

Since the streamwise section is not normal to the structural span of a swept wing, the sectional twist and camber change are closely approximated by the assumed modes in Eq. (2.15). In here, Λ and y_w are both negative values for the forward swept wing aircraft shown in Figure 2.2.

In studying the interaction between elastic and rigid body motions, not only the instability onset but also the aircraft

flying quality are of great concern [34]. The aircraft flying quality is characterized by its transient behavior such as decay rate, natural modes and frequencies. To describe these transient characteristics, airloads due to arbitrary wing motions, instead of harmonic airloads, must be used. One such method, in two-dimensional incompressible flow, is to approximate the generalized Theodorsen function, $C(\bar{p})$, in the Laplace domain by a rational polynomial,

$$C(\bar{p}) = \frac{b_1 \bar{p} + b_0}{\bar{p} + b_0} \quad (2.16)$$

where $b_1 = 0.55$, $b_0 = 0.15$, \bar{p} is the dimensionless Laplace variable $\bar{p} = pb/V$, and $p = \sigma + j\omega$. The above single pole approximation gives a reasonable fit to the Theodorsen function over the reduced frequency $k = b\omega/V$ from 0 to 1 as shown in Figure 2.4. It should be noted that the high frequency asymptote of the above approximation approaches 0.55 instead of the exact value of 0.50 which suggests some inaccuracy of the current approximation outside the low reduced frequency range. For the present study, the reduced frequency of body freedom flutter ranges from 0.02 to 0.05. The transformed airloads, as detailed in Appendix B, can then be described in the Laplace domain as

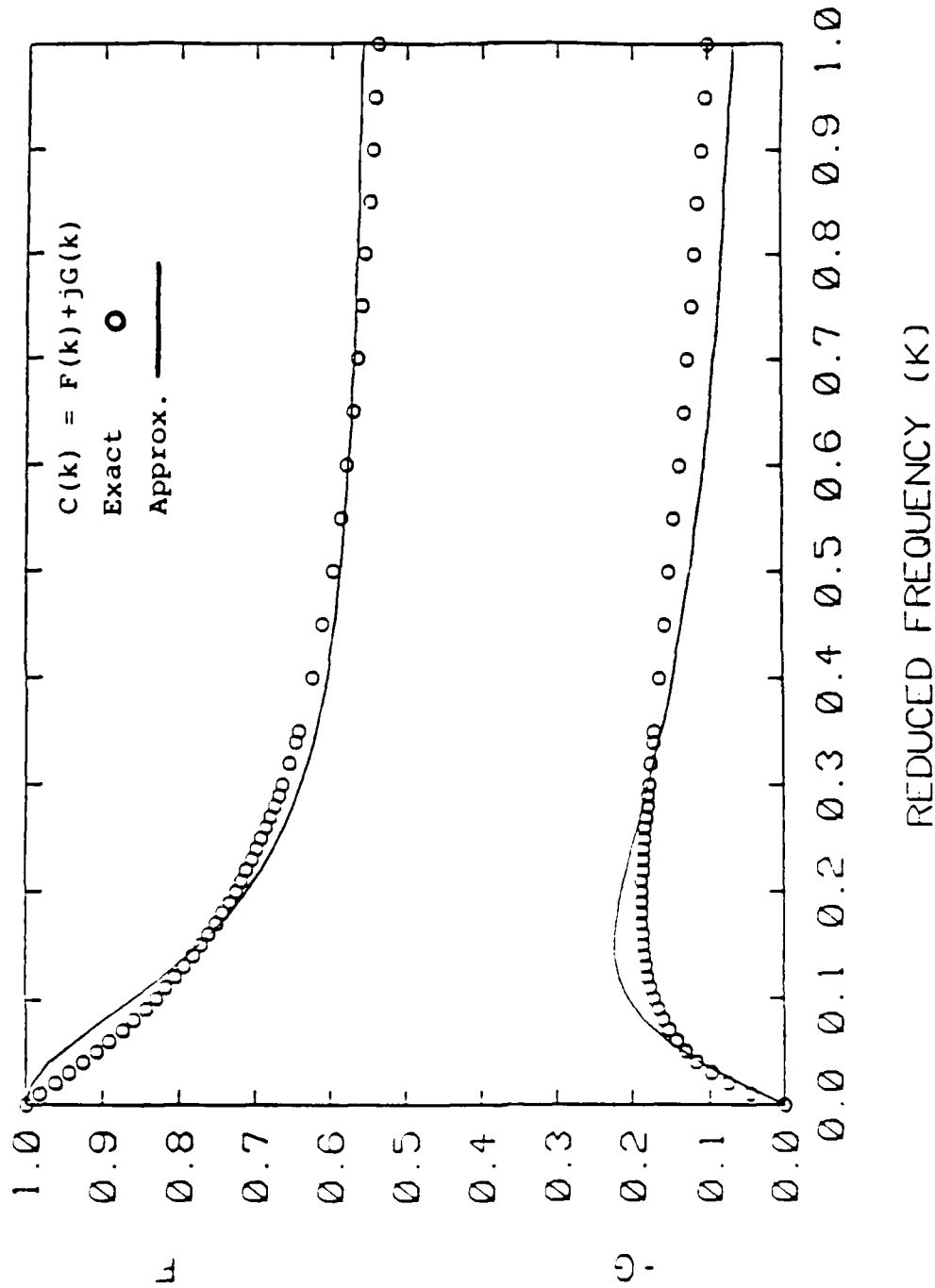


Fig. 2.4 Theodorsen Function Approximation

$$\begin{aligned} \hat{L}(\bar{p}) = & c_{\ell_{\alpha}} \rho v^2 b \\ & \left\{ \left[B_{2A} \bar{p}^2 + B_{1A} \bar{p} + B_{0A} + B_{3A} \bar{p}/(\bar{p}+b_0) \right] \hat{h}/b \right. \\ & + \left[B_{2B} \bar{p}^2 + B_{1B} \bar{p} + B_{0B} + B_{3B} \bar{p}/(\bar{p}+b_0) \right] \hat{\alpha} \\ & \left. + \left[B_{2C} \bar{p}^2 + B_{1C} \bar{p} + B_{0C} + B_{3C} \bar{p}/(\bar{p}+b_0) \right] \hat{\xi}/b \right\} \quad (2.17) \end{aligned}$$

$$\hat{M}(\bar{p}) = c_{\ell_{\alpha}} \rho v^2 b^2 \left\{ \left[\cdot \cdot \right] \hat{h}/b + \left[\cdot \cdot \right] \hat{\alpha} + \left[\cdot \cdot \right] \hat{\xi}/b \right\}$$

$$\hat{N}(\bar{p}) = c_{\ell_{\alpha}} \rho v^2 b \left\{ \left[\cdot \cdot \right] \hat{h}/b + \left[\cdot \cdot \right] \hat{\alpha} + \left[\cdot \cdot \right] \hat{\xi}/b \right\}$$

where the B_{2A} , B_{1A} , B_{0A} and B_{3A} etc represent the aerodynamic virtual mass, damping, stiffness and lag terms respectively, and $c_{\ell_{\alpha}}$ is the streamwise sectional lift-curve-slope. Placing Eq. (2.17) into (2.14), introducing h , α and ξ from Eq. (2.15), and defining new augmented state variables y_i such that

$$\hat{y}_i(\bar{p}) = \frac{\bar{p}}{\bar{p} + b_0} \hat{q}_i(\bar{p}) \quad \text{for } i = 1 \text{ to } 7 \quad (2.18)$$

allows one to take the inverse Laplace transform and write the generalized aerodynamic forces in transient form as

$$Q_i = \sum_{j=1}^7 \left(Q_{ij}^A \ddot{q}_j + Q_{ij}^B \dot{q}_j + Q_{ij}^C q_j + Q_{ij}^D y_j \right) \quad (2.19)$$

and

$$\dot{y}_i + \frac{b_0 V}{b} y_i = \dot{q}_i \quad \text{for } i = 1 \text{ to } 7 \quad (2.20)$$

where Q_{ij} 's are the aerodynamic coefficients detailed in Appendix B.

(c) Aeroelastic Analysis

The augmented states, introduced in the transient airloads modeling, increase the order of the system but allow the convenience of linear eigenvalue analysis of the constant coefficient ordinary differential equations. Placing Eq. (2.19) into (2.10) and incorporating the additional governing equations of aerodynamic lags, the resulting aeroelastic equation of motion are then expressed in the state variable form as

$$\begin{bmatrix} \underline{I} & 0 & 0 \\ 0 & (\underline{M} - \underline{Q}^A) & 0 \\ 0 & 0 & \underline{I} \end{bmatrix} \begin{bmatrix} \dot{\underline{q}} \\ \dot{\underline{q}} \\ \dot{\underline{y}} \end{bmatrix} = \begin{bmatrix} 0 & \underline{I} & 0 \\ (\underline{Q}^C - \underline{K}) & (\underline{Q}^B - \underline{C}) & \underline{Q}^D \\ 0 & \underline{I} & -\underline{H} \end{bmatrix} \begin{bmatrix} \underline{q} \\ \dot{\underline{q}} \\ \underline{y} \end{bmatrix} \quad (2.21)$$

where \underline{I} is the identity matrix and $\underline{H} = b_0 V / b \underline{I}$. This yields a set of twenty-one first order differential equations. For given values of dynamic pressure, the transient behavior and stability characteristics are determined by setting $\underline{q} = \hat{\underline{q}} e^{pt}$, $\underline{y} = \hat{\underline{y}} e^{pt}$, and finding the eigenvalues p of Eq. (2.21). The flutter and divergence boundaries are determined by solving the

successive eigenvalue problems until the instabilities occur. The transient aeroelastic behavior is represented by the successive eigenvalues and eigenvectors. If the assumed elastic modes are set equal to zero, the above stability analysis reduces identically to the rigid aircraft dynamic stability analysis in the space-fixed axis system.

Also, it is to be noted that since modern control theory is well developed for systems described by finite order, constant coefficient ordinary differential equations, the other motivation for using transient airload expressions is the potential of active control design interaction with the aeroelastic analysis.

For comparison purposes, the cantilever wing flutter and divergence analyses can be performed by setting rigid body modes to zero. For wing divergence analysis, the finite span effect will be accounted for by applying an overall correction factor suggested in Ref. 35 as

$$\frac{d}{d\alpha} C_L = a_0 \frac{AR}{AR + 4} \quad (2.22)$$

where a_0 is the two-dimensional lift-curve-slope for incompressible flow, 2π , and AR is the aspect ratio, $2\ell/c$ of the wing. This is equivalent to modifying the wing divergence speed V_D , found from the 2π lift-curve-slope, by the square root of the overall correction factor as

$$(V_D)_{AR} = \sqrt{\frac{AR + 4}{AR}} (V_D)_{2\pi} \quad (2.23)$$

For the cantilever wing flutter analysis, no finite span correction is used. This is because of the close resemblance to two-dimensional airload distribution due to the high frequency wing oscillatory motion at flutter condition.

2.3 Wind Tunnel Support Stability Analysis

In a "free flight" wind tunnel test, the support system not only physically restrains the model freedoms, but may also influence the overall dynamic characteristics and corresponding testing results. Without careful consideration of the support system dynamics, the testing results may be contaminated and an additional support instability may exist. For such "free flight" wind tunnel tests, various remedies have been developed as "ad hoc" compensation schemes with some degree of success, but no clear analytical explanation has been given.

A simplified longitudinal stability analysis model is shown in Figure 2.5. The aircraft model is considered to be "rigid" in this analysis. This support configuration provides freedoms in vertical translation, pitch and yaw motions. With the assumptions of small disturbances, the governing equations for the longitudinal mode are

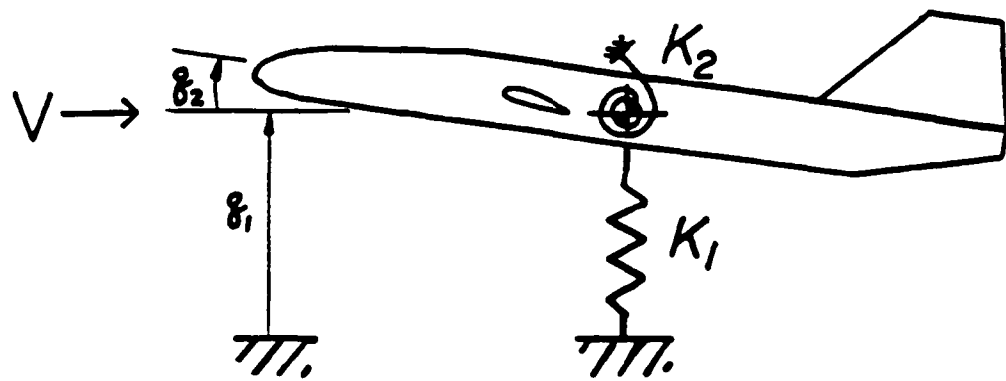


Fig. 2.5 Support Longitudinal Stability Model

$$\begin{aligned} M \ddot{q}_1 + K_1 q_1 &= L_A \\ I \ddot{q}_2 + K_2 q_2 &= M_A \end{aligned} \quad (2.24)$$

where M and I are model mass and pitch moment of inertia, and K_1 , K_2 are the support plunging and pitching stiffness constants. The yaw motion is uncoupled here from the longitudinal motion, i.e., plunge and pitch. Placing Eq. (2.11), L_A and M_A , into (2.24), the equation of motion becomes

$$\begin{aligned} M \ddot{q}_1 + K_1 q_1 &= q S_w C_{L_\alpha} (q_2 - \dot{q}_1/V) - q S_w c C_{M_\alpha} \dot{q}_2/V \\ I \ddot{q}_2 + K_2 q_2 &= q S_w c C_{M_\alpha} (q_2 - \dot{q}_1/V) + q S_w c^2 C_{M_\alpha} \dot{q}_2/V \end{aligned} \quad (2.25)$$

Using the following set of nondimensional parameters,

$$\begin{aligned} \tilde{q}_1 &= q_1/c & \tilde{\omega}_1 &= \omega_1/\omega_r & \tau &= \omega_r t \\ \tilde{q}_2 &= q_2 & \tilde{\omega}_2 &= \omega_2/\omega_r & \bar{V} &= \frac{V}{\omega_r c} \\ \mu &= \frac{M}{\rho S_w c} & r_g^2 &= \frac{I}{M c^2} \end{aligned} \quad (2.26)$$

the dimensionless equations of motion are obtained as

$$\ddot{\tilde{q}}_1 + 2\zeta_1 \tilde{\omega}_1 \dot{\tilde{q}}_1 + \tilde{\omega}_1^2 \tilde{q}_1 = - \frac{\bar{v}^2}{2\mu} \left(c_{L_\alpha} \frac{\dot{\tilde{q}}_1}{\bar{v}} + c_{M_\alpha} \frac{\dot{\tilde{q}}_2}{\bar{v}} - c_{L_\alpha} \tilde{q}_2 \right) \quad (2.27)$$

$$\ddot{\tilde{q}}_2 + 2\zeta_2 \tilde{\omega}_2 \dot{\tilde{q}}_2 + \tilde{\omega}_2^2 \tilde{q}_2 = - \frac{\bar{v}^2}{2\mu r_g^2} \left(c_{M_\alpha} \frac{\dot{\tilde{q}}_1}{\bar{v}} - c_{M_\alpha} \frac{\dot{\tilde{q}}_2}{\bar{v}} - c_{M_\alpha} \tilde{q}_2 \right)$$

where $(\dot{}) = d/d\tau$ and ω_r is the reference frequency. The modal viscous damping ratios, ζ_1 and ζ_2 , are introduced into Eq. (2.27) to account for the dissipating force and moment in the support system. Rearrange Eq. (2.27) into matrix form as

$$\begin{Bmatrix} \ddot{\tilde{q}}_1 \\ \ddot{\tilde{q}}_2 \end{Bmatrix} + \begin{bmatrix} c_{11} & c_{12} \\ c_{21} & c_{22} \end{bmatrix} \begin{Bmatrix} \dot{\tilde{q}}_1 \\ \dot{\tilde{q}}_2 \end{Bmatrix} + \begin{bmatrix} k_{11} & k_{12} \\ k_{21} & k_{22} \end{bmatrix} \begin{Bmatrix} \tilde{q}_1 \\ \tilde{q}_2 \end{Bmatrix} = \begin{Bmatrix} 0 \\ 0 \end{Bmatrix} \quad (2.28)$$

where

$$\begin{aligned}
 c_{11} &= 2\zeta_1 \tilde{\omega}_1 + \frac{1}{2\mu} c_{L_\alpha} \bar{v} & c_{12} &= \frac{1}{2\mu} c_{M_\alpha} \bar{v} \\
 c_{21} &= \frac{1}{2\mu r_g^2} c_{M_\alpha} \bar{v} & c_{22} &= 2\zeta_2 \tilde{\omega}_2 - \frac{1}{2\mu r_g^2} c_{M_\alpha} \bar{v} \\
 k_{11} &= \tilde{\omega}_1^2 & k_{12} &= -\frac{1}{2\mu} c_{L_\alpha} \bar{v}^2 \\
 k_{21} &= 0 & k_{22} &= \tilde{\omega}^2 - \frac{1}{2\mu r_g^2} c_{M_\alpha} \bar{v}^2
 \end{aligned} \tag{2.29}$$

For a linear stability problem, assuming solution in a form of $e^{\tilde{p}\tau}$ yields the stability characteristic equation as

$$\det \begin{vmatrix} (\tilde{p}^2 + c_{11}\tilde{p} + k_{11}) & (c_{12}\tilde{p} + k_{12}) \\ (c_{21}\tilde{p} + k_{21}) & (\tilde{p}^2 + c_{22}\tilde{p} + k_{22}) \end{vmatrix} = 0 \tag{2.30}$$

or

$$E_4 \tilde{p}^4 + E_3 \tilde{p}^3 + E_2 \tilde{p}^2 + E_1 \tilde{p} + E_0 = 0 \tag{2.31}$$

and

$$\begin{aligned}
 E_4 &= 1 \\
 E_3 &= C_{11} + C_{22} \\
 E_2 &= K_{11} + K_{22} + C_{11}C_{22} - C_{12}C_{21} \\
 E_1 &= K_{11}C_{22} + K_{22}C_{11} - K_{12}C_{21} \\
 E_0 &= K_{11}K_{22}
 \end{aligned} \tag{2.32}$$

The support system stability can then be determined by examining the real part of all the roots of Eq. (2.31). For a fourth order polynomial with multiple parameters embedded in its coefficients, one can determine the roots directly for given values of parameters. By doing so, however, the parameter dependency and the intrinsic mechanism of stability may be lost.

To obtain a closed form stability criterion without losing its generality, the equation of motion is simplified by ignoring the viscous damping ratios, ζ_1 and ζ_2 , and aerodynamic derivative $C_{M_{\alpha}}$. By determining the sign of the real part of all the roots, the Routh-Hurwitz criterion is useful in giving a stability condition in terms of polynomial coefficients and system parameters. The real part of all the roots are negative, hence asymptotically stable, if and only if all the coefficients E_4, E_3, E_2, E_1, E_0 and the discriminant $D = E_1E_2E_3 - E_0E_3^2 - E_4E_1^2$ are positive. Placing Eq. (2.29) into (2.32), the coefficients E_i and discriminant D become

$$\begin{aligned}
 E_4 &= 1 \\
 E_3 &= \frac{1}{2\mu} C_{L_\alpha} \bar{V} \\
 E_2 &= \bar{\omega}_1^2 + \bar{\omega}_2^2 - \frac{C_{M_\alpha}}{2\mu r_g^2} \left(1 + \frac{1}{2\mu} C_{M_\alpha}\right) \bar{V}^2 \\
 E_1 &= \bar{\omega}_1^2 \frac{1}{2\mu} C_{L_\alpha} \bar{V} \\
 E_0 &= \bar{\omega}_1^2 \left(\bar{\omega}_2^2 - \frac{1}{2\mu r_g^2} C_{M_\alpha} \bar{V}^2 \right) \\
 D &= \bar{\omega}_2^2 \frac{1}{8\mu^3 r_g^2} C_{L_\alpha}^2 C_{M_\alpha} \bar{V}^4 \left[\frac{\bar{\omega}_1^2}{\bar{\omega}_2^2} - \left(1 + \frac{1}{2\mu} C_{M_\alpha}\right) \right]
 \end{aligned} \tag{2.33}$$

For a statically stable aircraft, C_{L_α} is positive while C_{M_α} is negative. These coefficients E_i are then all positive, and the condition of positiveness for the discriminant D provides a constraint equation for the support stiffness required for stability, namely

$$\frac{\bar{\omega}_1}{\bar{\omega}_2} < \left(1 + \frac{1}{2\mu} C_{M_\alpha} \right)^{\frac{1}{2}} \tag{2.34}$$

Except for a very lightweight model, the second term, $C_{M_\alpha}/2\mu$, of Eq. (2.34) is usually small and can be neglected. Therefore, Eq. (2.34) simply states that the support plunging frequency must be lower than the pitching frequency in order to avoid the unwanted support instability. This is an important design criterion for the support stiffness of a "free flight"

wind tunnel test setup. It should be noted that the above analysis is not an "ad hoc" solution to the vertical rod support system used herein. The support stiffness can arise from any non-mechanical means such as cable restraining forces of a two cable mount system. The above criterion of support stiffness should be applicable to other type of wind tunnel support system.

By excluding ζ_1 , ζ_2 and C_{M_α} , Eq. (2.34) gives a sufficient stability criterion which is independent of the airspeed. Since ζ_1 , ζ_2 and C_{M_α} are all positive damping terms in diagonal positions, C_{11} and C_{22} , the inclusion of these damping terms will generally stabilize the system. As a result, there may exist a stability boundary or region as a function of airspeed in addition to the stability criterion of Eq. (2.34). The complete stability solution can only be determined by the successive polynomial solutions of Eq. (2.31). Figure 2.6 demonstrates the effect of plunging damping ratio in a complete stability analysis. With a finite amount of plunging damping ratio, the support system will be eventually stabilized.

The physical interpretation of support instability arises from the interaction between the plunge and pitch modes of a "rigid" model. Since the pitch frequency increases with airspeed due to aerodynamic stiffening while the plunge frequency is independent of the airspeed, there will be a frequency coalescence and mode transfer if the pitch frequency in still air is below the plunge frequency. Figure 2.7 illustrates this interaction phenomenon on an ω -V plot.

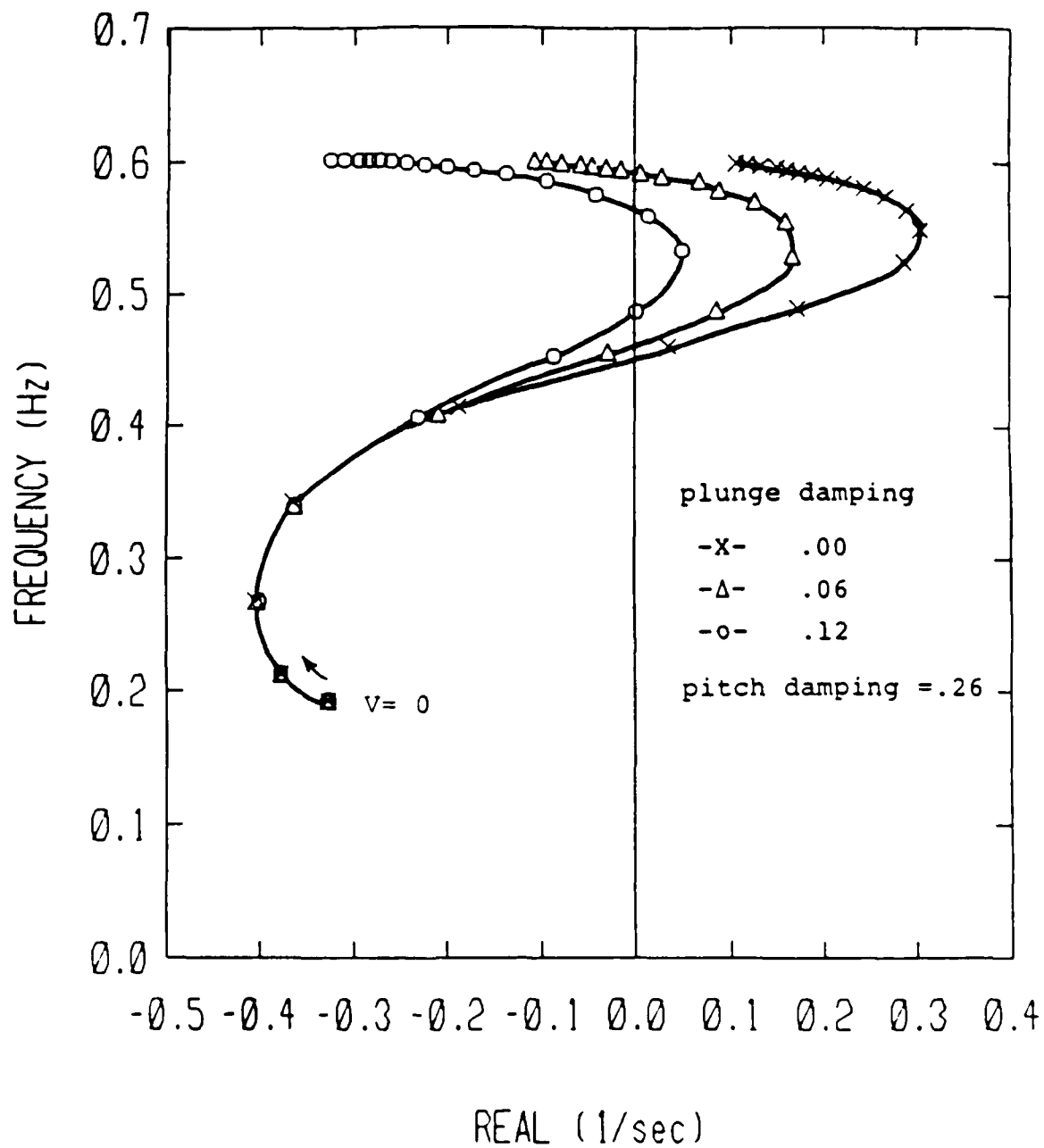


Fig. 2.6 Plunge Damping Effect on Support Instability
(Root Locus Plot, Rigid Aircraft Model)

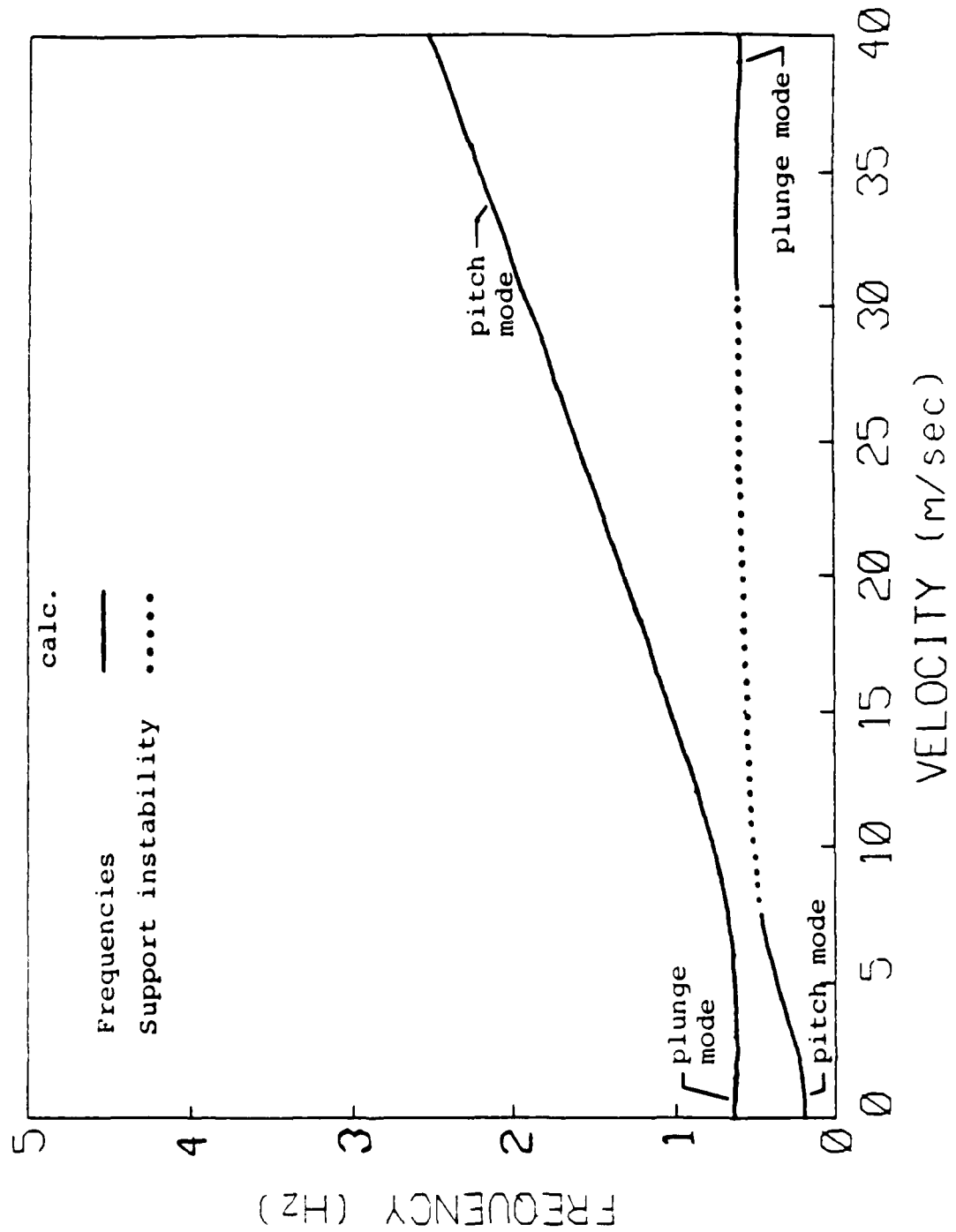


Fig. 2.7 ω -V plot, Original Support, Rigid Aircraft Model

CHAPTER THREE

EXPERIMENT

3.1 Wind Tunnel Model, Support System, and Instrumentation

(a) Flutter model

For the purposes of this investigation, a generic, full-span, forward swept wing aircraft model was constructed. Figure 3.1 shows the layout of the aircraft model and Figure 3.2 shows picture of the installed model on wind tunnel site. The principal components are (1) the interchangeable, 30-degree forward swept, graphite/epoxy flat plate wings, (2) a sturdy fuselage of balsa wood, and (3) a rigid, all moving canard surface.

The wing planform was chosen to be the same as those in Refs. 9 and 10 such that the present study complemented the previous cantilever wing studies and isolated the effect of rigid body freedoms. Instead of using semi-span wing models as in Refs. 9 and 10, full-span wing models were fabricated by bonding two 305 x 76 mm (12 x 3 inch) laminate plate onto the fiberglass center plate in a 30° forward swept configuration as shown in Figure 3.3. The laminate plate wings were made up of Hercules AS4/3501-6 graphite/epoxy which is supplied in 305 mm wide, resin impregnated tape ("prepreg"). Material properties for this material are indicated in Table 3.1.

The manufacturing of laminates followed the standard

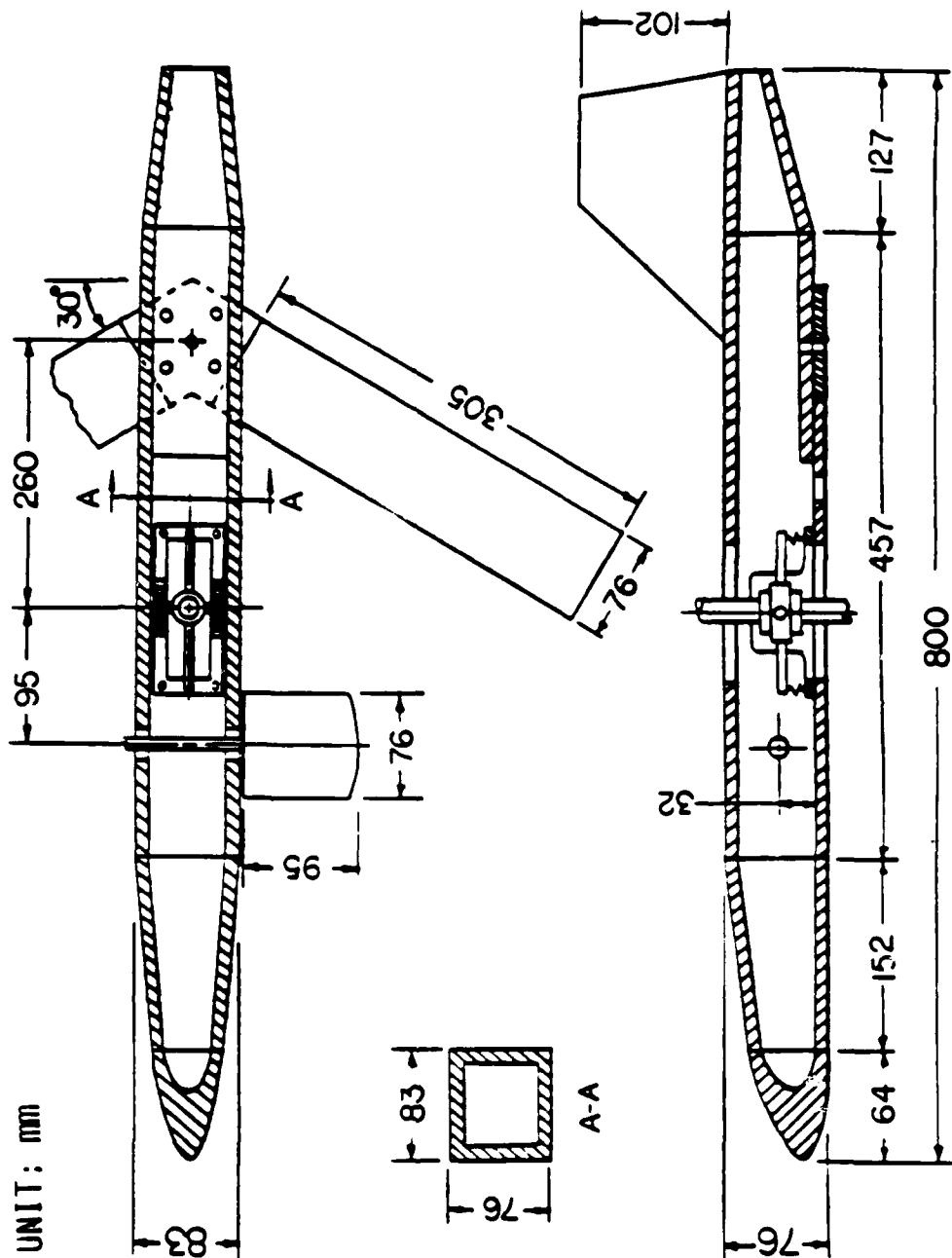


Fig. 3.1 Aircraft Model Layout

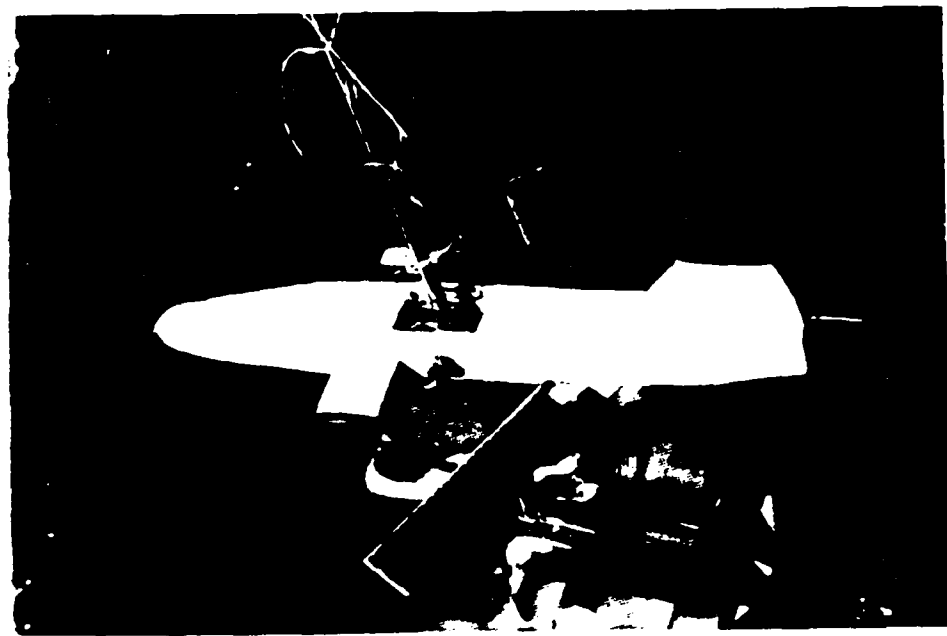


Fig. 3.2 Forward Swept Wing Aircraft Model

UNIT: mm

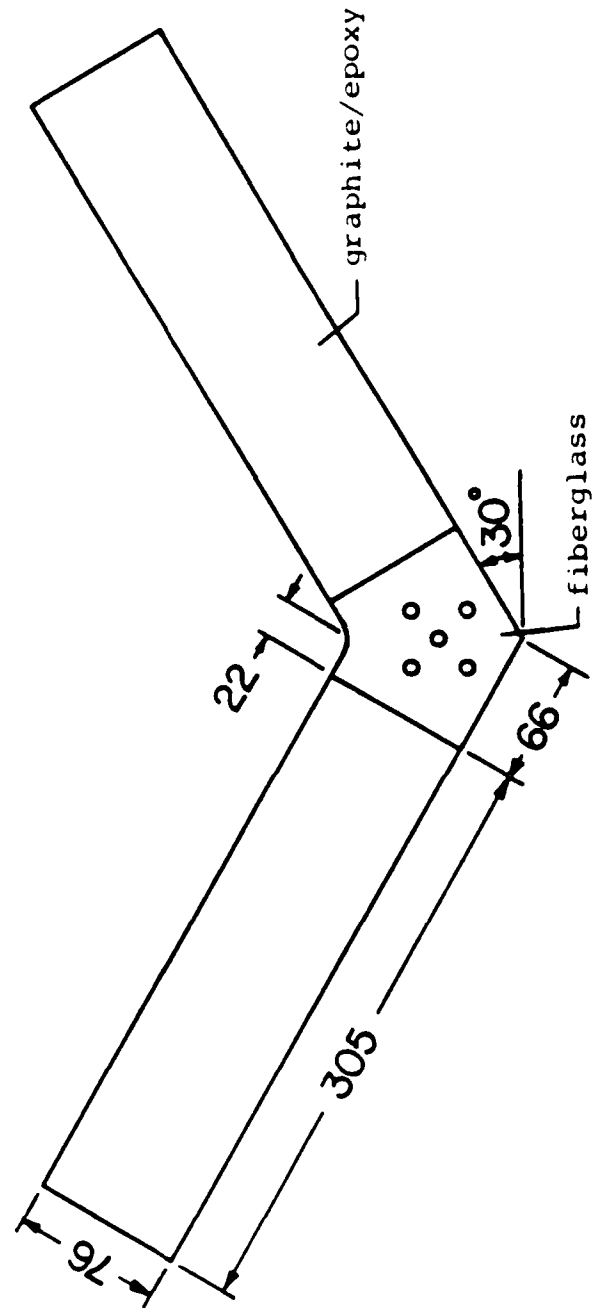


Fig. 3.3 Forward Swept Graphite/Epoxy Wing

Table 3.1 Graphite/Epoxy Material Properties

Hercules AS4/3501-6

<u>Property</u>	<u>Extensional</u>	<u>Flexural</u>
E_L (Gpa)	143.	106. ¹
E_T (Gpa)	9.7	7.9 ²
ν_{LT}	.3	.3
G_{LT} (Gpa)	4.9	4.9

Measured Ply Thickness = 0.131 mm

1 obtained from vibration tests

2 AS1/3501-6 property

procedures developed at TELAC over the years [36] except for the placement of paper bleeder for curing. This difference will be detailed in the following description of laminate manufacturing. The prepreg was first removed from its storage at -18°C and cut to size using Stanley knives. Templates were used to cut all the desired angle plies. The plies were then laid-up in 350 mm by 305 mm laminates and covered with peel-ply on both sides. The laminates were then placed on an aluminum cure plate sprayed with mold release and covered with non-porous teflon. Instead of placing three sheets of paper bleeder only on top of each 6-ply laminate, two sheets of paper bleeder were placed on each side of all the laminates for curing. Due to the manufacturing residual strain, previous symmetric, thin laminate often exhibited some degree of warping and unintended spanwise twisting. The purpose of this modification in manufacturing procedure was to minimize or eliminate any symmetric laminate warping by using a "symmetric" curing setup. Other necessary curing materials were stacked as well and the complete setup is illustrated in Figure 3.4.

The cure cycle used for the 3501-6 epoxy was a two-step process composed of a one-hour flow stage at 116°C and two-hour set stage at 176°C . Full vacuum was applied to the laminates and a 0.59 Mpa (85 psi) pressure was maintained inside the autoclave during the entire cure (see Figure 3.5). After that, the laminates were postcured for eight hours at 176°C in an oven with no pressure or vacuum.

Using a milling machine equipped with a diamond grit blade

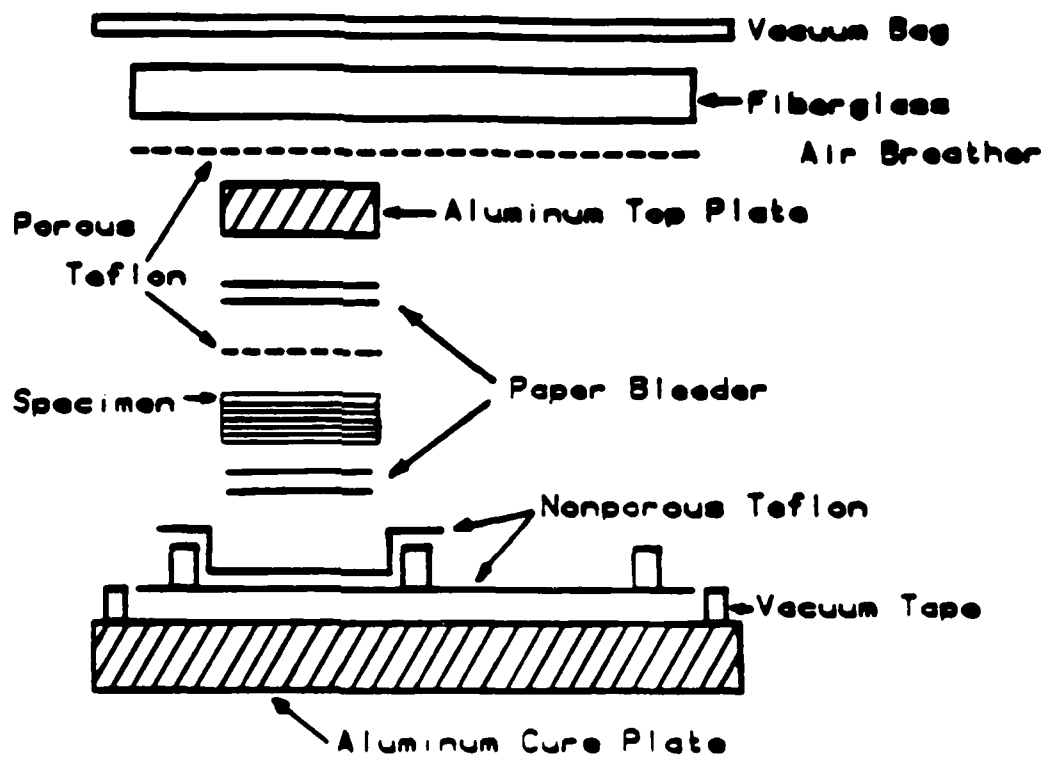


Fig. 3.4 Schematic of Curing Assembly Cross-Section

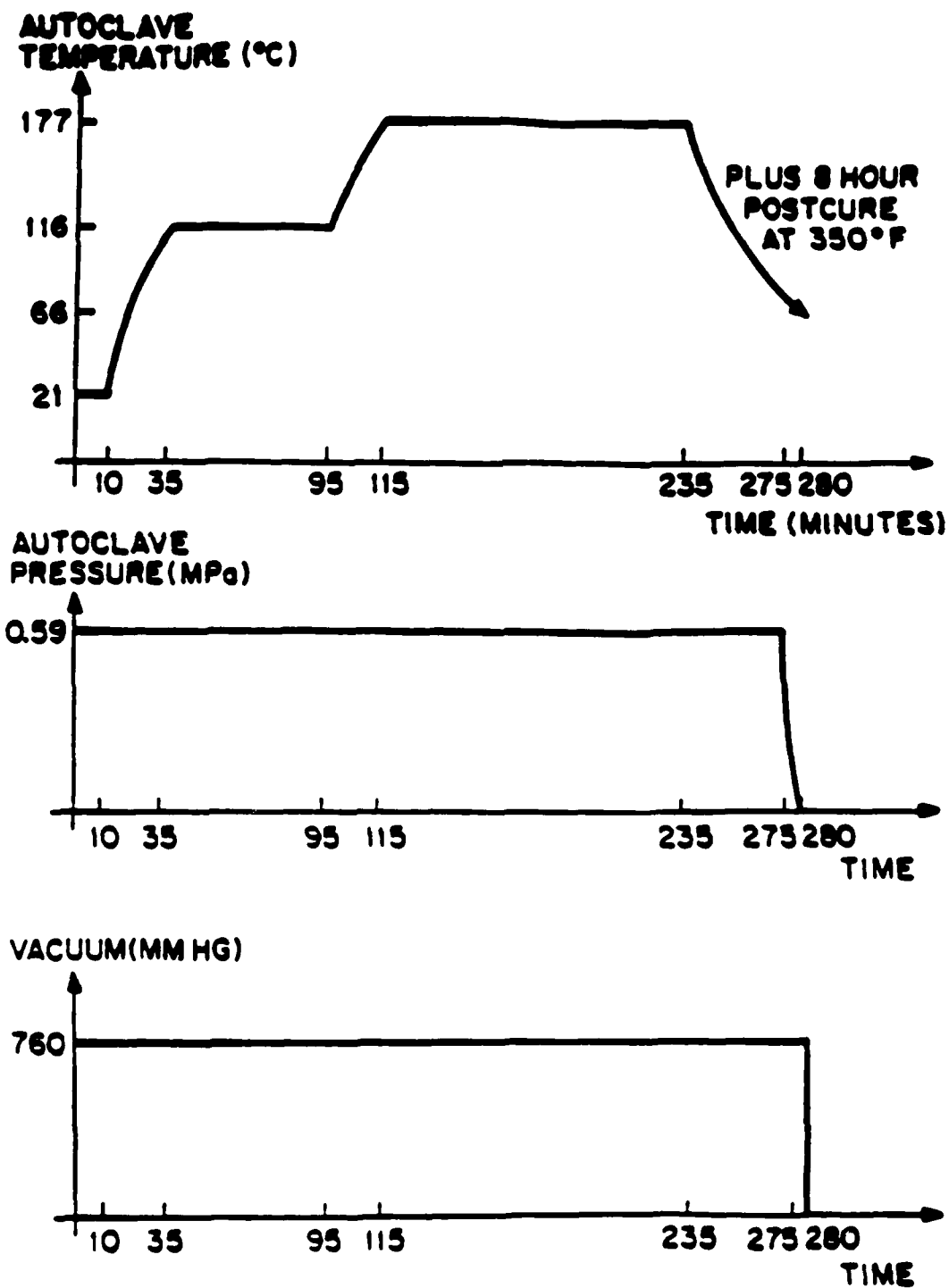


Fig. 3.5 AS4/3501-6 Graphite/Epoxy Cure Cycle

and water cooling, three wing strips (350 x 76.2 mm) were cut out of each laminate. From the same laminate two wing strips were selected to form the full-span wing by putting one of the wing strips upside down such that the ply orientation would be symmetric about the fuselage center line. The wing strips were then sandwiched bonded to between two Scotchply 1003 fiberglass, V-shaped center plates. The epoxy used for bonding was an Epon 815 resin and V40 hardener supplied by the Miller-Stephenson Company. The mixing ratio used was 60:40, resin to hardener by weight. The cure used was room temperature cure last for seven days. During the cure, the wing/center plate assemblies were firmly held together by five C-clamps.

The effects of aeroelastic tailoring were demonstrated by a set of four wings with bending-twisting coupling in both favorable and adverse fashions, namely, $[0_2/90]_s$, $[15_2/0]_s$, $[30_2/0]_s$, and $[-15_2/0]_s$ layups. The use of symmetric but unbalanced laminates provided a possible wide range of bending-twisting coupling. The bending-twisting coupling stiffness ratios, $D_{16}/\sqrt{D_{11}D_{66}}$ and the bending/twisting stiffness ratios, D_{11}/D_{66} , of all the specimens are tabulated in Table 3.2. For all wings, the zero degree ply was used as the inner ply to strengthen the intended "unidirectional" laminate except for the $[0_2/90]_s$ wing in which the inner ply angle was 90° to avoid true unidirectional laminate.

The fuselage section was a sturdy box structure design with 9.5 mm (3/8 inch) thick balsa wood and a pine wood nose

Table 3.2 Coupling Stiffness and Bending/Torsion Stiffness Ratios of Composite Wings

	$D_{16}/\sqrt{D_{11} D_{66}}$	D_{11}/D_{66}
$[0_2/90]_s$	0.	21.1
$[15_2/0]_s$.68	9.2
$[30_2/0]_s$.80	3.2
$[-15_2/0]_s$	-.68	9.2

cone. The wind tunnel support ran through the open holes of the fuselage, through the support interface, i.e., pitching/plunging bearing assembly, inside the fuselage. Two access doors were designed on top of the fuselage for easy assembly. The wing mount was underneath the rear fuselage section. Five built-in T-nuts were used to assure the mount rigidity. The wing mount section had a step recess so that the externally mounted wing would be flush with the fuselage bottom surface.

The airfoil shaped canard surfaces were mounted on a single shaft running through the mid-height of the fuselage sidewalls. Two teflon collars were used for the shaft/fuselage intersections. The canard was positioned by two clearance wedges.

The wing gage wires were directed inside of the fuselage through a passage hole, and lead outside of the fuselage along the suspension spring. All the wires were slackly attached to the suspension spring to minimize the wire/model interference. It was particularly advantageous to handle the wires near the pitching axle so that the pitching stiffness was less interfered with.

(b) Wind tunnel support system

Wind tunnel investigation of the body freedom flutter requires that the dynamic behavior of a freely flying model be simulated. In the wind tunnel study, however, the model

generally must be somehow restrained and the behavior may be altered to a certain degree by the support system. Without careful consideration of the dynamics of the overall system, an inherent support instability may exist. Various model support systems [37] were studied for the MIT low speed acoustic wind tunnel which has a 1.5 x 2.3 m (5 x 7.5 ft) free jet test section.

The general requirements were to have a soft, stable and simple model support system with negligible moving mass and low aerodynamic interference. Because of the physical limitation of minimum model weight, the preselected wing planform was not able to fly the model completely. This overweight factor, together with the requirement of soft support, lead to the selection of a vertical rod support system. The vertical rod support system was originally developed by Boeing Airplane Company and has been successfully used in low speed wind tunnel tests [38]. The modified support system for the MIT acoustic wind tunnel included

- (1) a 1.83 m (6 ft) long, vertically installed, Case hardened steel rod with a 19 mm (3/4 inch) diameter,
- (2) a Thomson super-12 linear bearing sliding on the rod and attached to the fuselage through a pitch bearing mount located at the model center of gravity,
- (3) a soft helical spring attached to the linear bearing which suspended the model from the top of the vertical rod,
- (4) a pair of linear springs attached to the pitch gimbals at forward and aft extended arms which, together with the

existing model pendulum stiffness provided the support pitching stiffness, and

(5) snubber cables attached to the fuselage at the nose and tail locations which lead outside the test section to control sticks.

With this test setup, the model was softly restrained in the plunge, pitch and yaw motions, but totally restrained in roll, lateral and fore-and-aft motions except for slight free play between the linear bearing and rod. Figures 3.6 and 3.7 show the wind tunnel setup. Details of the model properties and model support dynamic characteristics are given in Table 3.3.

Since the linear bearing could develop significant amount of friction from misalignment or applied moment, the properly assembled linear bearing and moment free condition became extremely important. In the model/support assembly, however, the helical suspension spring always applied a moment on the bearing due to the eccentric force at the spring periphery. The spring/model attachment was therefore arranged to cause only model roll unbalance but no pitch unbalance. This roll unbalance was subsequently counterbalanced by a roll balanced weight. The so-arranged model/support assembly was well balanced in pitch and roll before putting in the linear bearing.

MIT ACOUSTIC WIND TUNNEL

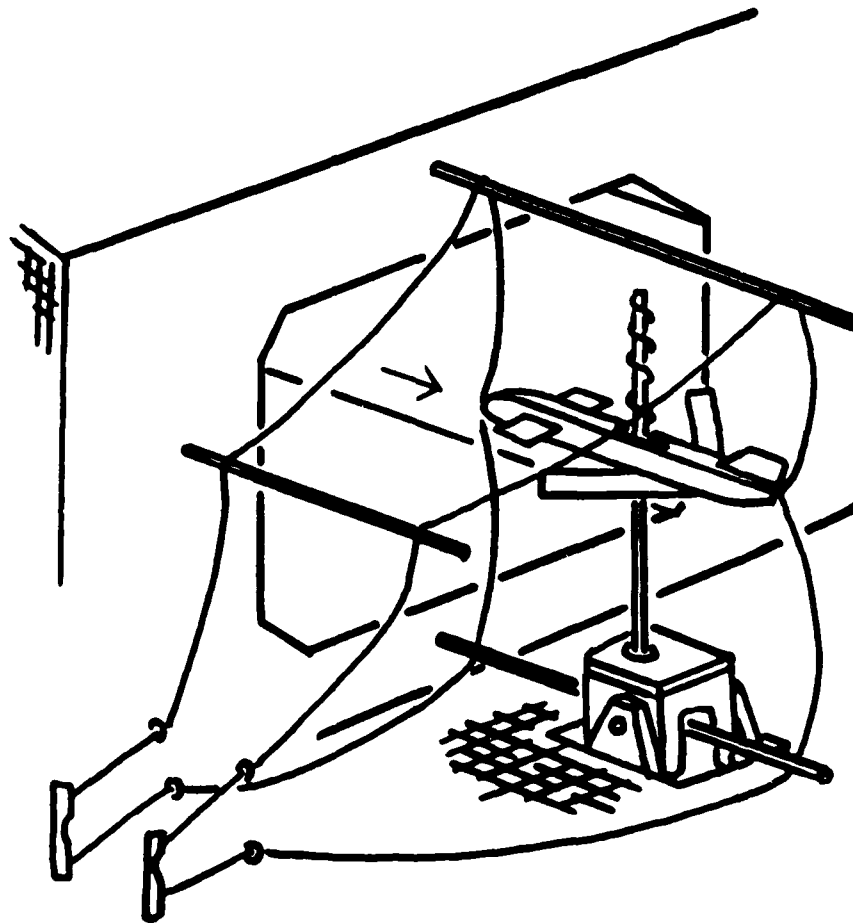


Fig. 3.6 Wind Tunnel Setup



Fig. 3.7 Wind Tunnel Setup

Table 3.3 Aircraft Model and Support Properties

Mass	0.956 Kg
Pitch Inertia	0.0178 Kg-m ²
Wing Mass	0.054 Kg
Wing Span	0.612 m
Wing Swept Angle	-30°
Wing Area	0.0538 m ²
Wing Aspect Ratio	7
Canard Area	0.0126 m ²
Fuselage Length	0.8 m
Model Plunge Freq.	0.63 Hz
Model Pitch Freq. (original)	0.20 Hz
Model Pitch Freq. (modified)	0.85 Hz

(c) Instrumentation

The model was instrumented to monitor the aeroelastic behavior including the model rigid body motions and wing elastic deformation. The wing root bending and torsional strain gages, on both sides of wings, monitored the wing motions. Figure 3.8 shows the arrangement of strain gages. The bending gages, M-M EA-13-187BB-120, were mounted on both faces of the wing to form a half Wheatstone bridge. To monitor the torsion response, the 2-element 90° rosette gages, M-M EA-06-250TK-120, were used, and a full Wheatstone bridge was formed by rosette gages on both faces of the wing.

A low friction, conductive film type potentiometer was used to monitor the model's pitch motion. This potentiometer was snugly connected to the pitching axle and mounted outside the fuselage as shown in Figure 3.9.

A thin, flexible 203 mm (8 inch) long, 0.51 mm (.020 inch) thick, cantilever steel beam with a root strain gage, Figure 3.10, was mounted near the top end of the vertical rod to record model's plunge motion. The free end of the cantilever steel beam was tied to near the second coil of the suspension spring. The movement of the free end would be fractions of the model plunge height as long as the spring deflection was within the linear range.

The wing bending and torsional gage signals were monitored on oscilloscopes and recorded on a strip chart recorder together with the pitch and plunge signals. For the four

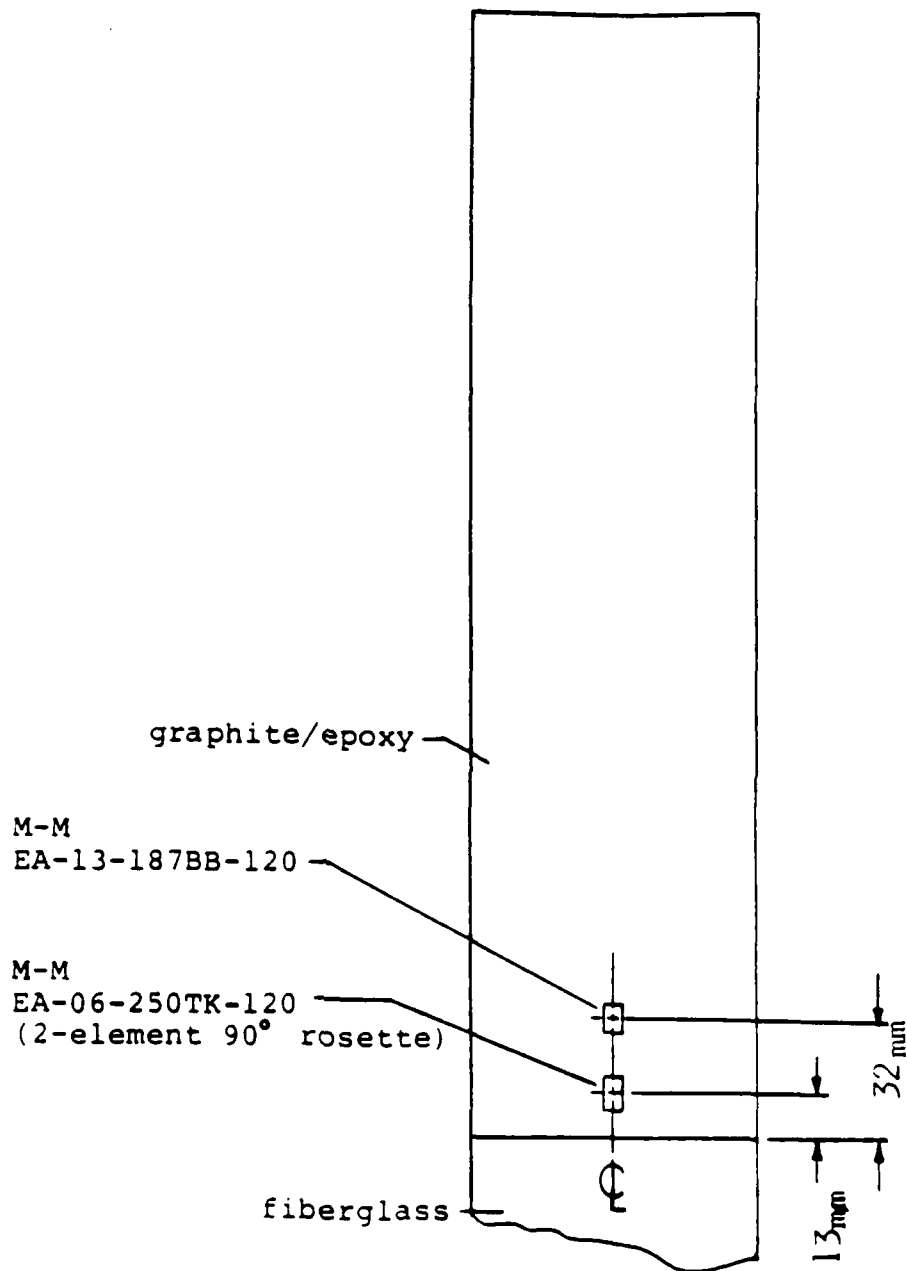


Fig. 3.8 Wing Root Strain Gages Arrangement

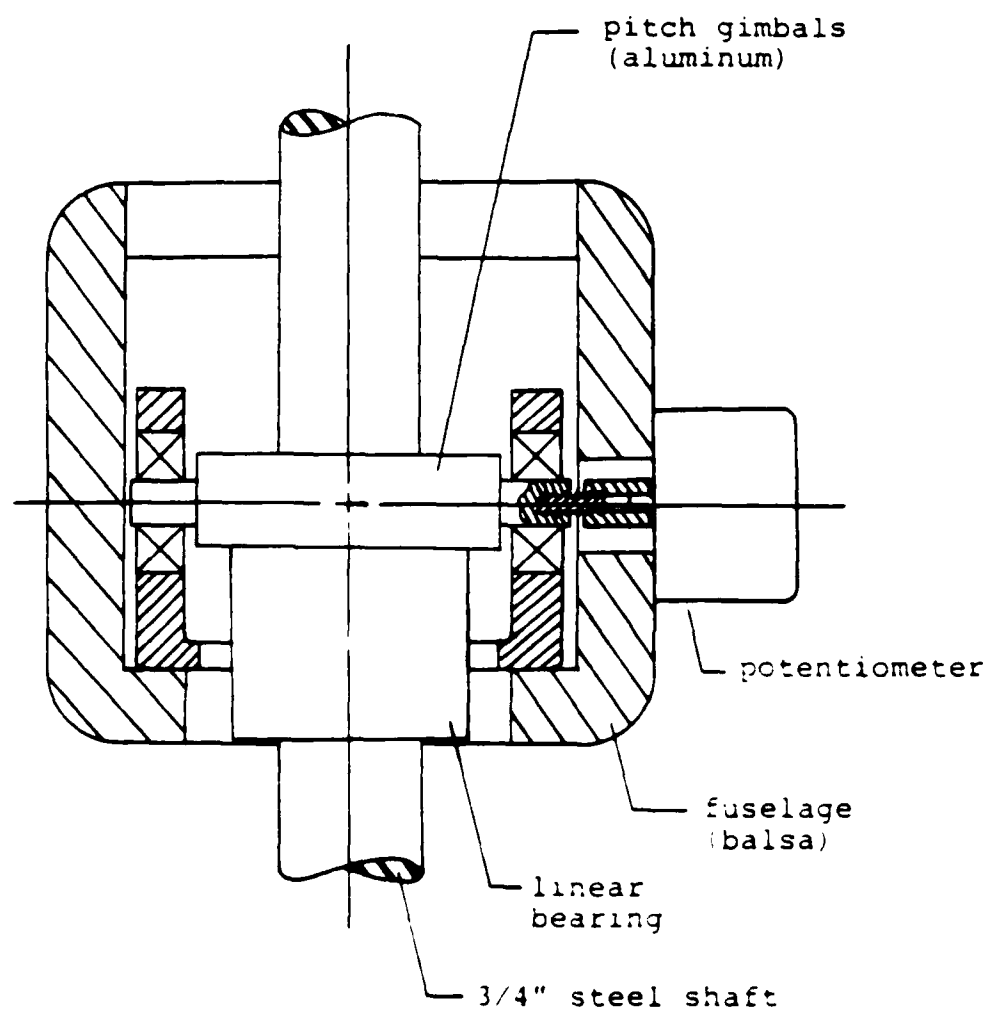


Fig. 3.9 Model Pitch Angle Measurement

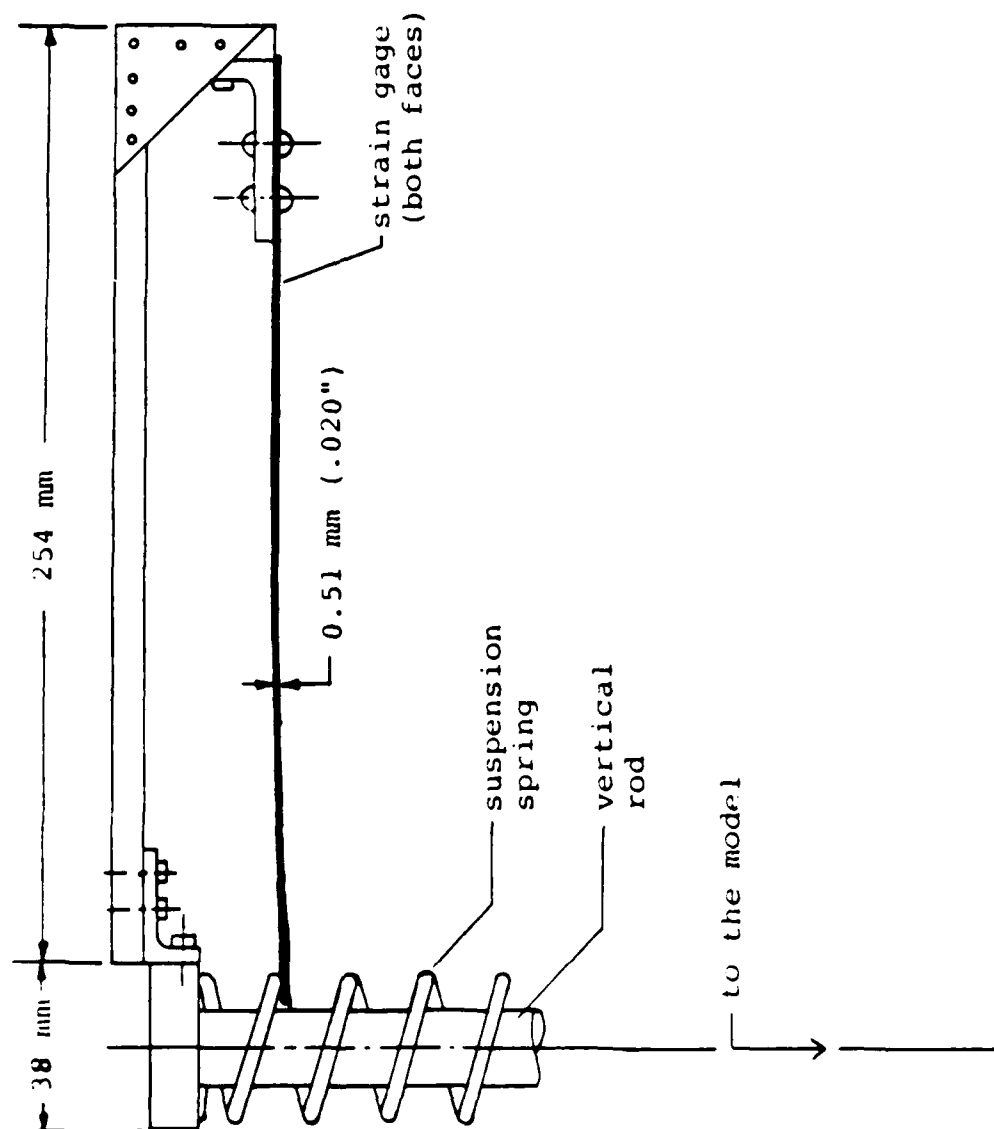


Fig. 3.10 Model Plunge Height Measurement

channel recorder used in the present testing, only a selected side of the wing root bending and torsional gage signals plus the pitch and plunge signals were recorded. The left side wing, facing the tunnel control station, was usually recorded while the right side wing was occasionally recorded for comparison purposes. During the tests, video movies of the model responses were also taken for future replay and demonstration.

3.2 Vibration Tests

The objectives of the vibration test were to determine the vibration frequencies of all wings, and to verify the closely tuned frequencies of the both sides of the full-span wing. Since the structure geometry was simple and had well separated vibration frequencies, the sine-dwell testing [39] proved to be very powerful and efficient. The wing model was horizontally mounted atop a Ling 420-1 shaker which was driven by the amplified sinusoidal signal. The vibration frequencies were tuned in by progressively varying excitation frequency and observing the steady state resonant responses. The excitation and response signals were also fed into an oscilloscope to observe the 90° phase shift during resonance. The excitation power was properly adjusted to observe the vibration modes without incurring large amplitude vibration. This procedure was repeated for both sides of the wing, which usually did not

resonate at exactly the same frequency. The aforementioned vibration tests were performed up to the third vibration mode for all wings.

3.3 Aerodynamic Tests

The objective of the aerodynamic tests was two-fold. One was to determine the model trimmed flight performance over the range of angle of attack. The other was to measure the longitudinal aerodynamic derivatives of the rigid model.

The model center of gravity was designed to be slightly below the pitching axle such that a stable pendulum mode was obtained. To maintain a common reference angle within a test and among other tests, an on-site model balancing was developed as a standard pre-testing procedure. With wind off and model locked in plunge motion, the model was balanced in the horizontal position, defined by a level and tail position on a retractable scale, by placing balance weights atop the fuselage. After the model was balanced, the pendulum stiffness was measured by placing incremental counterbalancing weights, 1 gm each, at positions six inches in front of and behind the pitching axle, and reading the corresponding pitch angles. The pendulum stiffness was then determined from the plot of balancing moment versus pitch angle. The model was then unlocked in plunge motion, to determine the plunge spring characteristics.

Calibrations of the model pitch angle and plunge height were performed before each group of aerodynamic tests. First, friction test was carried out by examining the model sticktion ("dead zone") in both plunge and pitch motions. Within this dead zone, the restoring force or moment could not overcome the friction force or moment such that the model could stay wherever it was. A 3.2 mm (.125 inch) plunge dead zone was usually regarded as acceptable, otherwise the linear bearing needed to be reassembled. With wind off, the pitch dead zone was about 4° to 5° for the original soft pitch support, but not noticeable for the later stiffer support. Since the hysteresis arose mainly from the pitch potentiometer, no improvement could be gained on the existing instrumentation to reduce the pitch dead zone in still air. Careful attention to hysteresis was taken during the static tests. It should be noted that the hysteresis was reduced due to the higher aerodynamic pitching stiffness while wind was on. Model pitch angle was then calibrated by the differential reading of the tail positions on a retractable scale. Model plunge height was calibrated by a small scale, 76.2 mm (3 inch) maximum, for aerodynamic testing and by a large scale, 304.8 mm (12 inch) and up, for flutter testing.

The aerodynamic characteristics of the "rigid" model were obtained on the actual flutter model in the wind tunnel, by setting the airspeed at 5 m/sec to avoid aeroelastic effect. For the $[0_2/90]_s$ wing, this testing speed was only 6% of the wing divergence dynamic pressure. The procedure of placing

counterbalancing weights was similar to that of the pendulum stiffness measurement except the tunnel was now running at a low speed. The balancing weight was increased at 2 gm each step until the model was stalled. The 1 gm increment was then used to fine tune the stall regions. At each incremental step, the pure aerodynamic moment was calculated by subtracting the corresponding pendulum moment from the counterbalancing moment. Also, the net lift was calculated by subtracting the counterbalancing weights from the change of the suspension spring force. The lift and moment coefficients were then calculated from $C_{L_\alpha} = \text{Lift}/qS_w$ and $C_{M_\alpha} = \text{Moment}/qS_w c$, and plotted against the pitch angle readings. This procedure was repeated for several canard settings, typical values being 0° , $\pm 2.5^\circ$, and $\pm 5^\circ$.

3.4 Cantilever Wing Tests

The objectives of the cantilever wing testing were to verify the analytical predictions and to obtain the baseline results for body freedom flutter comparison. The cantilever wing configuration was set up by blocking the model's plunging freedom with top and bottom stops, and varying the wing root angle of attack (model pitch angle) with the help of the snubber cables. The testing procedure explored the linear and nonlinear flutter and divergence boundaries. The testing variables were wind tunnel speed and wing root angle of attack

from 0 to 16 degrees. For each wing, the wind tunnel speed was initially set to be low enough such that no flutter or divergence was present up to large wing root angle of attack, i.e., 15° or 16° . The airspeed was then increased in 1 m/sec steps. At each incremental speed setting, the flutter point was determined by gradually increasing the wing root angle of attack in both the positive and negative sense, until flutter was encountered. This procedure was repeated until the flutter or divergence condition could not be avoided for any setting of the wing root angle of attack. In other words, the positive sense of critical angle of attack coincided with the negative one.

3.5 Body Freedom Flutter Tests

The testing objectives were to explore the aeroelastic behavior and instability boundaries of the "free" flying model, and to verify the analytical model. The tunnel airspeed was the only primary variable, while the canard setting was used as a secondary variable for flight trimming. For a given test, a canard setting was chosen to make the trimmed flight pitch angle slightly positive. From the previous aerodynamic tests, the model pitch angle was chosen at about 2° , since models flown at this angle had the most linear moment characteristics and a positive lift to raise the model into the middle of the test section.

For the given canard setting, normally 2.5° , the flutter point was determined by step increasing the tunnel airspeed until the body freedom flutter or wing flutter was encountered. For the purposes of correlating the transient behavior, subcritical measurements, such as frequency and decay rate of an impulse response, were made at each incremental speed step. The impulse responses of pitch and plunge freedoms were generated by two separate "kicks" at the tail and near the center of gravity locations. The wing elastic responses were also generated by kicking at the wing tip location. Because of the low airspeed and open test section, the needed "kick" was easily accomplished by using a 1.5 m (5 ft) long wooden stick reaching the model from downstream. In general this technique was simple and effective, but it became more difficult and dangerous to the model as the tunnel airspeed was increased. The danger arose from the large increment in the aerodynamic forces resulting from a minor pitch angle increment at high dynamic pressures. As a result, the model tended to instantly fly beyond the traveling limits. Without an active compensation scheme in addition to the manual snubber cables, the consequence could be catastrophic. So this "kick" was not given for the higher airspeeds.

For comparison purposes, the aeroelastic behavior of the model free in pitch only was also tested. The pitch only configuration was set up by blocking the model plunging freedom at the middle of the test section. The testing variables and procedure were the same as those in the testing of the model

free in pitch and plunge. Due to the absence of the plunge freedom, the risk of catastrophe was largely reduced in this test.

CHAPTER FOUR

RESULTS

4.1 Model Structural and Aerodynamic Characteristics

(a) Basic material properties

The material properties of Hercules AS4/3501-6 prepreg are summarized in Table 3.1. The longitudinal flexural modulus E_L was obtained from the results of the vibration test of the $[0_2/90]_S$ wing. The longitudinal flexural modulus, determined from the first and second bending frequencies is 106 Gpa which is 25% lower than the tensile extensional modulus of 143 Gpa. This stiffness reduction is about equal to that of AS1/3501-6 reported in Ref. 40. Since no testing was performed to determine the actual reduction in transverse flexural modulus, E_T , the value of AS1/3501-6 prepreg was used. This substitution for matrix dominant property was acceptable because the same matrix system was used in both materials. Ref. 40 also showed that the shear modulus and Poisson's ratios are almost the same for in-plane and out-of-plane loadings. The Hercules AS4/3501-6 product data of shear modulus and Poisson's ratio were therefore used in the subsequent analysis. For comparison purposes, the Hercules AS4/3501-6 product data of in-plane tensile loading are also summarized in Table 3.1. The longitudinal flexural modulus was also determined from the load-deflection slope of the cantilevered

$[0_2/90]_s$ wing. This result for E_L is 119 GPa.

(b) Vibration frequencies and modes

Wing alone vibration frequencies, both measured and calculated, are given in Table 4.1. The frequency variations with respect to the ply orientation agrees with the previous investigation in Ref. 30. For unbalanced laminated wings, the designations of "torsional mode" and "bending mode" are somewhat vague because of stiffness coupling.

Figures 4.1 to 4.4 show the predicted mode shapes, based on the seven-mode Rayleigh-Ritz analysis, as well as the observed vibration node line up to the third mode for all wings tested. For the $[0_2/90]_s$ wing, a skewed node line was observed in torsional mode. This may be due to the slight stiffness coupling because of the misaligned ply orientation. The other possible reason for the skewed node line is due to the vibration test setup for a 30° forward swept full-span wing. Since the swept wing is not symmetric with respect to the excitation point (shaker head), the inertia force contributions from each side of wing can affect the shaker head rigidity. Therefore, the observed node line may be a resultant motion of the shaker head deformation and the true wing torsional mode. The degree of abnormality, however, was actually amplified by the excessive excitation force in order to excite the relatively stiff torsional mode.

To assure this abnormality remained acceptable, static

Table 4.1 Vibration Frequencies of Cantilever Wings

Wing	<u>First Bending</u>		<u>First Torsion</u>		<u>Second Bending</u>	
	calc. (Hz)	exp. (Hz)	calc. (Hz)	exp. (Hz)	calc. (Hz)	exp. (Hz)
$[0_2/90]_s$						
left	11.1	11.4	36.2	37.6	69.3	71.8
right		11.7		37.1		72.8
$[15_2/0]_s$						
left	8.4	9.0	46.7	45.3	58.7	64.3
right		8.8		44.9		62.9
$[30_2/0]_s$						
left	5.6	5.8	40.5	37.4	60.6	58.4
right		6.0		37.9		57.7
$[-15_2/0]_s$						
left	8.4	8.8	46.7	45.8	58.7	64.0
right		8.9		46.5		62.6

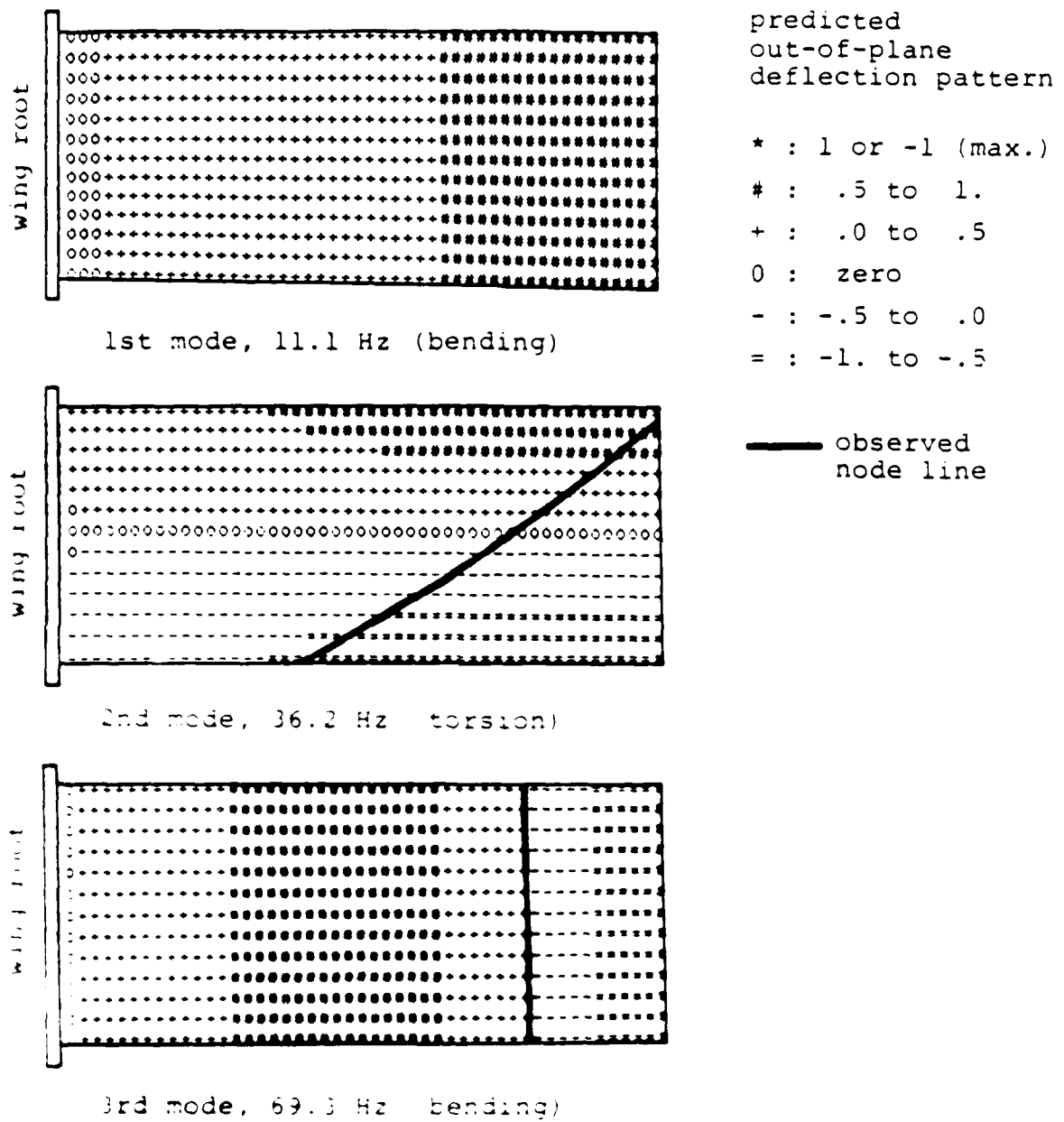
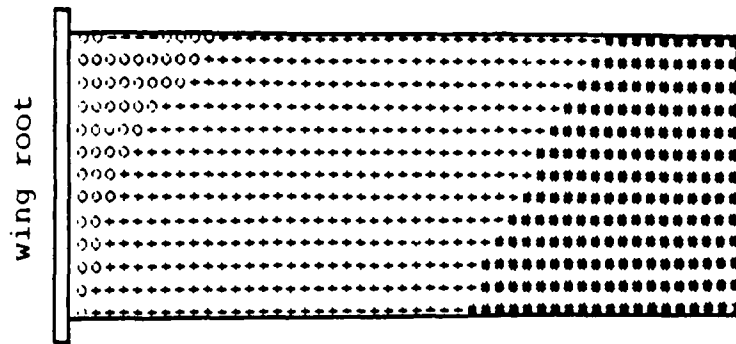


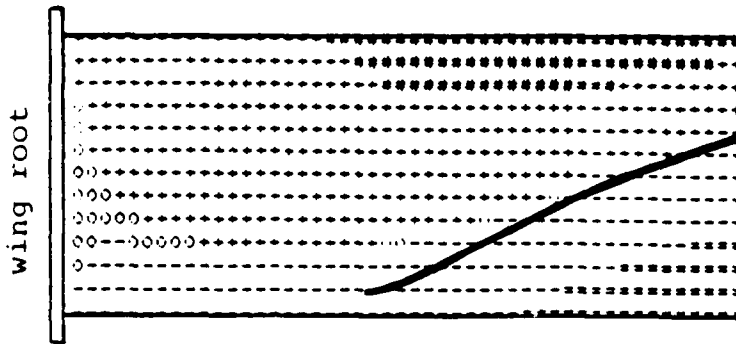
Fig. 4.1 Cantilever Wing Vibration Modes, $[0_2/90]_s$ Wing



1st mode, 8.4 Hz

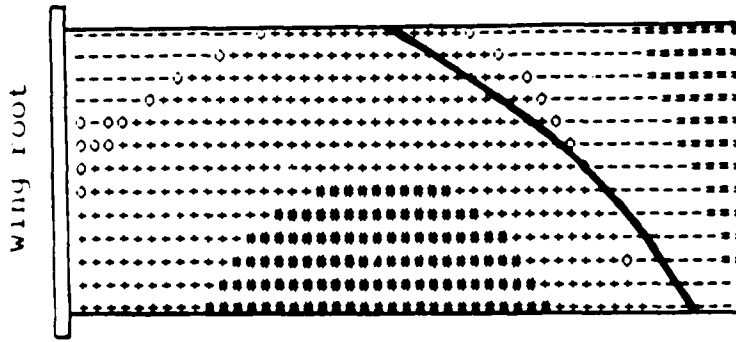
predicted
out-of-plane
deflection pattern

* : 1 or -1 (max.)
: .5 to 1.
+ : .0 to .5
0 : zero
- : -.5 to .0
= : -1. to -.5



2nd mode, 46.7 Hz

— observed
node line



3rd mode, 58.7 Hz

Fig. 4.2 Cantilever Wing Vibration Modes, $[15_2/0]_S$ Wing

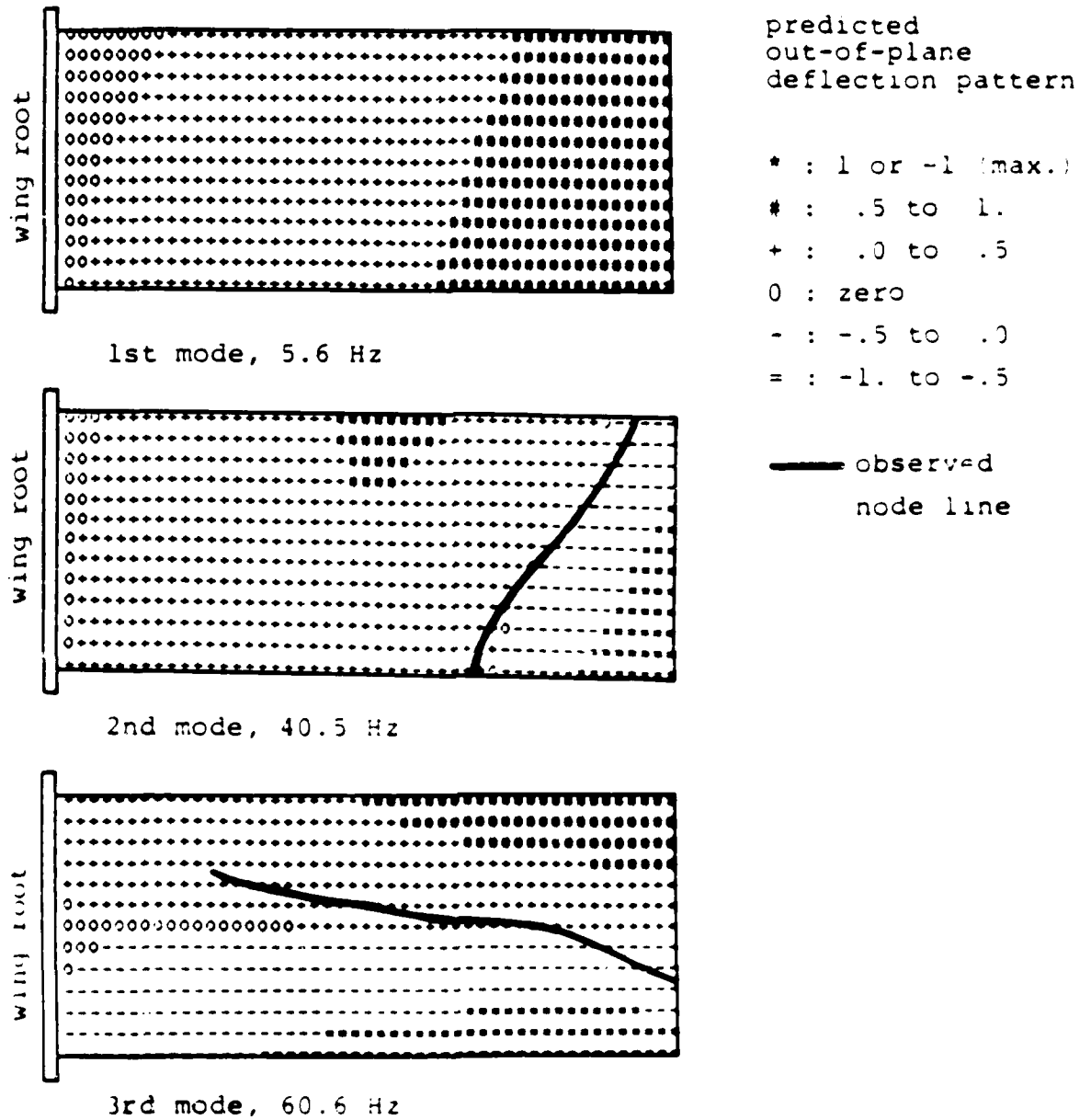
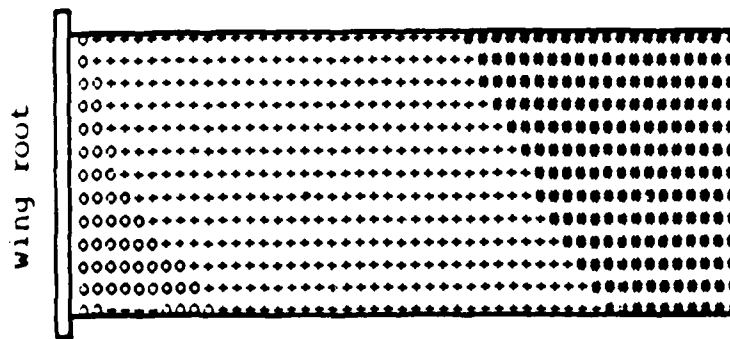
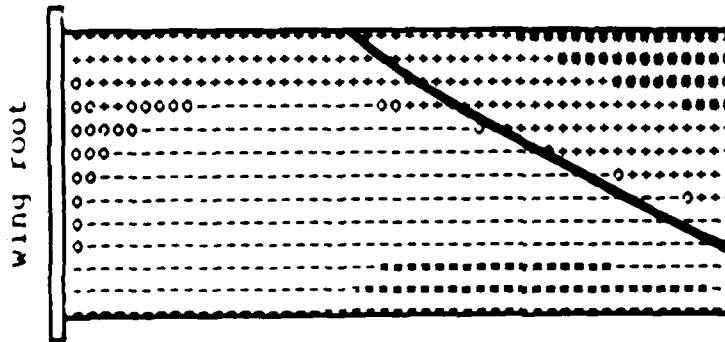


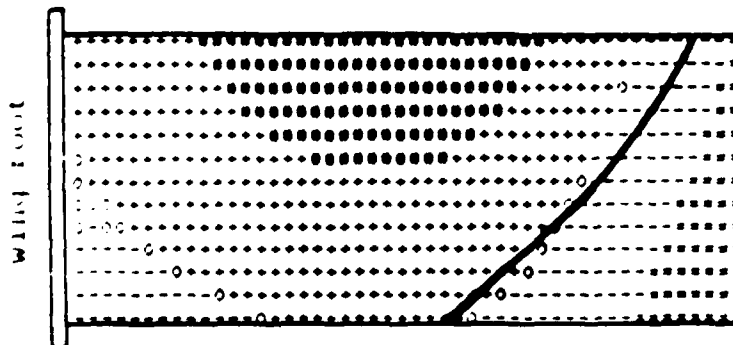
Fig. 4.3 Cantilever Wing Vibration Modes, $[30_2, 0]_S$ Wing



1st mode, 8.4 Hz



2nd mode, 46.7 Hz



3rd mode, 58.7 Hz

predicted
out-of-plane
deflection pattern

* : 1 or -1 (max.)

: .5 to 1.

+ : .0 to .5

0 : zero

- : -.5 to .0

= : -1. to -.5

— observed
node line

Fig. 4.4 Cantilever Wing Vibration Modes, $[-15_2/0]_s$ Wing

cantilever test was performed to measure the bending induced twisting angle. The wing was bent by a point load applied at the mid-chord of the wing tip section. The wing tip deflection and twisting angle were then measured at each incremental loading step. Testing results, as shown in Figure 4.5, showed the negligible wing tip twisting as wing bent. This test reassured the structural integrity of the $[0_2/90]_s$ wing.

No free-free vibration test was performed on the aircraft model. The calculated free-free vibration frequencies and modes are tabulated in Table 4.2. Comparison between the results of cantilever and free-free wings shows the slight increase in vibration frequencies for the free-free results as expected due to the inertia coupling of rigid body modes and wing elastic modes. All the vibration analyses include the virtual mass effect so that the results are comparable with actual vibration tests.

(c) Aircraft model aerodynamic derivatives

The aerodynamic lift and moment coefficients of the aircraft model are shown in Figures 4.6 and 4.7. The aerodynamic derivatives defined in the tunnel axis are given by the linear portion of the lift and moment curves. In general, the lift coefficients were consistent among all wings tested. The consistency is due to the low plunging friction incurred in the measuring procedure as described in Sec. 3.3, and partially due to less sensitivity to the wing warping. As shown in the

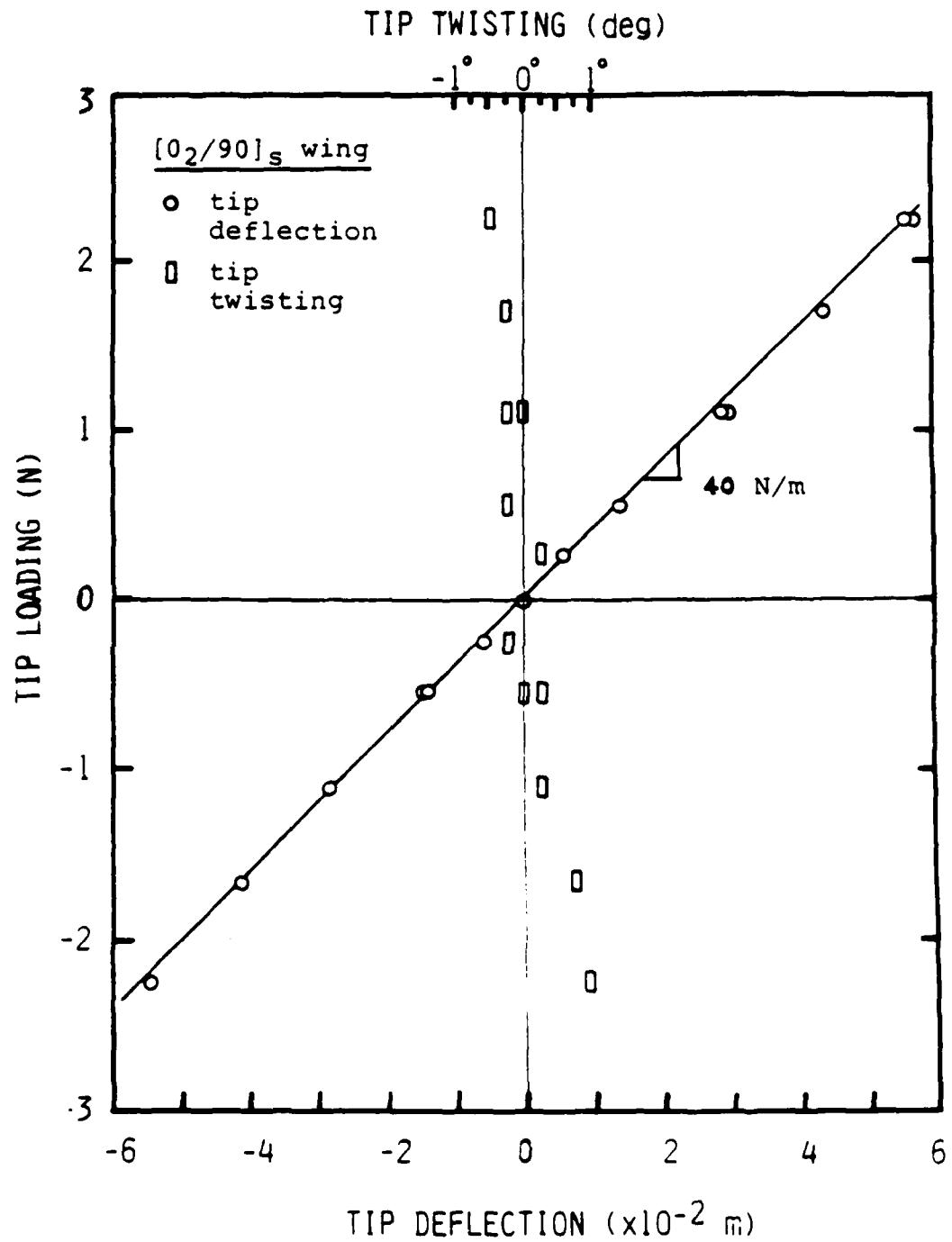


Fig. 4.5 Cantilever Load Deflection Curve, [0₂/90]_s Wing

Table 4.2 Calculated Fundamental Frequency and
Vibration Mode of Free-Free Wings

	$[0_2/90]_s$	$[15_2/0]_s$	$[30_2/0]_s$	$[-15_2/0]_s$
Freq.	11.3 Hz.	8.6 Hz.	6.0 Hz.	8.6 Hz.
q_1	-.04	-.04	-.04	-.04
q_2	.13	.13	.12	.13
q_3	1.0	1.0	1.0	1.0
q_4	.00	-.62	-.44	.62
q_5	.00	-.01	-.01	-.01
q_6	.00	-.05	-.04	.05
q_7	-.02	-.04	-.04	-.04

q_1 : plunge mode

q_2 : pitch mode

q_3 : first bending mode

q_4 : first torsional mode

q_5 : second bending mode

q_6 : second torsional mode

q_7 : chordwise bending mode

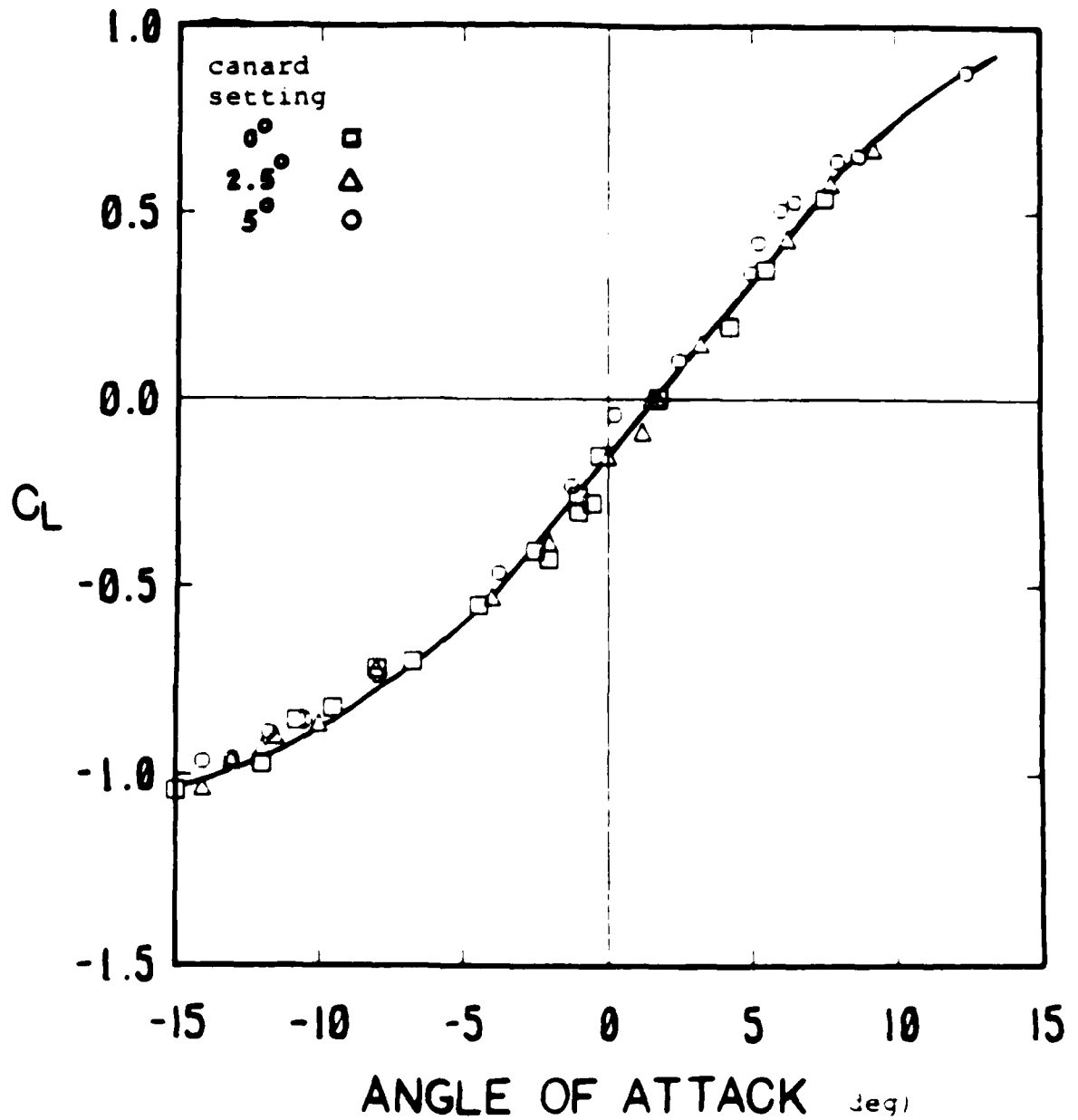


Fig. 4.6 Lift Coefficient for Aircraft Model

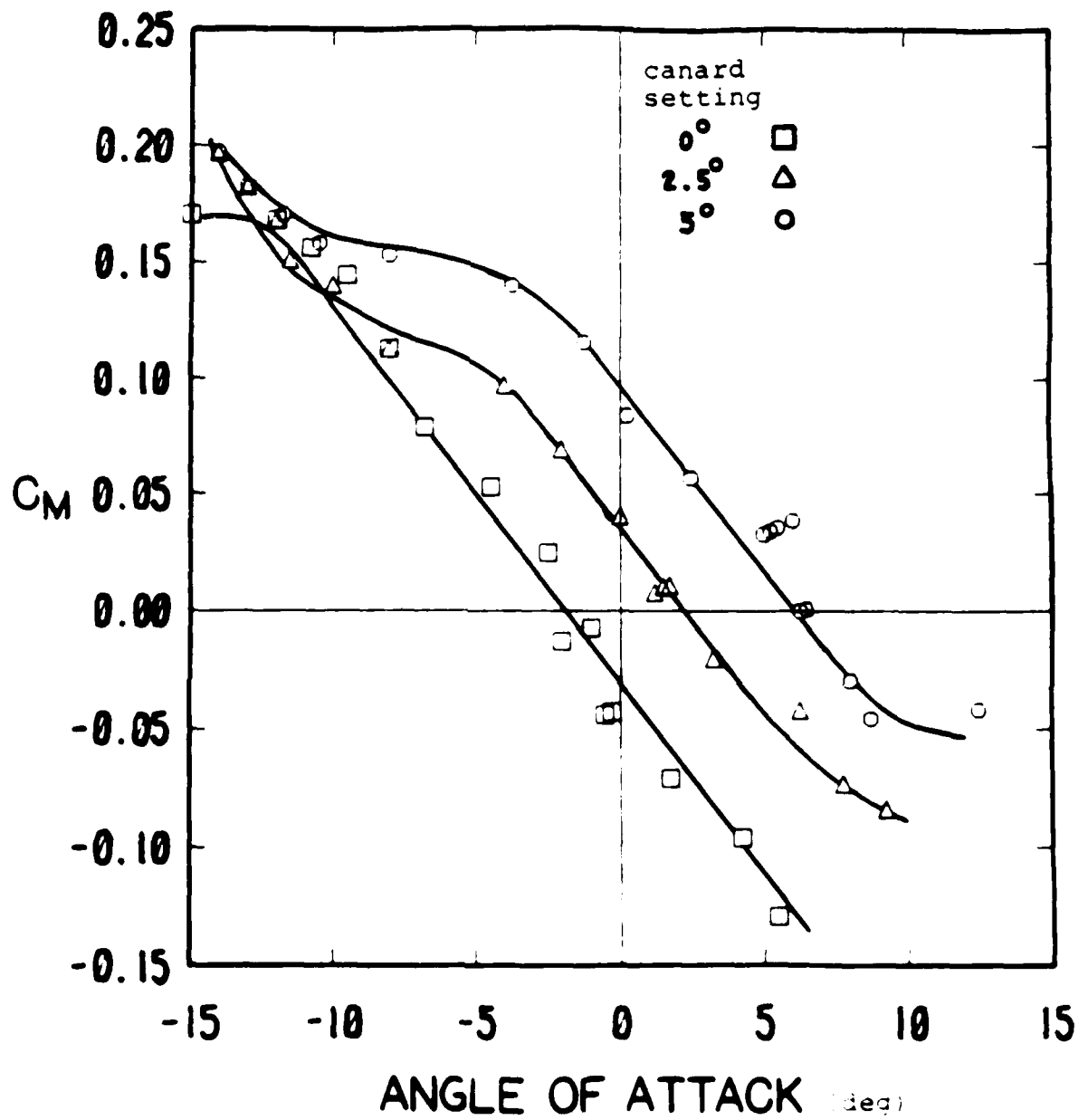


Fig. 4.7 Moment Coefficient for Aircraft Model

lift coefficient plot, the canard contributions to the overall lift are not really noticeable. The measurements of aerodynamic moment coefficients, however, experienced greater variations in the linear portion and stall regions. These variations in the linear range were possibly caused by the relatively higher pitch friction incurred in the measuring procedure, wing warping, and gage wire attachments leading outside the fuselage. The extreme sensitivity to the wing warping of aerodynamic moment is also evident in the results of varied canard setting. As shown in Figure 4.7, the aerodynamic moment coefficients are significantly changed as canard setting was moderately varied. The variation in the stall region was largely due to the nonlinearity of aerodynamic interference effect.

Based on Figures 4.6 and 4.7, the results show values of $C_{L_\alpha} = 5.33$ and $C_{M_\alpha} = -0.97$ which give the present aircraft model an 18% static margin, calculated from $-C_{M_\alpha}/C_{L_\alpha}$. In addition, the model pitch decay rates in still air and at 5 m/sec were calculated to give the C_{M_α} . The result shows value of $C_{M_\alpha} = -4.95$.

4.2 Cantilever Wing Divergence and Flutter

For comparison purposes, the flutter and divergence boundaries of the cantilever wing were tested and are presented in Figure 4.8. Because of the wing flexibility, the

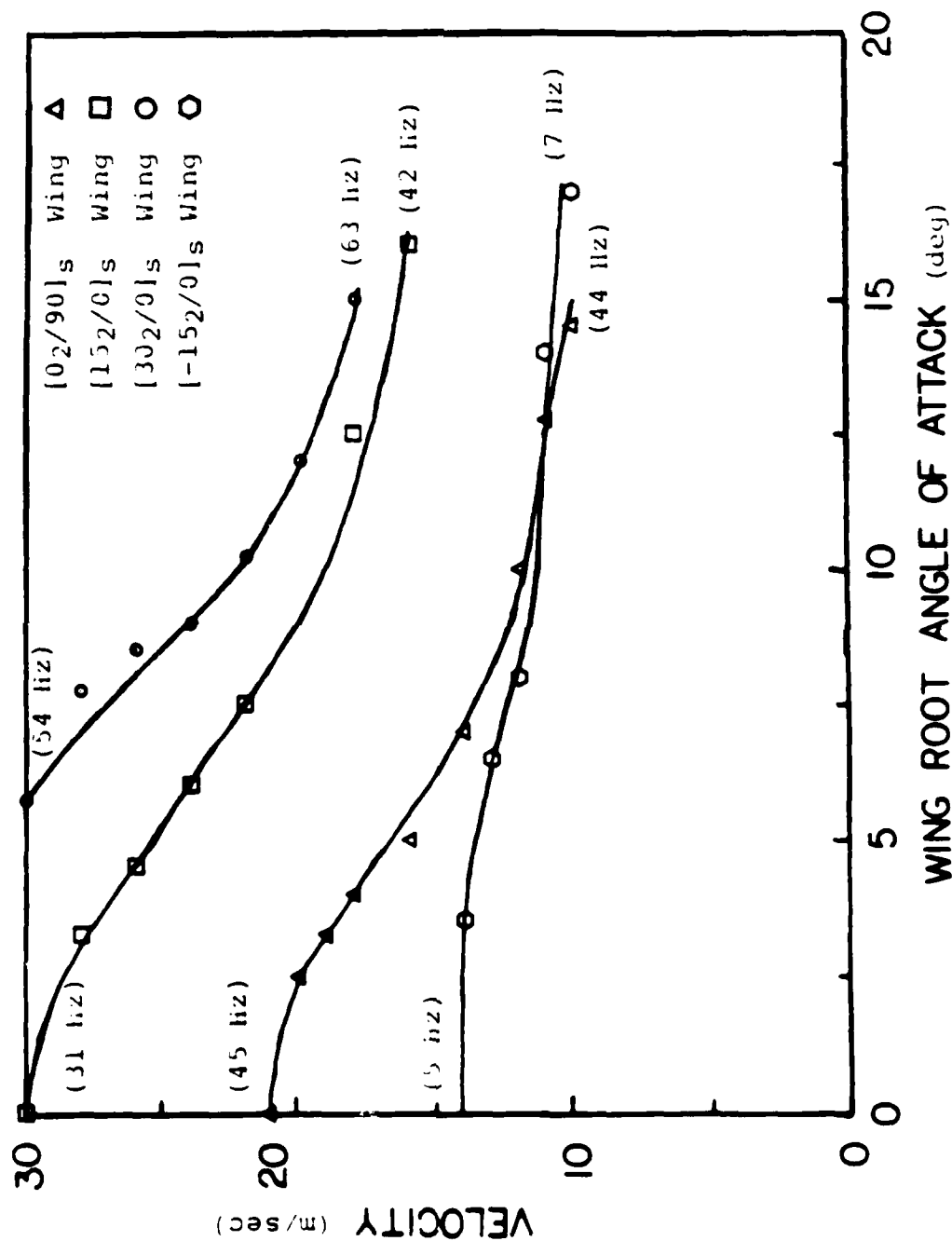


Fig. 4.8 Cantilever Wing Flutter and Divergence Boundaries

aerodynamic nonlinearity, i.e., wing stall, would occur before the wing model was overstressed or failed. Aeroelastic instability was thus encountered and observed in the form of limit cycle oscillation. Linear aeroelastic phenomena, i.e., wing divergence and bending-torsion wing flutter, were identified at low fuselage (wing root) angles of attack.

The cantilever wing results shown in Figure 4.8 are similar to those given in Ref. 10. For the $[15_2/0]_s$ and $[30_2/0]_s$ wings, bending-torsion flutter occurred at low fuselage angles of attack. At higher angles of attack, the bending-torsion wing flutter gradually changed to torsional-stall flutter (TSF) with an accompanying increase in the flutter frequency toward the still air torsional mode frequency, and a decrease in the flutter speed. Calculations of the linear bending-torsion flutter speed and frequency showed good agreement with experiment at low angles of attack. In the case of the $[15_2/0]_s$ wing, the bending-torsion flutter speed at zero angle of attack was 30 m/sec compared with the 28 m/sec calculated flutter speed. The measured and calculated flutter frequencies were 31 and 30 Hz respectively. As the fuselage angle of attack increased from 0° to 16° , a 46% drop in flutter speed was observed. In the case of the $[30_2/0]_s$ wing, at tunnel speed limit of 30 m/sec, flutter occurred only when fuselage angle of attack was beyond 7.5° . No flutter was observed with a smaller angle of attack at this speed limit. The predicted bending-torsion flutter speed is 38 m/sec which is beyond the tunnel speed limit. The measured torsional-stall

flutter speed dropped 40% as the wing root angle of attack increased from 6° to 15° .

For the $[0_2/90]_S$ and $[-15_2/0]_S$ wings, divergence occurred at low fuselage angles of attack. This divergence condition was noted when the fuselage angle of attack could not be set small enough to keep the wing from "flipping over" to either side. As the fuselage angle of attack was increased, the static divergence quickly changed to either a torsional-stall flutter ($[0_2/90]_S$ wing) or a bending-stall flutter (BSF) ($[-15_2/0]_S$ wing), with an accompanying decrease in flutter speed. In the case of the $[0_2/90]_S$ wing, the calculated divergence speed is 21 m/sec compared with the 21 m/sec measured wing divergence speed. When the divergence point was encountered, however, the $[0_2/90]_S$ wing still exhibited a 45 Hz torsional oscillation in addition to the phenomenon of "flipping over". This concurrence is due to the fact that divergence speed is only slightly lower than the flutter speed predicted at 23 m/sec. Like the previously mentioned flutter prone wings, the torsional-stall flutter existed at higher angles of attack and continued its presence as the "static" divergence was encountered at low angle of attack. The observed flutter speed dropped 52% as the fuselage angle of attack was changed from 0° to 15° . In the case of the $[-15_2/0]_S$ wing, the divergence speed was noted at 14 m/sec compared with the 13 m/sec calculated result. It should be noted that the so-called static divergence actually appeared as a dynamic bending-stall flutter. As fuselage angle of attack

was increased, the bending-stall flutter speed slowly decreased while its flutter frequency slowly increased toward the still air wing bending frequency. Since the phenomenon of bending-stall flutter persisted from low to high angle of attack, the $[-15_2/0]_S$ wing exhibits the most smooth transition with angle of attack change. In comparison, the flutter prone wings, $[15_2/0]_S$ and $[30_2/0]_S$ showed a more dramatic speed drop due to the transition from one phenomenon, bending-torsion flutter, to the other, torsional-stall flutter.

4.3 Body Freedom Flutter (BFF) and Support Instability

Body freedom flutter was predicted by the linear analysis and was observed in the wind tunnel tests. There also existed, however, an additional wind tunnel support related dynamic instability involving the model plunge and pitch motions. Since the support instability occurred before the body freedom flutter, it was of concern to the integrity of the aeroelastic behavior and the overall testing objective. Therefore, before presenting the body freedom flutter results, this support instability will first be described.

(a) Support instability

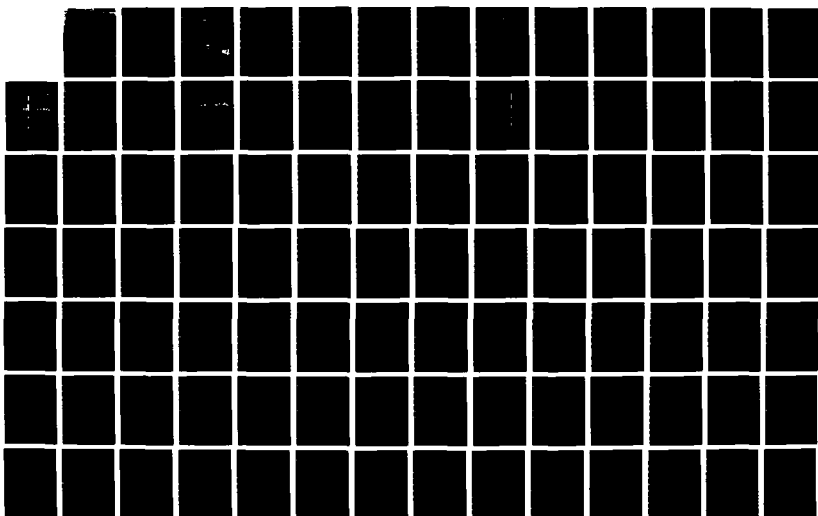
The aircraft model on the original support system had a 0.63 Hz plunging frequency which resulted from the suspension spring, but had no mechanical pitching stiffness except for a

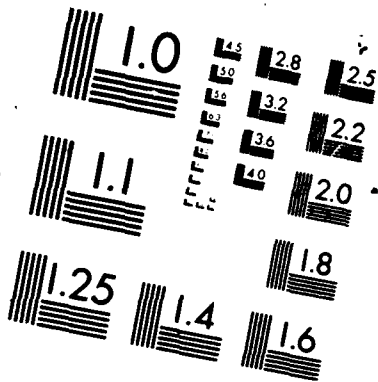
small amount of pendulum stiffness which gave a 0.20 Hz pitching frequency in still air. Measurements from aircraft model step responses gave values of support plunging and pitching equivalent viscous damping ratios of approximately 0.06 for plunge motion and 0.26 for pitch motion. With the averaged damping ratios, a simplified, two degrees of freedom longitudinal stability analysis, discussed in Sec. 2.3, showed that a support instability would occur at 8 m/sec and end at 31 m/sec. A useful tool showing the interaction of plunging and pitching motions is to plot the frequency components against the airspeed, namely an ω -V plot. Figure 2.7 shows the predicted interaction for a "rigid" wing aircraft model.

The complete 7-mode aeroelastic analyses, as discussed in Sec. 2.2, showed that wing flexibility could significantly modify the termination speed of the support instability, but not the onset speed. Table 4.3 shows the predicted and observed support instability boundaries and their good agreement for all four wings. The frequencies of the support instability were in the range of 0.5 to 0.6 Hz which is near the vibration frequency of the support plunge motion in still air. Figure 4.9 shows an example of support instability where the model was seen to plunge unboundedly until it hit the top and bottom plunge stops, and the wing was seen to behave "rigid" until high model pitch angle was induced. Figure 4.10 records of support instability versus increasing airspeed are also shown in Figure 4.10.

When the support instability was observed, the model was

NO-A102 713 DYNAMICS AND AEROELASTICITY OF COMPOSITE STRUCTURES(U) 2/3
MASSACHUSETTS INST OF TECH CAMBRIDGE TECHNOLOGY LAB FOR
ADVANC G CHEN ET AL 22 APR 87 TELAC-86-14A
UNCLASSIFIED AFOSR-TR-87-0845 F49620-84-C-0099 F/G 1/3. 12 NL





MICROCOPY RESOLUTION TEST CHART
NATIONAL BUREAU OF STANDARDS-1963-A

Table 4.3 Support Instability Boundaries

Wing	<u>calc.</u>		<u>exp.</u>	
	m/sec	(Hz)	m/sec	(Hz)
$[0_2/90]_s$	7 - 12	(.5 - .6)	10 - 12	(.5 - .6)
$[15_2/0]_s$	8 - 19	(.5 - .6)	10 - 20	(.5 - .6)
$[30_2/0]_s$	8 - 16	(.5 - .6)	10 - 23	(.5 - .6)
$[-15_2/0]_s$	7 - 10	(.5 - .6)	7 - 11	(.6 - .7)

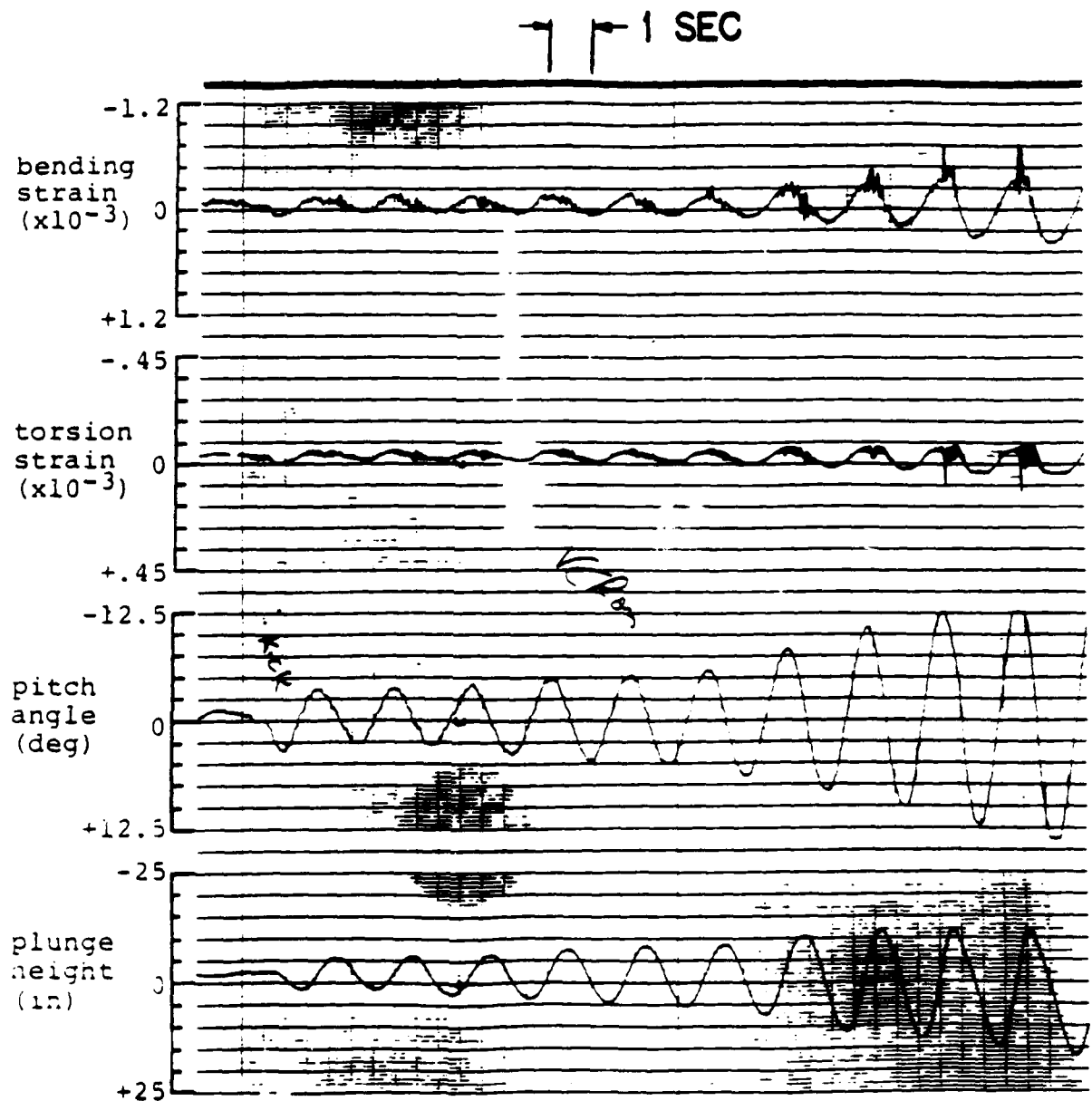


Fig. 4.9 Support Instability, $[0_2/90]_s$ Wing
($V = 10$ m/sec)

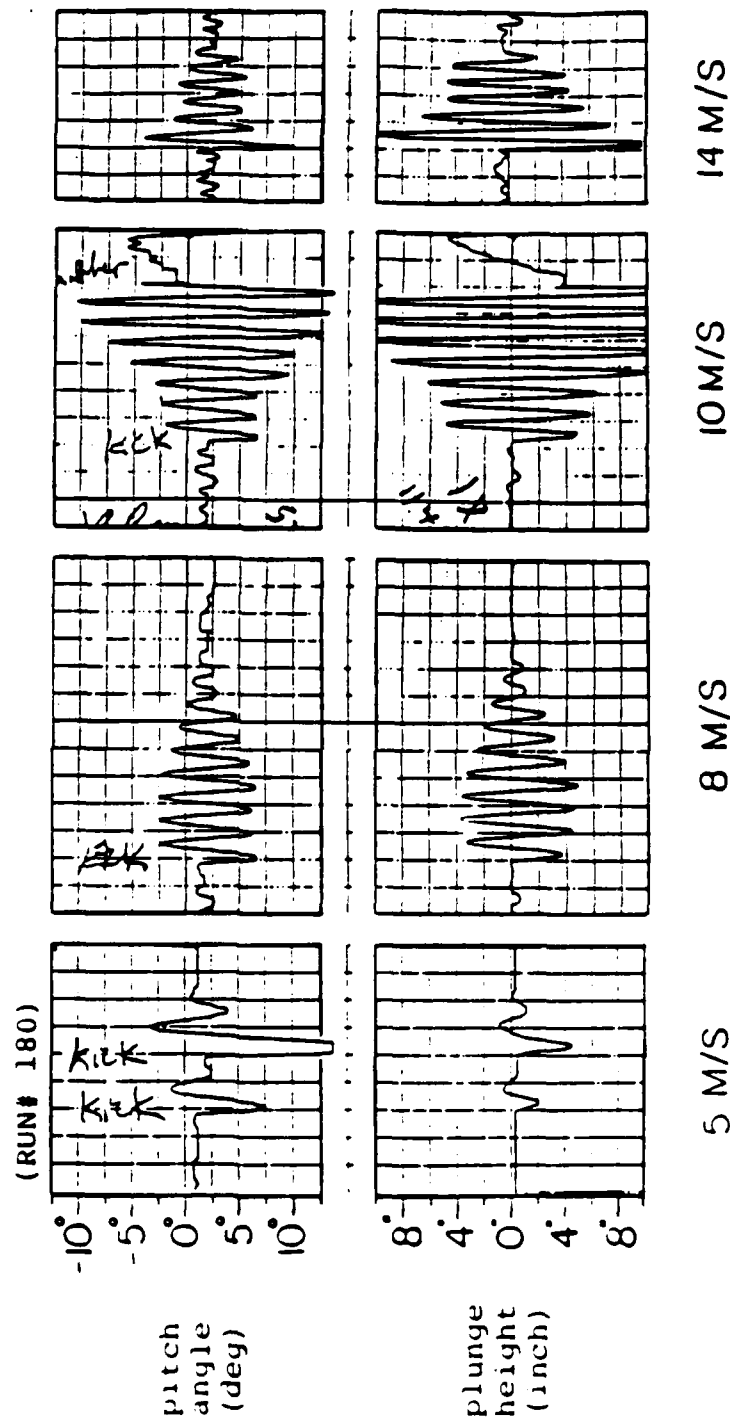


Fig. 4.10 Support Instabilities, $[0_2/90]_s$ Wing

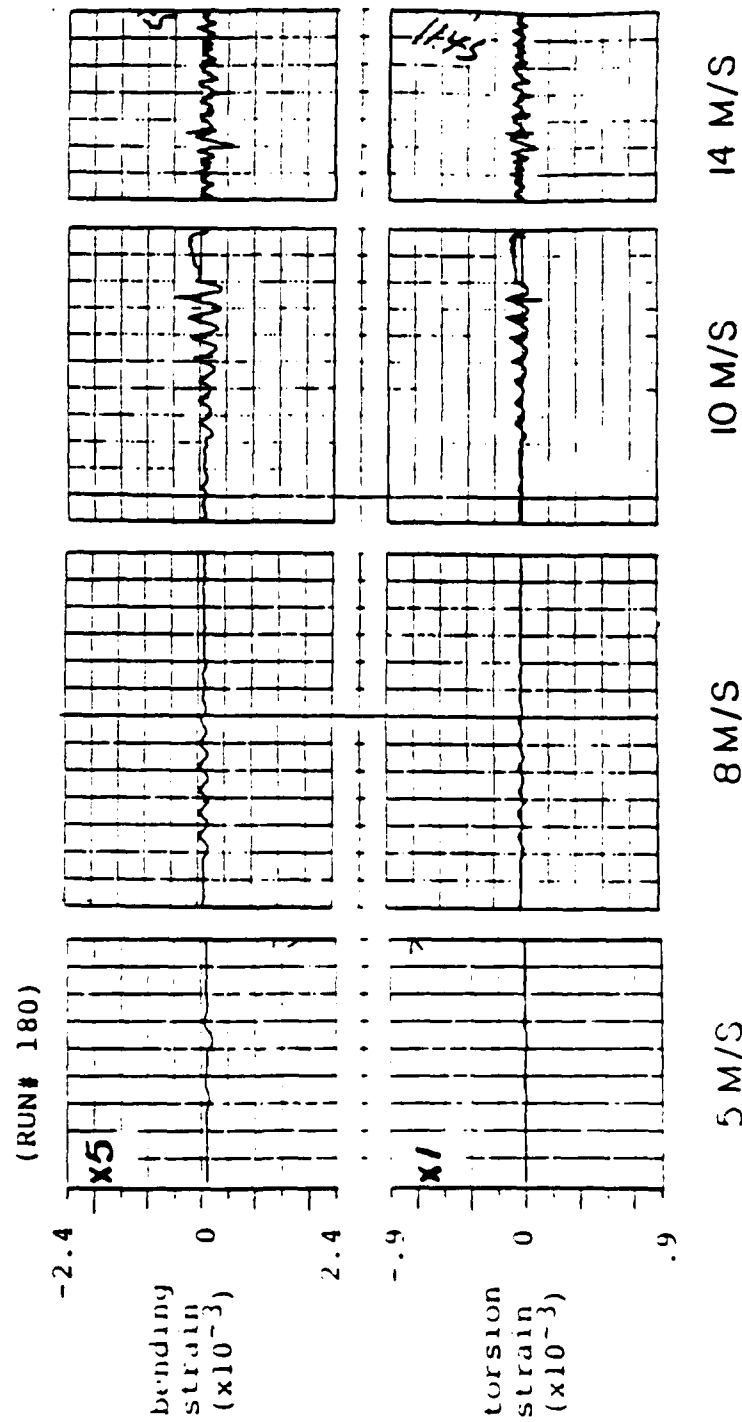


Fig. 4.10 (cont'd)

two factors vital to the survivability of the ongoing testing. One was the time constant (time to double the amplitude) of the unstable mode, the other was the model robustness. Without an active compensation scheme, an instability with a short time constant could not be limited by manually operated snubber cables. The unstable mode exhibited in the original support system, fortunately, appeared to be mild and with a long time constant, and therefore could be guarded and flown through if the model was not given much of an initial disturbance. This additional nonlinear phenomenon of disturbance magnitude dependency, which arose from friction in the support system, was often observed in the higher airspeed range and occasionally in the case of using a linear bearing which was contaminated by particles amid wind tunnel airflow after long hours of running.

To suppress the wind tunnel support related dynamic instability, the original pitching support was modified by adding mechanical pitching springs, so that the pitching frequency was increased from 0.20 Hz to 0.85 Hz as compared to the plunging frequency of 0.63 Hz. The modified support pitching damping ratio was now reduced to 0.03 due to the increased pitching frequency. This modified support system was tested and showed no signs of the support instability previously encountered.

(b) Body freedom flutter

The primary interest in flutter research usually centers on the flutter boundary and frequency of oscillation, while the flutter mode and subcritical behavior are often seen as of secondary interest. In the present study, the flutter mode and transient behavior were both monitored and played important roles in verifying the instability mechanism and assessing the preliminary aircraft flying quality. In this section, the body freedom flutter testing results will be presented in two stages. First, the general behavior will be described. Then, the results of each model will be detailed in following.

Body freedom flutter was observed during the tests wherever predicted analytically. The identification of the body freedom flutter boundary depended on the observation of model transient behavior. First, visual observation was made during the test. The oscillograph records of rigid body and wing responses were then examined in terms of frequency and phase relations. Lastly, video movies of the chronological events were replayed for flutter confirmation. Figure 4.11 shows a typical flutter onset of the model with the $[0_2/90]_S$ wing. In this figure, the aeroelastic responses, prior to and on the flutter onset, were seen to be in sharp contrast for this particular wing. The strength of instability, however, can be better understood via the results of root locus analysis which will be discussed later. Even though there were pitch decay rates estimated from subcritical measurements, the results showed too much scattering and insufficient convergence as shown in Figure 4.12, and could not be used to correlate the

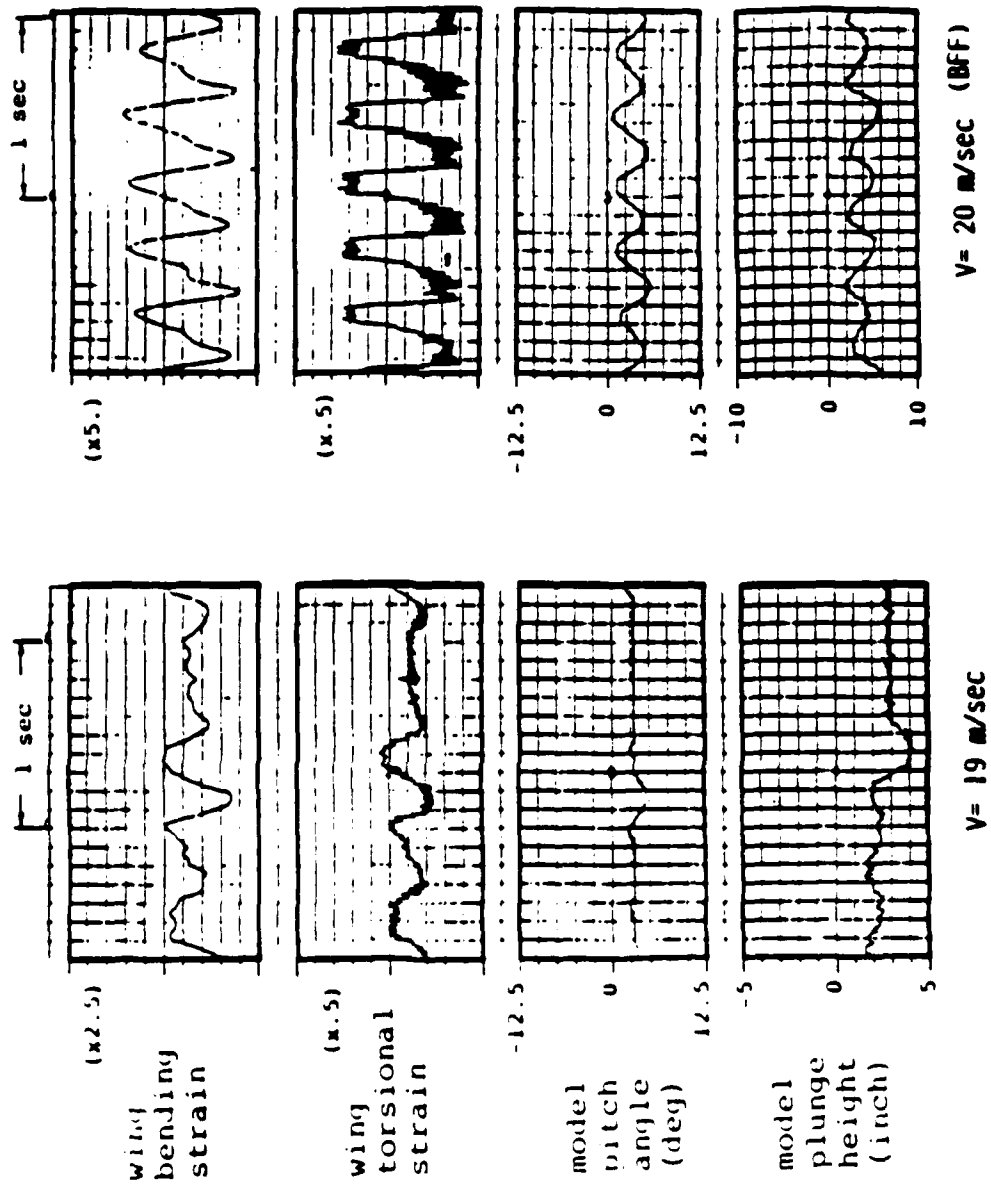


Fig. 4.11 Body Freedom Flutter Onset, $[0_2/90]_s$ Wing

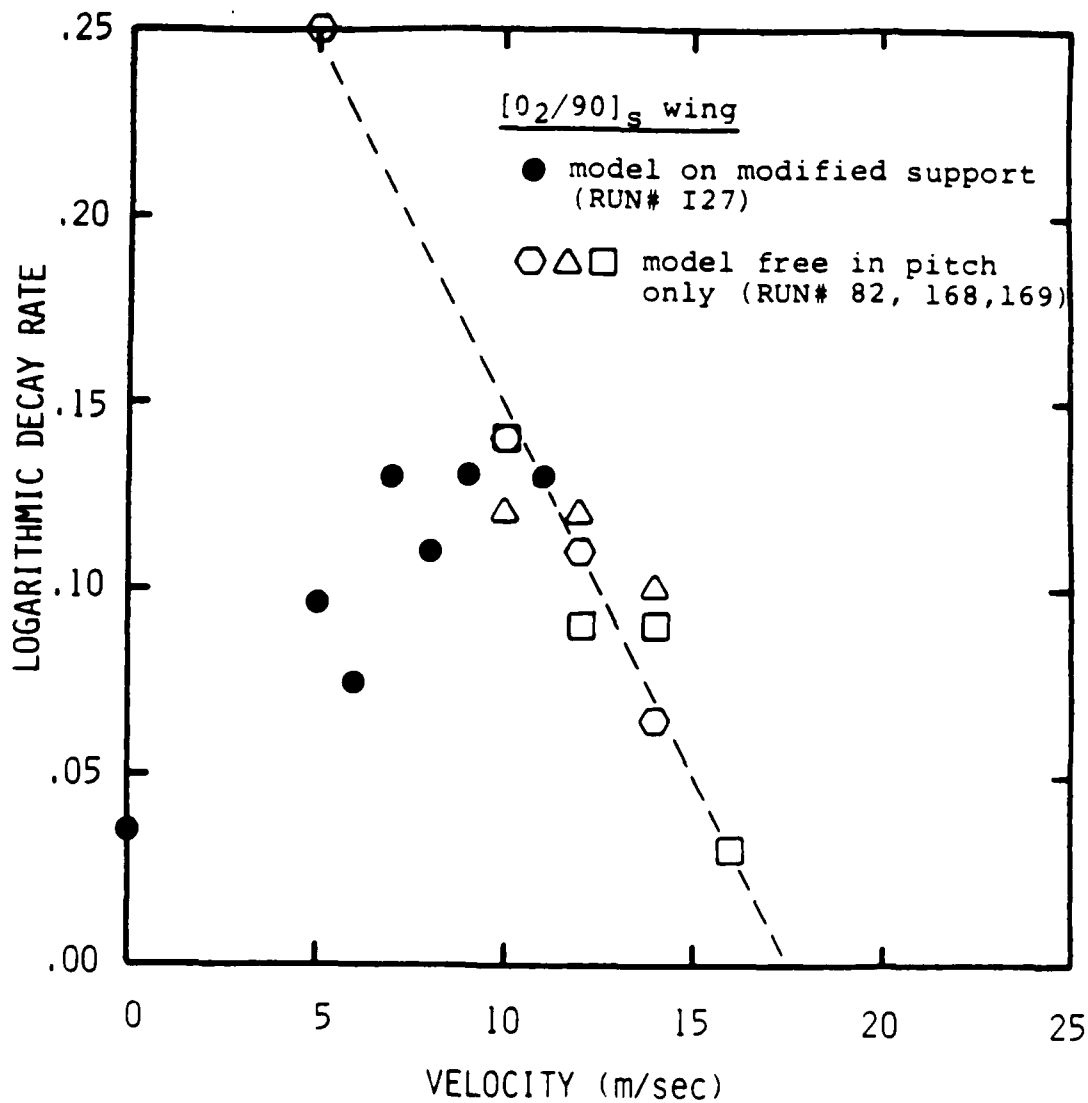


Fig. 4.12 Transient Decay Rate

instability onset. It is interesting to note that the results of model free in pitch only actually are fairly good and can be used to correlate the flutter results.

During the test, the body freedom flutter was observed to be mild and in the form of a limit cycle oscillation. The mild instability onset was partially a reflection of the low frequency (1.0 Hz to 2.8 Hz) of the instability. The limiting amplitude of the limit cycle oscillation was undoubtedly due to the aerodynamic nonlinear stalling phenomenon, rather than the structural nonlinearity. These features proved to be useful since it made close examination of the flutter modes and nonlinear behavior possible.

All the experimental flutter modes exhibited a nodal point near the model's nose position, while wing bending was approximately in-phase with the model pitch motion, and the plunge motion was about 180° out-of-phase. Wing torsional response was dictated by the inherent elastic coupling of the composite wings. The $[0_2/90]_s$ wing exhibited the typical aeroelastic effect of a forward swept wing with the wing's upward bending accompanied by leading edge up twisting. In the case of $[-15_2/0]_s$ wing, the leading edge up twisting was amplified by the adverse elastic coupling. For the $[15_2/0]_s$ and $[30_2/0]_s$ wings, the elastic coupling worked in an opposite way such that the torsional gages showed a leading edge down twisting as the wing bent upward. Table 4.4 summarizes the corresponding body freedom flutter mode predictions in terms of the contributions of the uncoupled assumed modes.

Table 4.4 Calculated Body Freedom Flutter Modes
(with modified support system)

Wing	$[0_2/90]_s$	$[30_2/0]_s$	$[-15_2/0]_s$
q_1	.45/-175°*	.68/-171°	.42/-174°
q_2	1.0/ 0°	1.0/ 0°	1.0/ 0°
q_3	.27/-13°	.87/-24°	.22/-14°
q_4	.12/-12°	.34/154°	.16/-14°
q_5	0	.01/21°	0
q_6	0	.05/159°	.01/-11°
q_7	0	.04/154°	.01/166°

q_1 : plunge mode

q_2 : pitch mode

q_3 : first bending mode

q_4 : first torsional mode

q_5 : second bending mode

q_6 : second torsional mode

q_7 : chordwise bending mode

* amplitude/phase angle

In the case of the model free in pitch only, the flutter modes were similar to those previously mentioned except that the model was forced to pitch about a fixed pitching axle. Table 4.5 summarizes the calculated body freedom flutter modes.

Another concern in observing the flutter boundary was the resemblance of the flutter mode and gust response. In the case of gust response, the wing will bend up elastically for a given nose-up pitch angle. Therefore, the behavior recorded at the body freedom flutter onset would be similar to the turbulent gust response or the intentional "kick" at subcritical speed. When the body freedom flutter onset was approached, the gust response became so lightly damped that the determination of body freedom flutter must be repeatedly examined. As a result, the flutter point was formally determined only after a harmonic oscillation was fully developed.

In the following, flutter behavior of all models tested will be described in detail. For the model with the $[0_2/90]_s$ wing, the experimental body freedom flutter mode was usually accompanied by a small high frequency torsional oscillation as shown in Figure 4.13. This torsional oscillation was a localized phenomenon and generally occurred at the peaks of body freedom flutter oscillation. This torsional frequency was close to that of the cantilever wing torsional-stall flutter shown before and occurred as the model went into the higher pitch angles of the body freedom flutter oscillation. Since the period of the body freedom flutter was much longer than

Table 4.5 Calculated Body Freedom Flutter Modes
(model free in pitch only)

Wing	$[0_2/90]_s$	$[30_2/0]_s$	$[-15_2/0]_s$
q_2	1.0/ 0°*	1.0/ 0°	1.0/ 0°
q_3	.18/-12°	.52/-16°	.15/-11°
q_4	.08/-13°	.20/163°	.11/-11°
q_5	0	0	0
q_6	0	.03/165°	.01/-9°
q_7	0	.02/162°	0

q_2 : pitch mode

q_3 : first bending mode

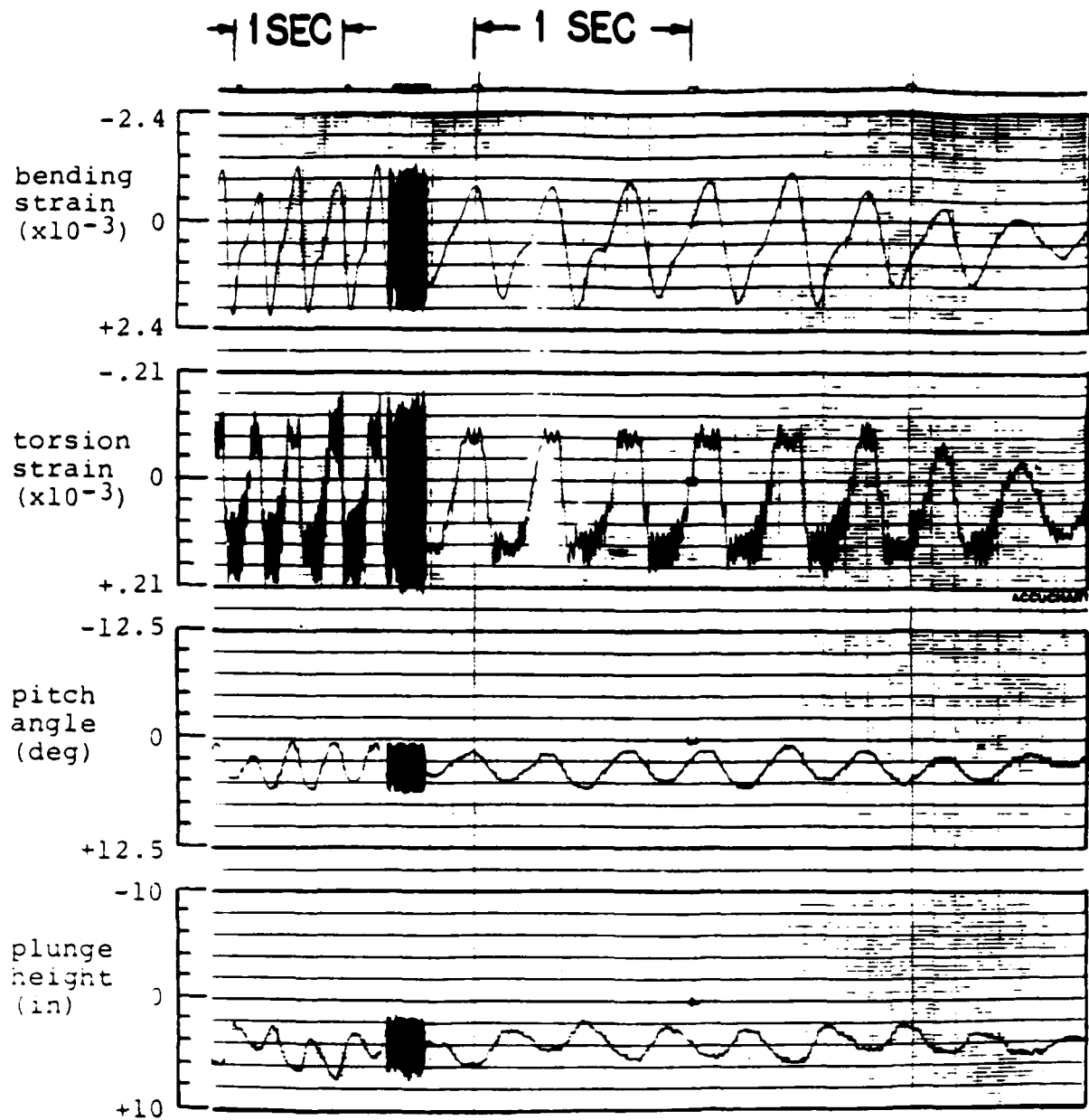
q_4 : first torsional mode

q_5 : second bending mode

q_6 : second torsional mode

q_7 : chordwise bending mode

* amplitude/phase angle



(RUN# I27)

Fig. 4.13 Body Freedom Flutter, $[0_2/90]_s$ Wing
($V = 20$ m/sec)

that of the torsional-stall flutter, the latter could build up several cycles before the model pitch angle became small again. The body freedom flutter speed and flutter frequency are summarized in Table 4.6 for all configurations tested, i.e., model in original and modified support systems, and model free in pitch only.

For the model with the $[15_2/0]_S$ wing, no body freedom flutter was encountered within the 30 m/sec tunnel speed limit, except for the model free in pitch only which exhibited a 1.4 Hz body freedom flutter at 22 m/sec. In steadily trimmed flight, without the presence of body freedom flutter, the wing alone exhibited a bending-torsion flutter at 29 m/sec, as shown in Figure 4.14, which became the critical unstable mode. Comparing with the cantilever wing results shows that the effect of rigid body freedoms on bending-torsion wing flutter are not noticeable. Table 4.7 summarizes the body freedom flutter testing results.

For the model with the $[30_2/0]_S$ wing, the observed body freedom flutter mode, as shown in Figure 4.15, was similar to that of the $[0_2/90]_S$ wing except that no torsional-stall flutter appeared in the body freedom flutter oscillation. This result was consistent with the cantilever wing testing in which no torsional-stall flutter occurred within the tunnel speed limit, unless a high pitch angle was present. Table 4.8 summarizes the body freedom flutter speed and flutter frequency for all the configurations tested.

For the model with the $[-15_2/0]_S$ wing, a clean

Table 4.6 Body Freedom Flutter Boundary, $[0_2/90]_g$ Wing

Model on Original Support

δ_c	run#	calc. m/sec (Hz)	exp. m/sec (Hz)
0.0°	185	19. (2.7)	19. (2.6)
2.5°	180		19. (2.7)
5.0°	181		19. (2.6)

Model on Modified Support

δ_c	run#	calc. m/sec (Hz)	exp. m/sec (Hz)
2.5°	127	19. (2.7)	20. (2.8)

Model Free in Pitch Only

δ_c	run#	calc. m/sec (Hz)	exp. m/sec (Hz)
0.0°	168	17. (2.0)	16. (1.7)
2.5°	169		17. (1.9)

δ_c : canard setting

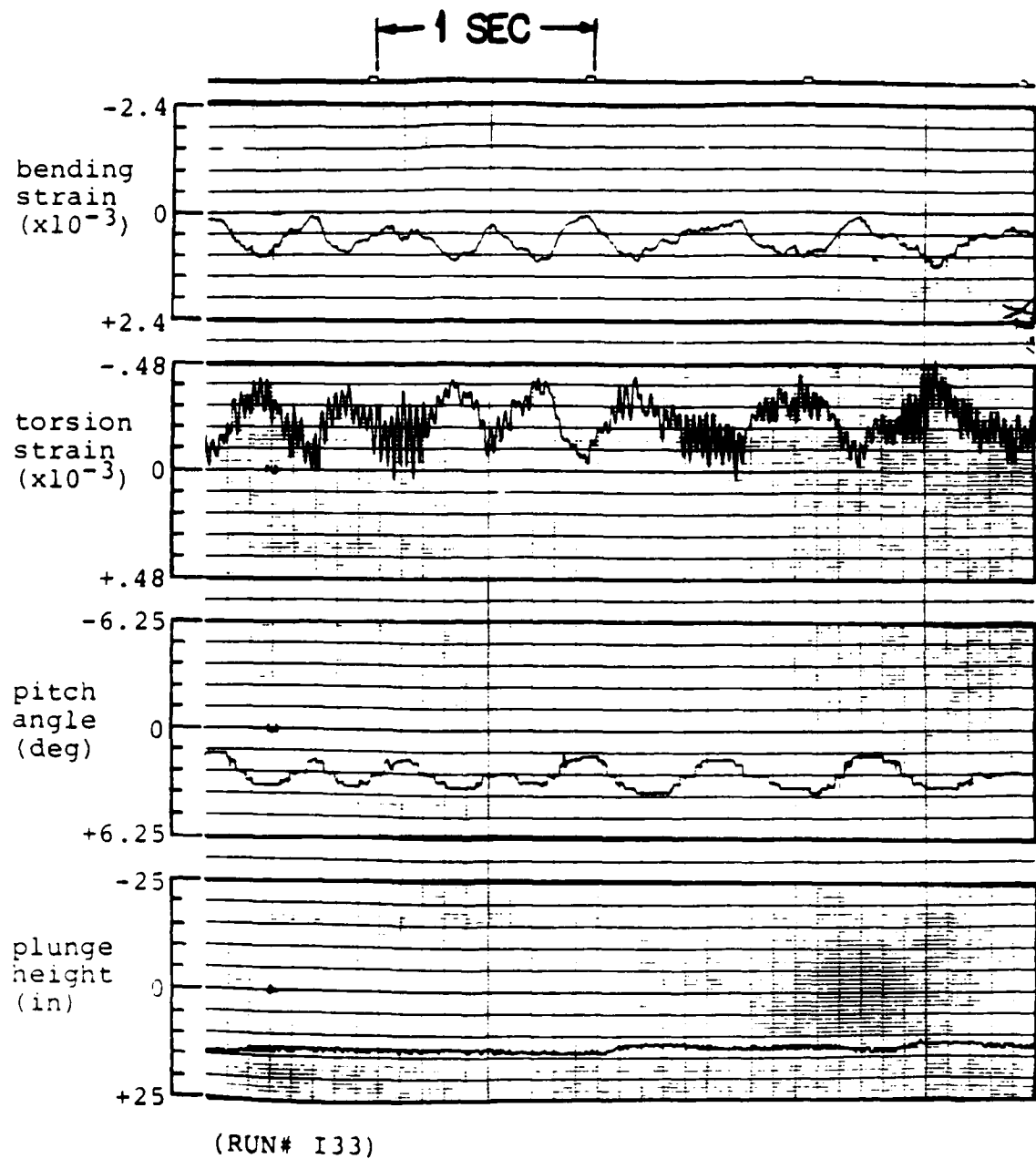


Fig. 4.14 Bending-Torsion Flutter, $[15_2/0]_s$ Wing
($V = 29$ m/sec)

Table 4.7 Body Freedom Flutter Boundary, $[15_2/0]_g$ Wing

Model on Original Support

δ_c	run#	calc. m/sec (Hz)	exp. m/sec (Hz)
2.5°	198	*	-
5.0°	199	*	-

Model on Modified Support

δ_c	run#	calc. m/sec (Hz)	exp. m/sec (Hz)
2.5°	133	*	-

Model Free in Pitch Only

δ_c	run#	calc. m/sec (Hz)	exp. m/sec (Hz)
0.0°	110	*	22. (1.4)
2.5°	112	*	22. (1.4)
-2.5°	113	*	20. (1.5)

δ_c : canard setting

* : No BFF predicted analytically

- : Wing flutter was encountered

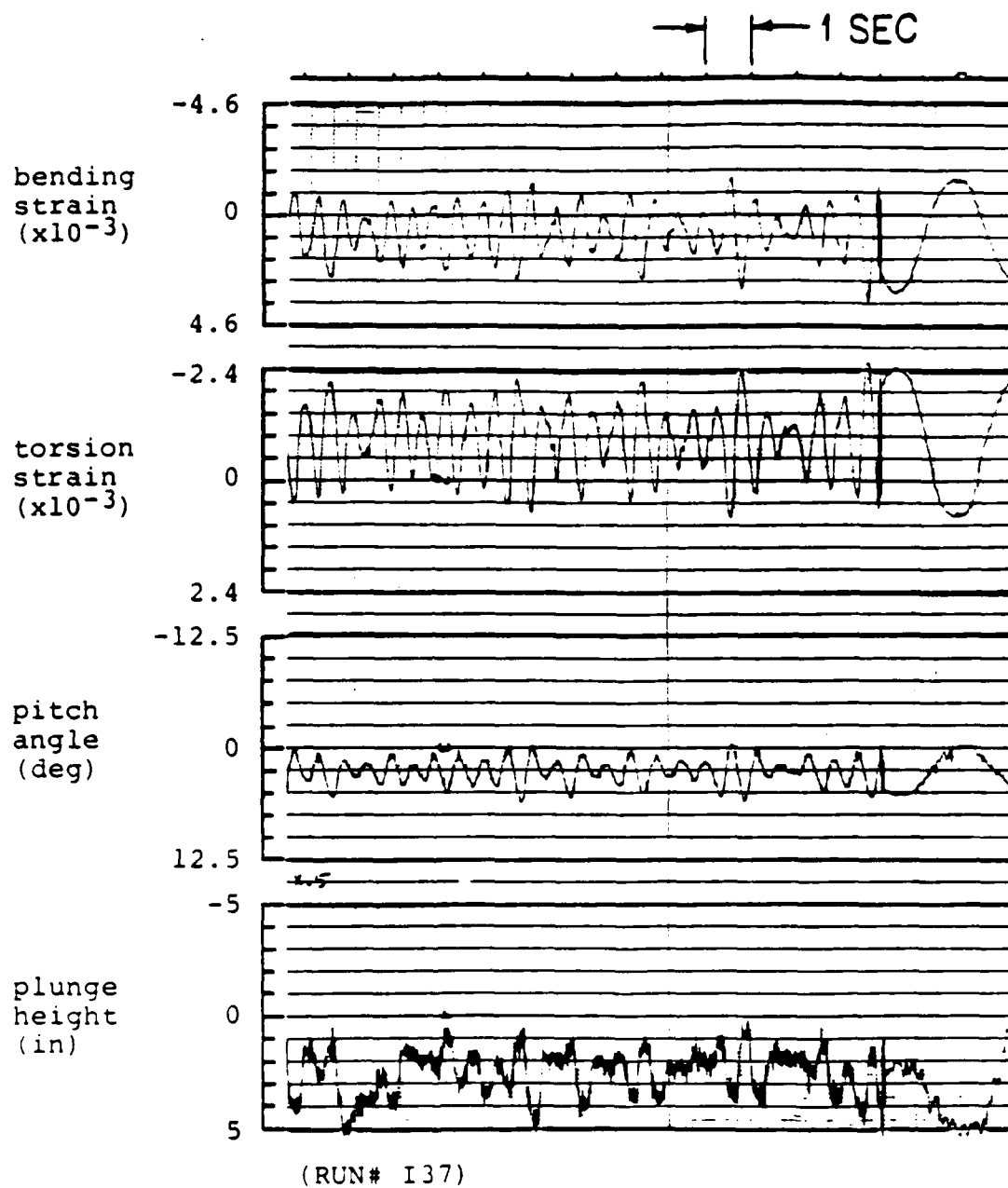


Fig. 4.15 Body Freedom Flutter, $[30_2/0]_s$ Wing
($V = 27$ m/sec)

Table 4.8 Body Freedom Flutter Boundary, $[30_2/0]_g$ Wing

Model on Original Support

δ_c	run#	calc. m/sec (Hz)	exp. m/sec (Hz)
0.0°	207	28. (2.6)	n.a.
2.5°	206		26. (1.7)
5.0°	211		n.a.

Model on Modified Support

δ_c	run#	calc. m/sec (Hz)	exp. m/sec (Hz)
2.5°	137	28. (2.6)	27. (1.8)

Model Free in Pitch Only

δ_c	run#	calc. m/sec (Hz)	exp. m/sec (Hz)
0.0°	129	21. (1.8)	19. (1.2)
2.5°	130		19. (1.2)
-2.5°	133		19. (1.3)

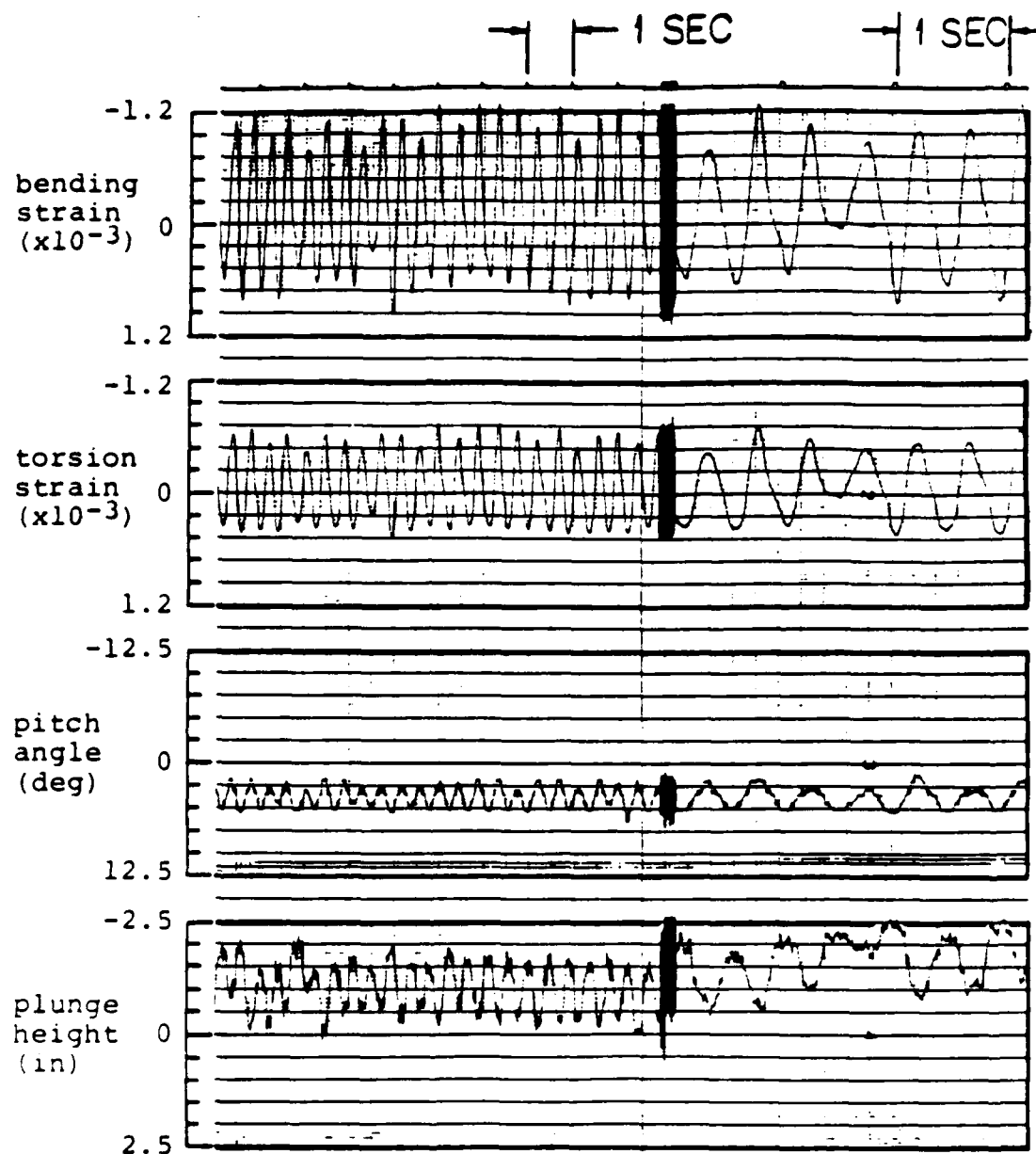
δ_c : canard setting

n.a. : data not available

pitch/bending oscillation of body freedom flutter was observed at the flutter onset as shown in Figure 4.16. The body freedom flutter speed and frequency are tabulated in Table 4.9.

As previously mentioned in cantilever wing testing, the static divergence of the $[-15_2/0]_s$ wing was actually observed as a dynamic bending-stall flutter with a somewhat lowered bending frequency. When the wing root boundary condition was relaxed, it was important to be able to distinguish the body freedom flutter from the bending-stall flutter. From the observations of the model's behavior, there were three features which existed for distinction between the two instabilities. First, the observed body freedom flutter mode was similar to that of models with the $[30_2/0]_s$ and the $[0_2/90]_s$ wings which did not experience any bending-stall flutter in the cantilever wing testing.

Secondly, the body freedom flutter oscillated in a relatively low frequency, 2.3 Hz for the model with the $[-15_2/0]_s$ wing, compared to the 5.0 Hz bending-stall flutter observed in the cantilever wing testing. Lastly, as the tunnel airspeed was increased beyond the body freedom flutter onset, the wing bending response was increased and accompanied by trace of bending-stall flutter at each peaks of the well developed body freedom flutter oscillation. The frequency of this localized bending-stall flutter was found to be close to the frequency of the cantilever wing bending-stall flutter. Therefore, the bending-stall flutter was concluded not to appear on a "free flight" testing except for the localized



(RUN# I46)

Fig. 4.16 Body Freedom Flutter, $[-15_2/0]_s$ Wing
($V = 13$ m/sec)

Table 4.9 Body Freedom Flutter Boundary, $[-15_2/0]_s$ Wing

Model on Original Support

δ_c	run#	calc. m/sec (Hz)	exp. m/sec (Hz)
0.0°	226	12. (1.8)	13. (2.1)
2.5°	227		13. (2.3)

Model on Modified Support

δ_c	run#	calc. m/sec (Hz)	exp. m/sec (Hz)
2.5°	I46	12. (1.9)	13. (2.3)

Model Free in Pitch Only

δ_c	run#	calc. m/sec (Hz)	exp. m/sec (Hz)
0.0°	152	11. (1.4)	10. (1.0)
2.5°	153		10. (1.1)
-2.5°	154		10. (1.0)

δ_c : canard setting

appearance in the body freedom flutter oscillation.

Unlike the torsional-stall flutter, the bending-stall flutter intensified quickly with a small increase in airspeed. The severe wing flapping motion in bending-stall flutter could induce significant inertia force in plunge motion to detach the friction-fitted linear bearing from the model, and interrupt the ongoing testing. In some of these cases, when model roll freedom was relaxed, due to loss of the bearing, and when the pitch angle was held by snubber cables, the $[-15_2/0]_S$ wing could exhibit either a 6 Hz symmetric bending-stall flutter or an 11 Hz anti-symmetric bending-stall flutter.

CHAPTER FIVE

DISCUSSION

In this chapter, the significant trends of the previous results will be summarized first. Then a comparison will be made with theoretical analysis for the flutter boundary and transient aeroelastic responses. With this well-verified analytical model, some parametric effects on body freedom flutter will be explored. Lastly, the aeroelastic effect on support instability will be further examined.

5.1 Summary of Results

Typical results of the various wings tested are summarized in Table 5.1. Figure 5.1 also gives an illustrative summary of the flutter boundary in terms of aeroelastic tailoring. From these results, four major trends are noted in following.

(a) Aeroelastic tailoring effect

The aircraft model with the $[15_2/0]_S$ wing demonstrated the best tailored aeroelastic behavior for all wings tested. From Figure 5.1, it can be seen that the "optimum" tailored wing, in terms of body freedom flutter, has a ply orientation between 15° and 20° . Due to the presence of the other type of instability, namely, wing bending-torsion flutter, the actual

Table 5.1 Summary of Divergence and Flutter Boundaries

Wing	[0 ₂ /90] _s		[15 ₂ /0] _s	
	calc. m/sec (Hz)	exp. m/sec (Hz)	calc. m/sec (Hz)	exp. m/sec (Hz)
Cantilever Wing Divergence	21	21	*** ¹	---
Cantilever Wing Flutter	23 (23.)	---	28 (30.)	30 (31.)
BFF (original support)	19 (2.7)	19 (2.7)	***	>30 ²
BFF (modified support)	19 (2.7)	20 (2.8)	***	>30
BFF (free in pitch only)	17 (2.0)	17 (1.9)	***	22 (1.4)
BFF (completely unrestrained)	19 (2.6)	n.a. ³	***	n.a.

1 No BFF predicted analytically

2 Wind tunnel speed limit = 30 m/sec

3 Not applicable

Table 5.1 Summary of Divergence and Flutter Boundaries
(cont'd)

Wing	[30 ₂ /0] _s		[-15 ₂ /0] _s	
	calc. m/sec (Hz)	exp. m/sec (Hz)	calc. m/sec (Hz)	exp. m/sec (Hz)
Cantilever Wing Divergence	45	---	13	14
Cantilever Wing Flutter	38 (33.)	>30	*** ¹	---
BFF (original support)	28 (2.6)	26 (1.7)	12 (1.8)	13 (2.3)
BFF (modified support)	28 (2.6)	27 (1.8)	12 (1.9)	13 (2.3)
BFF (free in pitch only)	21 (1.8)	19 (1.2)	11 (1.4)	10 (1.1)
BFF (completely unrestrained)	27 (2.5)	n.a. ³	12 (1.7)	n.a.

- 1 No BFF predicted analytically
 2 Wind tunnel speed limit = 30 m/sec
 3 Not applicable

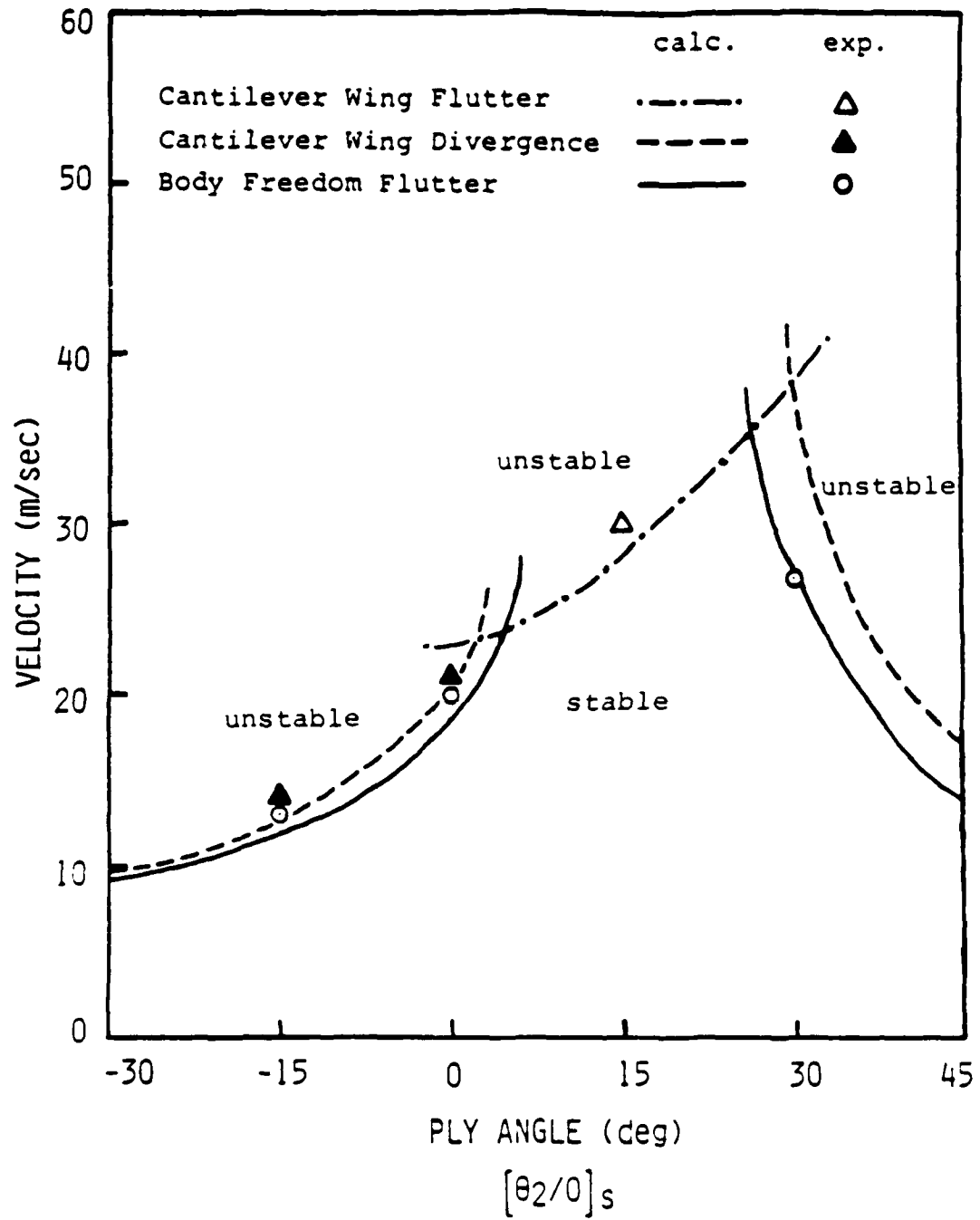


Fig. 5.1 Body Freedom Flutter Boundary,
Model on Modified Support System

"optimum" ply orientation may be altered. Examination of Figure 5.1 shows that the wing flutter speed can also be improved by rotating the ply orientation. However, with the same ply rotation angle, the improvement of wing flutter seems relatively mild compared to the body freedom flutter. In the present study, the overall "optimum" ply orientation is only slightly changed, and is in the vicinity of 25° . As expected, the model with the $[-15_2/0]_s$ wing has the most deteriorated performance because of the adverse elastic coupling as discussed in Chapter 2. Even though the $[30_2/0]_s$ wing has the highest coupling stiffness ratio, $D_{16}/\sqrt{D_{11}D_{66}}$ of 0.80, the body freedom flutter speed actually drops instead of increases. This is due to the fact that the wing bending stiffness ratio, D_{11}/D_{66} , is simultaneously decreased as the coupling stiffness ratio increases for this particular laminate. The adverse effect of reduced bending stiffness overwhelms the improving effect of stiffness coupling.

(b) Body freedom flutter vs. wing divergence

Comparing with the cantilever wing divergence boundary, body freedom flutter is shown to be more critical than wing divergence in Figure 5.1. The degree of criticality, however, is not uniform for all tailored wings. In other words, the aeroelastic tailoring effects on wing divergence and body freedom flutter are somewhat different. For example, the calculated wing divergence speed increased by 114% as ply

orientation rotates from 0° to 30° , while the body freedom flutter speed improved by only 42%. In general, the "optimum" tailored wing seems to be more sensitive to the presence of rigid body freedoms.

Examination of the body freedom flutter boundary in Figure 5.1 shows that the effect of aeroelastic tailoring on body freedom flutter follows the trend of cantilever wing divergence tailoring. This suggests that wing destiffening is still the primary triggering mechanism of the body freedom flutter as of the cantilever wing divergence. The presence of rigid body freedoms modify the boundary conditions of the aeroelastically destiffened wing mode, and ultimately changes the instability nature from the static divergence to dynamic flutter. The recognition of the "destiffened" wing mode (analogy to wing divergence mode) in body freedom flutter is not only important in understanding the underlying instability mechanism but also vital to the possible instability prevention.

The significance of the above observation is that the prevention of body freedom flutter will largely rely on the control of the "destiffened" wing mode instead of the flight dynamic modes, even though these involve significant rigid body motions in body freedom flutter. The aeroelastic tailoring in the present study serves exactly this purpose through the use of composite materials. It is interesting to note that Ref. 41 showed weak performance of the flight dynamics control by using a canard based stability augmentation system. Refs. 42 and 43

also demonstrated the possible application of wing based active control of the "destiffened" wing mode. Since the aeroelastic destiffening is a strong instability tendency while the short period mode is originally stable, the dominance of the "destiffened" wing mode in body freedom flutter would be expected.

Qualitatively speaking, the aeroelastic tailoring trends of the cantilever wing divergence can be used as a preliminary design for preventing the body freedom flutter. However, the tailoring effectiveness is not quite the same for these two types of instability. The actual body freedom flutter boundary, which is the most critical now, can only be obtained by the complete aeroelastic analysis including the rigid body freedoms.

(c) Pitch-plunge testing vs. pitch only testing

The absence of the plunging freedom resulted in a somewhat lowered body freedom flutter speed in the present study, thereby giving a conservative flutter boundary as shown in Figure 5.2. The stabilizing effect of plunging freedom is similar to the findings in Ref. 20. A possible explanation is that the model is stabilized by the favorable phase response of the pitch and plunge freedoms. When the aircraft was free to pitch and plunge, the flutter mode always exhibits a nodal point near the model nose position which is far ahead of pitching axle. The longer distance between the nodal point and

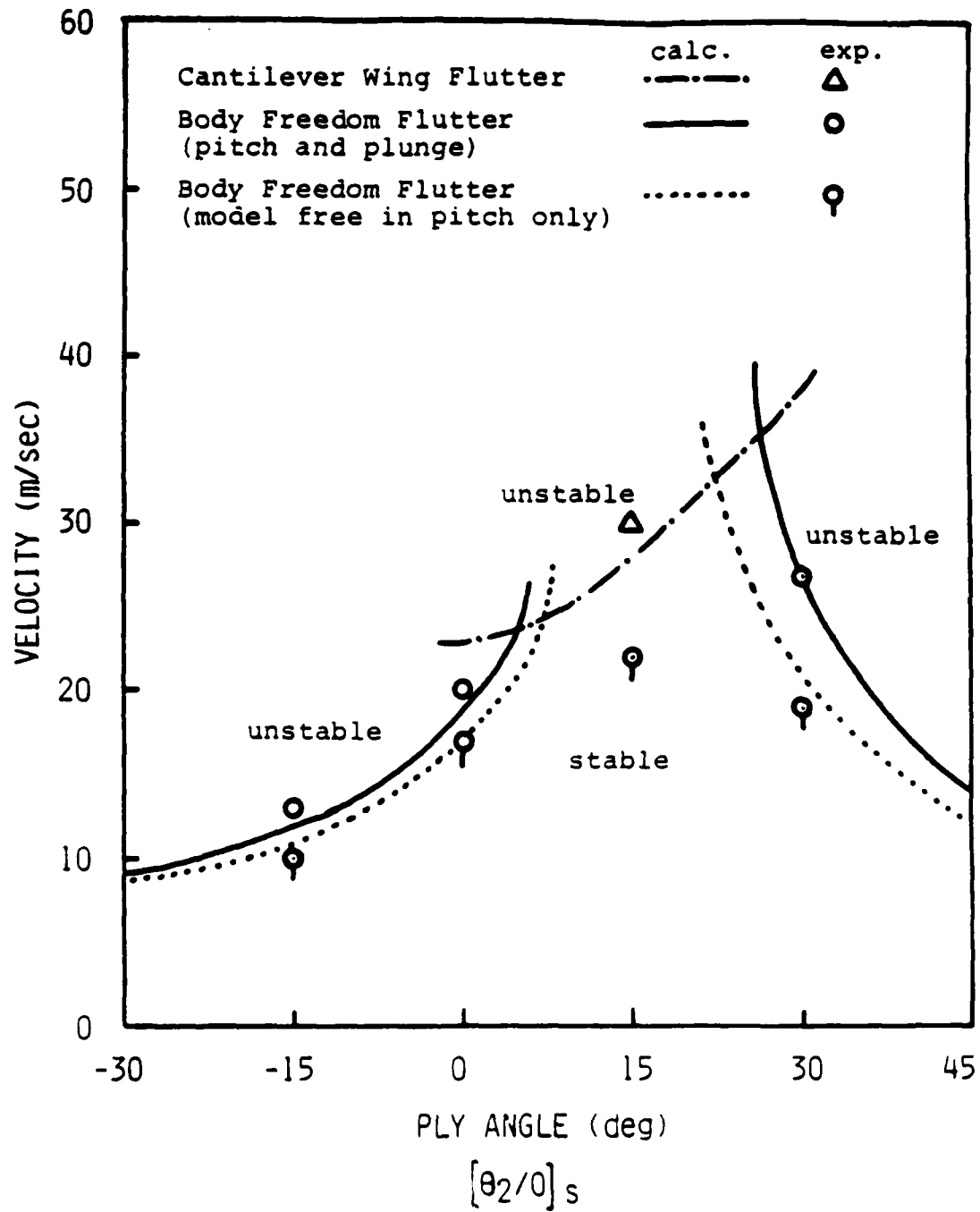


Fig. 5.2 Body Freedom Flutter Boundary,
Model Free in Pitch-Plunge vs. Pitch Only

aircraft aerodynamic center, slightly aft of the pitching axle, may be the major reason for delaying the instability. The resulting flutter frequencies, ranging from 1.4 to 2.0 Hz, were also found to be significantly lower than those of the models free in pitch and plunge freedoms.

Wind tunnel testing of the model free in pitch only is a relatively easy task and an attractive alternative for body freedom flutter testing. The aforementioned comparisons of flutter boundary and flutter behavior, however, show that the aircraft plunge freedom plays an important role in body freedom flutter instability. To obtain meaningful results and true insight of body freedom flutter of a forward swept wing aircraft, a more complicated testing, including both rigid body pitch and plunge freedoms, must be performed such as in the present study.

(d) Analytical Correlation

The aeroelastic analysis of the wind tunnel model was based on the analytical model formulated in Chapter 2. Good agreement between calculated and observed flutter boundary was obtained for most all cases. The flutter frequencies were found in between the support pitch frequency, 0.20 Hz or 0.85 Hz, and the corresponding wing bending frequencies. The best agreement between predicted and measured frequencies is the model with the $[0_2/90]_s$ wing. For model with the $[30_2/0]_s$ wing, the flutter frequencies were somewhat overpredicted in

all configurations, while those of the $[-15_2/0]_s$ wing were somewhat underpredicted. A possible explanation is that the overall pitching stiffness was not correctly predicted in the analytical model due to the aeroelastic twisting and untwisting of the bending-twisting coupled composite wings.

This well-correlated analytical model was attributed to the use of the modified strip theory and the measured aerodynamic derivatives as described in Chapter 2. The use of the static lift-curve-slope distribution in wing motion proved to be a good approximation because of the low flutter reduced frequency, $k = 0.02$ to 0.05 . For comparison purposes, the flutter boundary resulted from an overall finite span correction is also tabulated in Table 5.2. The overall correction factor is given by Eq. (5-223) of Ref. 35 as

$$\frac{d}{d\alpha} C_L = \frac{AR}{AR + a_0 \cos \Lambda / \pi} a_0 \cos \Lambda \quad (5.1)$$

where a_0 is the two dimensional lift-curve-slope for incompressible flow, 2π . Results show that Eq. (5.1) gives a too conservative prediction.

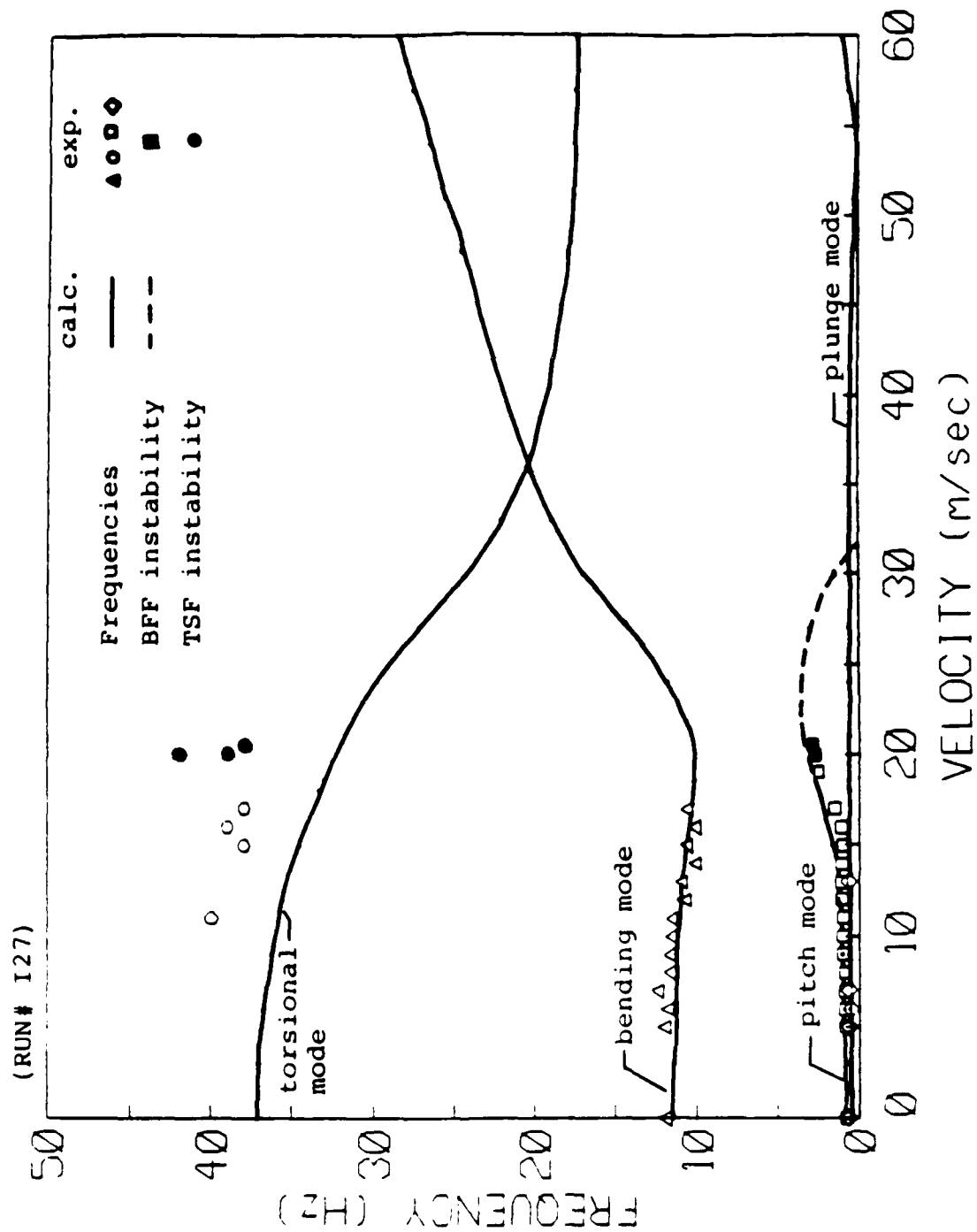
In addition to the flutter boundary and flutter frequency, the measured transient aeroelastic responses were also compared with the predicted responses. Figures 5.3 to 5.6 show the typical predicted and measured ω -V responses on the modified support system. Results of the other tests are included in Appendix C. In general, good agreement is obtained for most

**Table 5.2 Comparison of Body Freedom Flutter Boundaries
of Two Different Finite Span Corrections**

	Modified [*] Strip Theory	Correction by [*] Eq. (5.1)
	m/sec (Hz)	m/sec (Hz)
$[0_2/90]_s$	19 (2.7)	16 (2.3)
$[15_2/0]_s$	**	**
$[30_2/0]_s$	28 (2.6)	23 (2.1)
$[-15_2/0]_s$	12 (1.9)	10 (1.6)

* Theoretical prediction for models on
modified support system

** No BFF predicted analytically



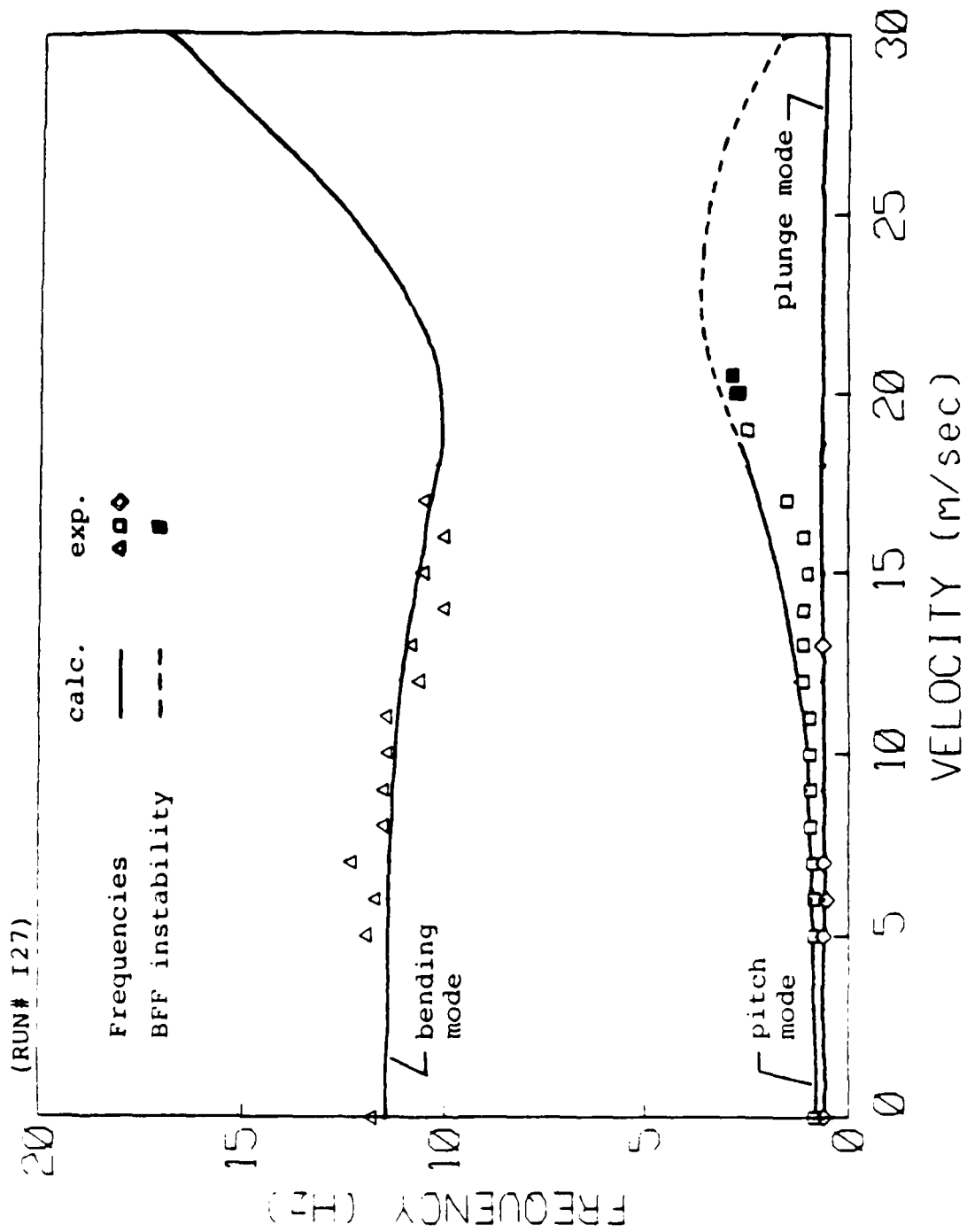


Fig. 5.3 ω -V Plot, Modified Support, $[0_2/90]_s$ Wing (cont'd)

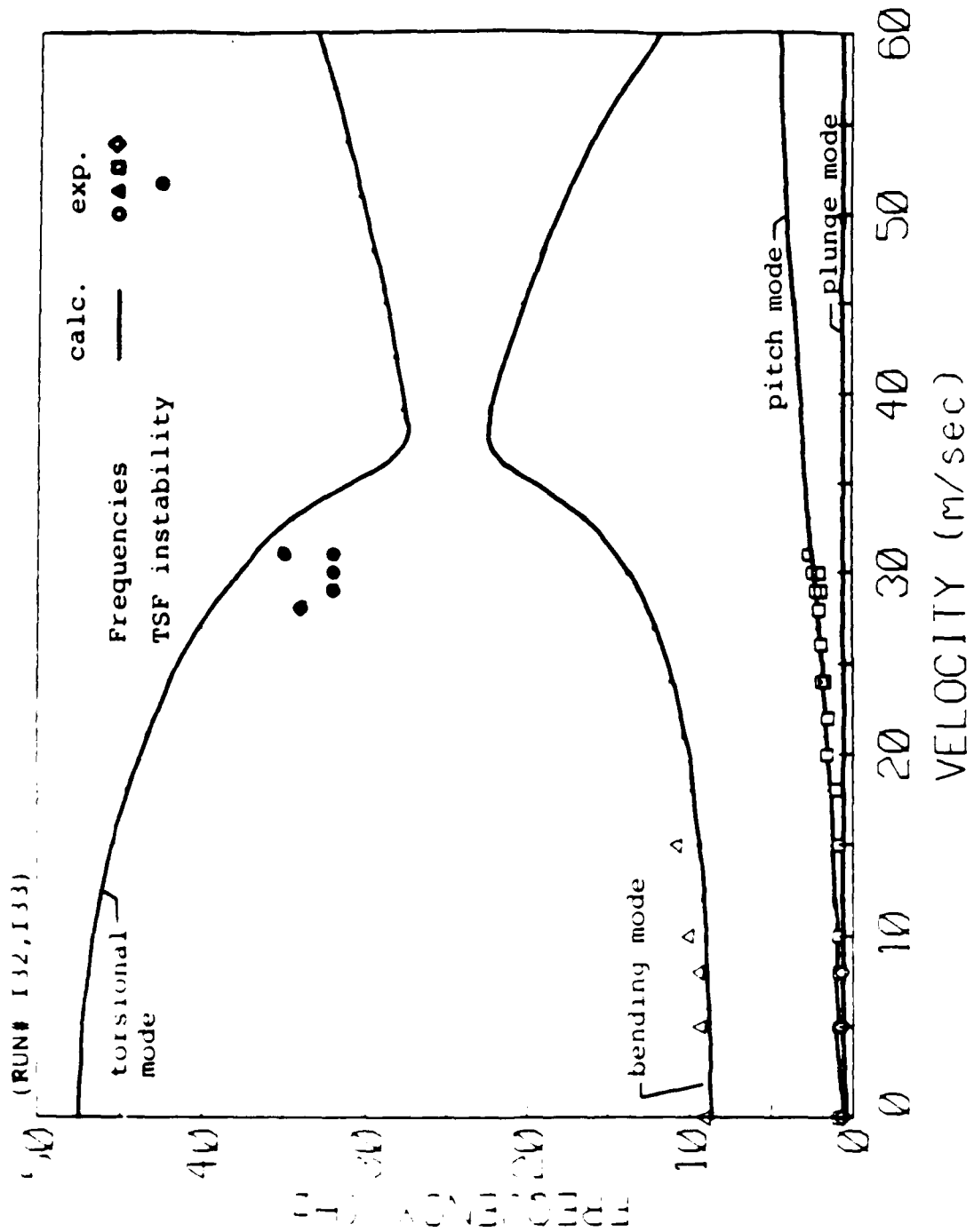


Fig. 5.4 ω -V Plot, Modified Support, $[15_2/0]_s$ Wing

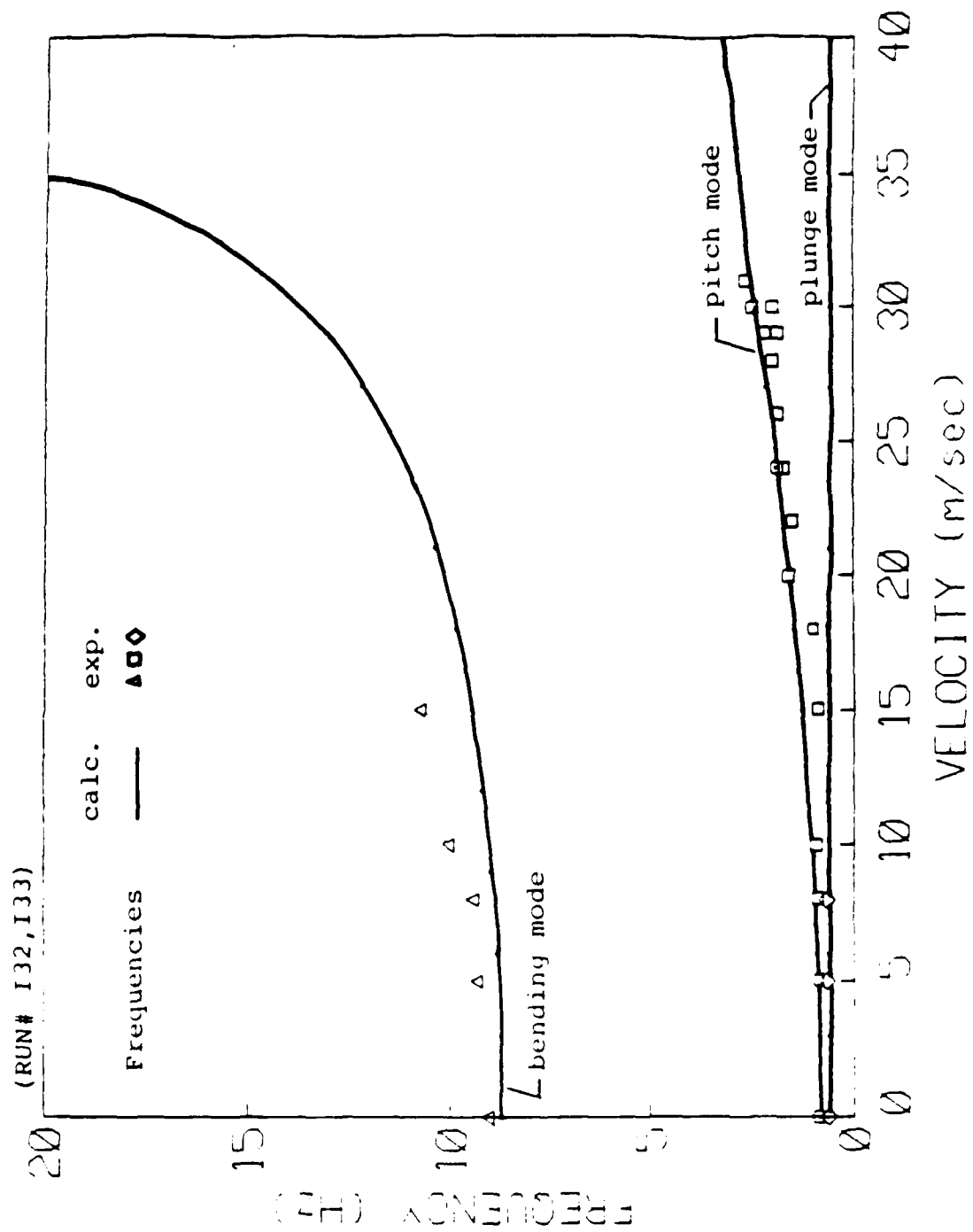


Fig. 5.4 ω -V Plot, Modified Support, $[15_2/0]_s$ Wing (cont'd)

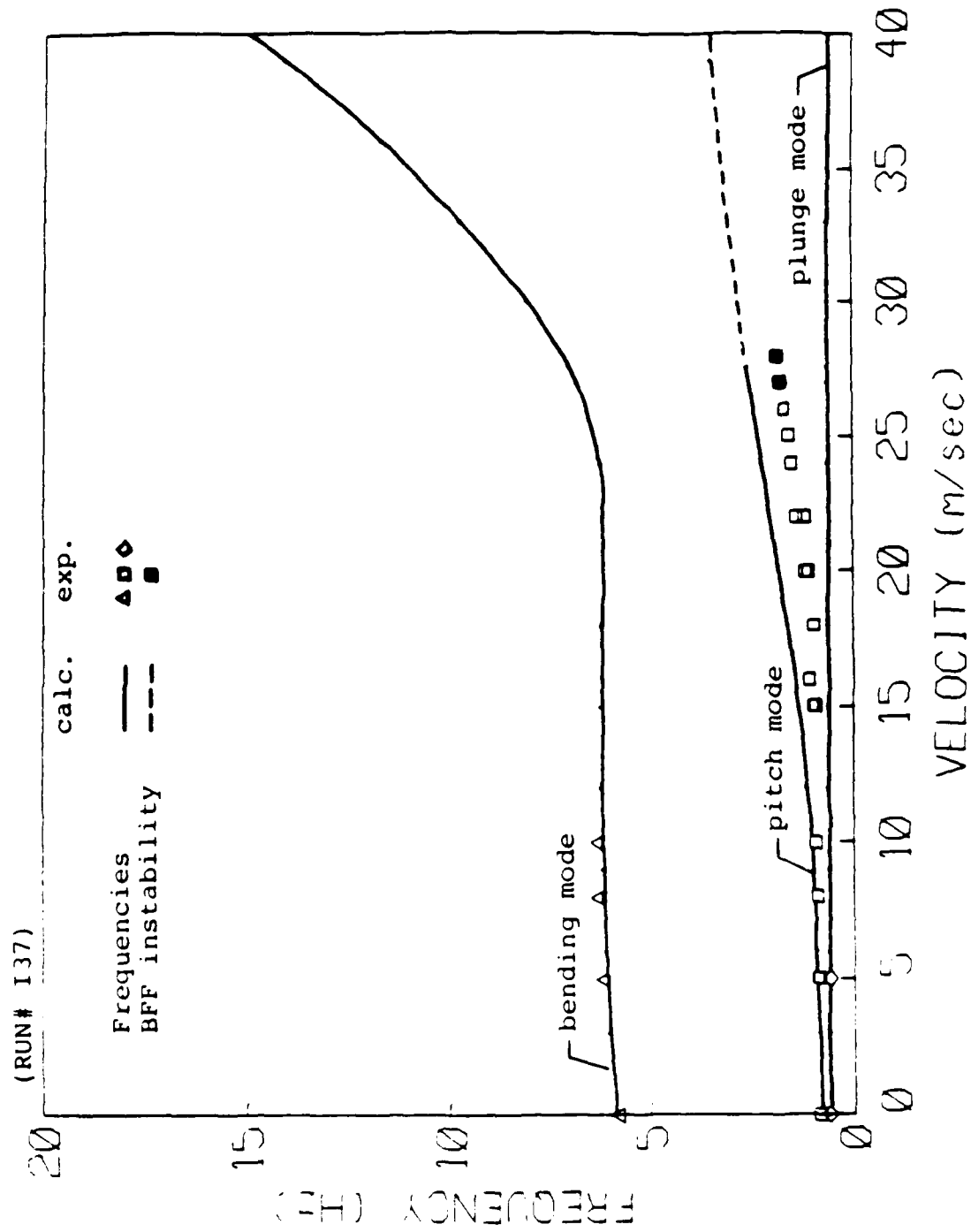


Fig. 5.5 ω -V Plot, Modified Support, $[30_2/0]_s$ Wing

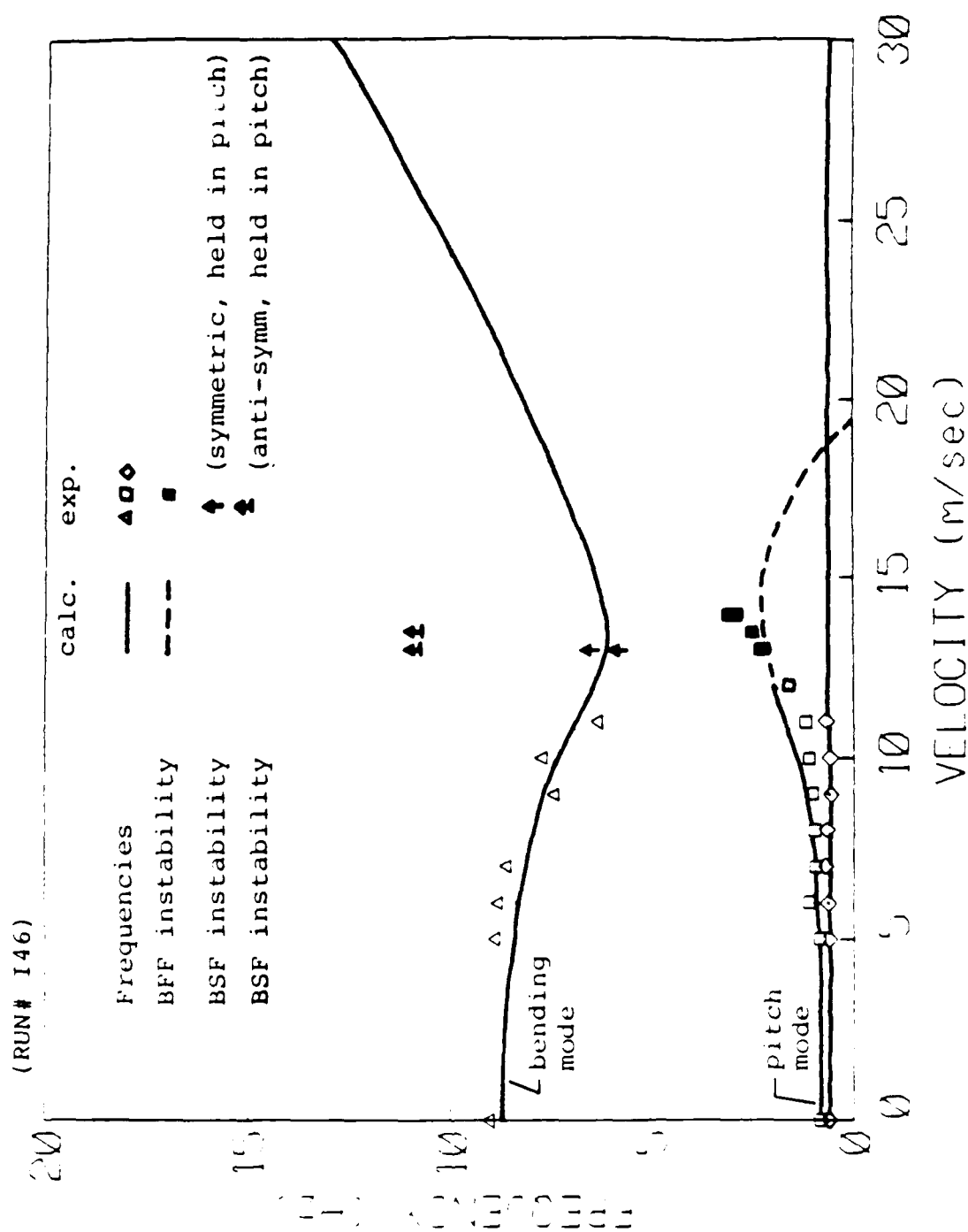


Fig. 5.6 ω -V Plot, Modified Support, $[-15_2/0]_s$ Wing

cases. Due to the support instability inherent in the original support system, the transient decay measurements incur large scattering in wing responses. This experimental scattering could arise from two sources when support instability is present. One is the difficulty in experimentally exciting the wing frequencies in this region, the other is the possible nonlinearity in flight dynamics (or relaxed wing root boundary condition). Nevertheless, results from the original and the modified support system converged well at the flutter point. Because of the better controlled testing environment, when the plunging mode was absent, the model free in pitch only exhibited the best correlated results.

In these ω -V plots, the torsional-stall and bending-stall flutter are also presented without analytical correlation. This stall flutter is a nonlinear phenomenon which added on to the body freedom flutter predicted by the present linear analysis.

5.2 Body Freedom Flutter of Completely Unrestrained Vehicle

In this section, the aeroelastic behavior of the completely unrestrained vehicle will be compared with tunnel supported configurations analytically. The root locus analysis will be used to illustrate the transient behavior and its instability onset.

In a root locus analysis, the complex roots of the

characteristic equation are plotted on the complex plane. Each branch of complex roots starts from the imaginary (frequency) axis. As airspeed increases, the complex roots move on the complex plane accordingly. If a branch of complex roots crosses the frequency axis and moves into the right half plane, then instability occurs. Figures 5.7 to 5.10 show root locus plots and low frequency highlights for all models in completely unrestrained flight condition. In these figures, each symbol represents a 3 m/sec airspeed increment.

Comparison of these root locus plots shows dramatic differences in transient behavior among all four models. For models with the $[0_2/90]_s$, $[30_2/0]_s$ and $[-15_2/0]_s$ wings, body freedom flutter instability occurs, since the pitch mode becomes unstable. Examining how "fast", (in terms of speed increment), the pitch mode moves into the right half plane, the plots show that the model with $[-15_2/0]_s$ wing has the strongest instability, while the model with $[30_2/0]_s$ wing exhibits a rather weak instability. The pitch mode of the $[30_2/0]_s$ wing is eventually stabilized again at higher speed as the pitch branch moves back to the left half plane. The model with the $[15_2/0]_s$ wing demonstrates the best aeroelastically tailored model, since the pitch mode never moves into the right half plane. In addition to the body freedom flutter, there also exists a wing bending-torsion flutter as indicated by the crossing of the torsional mode or bending mode into the right half plane. It should be noted that the designations of "pitch", "bending", and "torsional" modes are only for

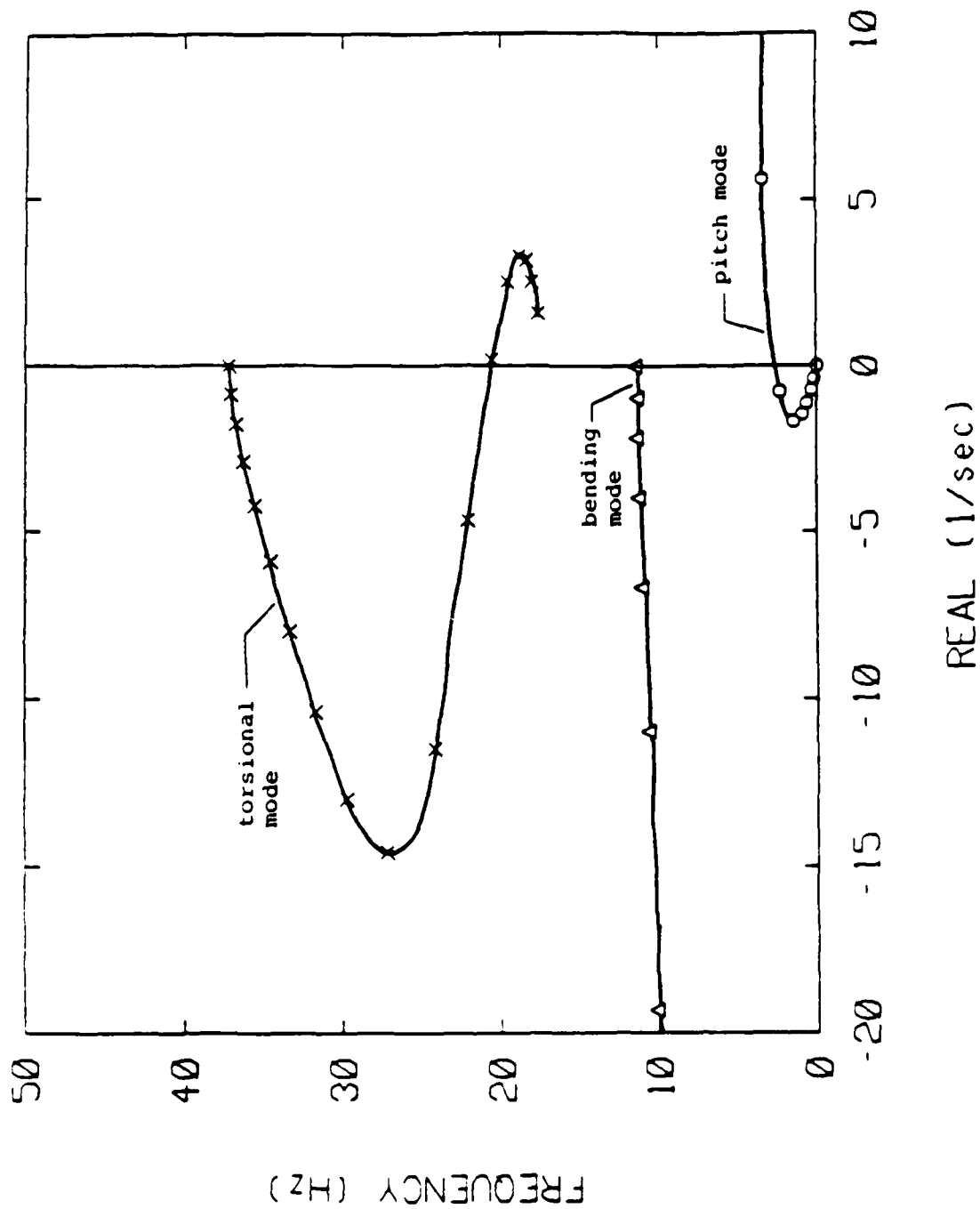


Fig. 5.7 Root Locus Plot, Completely Unrestrained Model with $[0_2/90]_s$ Wing

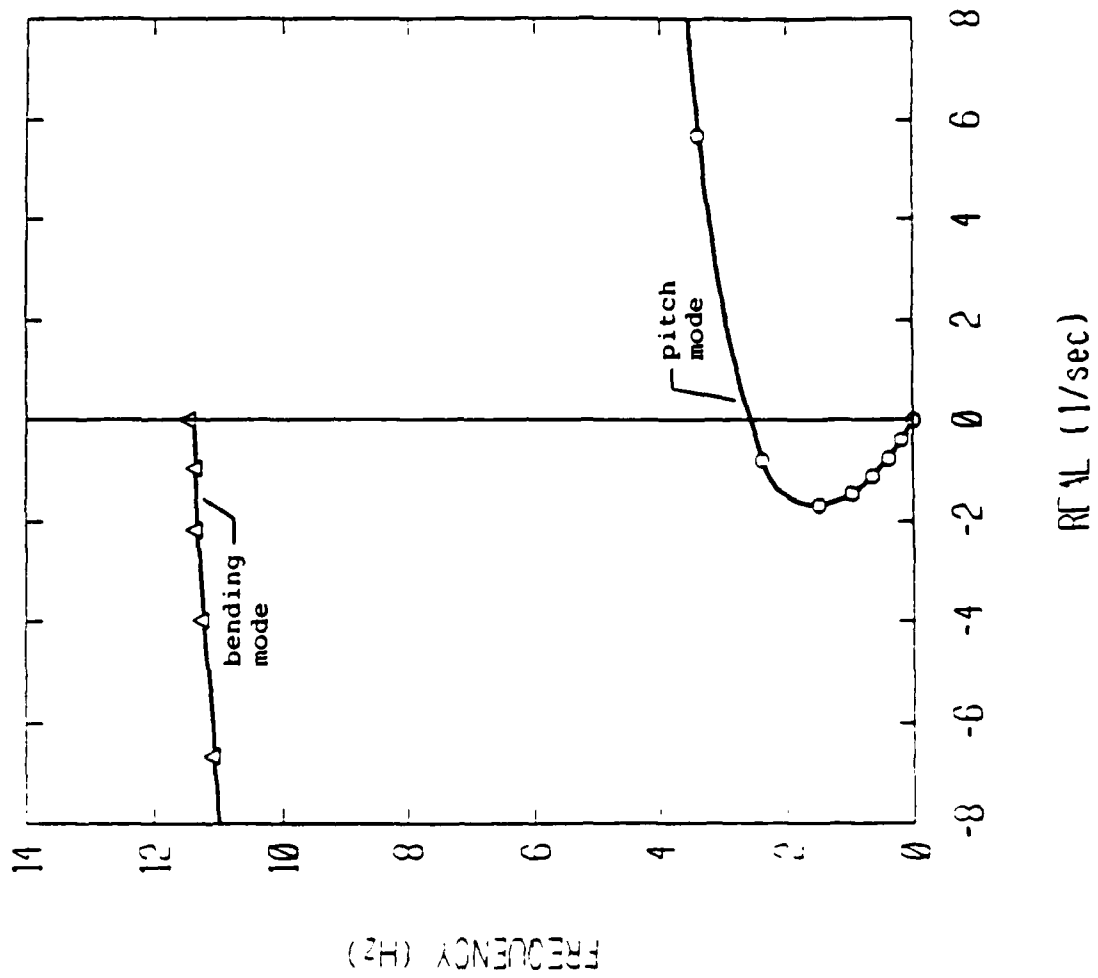


Fig. 5.7 Root Locus Plot, Completely Unrestrained Model with $[0_2/90]_s$ Wing (cont'd)

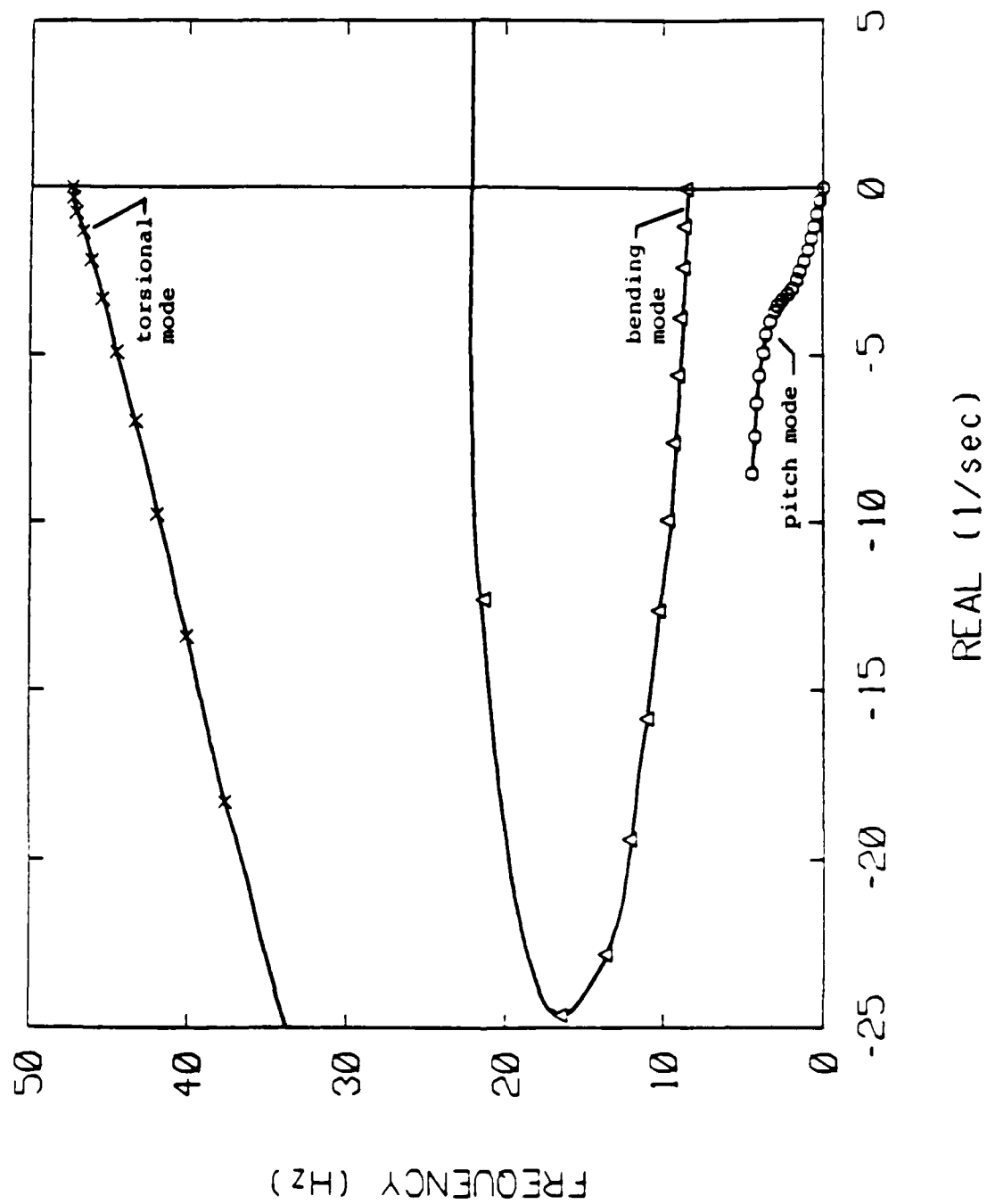


Fig. 5.8 Root Locus Plot, Completely Unrestrained Model with $[15_2/0]_s$ Wing

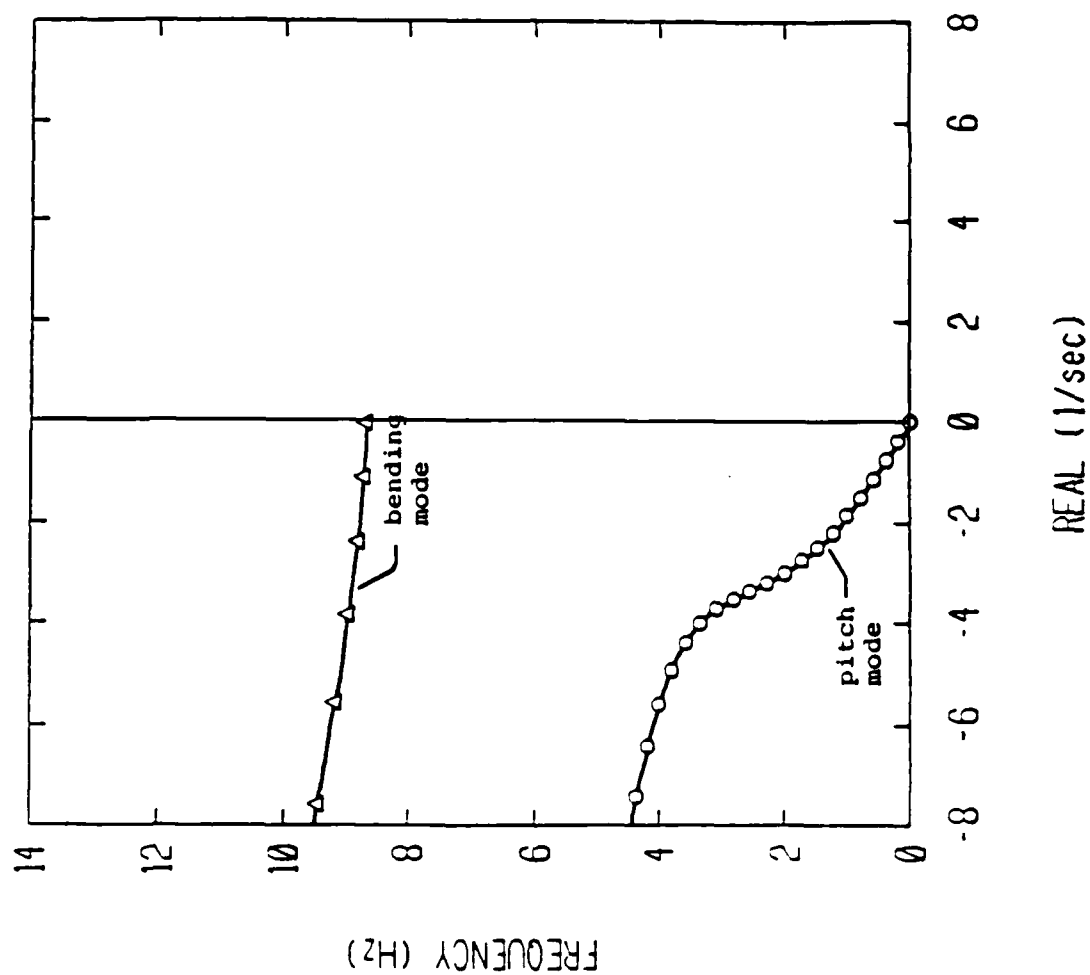


Fig. 5.8 Root Locus Plot, Completely Unrestrained Model with $[15_2/0]_s$ Wing (cont'd)

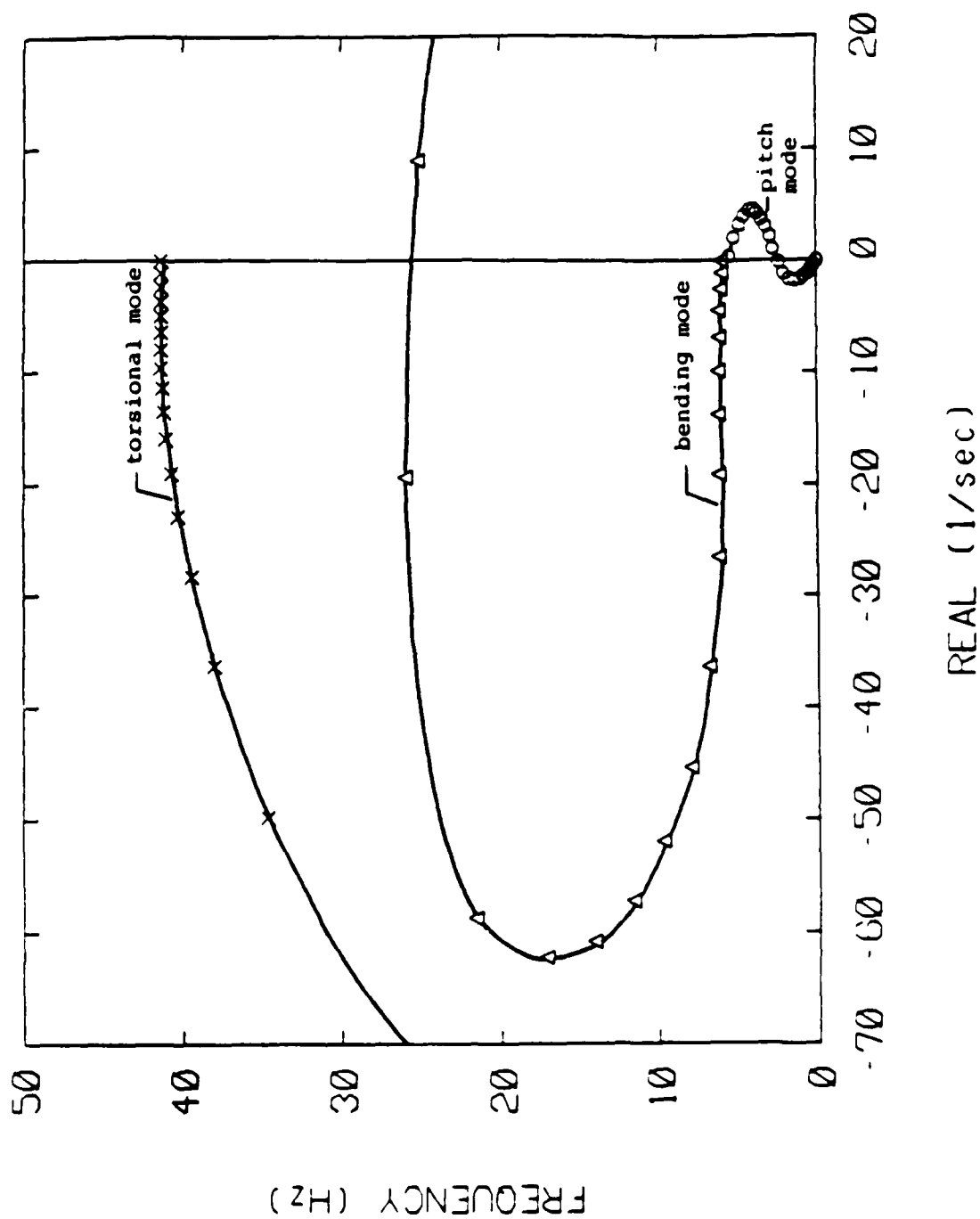


Fig. 5.9 Root Locus Plot, Completely Unrestrained Model with $[30_2/0]_s$ Wing

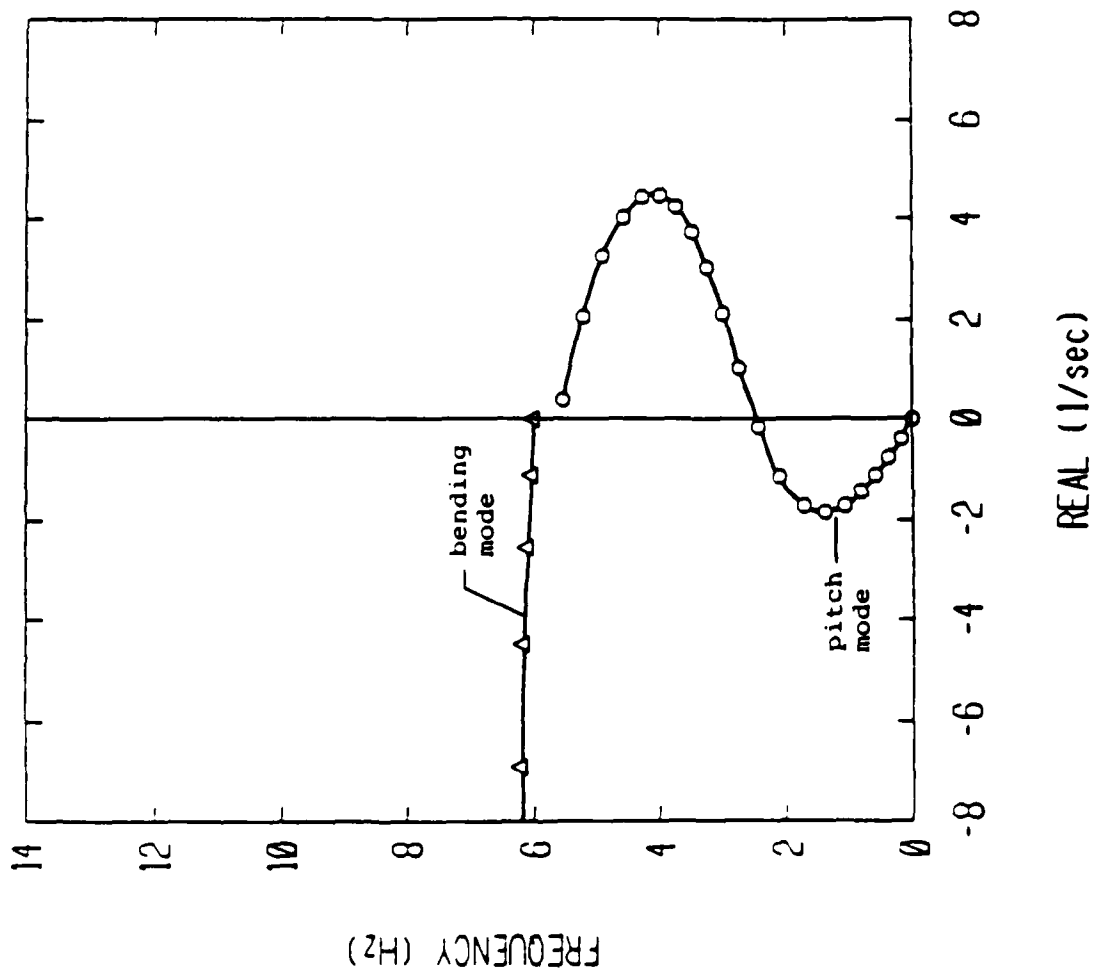


Fig. 5.9 Root Locus Plot, Completely Unrestrained Model
with $[30_2/0]_s$ Wing (cont'd)

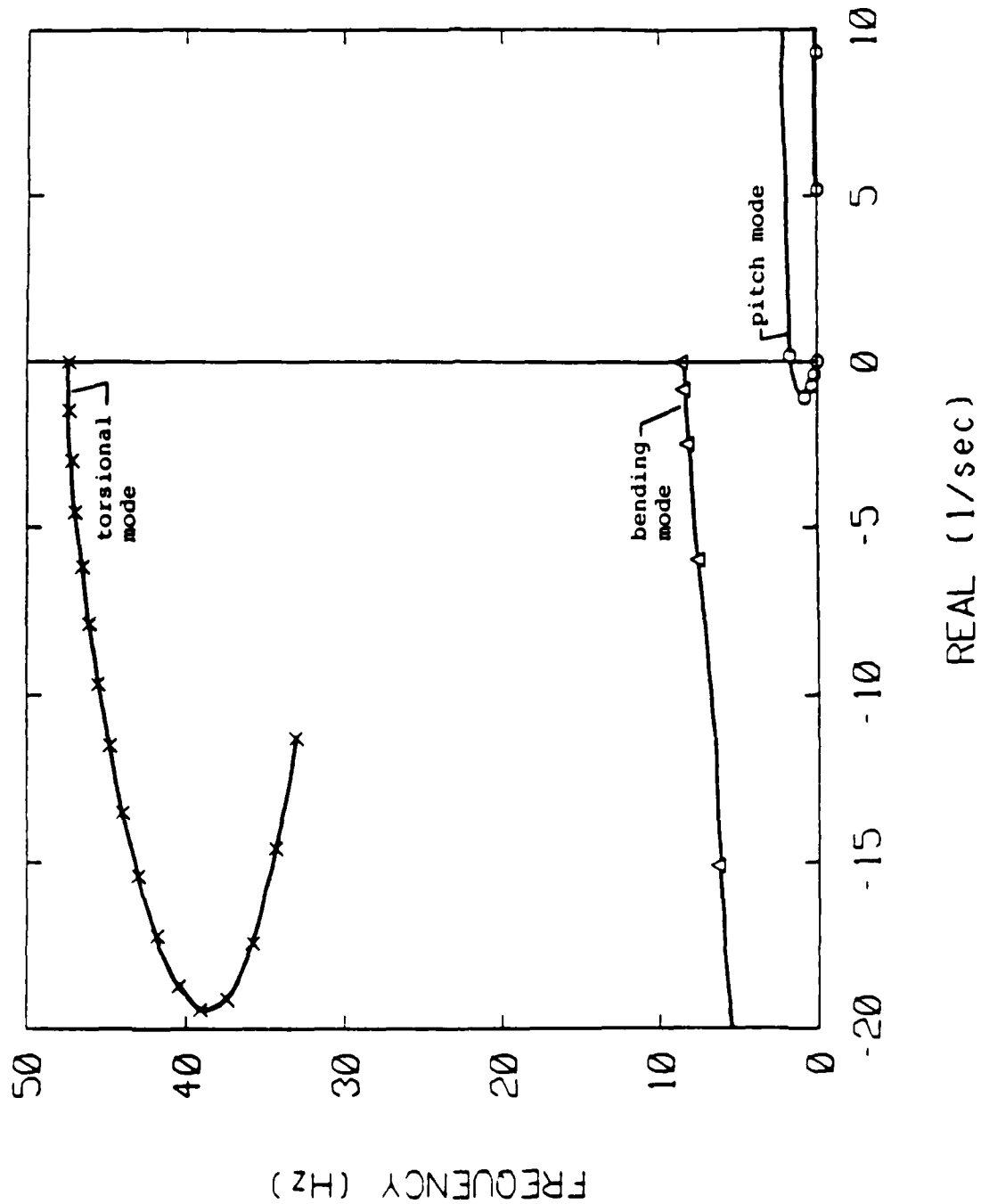


Fig. 5.10 Root Locus Plot, Completely Unrestrained Model with $[-15_2/0]_s$ Wing

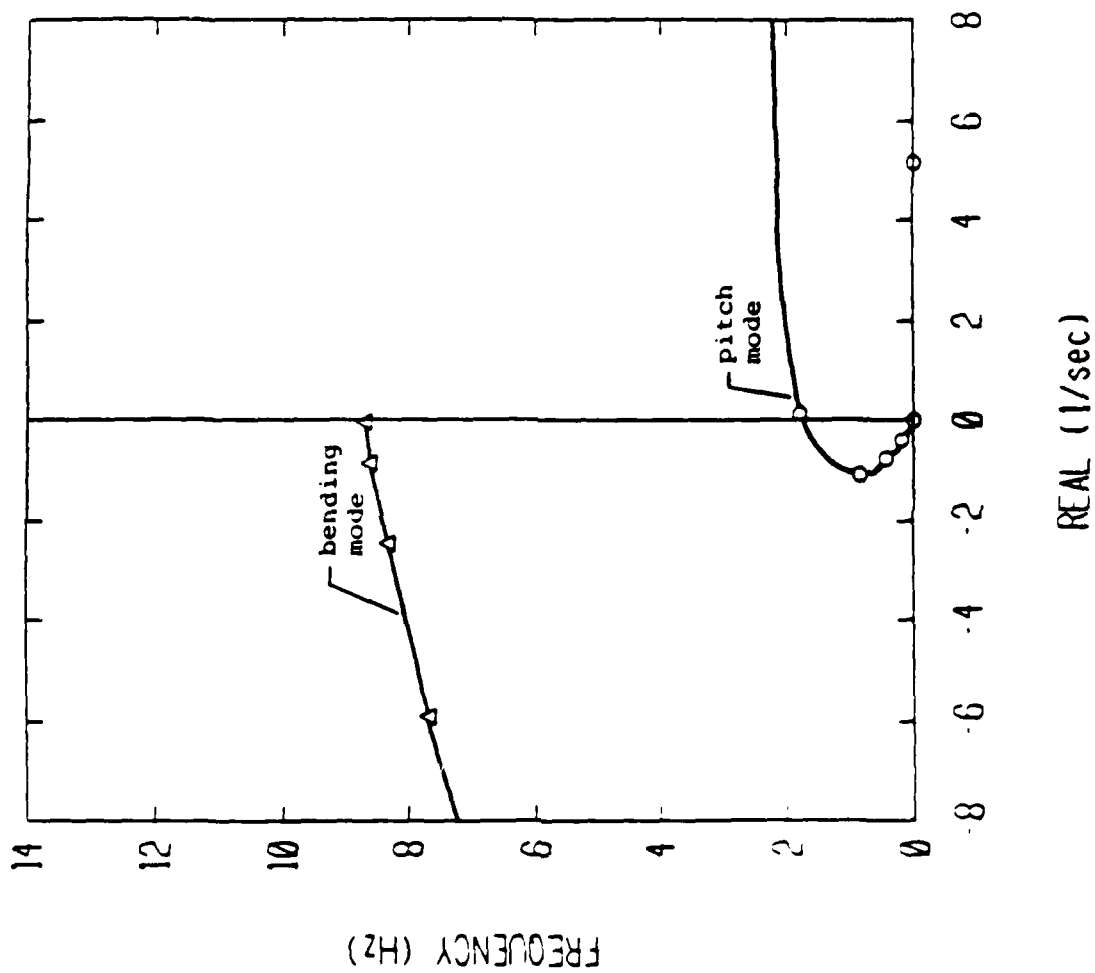


Fig. 5.10 Root Locus Plot, Completely Unrestrained Model with $[-15_2/0]_s$ Wing (cont'd)

convenience notation. As airspeed proceeds, each branch actually comprises contributions of various degrees of freedom. For example, when body freedom flutter occurs, the actual flutter mode consists of model pitch, model plunge, wing bending, and wing torsional responses as indicated in Table 4.4.

Since the present analytical model also gives the true damping (or transient decay rate) of the aeroelastic system, the influence of aeroelastic tailoring on longitudinal flying quality can be assessed in a preliminary fashion by comparing the damping of the short period mode (or pitch branch). For example, at low speed range, 12 m/sec, the damping (or pitch branch location) is relatively unaffected except for the model with the $[-15_2/0]_s$ wing. Using the flutter point of the model with $[0_2/90]_s$ wing, 18.5 m/sec, as the design point, a comparison between the $[15_2/0]_s$ and $[30_2/0]_s$ wing shows small change in the location of pitch branch. As airspeed increases, the $[30_2/0]_s$ wing mildly decreases its damping while the $[15_2/0]_s$ wing mildly increases its damping. At higher airspeed, the model with $[15_2/0]_s$ wing actually exhibits higher damping than does the rigid model.

The flutter boundaries and frequencies of the completely unrestrained vehicle are also summarized in Table 5.1. Comparisons show that the completely unrestrained vehicle is closely simulated by both soft (original) and stiff (modified) support systems. Figures 5.11 to 5.14 compare the model transient behavior of the modified support system with that of

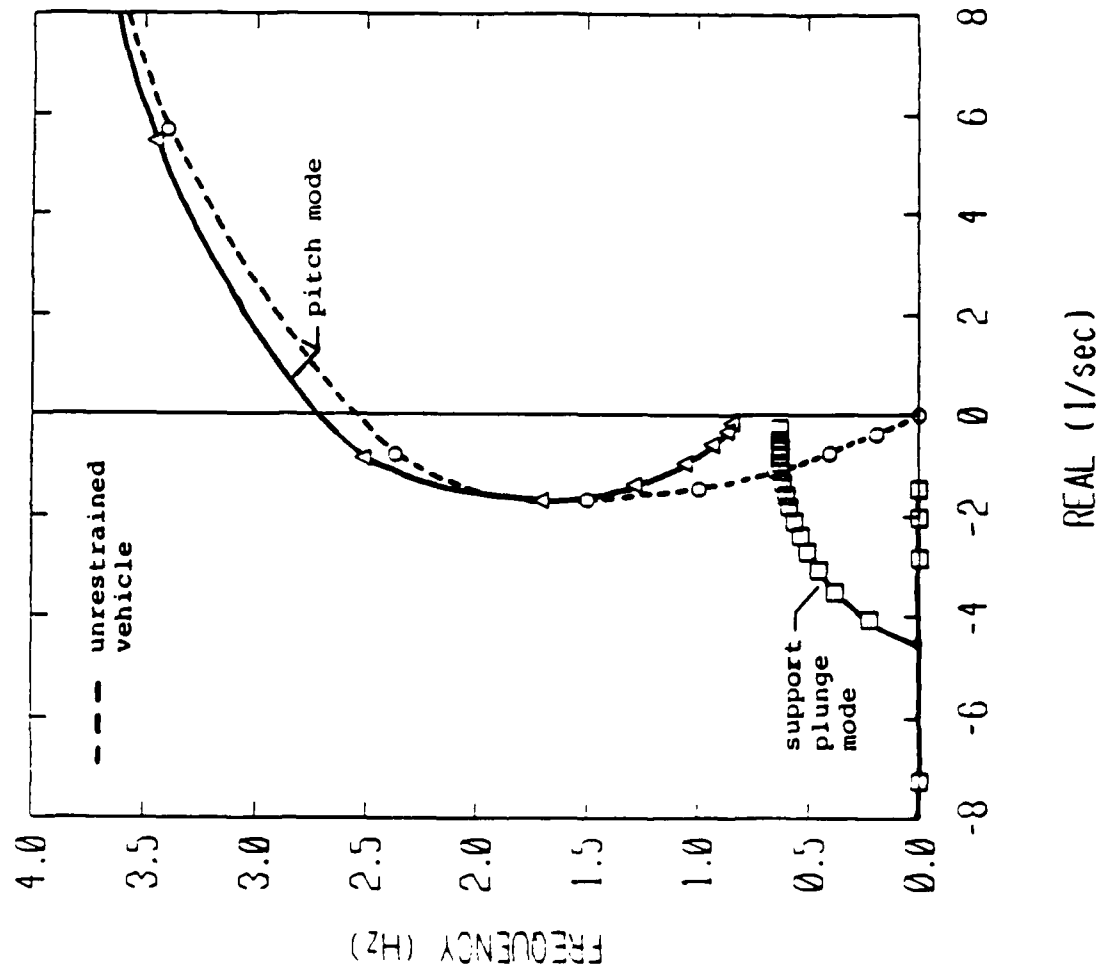


Fig. 5.11 Root Locus Comparison, $[0_2/90]$ Wing, Completely Unrestrained Model vs. Model on Modified Support

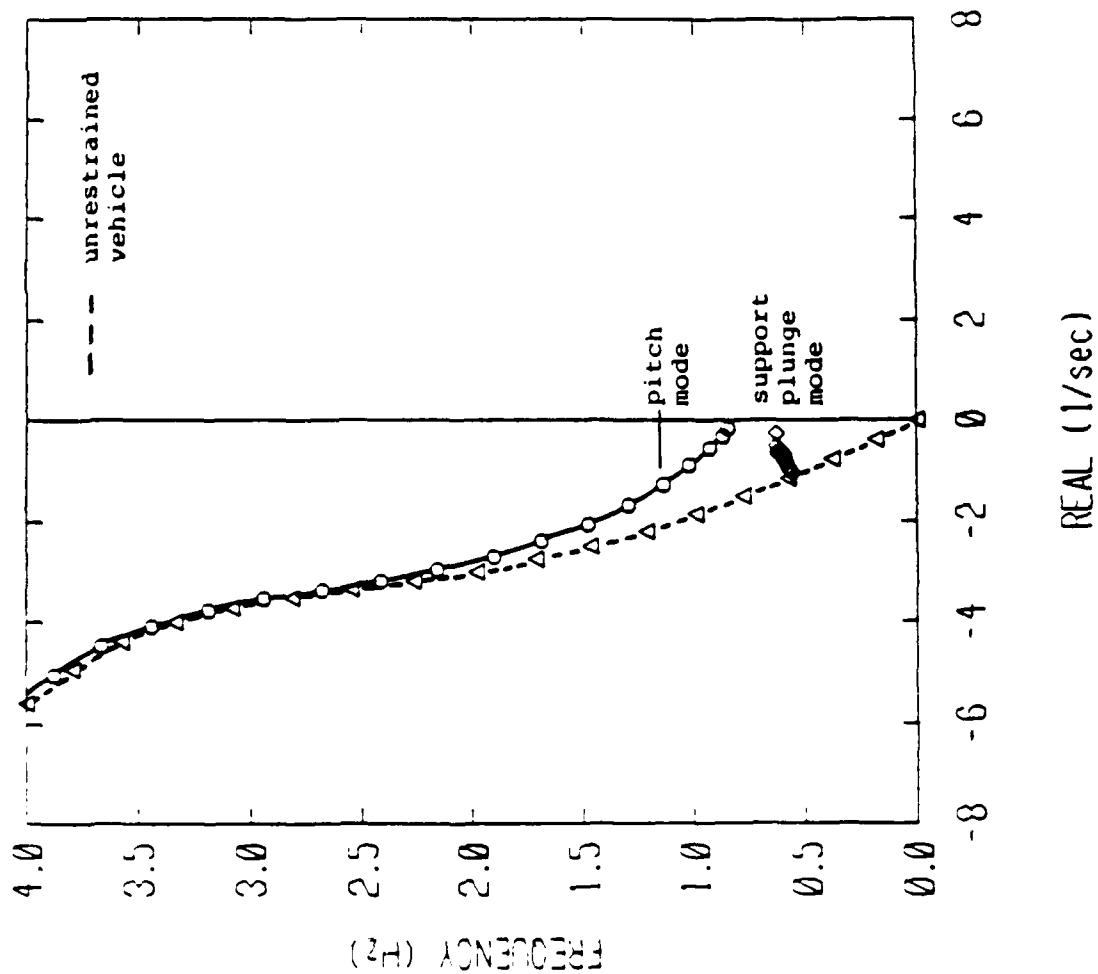


Fig. 5.12 Root Locus Comparison, $[15_2/0]$ Wing, Completely Unrestrained Model vs. Model on Modified Support

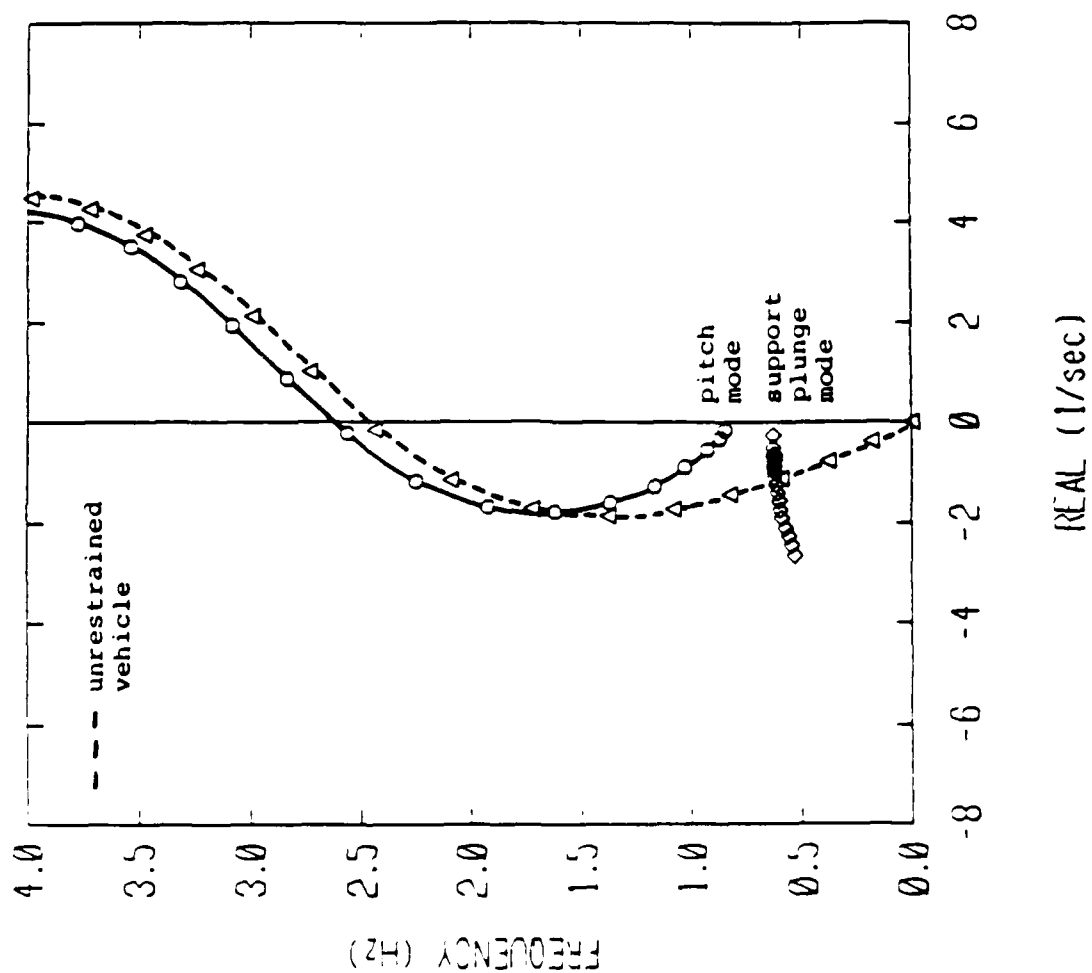


Fig. 5.13 Root Locus Comparison, $[30_2/0]$ Wing, Completely Unrestrained Model vs. Model on Modified Support

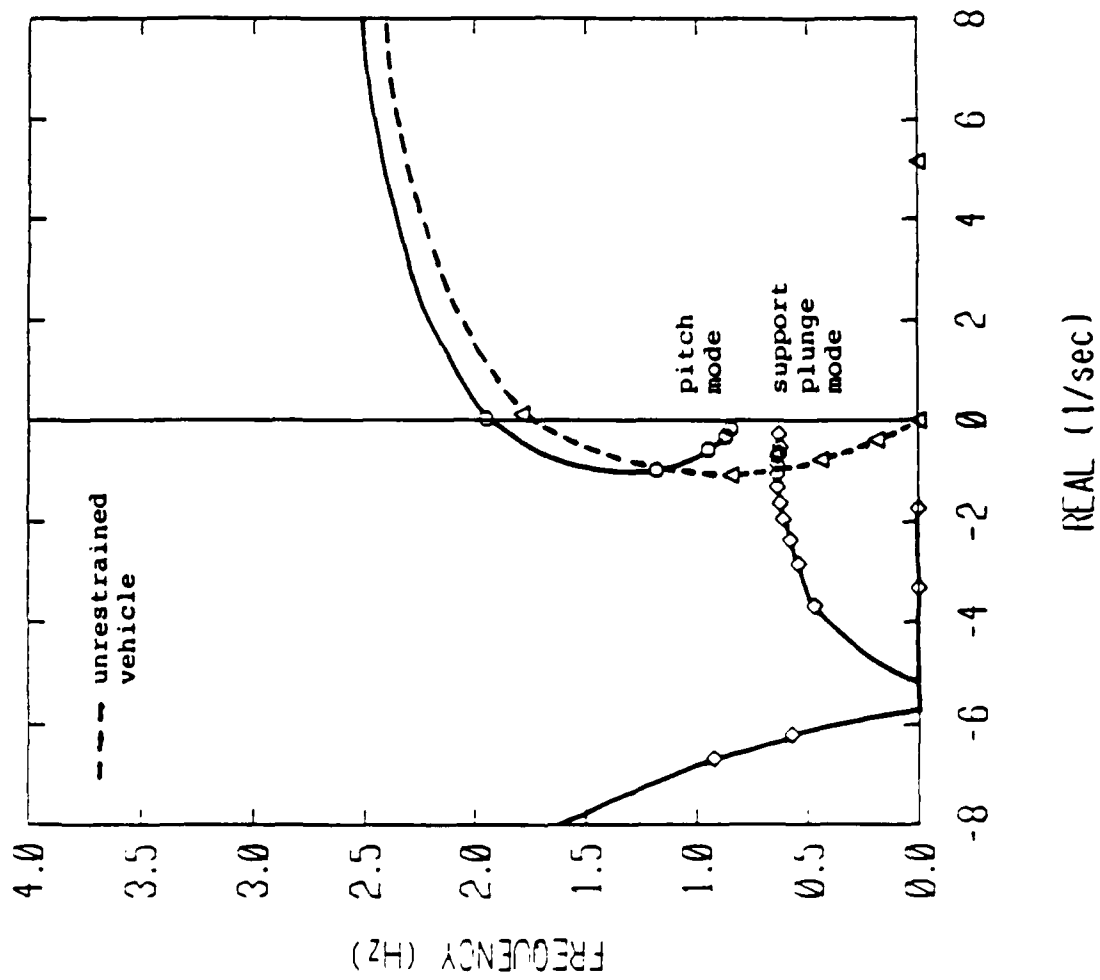


Fig. 5.14 Root Locus Comparison, $[-15, 0]_s$ Wing, Completely Unrestrained Model vs. Model on Modified Support

the completely unrestrained vehicle. Again, the airspeed incremental is set to be 3 m/sec for the root locus analyses. The results show a quick convergence to the behavior of the unrestrained vehicle, except that there exists a support plunge mode in the tunnel supported configuration. The dynamic characteristics of these support plunge modes varies with models. For models with the $[0_2/90]_s$ and $[-15_2/0]_s$ wings, the support plunge mode seems to be more active than is the model with the $[15_2/0]_s$ and $[30_2/0]_s$ wing. In general, however, the support plunge mode tends to move away from the pitch mode which is important in simulating the dynamics of a completely unrestrained vehicle.

The well-simulated free flight condition is attributed to the carefully designed support system. The support stiffness, in particular, is designed to be well separated from the suspected range of flutter frequencies, and support frictions are kept to a minimum to prevent contamination of the aerodynamic damping force which is important in pinpointing the body freedom flutter. Additionally, the support is designed such that the pitch frequency in still air is higher than the plunge frequency, in order to avoid the tunnel support dynamic instability reported earlier.

5.3 Effect of Some Parameters in Body Freedom Flutter

The body freedom flutter arises from the interaction of

the aeroelastically destiffened wing mode with the aerodynamically stiffened rigid body short period (pitch-plunge) mode. Due to the cantilever wing divergence tendency, the frequency of the wing mode decreases with airspeed, while the short period mode frequency increases with airspeed. As a result, there exists a dynamic instability characterized by the phenomenon of frequency coalescence. The exact occurrence of body freedom flutter will be functions of those parameters pertinent to the cantilever wing divergence and aircraft flight dynamics.

The so-called "aeroelastic destiffening", an underlying mechanism of the aeroelastic wing divergence, is not only a function of the wing frequencies (or stiffness) but also a function of the elastic coupling for an aeroelastically tailored wing. Effect of the elastic coupling has been summarized in Sec. 5.1.a. To isolate these two effects, the influence of wing frequencies will be discussed on the model with the $[0_2/90]_s$ wing. On the other hand, the flight dynamics effect in symmetric flight is primarily the short period mode effect. The important parameters involved in flight dynamics are the "rigid" aircraft static margin and inertia coupling of wing elastic modes and rigid body modes.

With this verified analytical model, the aeroelastic behavior of forward swept wing aircraft can be further understood from discussions of the aforementioned parameters. It should be noted that, for the purposes of parametric predictions, each parameter will be discussed seperately.

However, the intended parametric configuration may not be physically possible. In other words, a real design parameter, e.g., wing root position, may affect several parameters, i.e., aircraft static margin and inertia coupling.

(a) Influence of wing frequencies

As mentioned earlier, the influence of wing frequencies will be discussed only for the model with the $[0_2/90]_s$ wing. Using the current analytical model, the parametric predictions are illustrated in Figure 5.15. The wing fundamental bending frequency is changed by artificially varying the E_L value of the AS4/3501-6 graphite/epoxy while the other material properties remain unchanged. Similarly, the wing torsional frequency is changed by parametrically varying the G_{LT} value only.

The resulting body freedom flutter speeds show the decreasing trend with lowered wing bending frequency. The outcome is expected as the possibility of frequency coalescence and wing destiffening are both enhanced by lowered wing fundamental bending frequency. On the other hand, an important but less familiar finding shows that the body freedom flutter speed also decreases with the lowered wing torsional frequency which is presumed to be less relevant to the interaction mechanism. For a cantilever wing, the torsional stiffness (torsional frequency) is known to be a deciding factor in torsional divergence. This result reconfirms an important

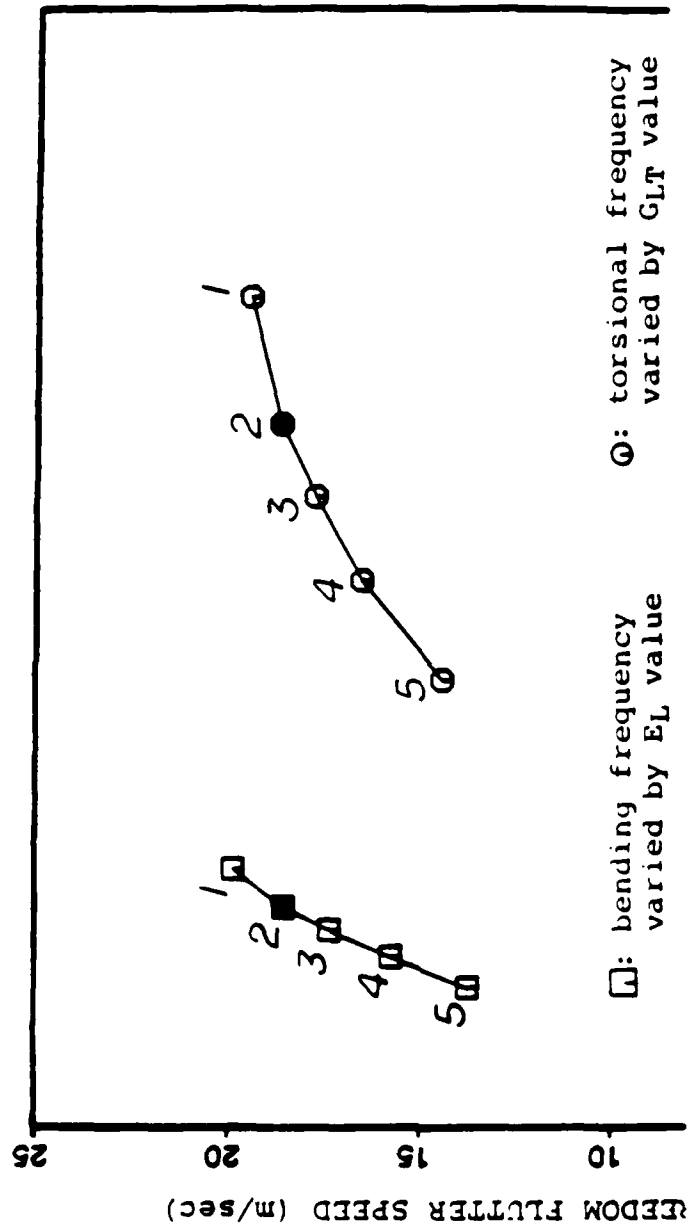


Fig. 5.15 Influence of Wing Frequency Flutter, $[0_2/90]_s$ wing

mechanism in the body freedom flutter, i.e., the interaction of the destiffened wing mode (or wing "divergence" mode). This parametric study, identifies an ancestry root of wing "divergence" mode in the body freedom flutter instability. This result also suggests that a realistic body freedom flutter analysis should at least include both wing bending and torsional freedoms to prevent the erroneous conclusions.

(b) Effect of "rigid" aircraft static margin

The presence of flight dynamics interaction can be physically seen as the modification of boundary conditions of the destiffened wing mode. These modified boundary conditions include both "stiffness" and "damping" effects resulting from the aircraft aerodynamic characteristics. The "rigid" aircraft static margin, determined by the relative positions of aircraft center of mass and lifting surfaces, is conveniently used to characterize these aerodynamic properties. In the aeroelastic analysis, however, varied static margin accomplished by lifting surfaces relocation will also affect the degree of inertia coupling between the elastic and rigid body motions. For the present analytical model, the use of rigid model aerodynamic derivatives makes an isolated parametric study of static margin effect possible. In other words, the static margin, ratio of $-C_{M_\alpha}$ to C_{L_α} , will be varied by changing the C_{M_α} accordingly while maintaining the C_{L_α} value the same.

This parametric study is equivalent to relocating canard

surface only, but neglecting its inertia effect which is true for a rigid canard model. To hypothesize a wide range of static margin, 0% to 60% of streamwise chord length, the actual canard position may be physically off the fuselage or interfering with other lifting surfaces, but these effects are ignored here.

Figure 5.16 illustrates the static margin effect on body freedom flutter. Both flutter speed and frequency are increased as static margin increases. This effect is consistent for all wings but with varied degrees of sensitivity to static margin. For example, when static margin is increased from 0% to 60%, the model with $[0_2/90]_s$ wing has only 2% increase in flutter speed, while the $[30_2/0]_s$ wing registered a 13% increase. To demonstrate the possibility of dramatic influence of static margin, the model with $[10_2/0]_s$ wing is included in this study. The results show that the body freedom flutter can be significantly delayed or eliminated by the increased static margin. At the first glance, the results seem to contrast to the physical interpretation of the adverse effect of "aerodynamic stiffening". Since the aerodynamic stiffness is proportional to the aircraft static margin, or C_{M_α} , the increase of static margin should promote the possibility of earlier frequency coalescence, and result in a lowered flutter speed. However, the increased static margin will also simultaneously increase the coupled aerodynamic damping and its stabilizing effect. As a result, the aerodynamic damping is significant enough to delay the

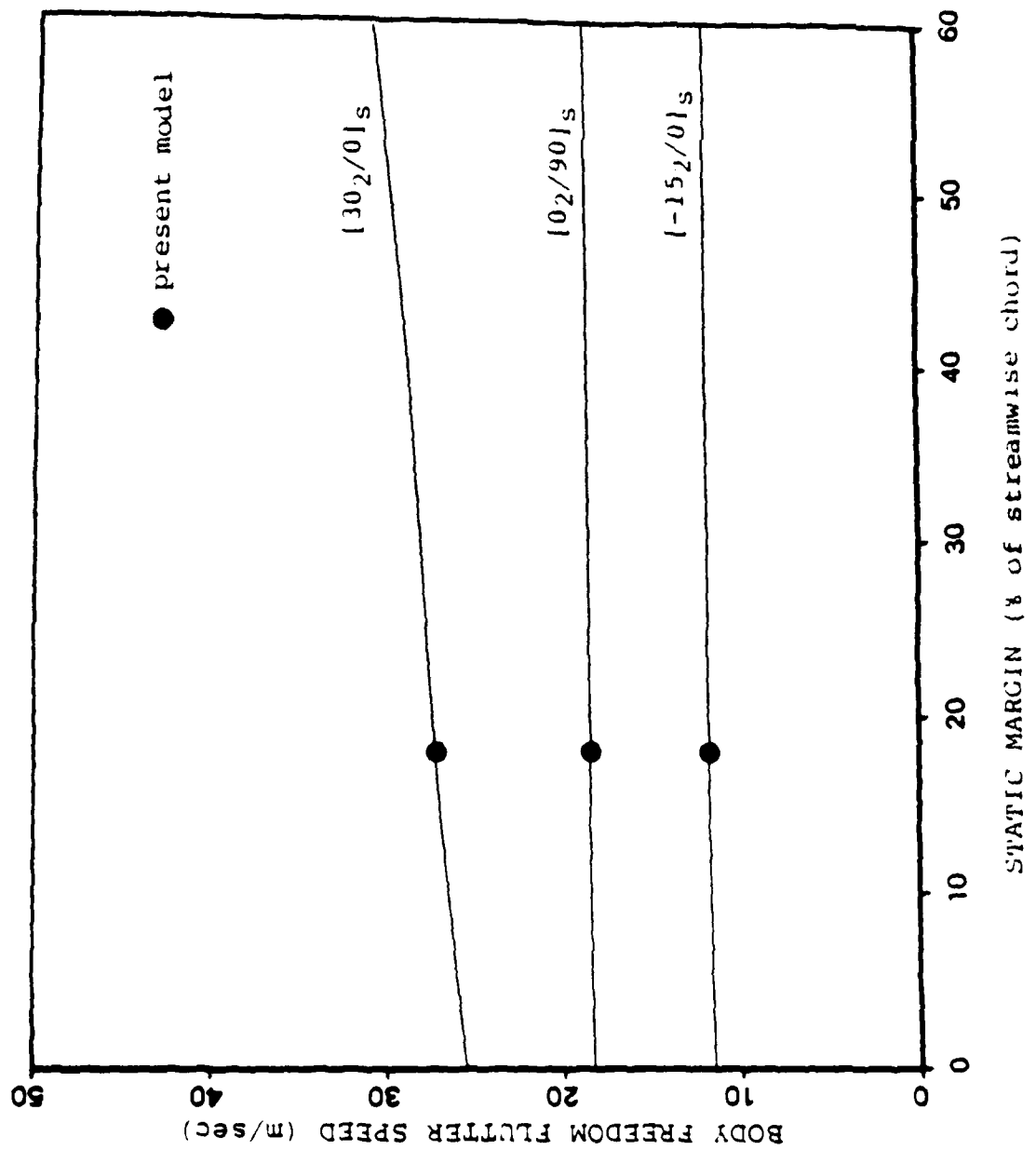


Fig. 5.16 Static Margin Effect on Body Freedom Flutter

destabilizing trend of frequency coalescence. It is interesting to note that the analysis with mechanical pitching stiffness can demonstrate the isolated pitching stiffness effect. As expected, the more the added mechanical pitching stiffness, the lower the body freedom flutter speed.

For aircraft with negative static margin, the aircraft static instability is more critical than is the body freedom flutter. The investigation of body freedom flutter then becomes meaningless unless a stability augmentation system (SAS) is implemented and incorporated in the analytical model. In Ref. 24, body freedom flutter was found to be dependent on the closed loop characteristics of the SAS, and similar to the behavior of a statically stable aircraft.

(c) Inertia Coupling Effect

In addition to the "stiffness" and "damping" effects introduced by aircraft flight dynamics, the presence of rigid body freedoms also provides the inertia coupling effect (or inertia relief) between wing elastic modes and rigid body modes. With the present analytical model, this coupling effect is examined by varying wing root position while keeping the "rigid" aircraft static margin the same. Figure 5.17 shows that body freedom flutter decreases as the wing moves aft. This is due to the increased pitch inertia coupling, m_{23} in present study, as evident by the corresponding vibration mode.

Another straightforward indication of inertia coupling is

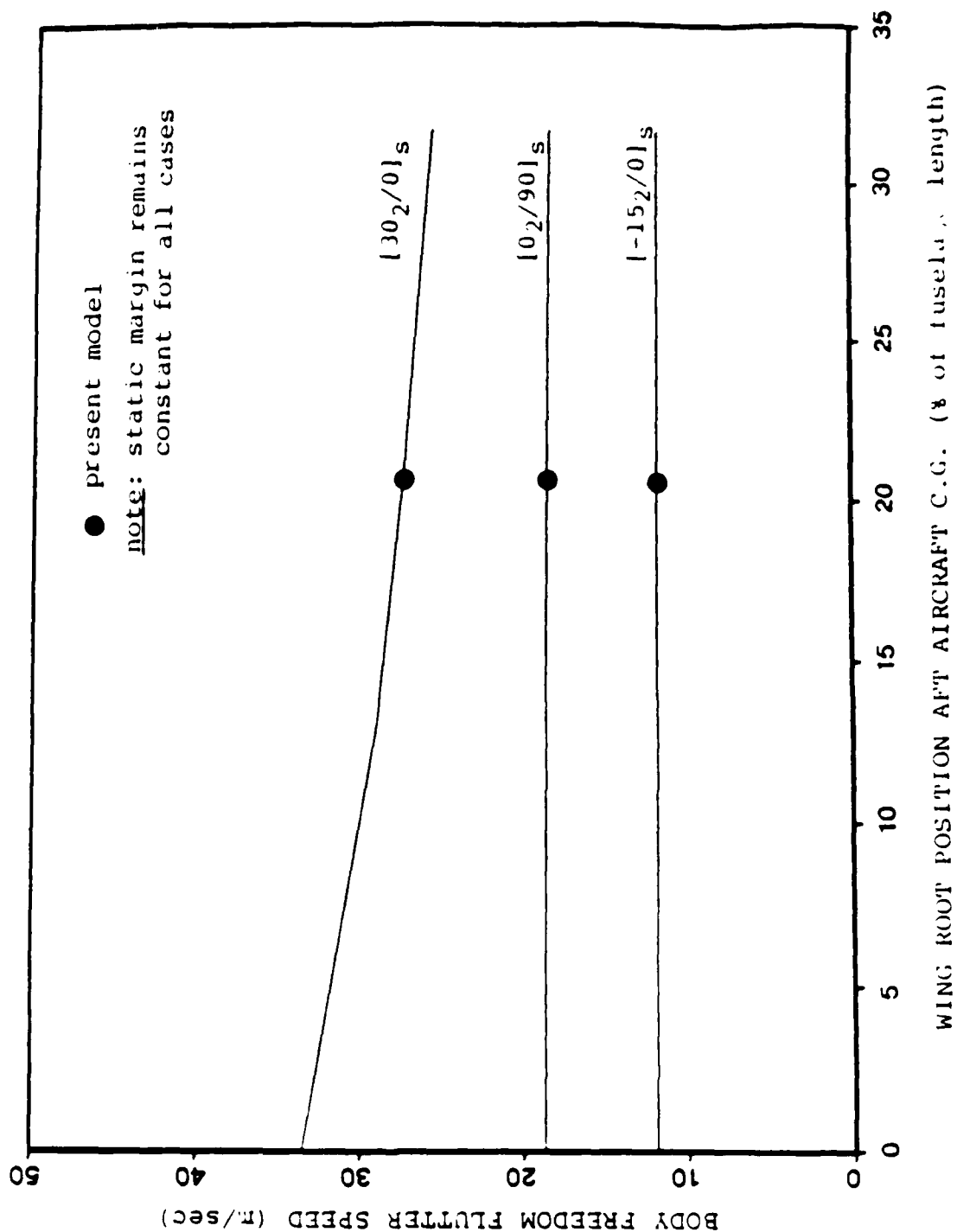


Fig. 5.17 Influence of Wing Root Position on Body Freedom Flutter

the wing to aircraft mass ratio. Practically, any change in wing mass ratio will affect both pitch and plunge inertia coupling simultaneously. For the purposes of isolated parametric study, the wing mass and pitch inertia ratios will be varied separately by changing the overall aircraft mass and pitch inertia respectively without changing wing mass. Figure 5.18 shows the adverse effect of increased wing pitch inertia ratio (decreased aircraft pitch inertia), or increased pitch inertia coupling, m_{23}/m_{22} . Figure 5.19 shows the favorable effect of increased wing mass ratio (decreased aircraft mass), or increased plunge inertia coupling, m_{13}/m_{11} . For the present wind tunnel model, the measured wing mass and pitch inertia ratios are 5.6% and 3.1% respectively.

5.4 Aeroelastic Effect on Support Instability

The testing and analytical results have shown that the model support instability interferes very little with the body freedom flutter. It is also of interest to further explore the mechanism involved, and to foster the understanding of both instabilities.

From the analysis, it is shown that the lower limit of the support instability zone is dictated by the support pitch damping force, while the upper limit is determined by the support plunge damping force. When the wing flexibility is taken into account, there are additional aerodynamic damping

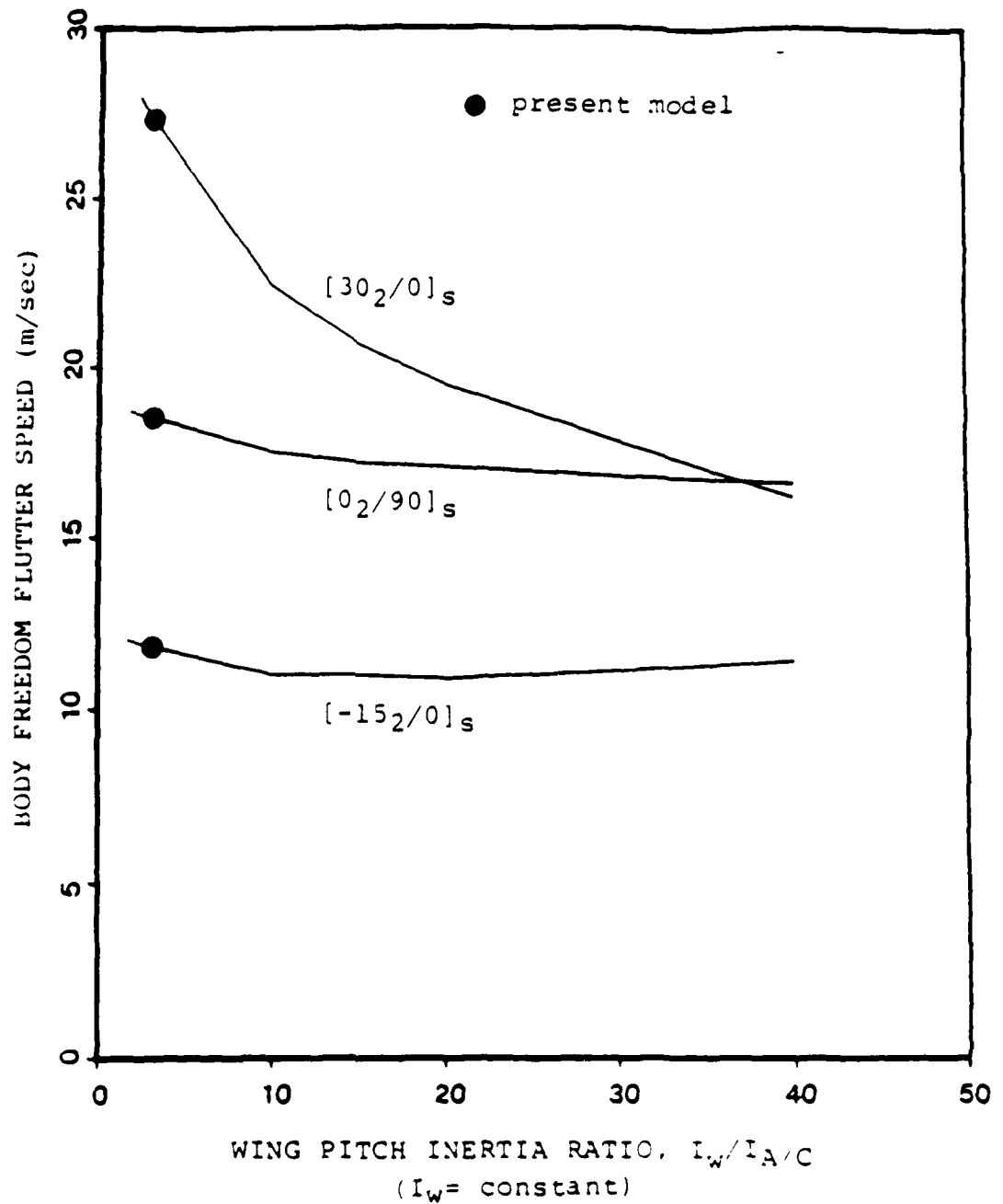


Fig. 5.18 Pitch Inertia Coupling Effect on Body Freedom Flutter

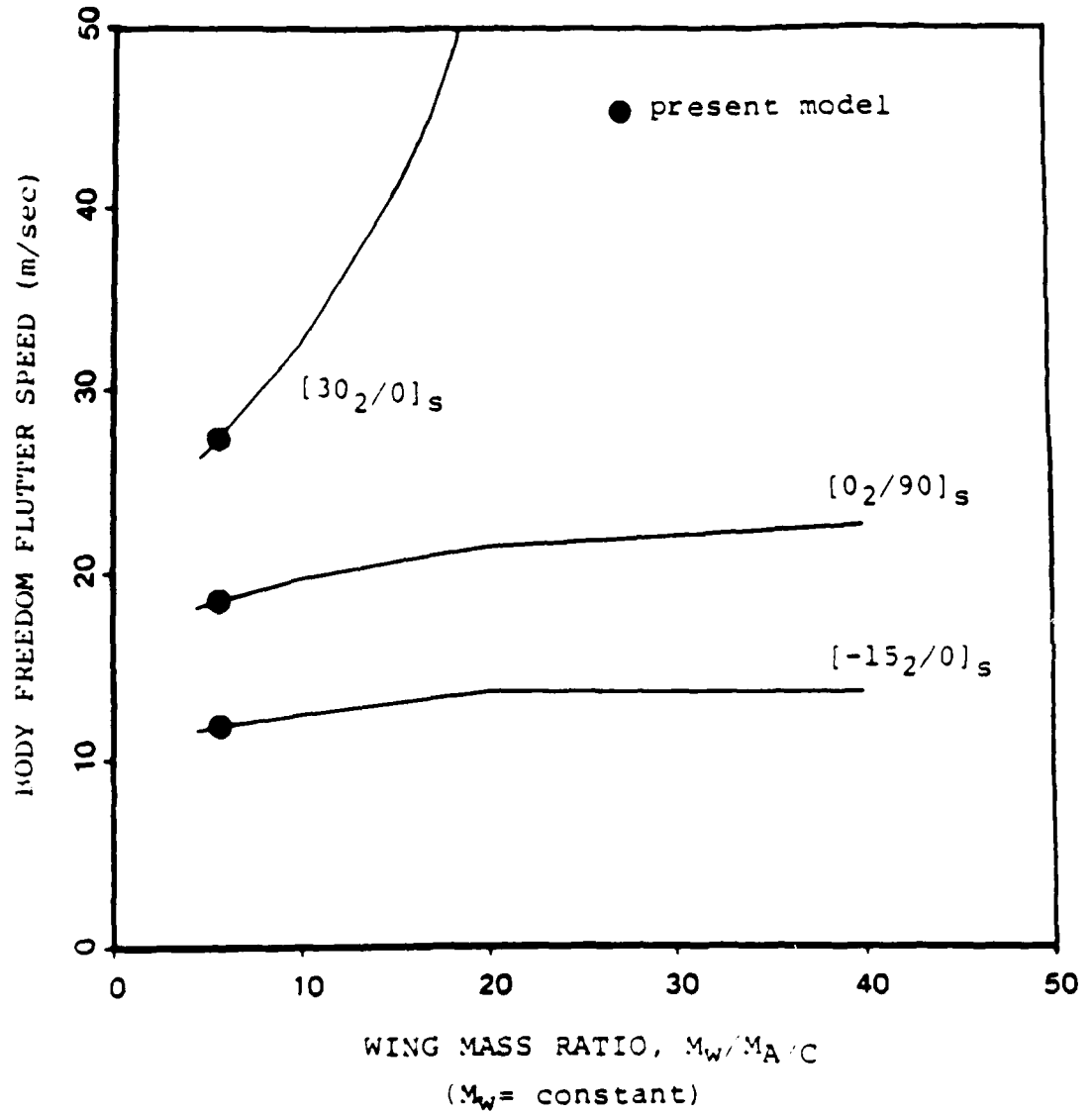


Fig. 5.19 Plunge Inertia Coupling Effect on Body Freedom Flutter

contributions from the wing elastic motions. In general, the wing motions can be decomposed into wing bending and twisting components. The aerodynamic damping incurred by the wing bending motion is usually significant and additive to the overall plunge damping. The wing bending contribution to the overall pitch damping is less significant due to the proximity in location of pitching axle and wing tip which would have the most wing bending motion. On the other hand, the wing twisting motion is relatively small in amplitude, and its contribution to the overall plunge and pitch damping about model pitching axle is negligible. As a result, the aeroelastic effect on support instability come mainly from the wing bending motion and its contribution to the overall plunge damping force. This effect was observed in wind tunnel tests and predicted from the analytical model. The results are illustrated in Figure 5.20.

A close examination of Figure 5.20 shows that the upper instability boundary, 31 m/sec for "rigid" model, primarily follows the trend of the body freedom flutter. This is because the body freedom flutter mode always contains significant wing bending motion. Without the presence of any aeroelastic instability, the aeroelastic response is usually small. When the body freedom flutter instability is approached, the wing bending response becomes significant and the overall plunge damping is eventually dominated by the wing bending motion. The upper boundary of support instability is therefore dictated by the trend of body freedom flutter boundary. In general, any aeroelastic instability involving wing bending motion such as

bending-torsion wing flutter will have the same effect as body freedom flutter does. The support instability of the model with the $[15_2/0]_S$ wing, which is "optimum" in term of body freedom flutter, is actually controlled by the critical bending-torsion flutter instead of the body freedom flutter.

Since the body freedom flutter boundary is well predicted in the present analysis, the upper limit of support instability is subsequently shown to be in good agreement with the testing results except for the model with the $[30_2/0]_S$ wing. In this case, the support instability terminates at 23 m/sec compared with the predicted value of 16 m/sec. A close examination of the testing records shows that, between the upper limit of support instability and the body freedom flutter onset, the system was so lightly damped that any small disturbance would cause the model to plunge significantly at such airspeed. During wind tunnel tests, it was difficult to distinguish such responses from the support instability even though it may be due to a turbulent gust.

Unlike the upper limit, the lower limit of support instability is governed by the support pitch damping force. This involves very little aeroelastic effect, and the accuracy of the lower limit depends on the correct estimation of the support pitch damping. Because the model was heavily damped in pitch freedom in the original support system, only about one and one half cycle of a step response was observable, and this led to some scattering and uncertainty in determining the damping ratio. Nevertheless the slight underpredictions in

lower limit of support instability are consistent among all wings and within the experimental error range.

Since the body freedom flutter has a "healing" effect on the support instability, which occurs first, the latter is seen to have little opportunity to affect the former. This conclusion of a "one way" effect is proved from the analysis and testing results.

CHAPTER SIX

CONCLUSIONS AND RECOMMENDATIONS

An analytical and experimental investigation was made of the aeroelastic flutter and divergence behavior of a forward swept graphite/epoxy wing aircraft with rigid body pitch and plunge freedoms. Experimental wind tunnel data were obtained for a generic, full-span, 30° forward swept wing, 18% static margin aircraft model in a low speed wind tunnel. The free flying behavior was simulated on a softly restrained vertical rod support system. Based on the results of this investigation, the following conclusions are drawn:

1. The tests revealed large variations in aeroelastic behavior for the aircraft model with four different ply layup wings. Body freedom flutter and bending-torsion wing flutter were observed on the free flying model, and regions of their occurrence were mapped out.
2. The forward swept wing aircraft model developed body freedom flutter rather than divergence when rigid body freedoms were present. This body freedom flutter occurred at a lower airspeed than cantilever wing divergence, and arose from the interaction of the destiffened wing mode and the aircraft short period mode. The presence of flight dynamics effects modified the boundary conditions of the destiffened wing mode, and ultimately changed the

instability nature from static divergence to dynamic flutter.

3. The aeroelastic tailoring effect on body freedom flutter was found to follow the trend of cantilever wing divergence tailoring. The model with the $[15_2/0]_s$ wing demonstrated the best tailored aeroelastic behavior, and bending-torsion wing flutter was encountered there instead of body freedom flutter. The presence of flight dynamics was found to have little effect on this bending-torsion type of wing flutter.
4. A support related dynamic instability, involving the model's pitch and plunge motions, was also encountered at low airspeeds. This support instability could be eliminated by making the still air model pitch frequency greater than the model plunge frequency, thereby avoiding a possible frequency coalescence at certain airspeed. It was also found that this support instability was banded in airspeed, and caused almost no effect on the body freedom flutter boundaries, if the model could fly through the instability zone.
5. For the model free in pitch only, body freedom flutter was again encountered, but at a lower airspeed, and lower flutter frequency. The presence of the plunge freedom apparently played an important and favorable role in body

freedom flutter, and should not be overlooked in body freedom flutter analysis or test.

6. Tests conducted on the cantilever wings, i.e., the aircraft model locked in plunge motion and restrained in pitch motion by the snubber cables, revealed the same aeroelastic behavior as noted earlier in Ref. 10. Linear wing divergence and bending-torsion wing flutter occurred at low angles of attack, and nonlinear torsional-stall flutter and bending-stall flutter occurred with lowered airspeed at the higher angles of attack. Depending on the wing layups, the static wing divergence condition could change to either a torsional-stall flutter or bending-stall flutter as wing root angle of attack was increased. The flutter prone wing always exhibited torsional-stall flutter at the higher angles of attack.
7. An accurate and efficient linear flutter analysis was developed by using Rayleigh-Ritz approximation, modified strip theory in transient representation, and measured aircraft aerodynamic derivatives. Good agreement was obtained for all cases in both the flutter boundaries and transient behavior. The use of static lift-curve-slope distribution in modified strip theory was shown to be a good approximation because of the low body freedom flutter reduced frequency, $k = 0.02$ to 0.05 .

8. Parametric studies based on the analysis developed here showed that both the wing bending and torsional frequencies were critical to the body freedom flutter as well as to the cantilever wing divergence. The increased rigid aircraft static margin showed a favorable effect in body freedom flutter speed for all wings analyzed. The plunge inertia coupling of the wing elastic modes and rigid body modes shows a favorable effect, whereas the pitch inertia coupling shows an adverse result.

The present study has provided analytical and experimental insight into the actual aeroelastic behavior of a forward swept wing aircraft in free flight. However, there are several other important analytical and experimental aspects related to this subject that require additional investigation. Recommendations for further study are given below.

1. From an analytical viewpoint, the effects of compressibility should be evaluated to complete the parametric trend prediction.
2. Regarding aerodynamics, the effect of nonlinearity at higher angle of attack, which cause a transition from linear behavior to torsional-stall and bending-stall flutter, deserves further investigation.

3. Based on this well-verified aeroelastic plant model, there is a desire to demonstrate, through analysis and wind tunnel tests, the integration of aeroelastic tailoring technique and active control technology for instability suppression. The inclusion of rigid body freedom are certainly desired here.
4. Analyses and wind tunnel tests also need to be conducted to evaluate the antisymmetric aeroelastic behavior of a forward swept wing aircraft in free flight. From there, the study can be further extended to the subject of oblique wing design.

REFERENCES

1. Krone, N.J., "Divergence Elimination with Advanced Composites," AIAA 1975 Aircraft Systems and Technology Meeting, Los Angeles, California, August 1975, AIAA paper 75-1009.
2. Wilkinson, K., and Rauch, F., "Predicted and Measured Divergence Speeds of An Advanced Composite Forward Swept Wing Model," AFWAL-TR-80-3059, July 1980.
3. Ellis, J.W., Dobbs, S.K., Miller, G.D., "Structural Design and Wind Tunnel Testing of a Forward Swept Fighter Wing," AFWAL-TR-80-3073, July 1980.
4. Weisshaar, T.A., "Aeroelastic Tailoring of Forward Swept Composite Wings," J. of Aircraft, Vol. 18, No. 8, August 1981, pp. 669-676.
5. Scherrer, V.C., Hertz, T.J., and Shirk, M.H., "Wind Tunnel Demonstration of Aeroelastic Tailoring Applied to Forward Swept Wings," J. of Aircraft, Vol. 18, No. 11, November 1981, pp. 976-983.
6. Hertz, T.J., Shirk, M.H., Ricketts, R. H., and Weisshaar, T.A., "On the Track of Practical Forward Swept Wings," Aeronautics and Astronautics, Vol. 20, No. 1, January 1982, pp. 40-53.
7. Weisshaar, T.A., Zeiler, T.A., Hertz, T. J., and Shirk, M. J., "Flutter of Forward Swept Wings, Analyses and Tests," 23rd AIAA/ASME/ASCE/AHS structures. Structural Dynamics, and Materials Conference, New Orleans, Louisiana, May 1982, AIAA Paper 82-0646.
8. Weisshaar, T.A., and Foist, B.L., "Vibration and Flutter of Advanced Composite Lifting Surfaces," 24th AIAA/ASME/ASCE/AHS Structures, Structural Dynamics, and Materials Conference, Lake Tahoe, NV, May 1983, AIAA paper 83-0961.
9. Hollowell, S.J., and Dugundji, J., "Aeroelastic Flutter and Divergence of Stiffness Coupled, Graphite/Epoxy Cantilevered Plates," J. of Aircraft, Vol. 21, No. 1, January 1984, pp. 69-76.
10. Landsberger, B., and Dugundji, j., "Experimental Aeroelastic Behavior of Unswept and Forward Swept Graphite/Epoxy Wings," J. of Aircraft, Vol 22, No. 8, August 1985, pp. 679-686.

11. Lottati, I., "Flutter and Divergence Aeroelastic Characteristics for Composite Forward Swept Cantilevered Wing," J. of Aircraft, Vol. 22, No. 11, November, 1985, pp. 1001-1007.
12. Shirk, M.H., Hertz, T.J., and Weisshaar, T.J., "Aeroelastic Tailoring - Theory, Practice, and Promise," J. of Aircraft, Vol. 23, No. 1., January 1986, pp. 6-18.
13. Chipman, R., Zislin, A., and Waters, C., "Control of Aeroelastic Divergence," 23rd AIAA/ASME/ASCE/AHS Structures, Structural Dynamics, and Materials Conference, New Orleans, Louisiana, May 1982, AIAA paper 82-0684.
14. Griffin, K.E., and Eastep, F.E., "Active Control of Forward Swept Wings with Divergence and Flutter Aeroelastic Instabilities," 22nd AIAA/ASME/ASCE/AHS Structures, Structural Dynamics, and Materials Conference, Atlanta, Georgia, April 1981, AIAA paper 81-0637.
15. Frazer, R.A., and Duncan, W.J., "Wing Flutter as Influenced by the Mobility of the Fuselage", British Aero. Research Council, R. & M. No. 1207, September 1929.
16. Gaukroger, D.R., "Wind Tunnel Flutter Tests on Model Delta Wing under Fixed and Free-root Conditions," British Aero. Research Council, R. & M. No. 2826, September 1950.
17. Gaukroger, D.R., "Wing Tunnel Test on the Symmetric and Antisymmetric Flutter of Swept-back Wings," British Aero. Research Council, R. & M. No. 2911, March 1953.
18. Gaukroger, D.R., "Wing Flutter," AGARD Manual on Aeroelasticity, Part V, Chapter 2, 1960.
19. McLaughlin, M.D., "A Theoretical Investigation of the Short-Period Dynamic Longitudinal Stability of Airplane Configurations Having Elastic Wings of 0° to 60° Sweepback," NACA TN 3251, December 1954.
20. Cunningham, H.J., and Lundstrom, R.R., "Description and Analysis of a Rocket-Vehicle Experiment on Flutter Involving Wing Deformation and Body Motions," NACA TN 3311, January 1955.
21. Jones, R.T., and Nisbet, J. W., "Aeroelastic Stability and Control of an Oblique Wing," The Aeronautical Journal of the Royal Aeronautical Society, Vol. 80, August 1976, pp. 365-369.
22. Miller, G.D., Wykes, J.H., Brosman, M.J., "Rigid Body-Structural Mode Coupling on a Forward Swept Wing

- Aircraft," 23rd AIAA/ASME/ASCE/AHS Structures, Structural Dynamics, and Materials Conference, New Orleans, Louisiana, May 1982, AIAA Paper 82-0683.
23. Weisshaar, T.A., Zeiler, T.A., Hertz, T.J., and Shirk, M.J., "Flutter of Forward Swept Wings, Analyses and Tests," 23rd AIAA/ASME/AHS Structures, Structural Dynamics, and Materials Conference, New Orleans, Louisiana, May 1982, AIAA Paper 82-0646.
 24. Chipman, R., Rauch, F., Rimer, M., and Muniz, B., "Body-Freedom Flutter of a 1/2 Scale Forward-Swept-Wing Model, An Experimental and Analytical Study," NASA CR 172324, April 1984.
 25. Chipman, R., Rauch, F., Rimer, M., Muniz, B., and Ricketts, R.H., "Transonic Tests of a Forward Swept Wing Configuration Exhibiting Body Freedom Flutter," 26th AIAA/ASME/AHE Structures, Structural Dynamics, and Materials Conference, Orlando, Florida, April 1985, AIAA Paper 85-0689.
 26. Munk, M.M., "Propeller Containing Diagonally Disposed Fibrous Material," U.S. Patent 2,484,308,1111, October, 1949.
 27. "Sherpa Takes the Air," Flight and Aircraft Engineer, No. 2334, Vol. LXIV, October 16, 1953, pp. 535.
 28. Robinson, M.R., and Silverman, S.M., "From HiMAT to Future Fighters," AIAA Aircraft Systems and Technology meeting, August 20-22, 1979, AIAA paper 79-1816.
 29. Jones, R., Mechanics of Composite Materials, McGraw-Hill Book Company, 1975.
 30. Jensen, D.W., Crawley, E.F., and Dugundji, J., "Vibration of Cantilevered Graphite/Epoxy Plates with Bending-torsion Coupling," J. of Reinforced Plastics and Composites, Vol. 1, July 1982, pp. 254.
 31. Spielberg, I.N., "The Two-Dimensional Incompressible Aerodynamic Coefficients for Oscillatory Changes in Airfoil Camber," Journal of the Aeronautical Sciences, June 1953.
 32. Yates, E.C., Jr., "Calculation of Flutter Characteristics for Finite-Span Swept or Unswept wings at Subsonic or Supersonic Speeds by a Modified Strip Analysis," NACA RM L57L10, 1958.
 33. DeYoung, J. and Harper, C.W., "Theoretical Symmetric Span Loading at Subsonic Speeds for Wings Having Arbitrary

Planforms," NACA Report 921, 1948.

34. Swaim, R.L., "Aeroelastic Interaction with Flight Control (A Survey paper)," AIAA Guidance and Control Conference, Gatlinburg, Tennessee, August 1983, AIAA Paper 83-2219.
35. Bisplinghoff, R.J., Ashley, H. and Halfman, R.L., Aeroelasticity, Addison-Wesley Publishing Co., 1955.
36. Lagace, P.A., and Brewer, J.C., Telac Manufacturing Class Notes, unpublished, 1981.
37. Reed, W.H., III, and Abbott, F.T., Jr., "A New 'Free-Flight' Mount System for High-Speed Wind-Tunnel Flutter Models," Proceedings of Symposium on Aeroelastic and Dynamics Modeling Technology, AFFDL-63-4197, Part I, March 1964.
38. Kinnaman, E.B., "Flutter Analysis of Complex Airplanes by Experimental Methods," J. of Aeronautical Sciences, Vol. 19, No. 9, September 1952, pp. 577-584.
39. Lewis, R.C., and Wrisley, D.L., "A system for the excitation of Pure Natural Modes of Complex Structures," J. of Aeronautical Sciences, Vol. 17, No. 11, 1950, pp. 705-722.
40. Tunner, M.D., "Comparison of Static and Dynamic Test Methods for Determining the Stiffness Properties of Graphite/Epoxy Laminates," M. S.Thesis, Department of Aeronautics and Astronautics, M.I.T., 1979.
41. Rimer, M., Chipman, R. and Mercadante, R., "Divergence Suppression System for A Forward Swept Wing Configuration with Wing-Mounted Stores," J. of Aircraft, Vol. 21, No. 8, August 1984.
42. Rimer, M., Chipman, R., and Muniz, B., "Control of Forward Swept Wing Configurations Dominated by Flight-Dynamic/Aeroelastic Interactions," AIAA Guidance and Control Conference, Seattle, Washington, August 1984, AIAA Paper 84-1866.
43. Noll, T.E., Eastep, F.E., and Calico, R.A., "Active Suppression of Aeroelastic Instability on a Forward Swept Wing," J. of Aircraft, Vol. 21, No. 3, March 1984, pp. 202-208.
44. Crawley, E.F., and Dugundji, J., "Frequency Determination and Non-dimensionalization for Composite Cantilever Plates," J. of Sound and Vibration, Vol. 72, No. 1, September 1980, pp. 1-10.

45. Vepa, R., "On the Use of Pade Approximants to Represent Unsteady Aerodynamic Loads for Arbitrary Small Motions of Wings," AIAA 14th Aerospace Sciences Meeting, Washington, D.C., January 1976, AIAA paper 76-17.
46. Edwards, J.E., Ashley, H., and Breakwell, J.V., "Unsteady Aerodynamic Modeling for Arbitrary Motions," AIAA Journal, Vol. 17, No. 4, April 1979, pp. 365-374.
47. Dowell, E.H., "A Simple Method for Converting Frequency Domain Aerodynamics to The Time Domain," NASA TM-81844, 1980.
48. Peterson, L., and Crawley, E.F., "Time Series Approximation of Unsteady Aerodynamics Including Pole Locations As A Free Parameters," 26th AIAA/ASME/ASCE/AHS Structures, Structural Dynamics, and Materials Conference, Orlando, Florida, April 1985, AIAA Paper 85-0663.

APPENDIX A

STRUCTURAL INERTIA AND STIFFNESS COEFFICIENTS

A.1 INERTIA COEFFICIENTS

Based on the 7-mode Rayleigh-Ritz analysis and parameters defined in Figure 2.2, the inertia coefficients, given by Eq. (2.8), are

$$\begin{aligned}
 m_{11} &= M \\
 m_{13} &= M_w I_{45} \\
 m_{14} &= M_w I_{46} \\
 m_{22} &= I \\
 m_{23} &= M_w (I_{53} \sin \Lambda + I_{45} Y_w) \\
 m_{24} &= M_w I_{47} I_{60} \bar{c} \cos \Lambda \\
 m_{25} &= M_w (I_{54} \sin \Lambda + I_{46} Y_w) \\
 m_{26} &= M_w I_{48} I_{61} \bar{c} \cos \Lambda \\
 m_{33} &= M_w I_1 \\
 m_{44} &= M_w I_3 / 12 \\
 m_{55} &= M_w I_2 \\
 m_{66} &= M_w I_4 / 12 \\
 m_{77} &= M_w I_5 \quad 4/45 \\
 \text{other } m_{ij}'s &= 0
 \end{aligned}$$

where M and I are aircraft model mass and pitch moment of inertia, M_w is the wing mass, and I_i 's are the integration constants as tabulated in Table A.1. It should be noted that

the chosen mode shapes uncouple the elastic degrees of freedom, but there still exists inertia coupling between the rigid body and elastic modes, i.e., m_{13} , m_{23} etc.

A.2 STIFFNESS COEFFICIENTS

Similarly, the stiffness coefficients given by Eq. (2.8) are

$$\begin{aligned}
 k_{33} &= \frac{D_{11}\bar{c}}{\bar{\ell}^3} I_6 & k_{34} &= \frac{2D_{16}}{\bar{\ell}^2} I_7 \\
 k_{35} &= 0 & k_{36} &= \frac{2D_{16}}{\bar{\ell}^2} I_8 & k_{37} &= \frac{8D_{12}}{\bar{\ell}\bar{c}} I_9 \\
 k_{44} &= \frac{4D_{66}}{\bar{\ell}\bar{c}} I_{15} \left(\frac{k_{1t}}{\pi/2}\right)^2 & k_{45} &= \frac{2D_{16}}{\bar{\ell}^2} I_{11} \\
 k_{46} &= 0 & k_{47} &= \frac{4D_{16}}{3\bar{\ell}^2} I_{16} + \frac{16D_{26}}{\bar{c}^2} I_{17} \\
 k_{55} &= \frac{D_{11}\bar{c}}{\bar{\ell}^3} I_{10} & k_{56} &= \frac{2D_{16}}{\bar{\ell}^2} I_{12} & k_{57} &= \frac{8D_{12}}{\bar{\ell}\bar{c}} I_{13} \\
 k_{66} &= \frac{4D_{66}}{\bar{\ell}\bar{c}} I_{19} \left(\frac{k_{2t}}{3\pi/2}\right)^2 \\
 k_{67} &= \frac{4D_{16}}{3\bar{\ell}^2} I_{20} + \frac{16D_{26}}{\bar{c}^2} I_{21} \\
 k_{77} &= \frac{4D_{11}\bar{c}}{45\bar{\ell}^3} I_{22} + \frac{64D_{22}\bar{\ell}}{\bar{c}^3} I_5 + \frac{64D_{66}}{3\bar{c}\bar{\ell}} I_{23}
 \end{aligned}$$

It should be noted that the torsional stiffness terms, k_{44} and k_{66} , are modified for the additional warping stiffness by correction factors, k_{1t} and k_{2t} . This is because that the assumed St. Venant's torsional modes are free to warp which is incompatible with the root boundary condition of the plate model. Reference 43 detailed these warping corrections based on the partial Ritz solution of a symmetric laminated plate without bending-twisting coupling, i.e., $D_{16}=0$ and $D_{26}=0$. Figure A.1, reproduced from Ref. 10, shows k_{1t} and k_{2t} versus the effective aspect ratio, β , which is defined as

$$\beta = \frac{1}{48} \frac{D_{11} \bar{c}^2}{D_{66} \bar{z}^2}$$

Table A.1 Mode Shape Integrals

$$I_1 = \frac{1}{\bar{L}} \int_0^{\bar{L}} (\phi_3)^2 d\bar{x} = 1.$$

$$I_2 = \frac{1}{\bar{L}} \int_0^{\bar{L}} (\phi_5)^2 d\bar{x} = 1.$$

$$I_3 = \frac{1}{\bar{L}} \int_0^{\bar{L}} (\phi_4)^2 d\bar{x} = 0.5$$

$$I_4 = \frac{1}{\bar{L}} \int_0^{\bar{L}} (\phi_6)^2 d\bar{x} = 0.5$$

$$I_5 = \frac{1}{\bar{L}} \int_0^{\bar{L}} (\phi_7)^2 d\bar{x} = 0.0333$$

$$I_6 = \bar{L}^3 \int_0^{\bar{L}} (\phi_3'')^2 d\bar{x} = 12.36$$

$$I_7 = \bar{L}^2 \int_0^{\bar{L}} (\phi_3'' \phi_4') d\bar{x} = 3.744$$

$$I_8 = \bar{L}^2 \int_0^{\bar{L}} (\phi_3'' \phi_6') d\bar{x} = 3.249$$

$$I_9 = \bar{L} \int_0^{\bar{L}} (\phi_3'' \phi_7) d\bar{x} = 0.4340$$

$$I_{10} = \bar{L}^3 \int_0^{\bar{L}} (\phi_5'')^2 d\bar{x} = 485.5$$

Table A.1 Mode Shape Integrals (cont'd)

$$I_{11} = \bar{\ell}^2 \int_0^{\bar{\ell}} (\phi_5'' \phi_4') d\bar{x} = -6.700$$

$$I_{12} = \bar{\ell}^2 \int_0^{\bar{\ell}} (\phi_5'' \phi_6') d\bar{x} = 63.54$$

$$I_{13} = \bar{\ell} \int_0^{\bar{\ell}} (\phi_5'' \phi_7) d\bar{x} = -2.868$$

$$I_{15} = \bar{\ell} \int_0^{\bar{\ell}} (\phi_4')^2 d\bar{x} = 1.234$$

$$I_{16} = \bar{\ell}^2 \int_0^{\bar{\ell}} (\phi_4'' \phi_7') d\bar{x} = .4292$$

$$I_{17} = \int_0^{\bar{\ell}} (\phi_4' \phi_7) d\bar{x} = .1739$$

$$I_{19} = \bar{\ell} \int_0^{\bar{\ell}} (\phi_6')^2 d\bar{x} = 11.10$$

$$I_{20} = \bar{\ell}^2 \int_0^{\bar{\ell}} (\phi_6'' \phi_7') d\bar{x} = -6.712$$

$$I_{21} = \int_0^{\bar{\ell}} (\phi_6' \phi_7) d\bar{x} = -.3023$$

$$I_{22} = \bar{\ell}^3 \int_0^{\bar{\ell}} (\phi_7'')^2 d\bar{x} = 4.$$

Table A.1 Mode Shape Integrals (cont'd)

$$I_{23} = \bar{\ell} \int_0^{\bar{\ell}} (\phi_7')^2 d\bar{x} = .3333$$

$$I_{45} = \frac{1}{\bar{\ell}} \int_0^{\bar{\ell}} \phi_3 d\bar{x} = .7830$$

$$I_{46} = \frac{1}{\bar{\ell}} \int_0^{\bar{\ell}} \phi_5 d\bar{x} = .4339$$

$$I_{47} = \frac{1}{\bar{\ell}} \int_0^{\bar{\ell}} \phi_4 d\bar{x} = 2/\pi$$

$$I_{48} = \frac{1}{\bar{\ell}} \int_0^{\bar{\ell}} \phi_6 d\bar{x} = 2/3\pi$$

$$I_{53} = \frac{1}{\bar{\ell}^2} \int_0^{\bar{\ell}} (\bar{x} \phi_3) d\bar{x} = .5688$$

$$I_{54} = \frac{1}{\bar{\ell}^2} \int_0^{\bar{\ell}} (\bar{x} \phi_5) d\bar{x} = .09077$$

$$I_{60} = \int_{-\bar{c}/2}^{\bar{c}/2} \bar{y} \psi_4 d\bar{y} = \frac{\bar{c}^2}{12}$$

$$I_{61} = \int_{-\bar{c}/2}^{\bar{c}/2} \bar{y} \psi_6 d\bar{y} = \frac{\bar{c}^2}{12}$$

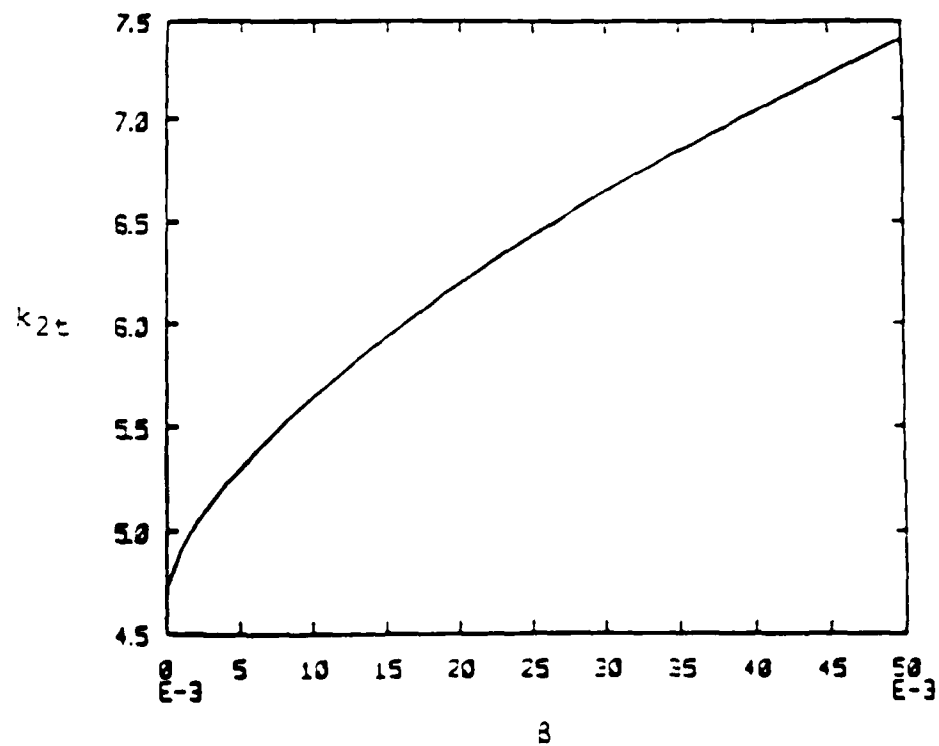
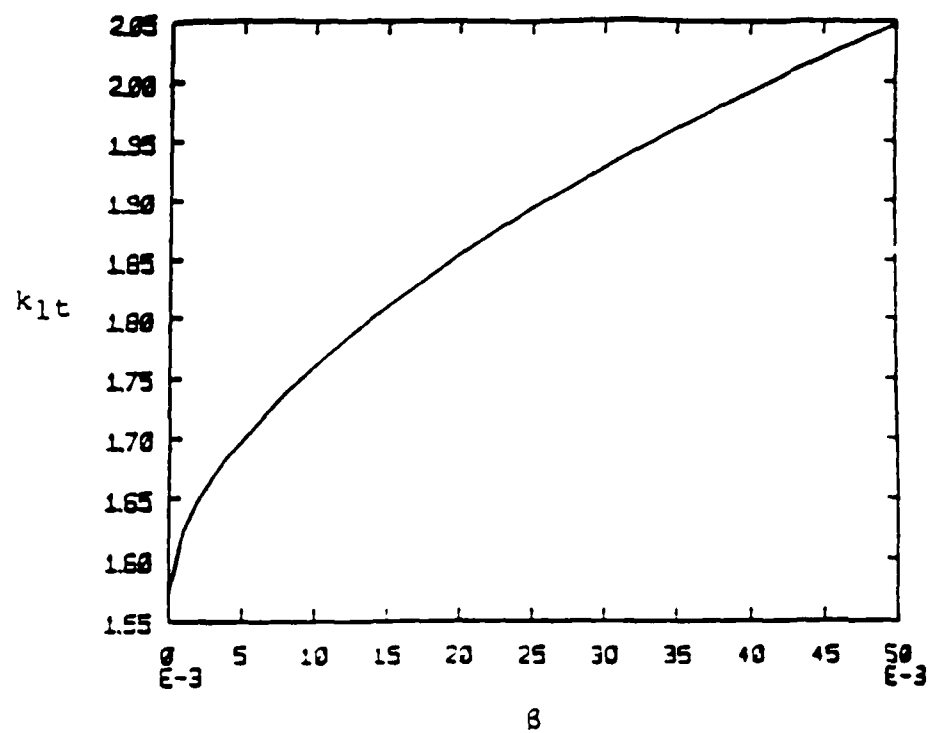


Fig. A.1 k_{1t} and k_{2t} vs. Effective Aspect Ratio, B

APPENDIX B

TRANSIENT AERODYNAMIC COEFFICIENTS

The two-dimensional incompressible harmonic airloads, including the effect of camber oscillation, was given by Spielberg in Ref. 31. Using the sign conventions and cambering mode (chordwise bending mode) defined in Chapter 2, this result, about mid-chord location, was rederived and are given in the following expressions as

$$\begin{aligned}\hat{L} &= \pi \rho b^3 \omega^2 \cos \Lambda \left[L_A \frac{\hat{h}}{b} + L_B \hat{\alpha} + L_C \frac{\hat{\xi}}{b} \right] \\ \hat{M} &= \pi \rho b^4 \omega^2 \cos \Lambda \left[M_A \frac{\hat{h}}{b} + M_B \hat{\alpha} + M_C \frac{\hat{\xi}}{b} \right] \\ \hat{N} &= \pi \rho b^3 \omega^2 \cos \Lambda \left[N_A \frac{\hat{h}}{b} + N_B \hat{\alpha} + N_C \frac{\hat{\xi}}{b} \right]\end{aligned}\tag{B.1}$$

where

$$\begin{aligned}L_A &= 1 - j \frac{2}{k} C(k) \\ L_B &= j \frac{1}{k} + \left(\frac{2}{k^2} + j \frac{1}{k} \right) C(k) \\ L_C &= -\frac{1}{12} - \left(\frac{2}{k^2} + j \frac{1}{3k} \right) C(k) \\ M_A &= -j \frac{1}{k} C(k) \\ M_B &= \left(\frac{1}{8} - j \frac{1}{2k} \right) + \left(\frac{1}{k^2} + j \frac{1}{2k} \right) C(k) \\ M_C &= \left(\frac{1}{k^2} + j \frac{1}{2k} \right) - \left(\frac{1}{k^2} + j \frac{1}{6k} \right) C(k)\end{aligned}$$

$$N_A = -\frac{1}{12} - j \frac{1}{3k} C(k)$$

$$N_B = -j \frac{1}{3k} + \left(\frac{1}{3k^2} + j \frac{1}{6k} \right) C(k)$$

$$N_C = \left(\frac{1}{36} + \frac{1}{2k^2} \right) - \left(\frac{1}{3k^2} + j \frac{1}{18k} \right) C(k)$$

To obtain the transient airload expressions, a key step is to generalize the airload expressions from the frequency axis into the complex variable domain [45,46]. For the aerodynamic model used in the presnet study, one can first substitutes nondimensional Laplace variable, \bar{p} , for jk and generalized Theodorsen function, $C(\bar{p})$, for $C(k)$ in Eq. (B.1), i.e.,

$$\begin{aligned} \hat{L} = 2\pi\rho V^2 b \cos\Lambda & \left\{ \left[A_{2a}\bar{p}^2 + A_{1a}\bar{p} + A_{0a} + (A_{4a}\bar{p} + A_{3a})C(\bar{p}) \right] \frac{\hat{h}}{b} \right. \\ & \left[A_{2b}\bar{p}^2 + A_{1b}\bar{p} + A_{0b} + (A_{4b}\bar{p} + A_{3b})C(\bar{p}) \right] \hat{\alpha} \\ & \left. \left[A_{2c}\bar{p}^2 + A_{1c}\bar{p} + A_{0c} + (A_{4c}\bar{p} + A_{3c})C(\bar{p}) \right] \frac{\hat{\xi}}{b} \right\} \\ \hat{M} = 2\pi\rho V^2 b^2 \cos\Lambda & \left\{ \left[A_{2d}\bar{p}^2 + A_{1d}\bar{p} + A_{0d} + (A_{4d}\bar{p} + A_{3d})C(\bar{p}) \right] \frac{\hat{h}}{b} \right. \\ & \left[A_{2e}\bar{p}^2 + A_{1e}\bar{p} + A_{0e} + (A_{4e}\bar{p} + A_{3e})C(\bar{p}) \right] \hat{\alpha} \\ & \left. \left[A_{2f}\bar{p}^2 + A_{1f}\bar{p} + A_{0f} + (A_{4f}\bar{p} + A_{3f})C(\bar{p}) \right] \frac{\hat{\xi}}{b} \right\} \end{aligned} \quad (B.2)$$

$$\hat{N} = 2\pi\rho V^2 b \cos\Lambda \left\{ \left[A_{2g}\bar{p}^2 + A_{1g}\bar{p} + A_{0g} + (A_{4g}\bar{p} + A_{3g})C(\bar{p}) \right] \frac{\hat{h}}{b} \right. \\ \left[A_{2h}\bar{p}^2 + A_{1h}\bar{p} + A_{0h} + (A_{4h}\bar{p} + A_{3h})C(\bar{p}) \right] \frac{\hat{a}}{a} \\ \left. \left[A_{2i}\bar{p}^2 + A_{1i}\bar{p} + A_{0i} + (A_{4i}\bar{p} + A_{3i})C(\bar{p}) \right] \frac{\hat{i}}{b} \right\}$$

where

$A_{4a} = -1$	$A_{3a} = 0$	$A_{2a} = -\frac{1}{2}$	$A_{1a} = 0$	$A_{0a} = 0$
$A_{4b} = \frac{1}{2}$	$A_{3b} = 1$	$A_{2b} = 0$	$A_{1b} = \frac{1}{2}$	$A_{0b} = 0$
$A_{4c} = -\frac{1}{6}$	$A_{3c} = -1$	$A_{2c} = \frac{1}{24}$	$A_{1c} = 0$	$A_{0c} = 0$
$A_{4d} = 0$	$A_{3d} = -\frac{1}{2}$	$A_{2d} = 0$	$A_{1d} = 0$	$A_{0d} = 0$
$A_{4e} = \frac{1}{4}$	$A_{3e} = \frac{1}{2}$	$A_{2e} = -\frac{1}{16}$	$A_{1e} = -\frac{1}{4}$	$A_{0e} = 0$
$A_{4f} = -\frac{1}{12}$	$A_{3f} = -\frac{1}{2}$	$A_{2f} = 0$	$A_{1f} = \frac{1}{4}$	$A_{0f} = \frac{1}{2}$
$A_{4g} = -\frac{1}{6}$	$A_{3g} = 0$	$A_{2g} = \frac{1}{24}$	$A_{1g} = 0$	$A_{0g} = 0$
$A_{4h} = \frac{1}{12}$	$A_{3h} = \frac{1}{6}$	$A_{2h} = 0$	$A_{1h} = -\frac{1}{6}$	$A_{0h} = 0$
$A_{4i} = -\frac{1}{36}$	$A_{3i} = -\frac{1}{6}$	$A_{2i} = -\frac{1}{72}$	$A_{1i} = 0$	$A_{0i} = \frac{1}{4}$

The next step is to approximate these motion-dependent airloads by functions of displacements, their derivatives, and finite number of lag terms as

$$\begin{aligned}
 \hat{L} &= 2\pi\rho V^2 b \cos\Lambda \left\{ \left[B_{2a}\bar{p}^2 + B_{1a}\bar{p} + B_{0a} + \sum_{n=3}^L B_{na} \frac{\bar{p}}{\bar{p}+g_n} \right] \frac{\hat{h}}{b} \right. \\
 &\quad \left[B_{2b}\bar{p}^2 + B_{1b}\bar{p} + B_{0b} + \sum_{n=3}^L B_{nb} \frac{\bar{p}}{\bar{p}+g_n} \right] \hat{\alpha} \\
 &\quad \left. \left[B_{2c}\bar{p}^2 + B_{1c}\bar{p} + B_{0c} + \sum_{n=3}^L B_{nc} \frac{\bar{p}}{\bar{p}+g_n} \right] \frac{\hat{\xi}}{b} \right\} \\
 \hat{M} &= 2\pi\rho V^2 b^2 \cos\Lambda \left\{ \left[B_{2d}\bar{p}^2 + B_{1d}\bar{p} + B_{0d} + \sum_{n=3}^L B_{nd} \frac{\bar{p}}{\bar{p}+g_n} \right] \frac{\hat{h}}{b} \right. \\
 &\quad \left[B_{2e}\bar{p}^2 + B_{1e}\bar{p} + B_{0e} + \sum_{n=3}^L B_{ne} \frac{\bar{p}}{\bar{p}+g_n} \right] \hat{\alpha} \\
 &\quad \left. \left[B_{2f}\bar{p}^2 + B_{1f}\bar{p} + B_{0f} + \sum_{n=3}^L B_{nf} \frac{\bar{p}}{\bar{p}+g_n} \right] \frac{\hat{\xi}}{b} \right\} \\
 \hat{N} &= 2\pi\rho V^2 b \cos\Lambda \left\{ \left[B_{2g}\bar{p}^2 + B_{1g}\bar{p} + B_{0g} + \sum_{n=3}^L B_{ng} \frac{\bar{p}}{\bar{p}+g_n} \right] \frac{\hat{h}}{b} \right. \\
 &\quad \left[B_{2h}\bar{p}^2 + B_{1h}\bar{p} + B_{0h} + \sum_{n=3}^L B_{nh} \frac{\bar{p}}{\bar{p}+g_n} \right] \hat{\alpha} \\
 &\quad \left. \left[B_{2k}\bar{p}^2 + B_{1k}\bar{p} + B_{0k} + \sum_{n=3}^L B_{nk} \frac{\bar{p}}{\bar{p}+g_n} \right] \frac{\hat{\xi}}{b} \right\}
 \end{aligned} \tag{B.3}$$

The coefficients of Eq. (B.3), e.g., B_{2A} , B_{1A} , B_{0A} , and B_{nA} , can be thought of as the aerodynamic inertia, damping, stiffness, and lag terms.

To determine those coefficients of Eq. (B.3), one can usually fits Eq. (B.2) to a table of harmonic airloads computed for a chosen set of reduced frequencies. In the case of two-dimensional incompressible flow, this curve fitting can be

actually performed for the generalized Theodorsen function, $C(\bar{p})$, instead of the entire airloads calculated from Eq. (B.2).

For numerical fitting, the number of lag terms and corresponding pole locations are somewhat arbitrary, but influence the accuracy of the functional fit. In many cases, the least squares error function minimization was often used in finding these coefficients or pole locations [47,48]. Typically, numerical experimentation is used to obtain reasonable fits in the anticipated reduced frequency range with as few lag terms as possible.

For the present investigation, a single-lag approximation was chosen with pole located at -0.15, i.e.,

$$C(\bar{p}) = \frac{b_1 \bar{p} + b_0}{\bar{p} + b_0} \quad (B.4)$$

where $b_1 = 0.55$ and $b_0 = 0.15$. Placing Eq. (B.4) into (B.2), and rearranging terms according to Eq. (B.3) with $L=3$ results in the following set of coefficients

$B_{0a} = 0$	$B_{1a} = -b_1$	$B_{2a} = -\frac{1}{2}$	$B_{3a} = (b_1-1)b_0$
$B_{0b} = 1$	$B_{1b} = \frac{1}{2}(1+b_1)$	$B_{2b} = 0$	$B_{3b} = (b_1-1)(1-\frac{b_0}{2})$
$B_{0c} = -1$	$B_{1c} = -\frac{1}{6}b_1$	$B_{2c} = \frac{1}{24}$	$B_{3c} = (b_1-1)(\frac{b_0}{6}-1)$
$B_{0d} = 0$	$B_{1d} = -\frac{1}{2}b_1$	$B_{2d} = 0$	$B_{3d} = (b_1-1)\frac{b_0}{2}$
$B_{0e} = \frac{1}{2}$	$B_{1e} = \frac{1}{4}(b_1-1)$	$B_{2e} = -\frac{1}{16}$	$B_{3e} = (b_1-1)(\frac{1}{2}-\frac{b_0}{4})$
$B_{0f} = 0$	$B_{1f} = \frac{1}{4}-\frac{1}{12}b_1$	$B_{2f} = 0$	$B_{3f} = (b_1-1)(\frac{b_0}{12}-\frac{1}{2})$
$B_{0g} = 0$	$B_{1g} = -\frac{1}{6}b_1$	$B_{2g} = \frac{1}{24}$	$B_{3g} = (b_1-1)\frac{b_0}{6}$
$B_{0h} = \frac{1}{6}$	$B_{1h} = -\frac{1}{6}+\frac{1}{12}b_1$	$B_{2h} = 0$	$B_{3h} = (b_1-1)(\frac{1}{6}-\frac{b_0}{12})$
$B_{0k} = \frac{1}{12}$	$B_{1k} = -\frac{1}{36}b_1$	$B_{2k} = -\frac{1}{72}$	$B_{3k} = (b_1-1)(\frac{b_0}{36}-\frac{1}{6})$

and $g_3 = b_0$. Expressing h , α , and ξ in terms of the generalized coordinates, q_i 's, as detailed in Eq. (2.15), gives

$$\begin{aligned} \hat{L} = & 2\pi\rho V^2 b \cos\Lambda \\ & \left\{ [B_{2a}\bar{p}^2 + B_{1a}\bar{p} + B_{0a}] \sum_{i=1}^7 \eta_i \frac{\hat{q}_i}{b} + B_{3a} \sum_{i=1}^7 \left(\eta_i \frac{\bar{p}}{\bar{p}+b_0} - \frac{\hat{q}_i}{b} \right) \right. \\ & [B_{2b}\bar{p}^2 + B_{1b}\bar{p} + B_{0b}] \sum_{i=1}^7 \theta_i \frac{\hat{q}_i}{b} + B_{3b} \sum_{i=1}^7 \left(\theta_i \frac{\bar{p}}{\bar{p}+b_0} - \frac{\hat{q}_i}{b} \right) \\ & \left. [B_{2c}\bar{p}^2 + B_{1c}\bar{p} + B_{0c}] \sum_{i=1}^7 \zeta_i \frac{\hat{q}_i}{b} + B_{3c} \sum_{i=1}^7 \left(\zeta_i \frac{\bar{p}}{\bar{p}+b_0} - \frac{\hat{q}_i}{b} \right) \right\} \end{aligned}$$

$$\begin{aligned} \hat{M} = & 2\pi\rho V^2 b^2 \cos\Lambda \\ & \left\{ [B_{2d}\bar{p}^2 + B_{1d}\bar{p} + B_{0d}] \sum_{i=1}^7 \eta_i \frac{\hat{q}_i}{b} + B_{3d} \sum_{i=1}^7 \left(\eta_i \frac{\bar{p}}{\bar{p} + b_0} \frac{\hat{q}_i}{b} \right) \right. \\ & [B_{2e}\bar{p}^2 + B_{1e}\bar{p} + B_{0e}] \sum_{i=1}^7 \theta_i \frac{\hat{q}_i}{b} + B_{3e} \sum_{i=1}^7 \left(\theta_i \frac{\bar{p}}{\bar{p} + b_0} \frac{\hat{q}_i}{b} \right) \\ & \left. [B_{2f}\bar{p}^2 + B_{1f}\bar{p} + B_{0f}] \sum_{i=1}^7 \zeta_i \frac{\hat{q}_i}{b} + B_{3f} \sum_{i=1}^7 \left(\zeta_i \frac{\bar{p}}{\bar{p} + b_0} \frac{\hat{q}_i}{b} \right) \right\} \end{aligned} \quad (B.5)$$

$$\begin{aligned} \hat{N} = & 2\pi\rho V^2 b \cos\Lambda \\ & \left\{ [B_{2g}\bar{p}^2 + B_{1g}\bar{p} + B_{0g}] \sum_{i=1}^7 \eta_i \frac{\hat{q}_i}{b} + B_{3g} \sum_{i=1}^7 \left(\eta_i \frac{\bar{p}}{\bar{p} + b_0} \frac{\hat{q}_i}{b} \right) \right. \\ & [B_{2h}\bar{p}^2 + B_{1h}\bar{p} + B_{0h}] \sum_{i=1}^7 \theta_i \frac{\hat{q}_i}{b} + B_{3h} \sum_{i=1}^7 \left(\theta_i \frac{\bar{p}}{\bar{p} + b_0} \frac{\hat{q}_i}{b} \right) \\ & \left. [B_{2k}\bar{p}^2 + B_{1k}\bar{p} + B_{0k}] \sum_{i=1}^7 \zeta_i \frac{\hat{q}_i}{b} + B_{3k} \sum_{i=1}^7 \left(\zeta_i \frac{\bar{p}}{\bar{p} + b_0} \frac{\hat{q}_i}{b} \right) \right\} \end{aligned}$$

Introducing new augmented state variables, y_i , such that

$$\hat{y}_i(\bar{p}) = \frac{\bar{p}}{\bar{p} + b_0} \hat{q}_i(\bar{p}) \quad i = 1 \text{ to } 7 \quad (B.6)$$

and placing these augmented state variables into Eq. (B.5) leads to the following mixed variable expressions

$$\begin{aligned}
 \hat{L} &= 2\pi\rho V^2 b \cos\Lambda \\
 &\left\{ \left[B_{2a}\bar{p}^2 + B_{1a}\bar{p} + B_{0a} \right] \sum_{i=1}^7 \eta_i \frac{\hat{q}_i}{b} + B_{3a} \sum_{i=1}^7 \eta_i \frac{\hat{y}_i}{b} \right. \\
 &\quad \left[B_{2b}\bar{p}^2 + B_{1b}\bar{p} + B_{0b} \right] \sum_{i=1}^7 \theta_i \frac{\hat{q}_i}{b} + B_{3b} \sum_{i=1}^7 \theta_i \frac{\hat{y}_i}{b} \\
 &\quad \left. \left[B_{2c}\bar{p}^2 + B_{1c}\bar{p} + B_{0c} \right] \sum_{i=1}^7 \zeta_i \frac{\hat{q}_i}{b} + B_{3c} \sum_{i=1}^7 \zeta_i \frac{\hat{y}_i}{b} \right\} \\
 \hat{M} &= 2\pi\rho V^2 b^2 \cos\Lambda \cdots \text{etc} \\
 \hat{N} &= 2\pi\rho V^2 b \cos\Lambda \cdots \text{etc}
 \end{aligned} \tag{B.7}$$

Taking the inverse Laplace transform of Eq. (B.7) and (B.6) results in a two-dimensional, incompressible airload expressions in time domain and governing equations for aerodynamic lag terms. To approximate the aerodynamic effect of a finite span wing, these sectional airload expressions will be modified by substituting the static lift-curve-slope distribution, C_{l_α} , for $2\pi\cos\Lambda$ such that

$$\begin{aligned}
 L &= \rho V^2 b C_{l_\alpha} \\
 &\sum_{i=1}^7 \left(B_{2a} \frac{b^2}{V^2} \eta_i \frac{\ddot{q}_i}{b} + B_{1a} \frac{b}{V} \eta_i \frac{\dot{q}_i}{b} + B_{0a} \eta_i \frac{q_i}{b} + B_{3a} \eta_i \frac{\dot{y}_i}{b} \right. \\
 &\quad + B_{2b} \frac{b^2}{V^2} \theta_i \frac{\ddot{q}_i}{b} + B_{1b} \frac{b}{V} \theta_i \frac{\dot{q}_i}{b} + B_{0b} \theta_i \frac{q_i}{b} + B_{3b} \theta_i \frac{\dot{y}_i}{b} \\
 &\quad \left. + B_{2c} \frac{b^2}{V^2} \zeta_i \frac{\ddot{q}_i}{b} + B_{1c} \frac{b}{V} \zeta_i \frac{\dot{q}_i}{b} + B_{0c} \zeta_i \frac{q_i}{b} + B_{3c} \zeta_i \frac{\dot{y}_i}{b} \right)
 \end{aligned}$$

AD-A182 713

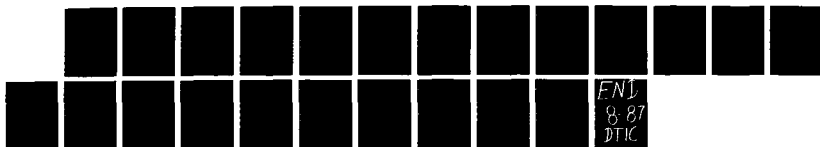
DYNAMICS AND AEROELASTICITY OF COMPOSITE STRUCTURES(U)
MASSACHUSETTS INST OF TECH CAMBRIDGE TECHNOLOGY LAB FOR
ADVANC. G CHEN ET AL. 22 APR 87 TELAC-86-14A

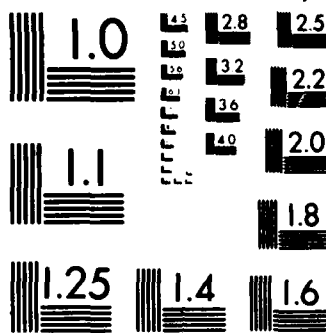
3/3

UNCLASSIFIED

AFOSR-TR-87-0845 F49620-84-C-0099

F/G 1/3.12 NL





MICROCOPY RESOLUTION TEST CHART
NATIONAL BUREAU OF STANDARDS 1963-A

$$\begin{aligned}
 M = \rho V^2 b^2 C_{\ell \alpha} \\
 \sum_{i=1}^7 \left(B_{2d} \frac{b^2}{V^2} \eta_i \frac{\ddot{q}_i}{b} + B_{1d} \frac{b}{V} \eta_i \frac{\dot{q}_i}{b} + B_{0d} \eta_i \frac{q_i}{b} + B_{3d} \eta_i \frac{y_i}{b} \right. \\
 + B_{2e} \frac{b^2}{V^2} \theta_i \frac{\ddot{q}_i}{b} + B_{1e} \frac{b}{V} \theta_i \frac{\dot{q}_i}{b} + B_{0e} \theta_i \frac{q_i}{b} + B_{3e} \theta_i \frac{y_i}{b} \\
 \left. + B_{2f} \frac{b^2}{V^2} \zeta_i \frac{\ddot{q}_i}{b} + B_{1f} \frac{b}{V} \zeta_i \frac{\dot{q}_i}{b} + B_{0f} \zeta_i \frac{q_i}{b} + B_{3f} \zeta_i \frac{y_i}{b} \right) \quad (B.8)
 \end{aligned}$$

$$\begin{aligned}
 N = \rho V^2 b C_{\ell \alpha} \\
 \sum_{i=1}^7 \left(B_{2g} \frac{b^2}{V^2} \eta_i \frac{\ddot{q}_i}{b} + B_{1g} \frac{b}{V} \eta_i \frac{\dot{q}_i}{b} + B_{0g} \eta_i \frac{q_i}{b} + B_{3g} \eta_i \frac{y_i}{b} \right. \\
 + B_{2h} \frac{b^2}{V^2} \theta_i \frac{\ddot{q}_i}{b} + B_{1h} \frac{b}{V} \theta_i \frac{\dot{q}_i}{b} + B_{0h} \theta_i \frac{q_i}{b} + B_{3h} \theta_i \frac{y_i}{b} \\
 \left. + B_{2k} \frac{b^2}{V^2} \zeta_i \frac{\ddot{q}_i}{b} + B_{1k} \frac{b}{V} \zeta_i \frac{\dot{q}_i}{b} + B_{0k} \zeta_i \frac{q_i}{b} + B_{3k} \zeta_i \frac{y_i}{b} \right)
 \end{aligned}$$

Placing Eq. (B.8) into the virtual work expression, Eq. (2.14), introducing h , α , and ξ from Eq. (2.15), and integrating over the wing span concludes the generalized aerodynamic forces in time domain as

$$Q_i = \sum_{j=1}^7 \left(Q_{ij}^A \ddot{q}_j + Q_{ij}^B \dot{q}_j + Q_{ij}^C q_j + Q_{ij}^D y_j \right) \quad (B.9)$$

APPENDIX C

ω -V PLOTS

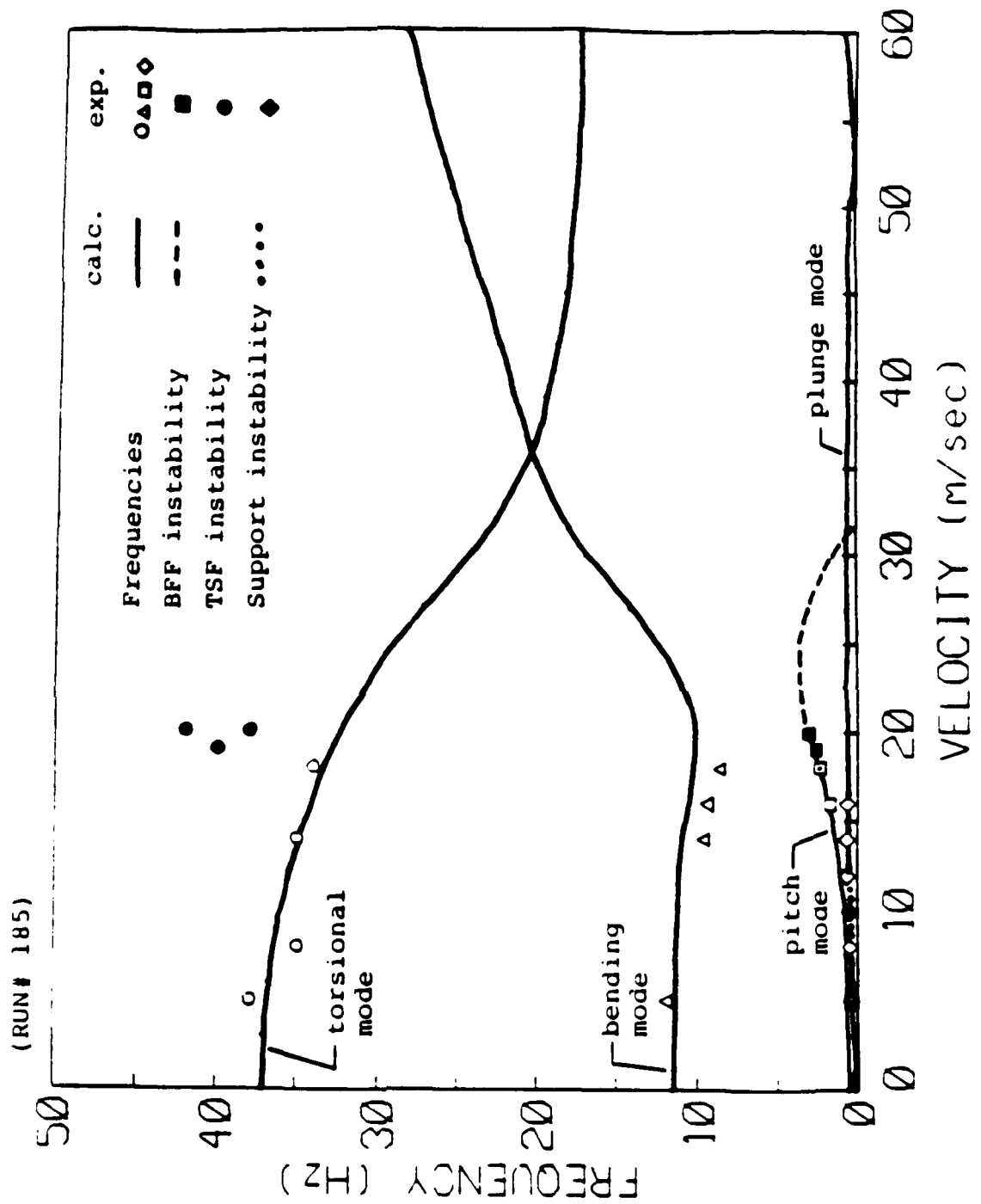


Fig. C.1 ω -V plot, Original Support, $[0_2/90]_s$ Wing
($\delta_c = 0^\circ$)

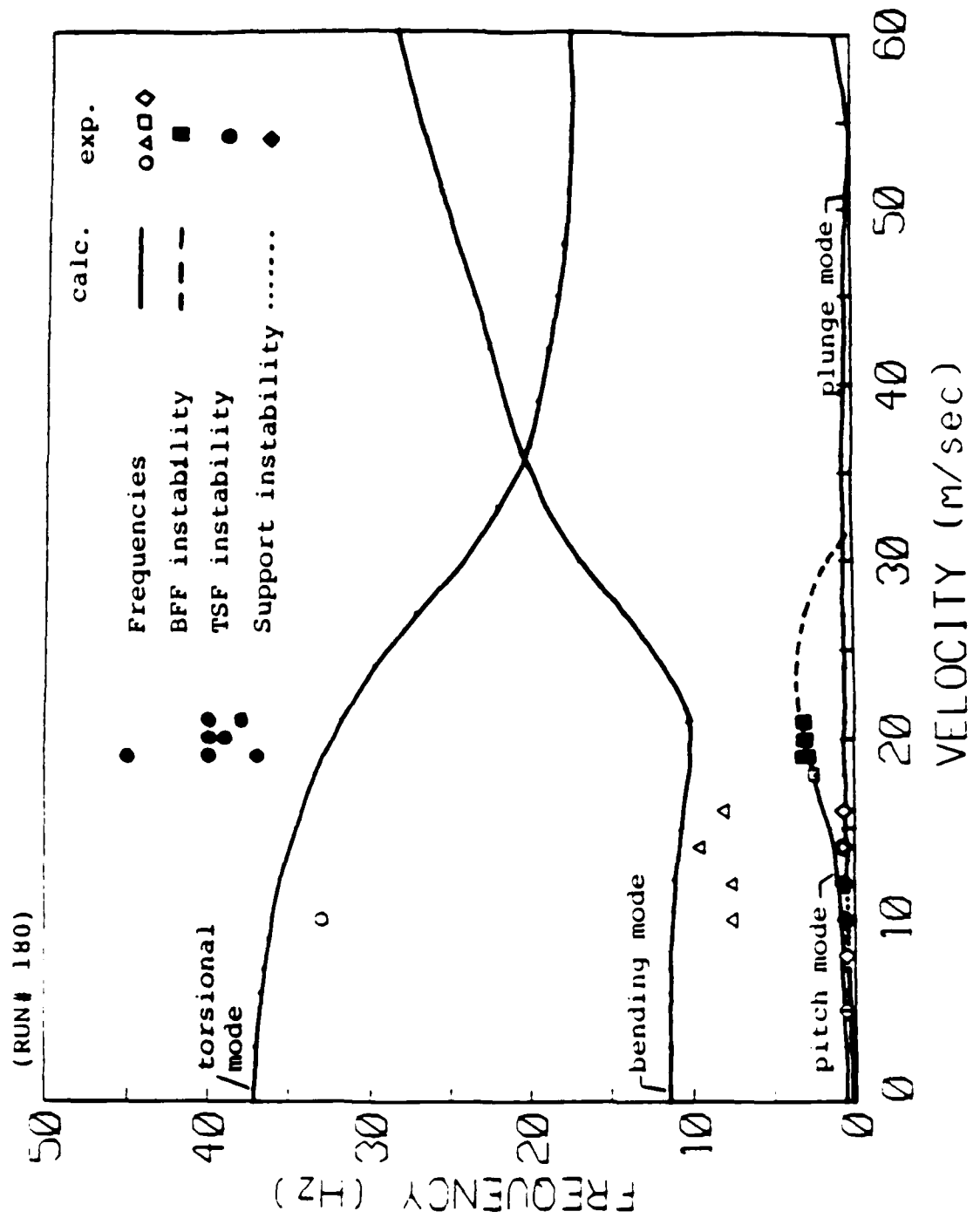


Fig. C.2 ω -V plot, Original Support, $[0_2/90]_s$ Wing ($\delta_c = 2.5^\circ$)

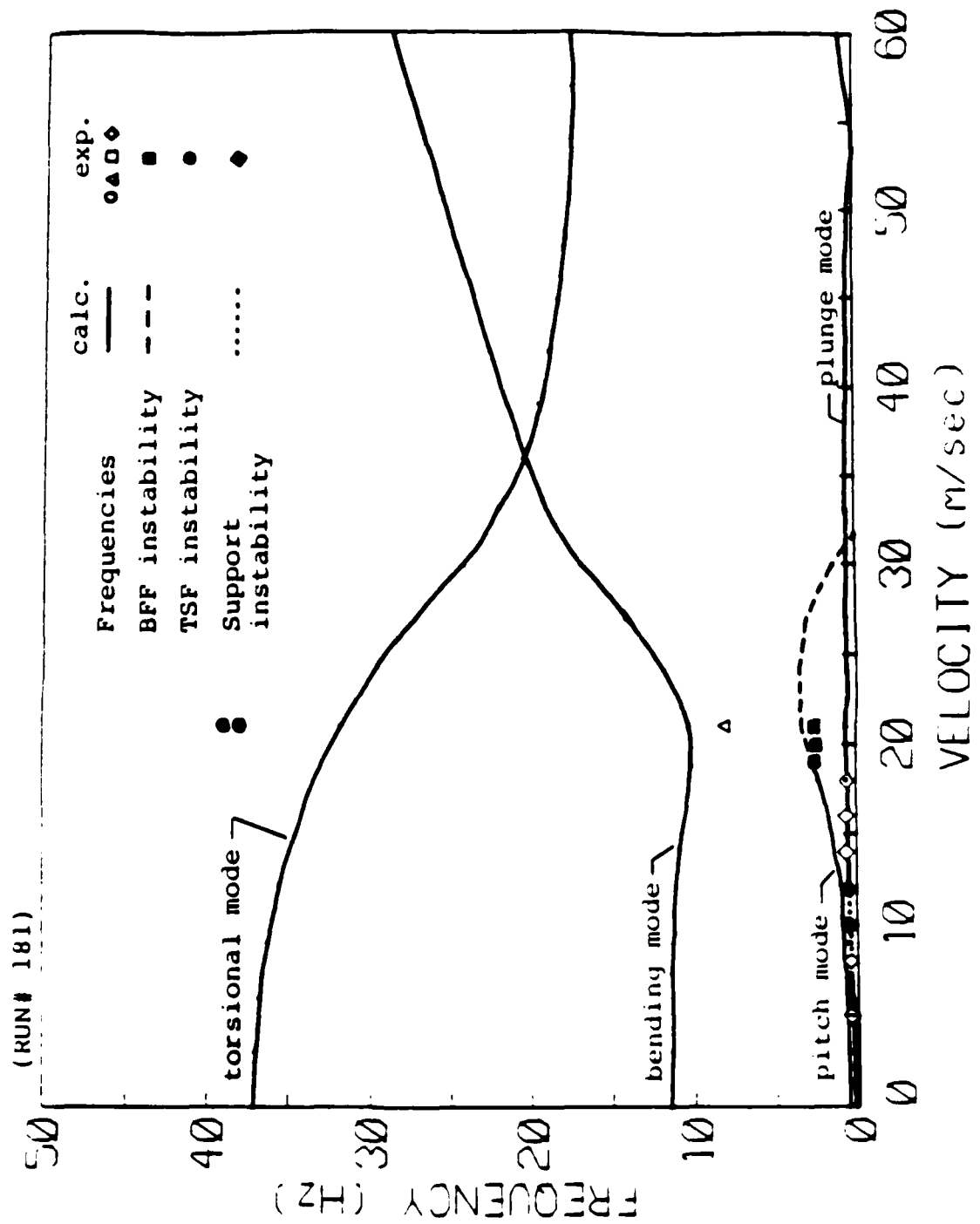


Fig. C.3 ω -V plot, Original Support, $[0_2/90]_s$ Wing
($\delta_c = 5^\circ$)

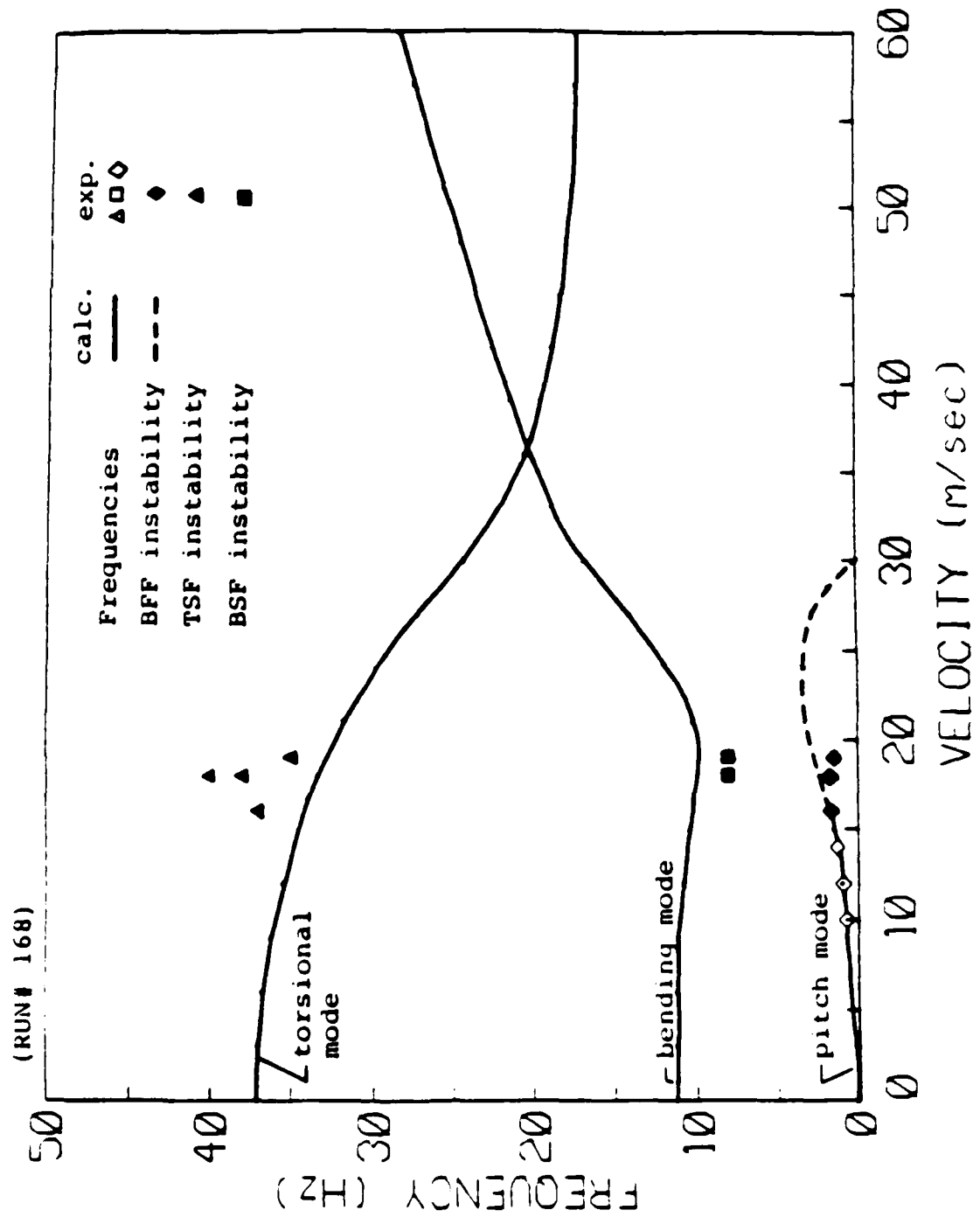


Fig. C.4 ω -V plot, Model Free in Pitch Only, $[0_2/90]_s$ Wing ($\delta_c = 0^\circ$)

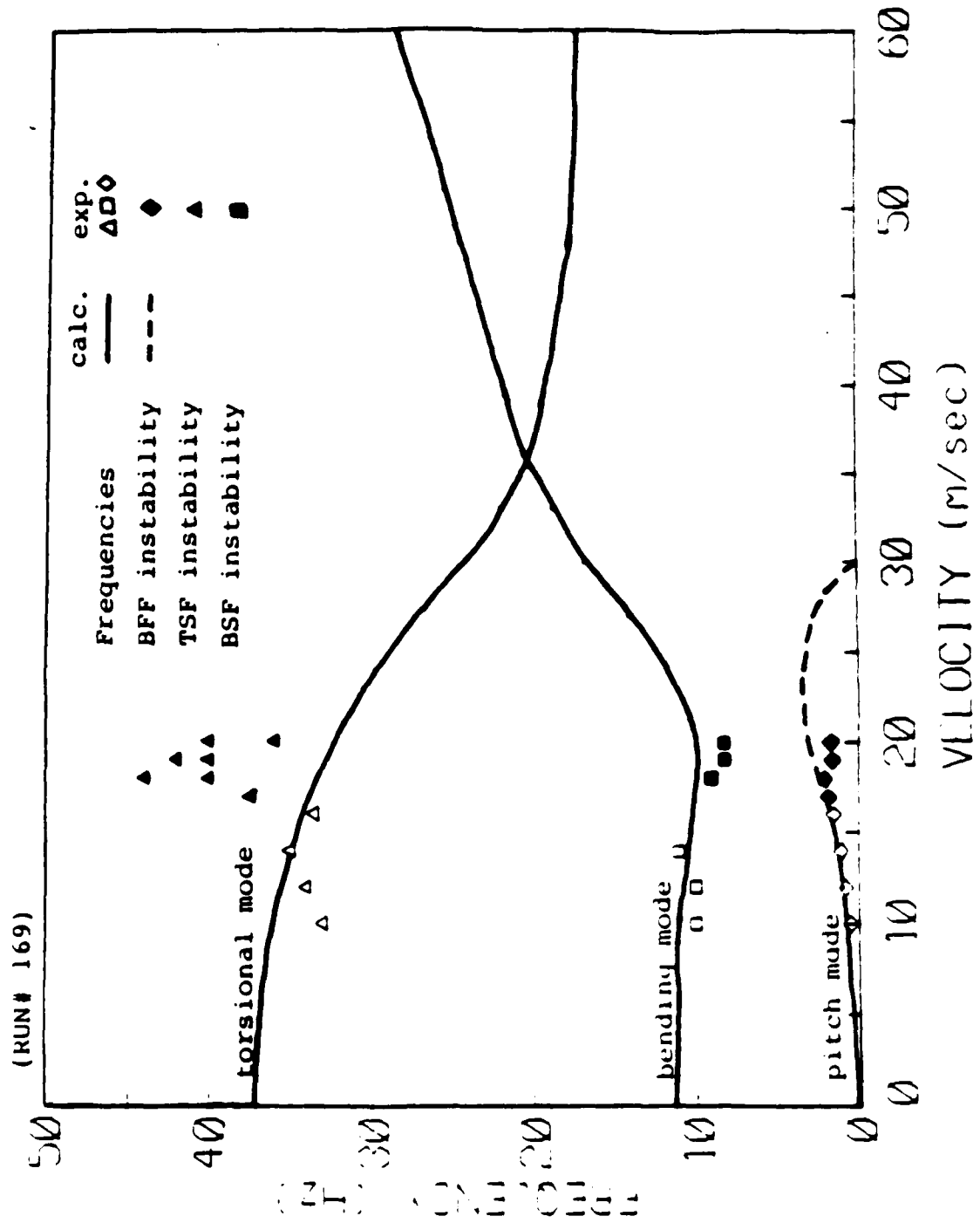


Fig. C.5 ω -V plot, Model Free in Pitch Only, $[0_2/90]_s$ Wing ($\delta_c = 2.5^\circ$)

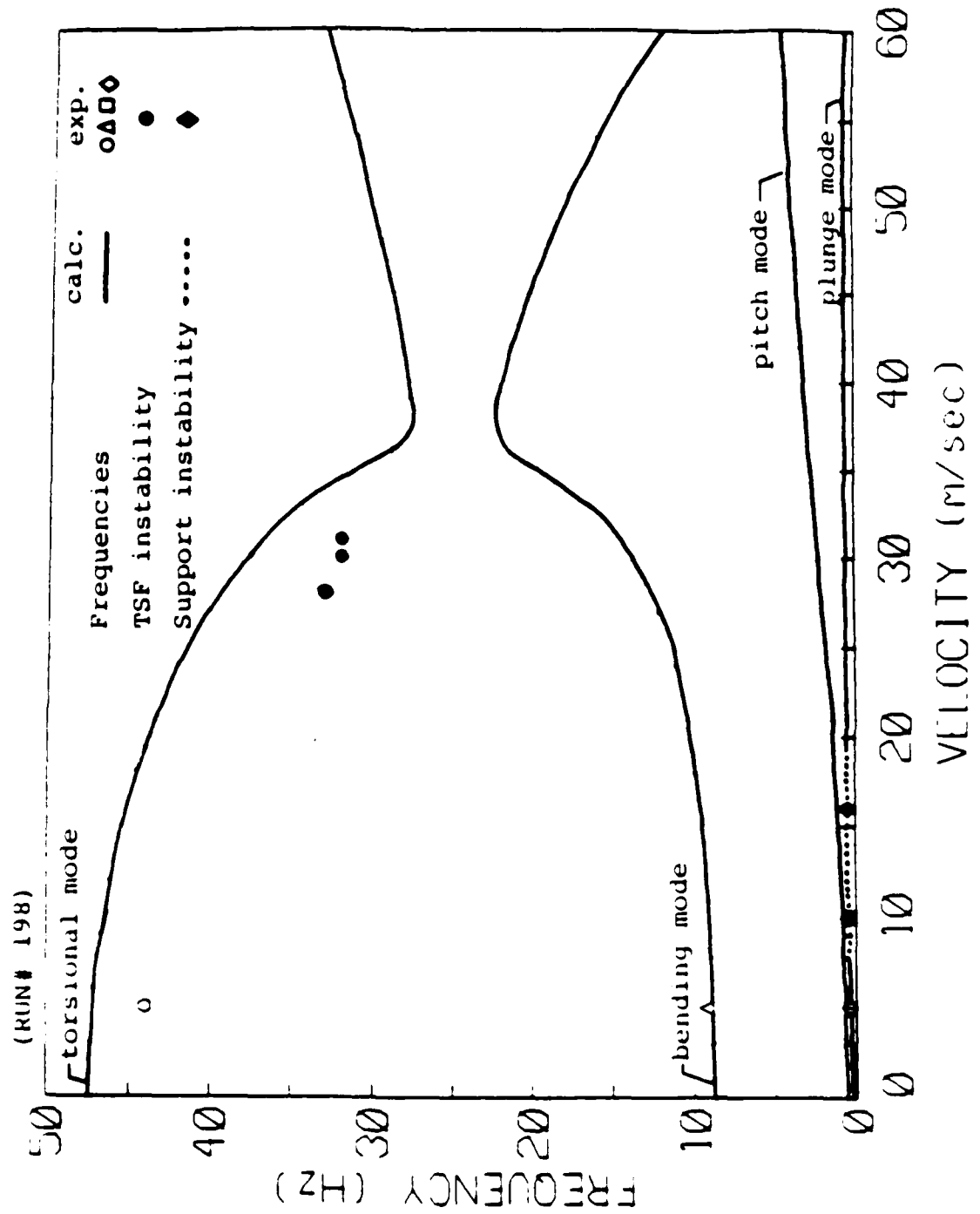


Fig. C.6 ω -V plot, Original Support, $[15_2/0]_s$ Wing
($\delta_c = 2.5^\circ$)

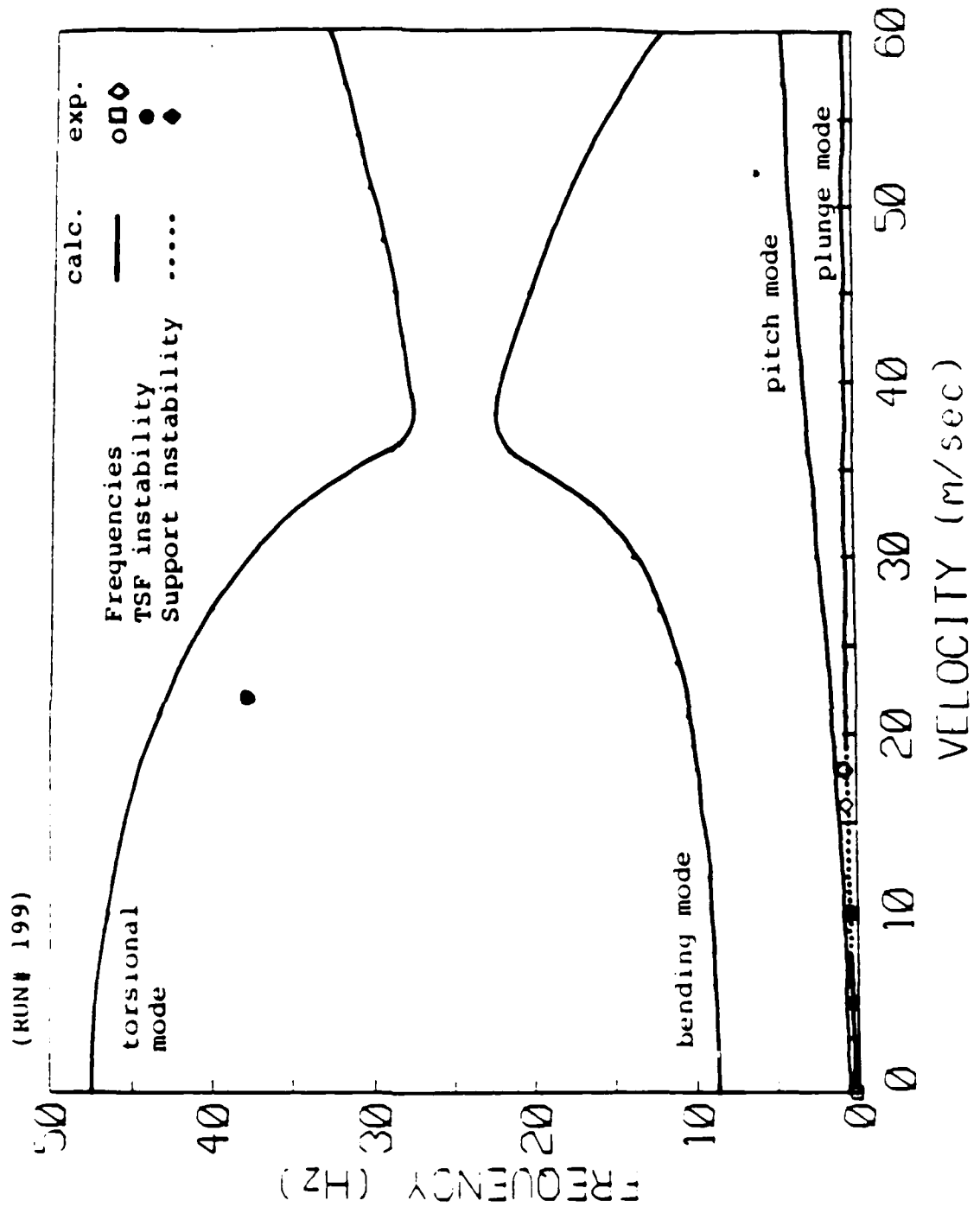


Fig. C.7 ω -V plot, Original Support, $[15_2/0]_s$ Wing
($\delta_c = 5^\circ$)

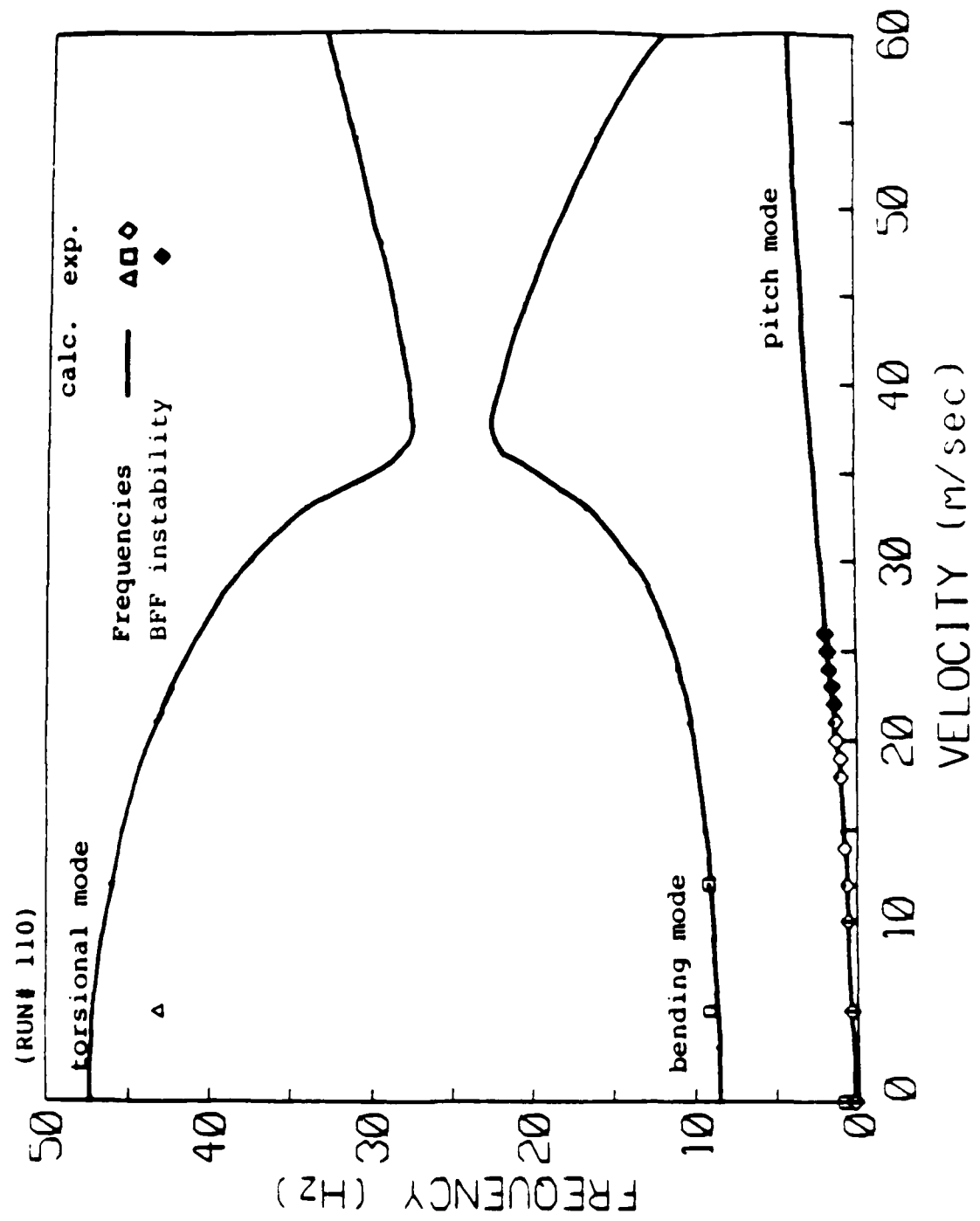


Fig. C.8 ω -V plot, Model Free in Pitch Only, $[15_2/0]_8$ Wing ($\delta_c = 0^\circ$)

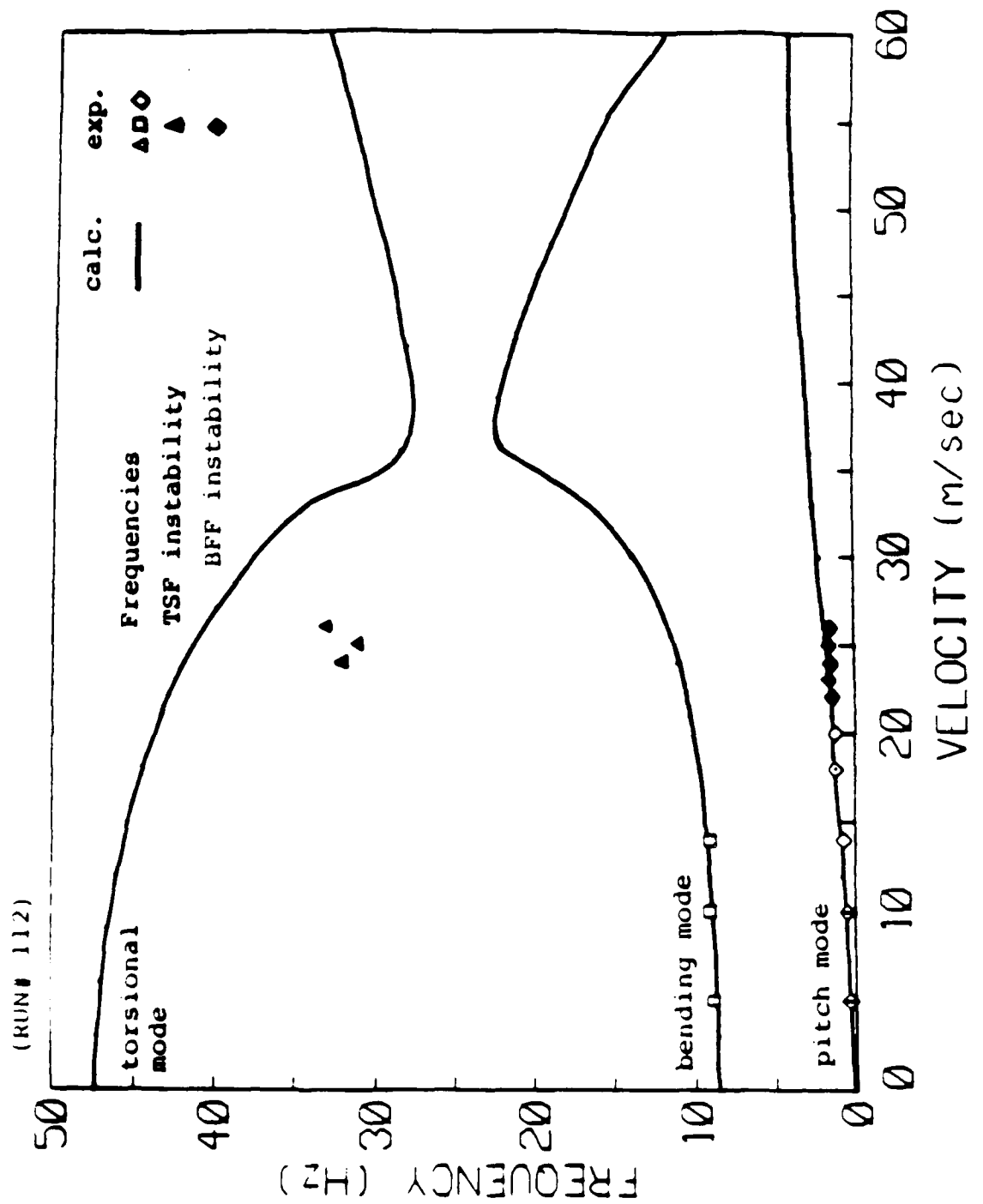


Fig. C.9 ω -V plot, Model Free in Pitch Only, $[15_2/0]_8$ Wing ($\delta_c = 2.5^\circ$)

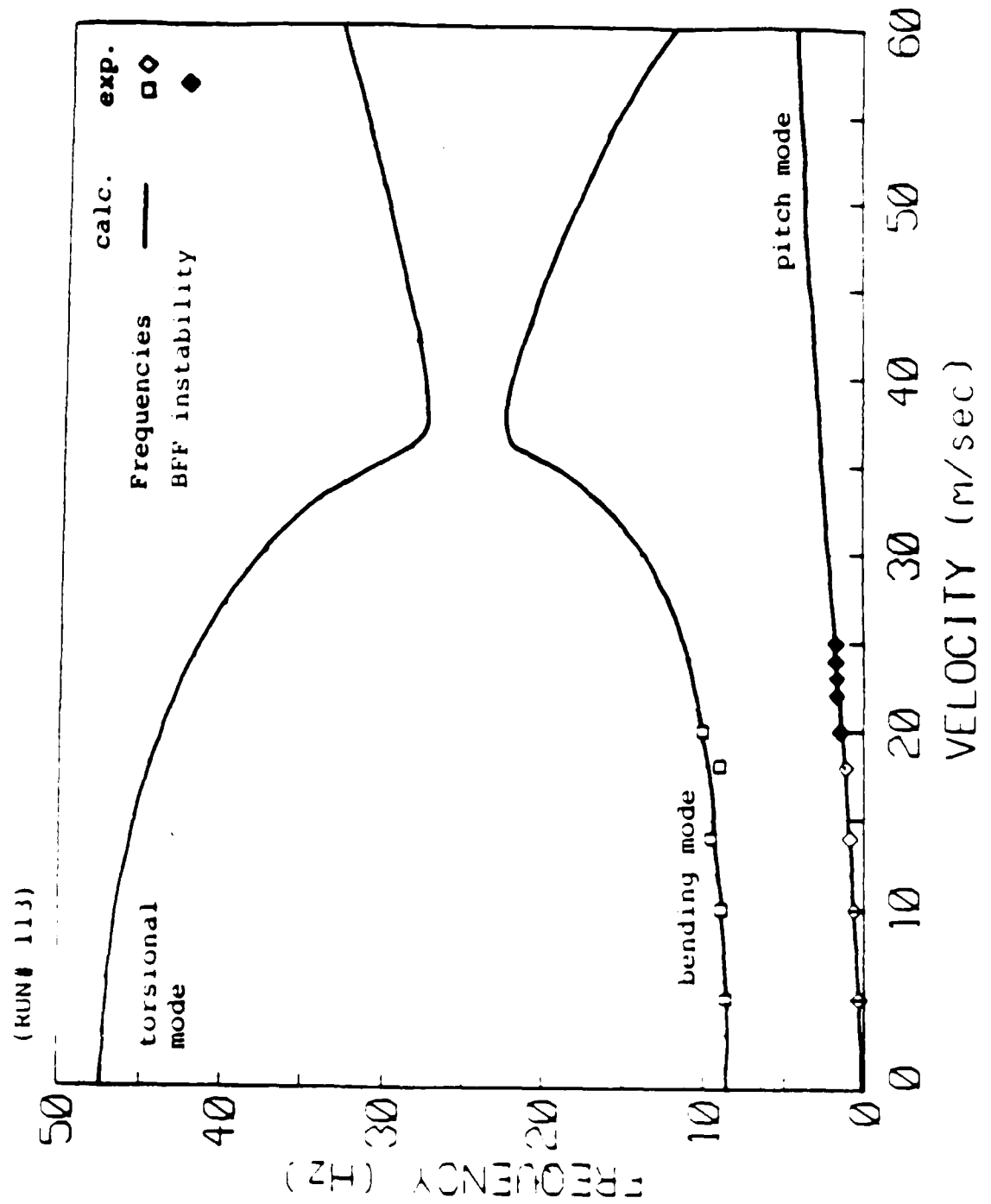


Fig. C.10 ω -V plot, Model Free in Pitch Only, $(15_2/0)_s$ Wing
 $(\delta_c = -2.5^\circ)$

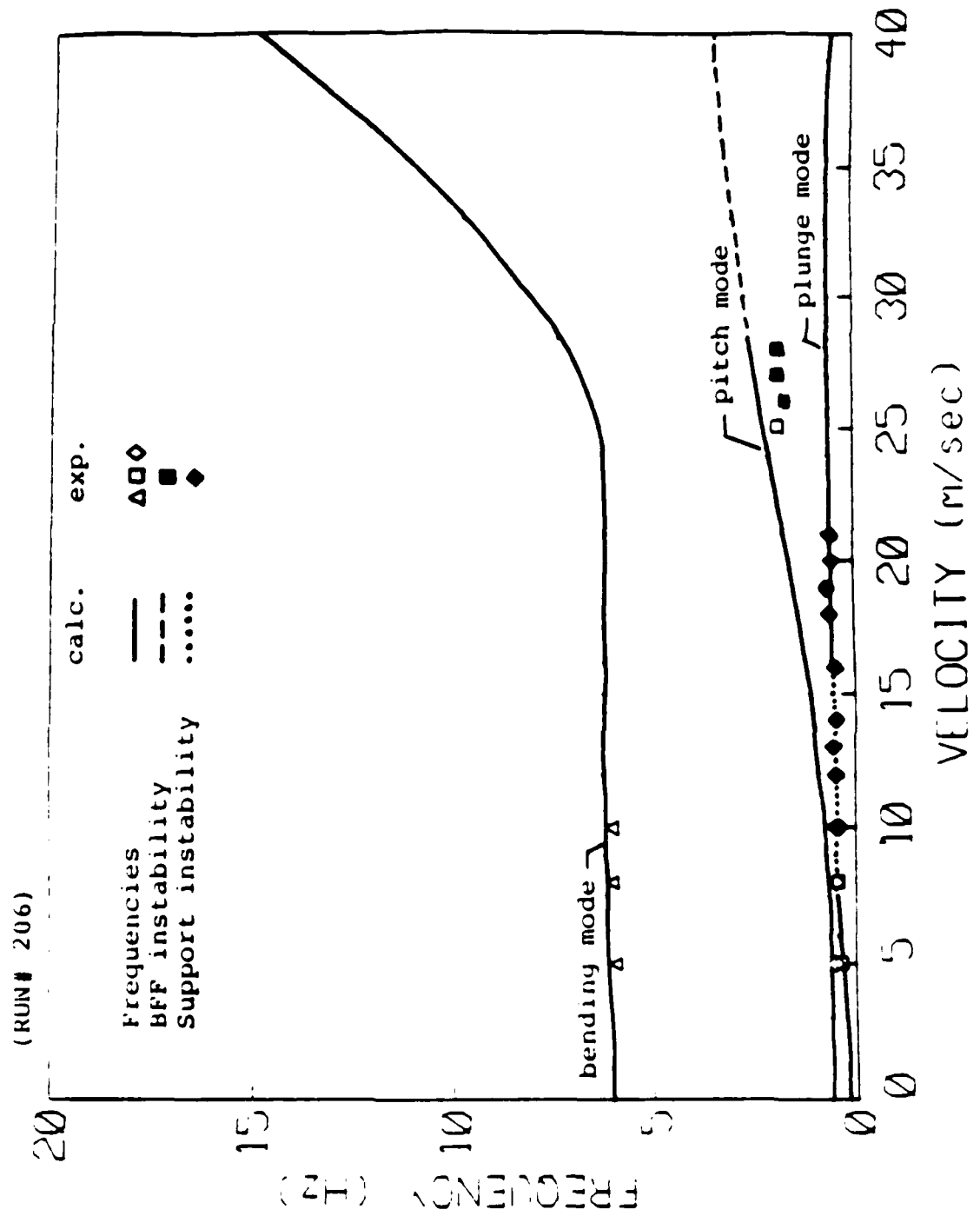


Fig. C.12 ω -V plot, Original Support, $(30_2/0)_s$ Wing
 $(\delta_c = 2.5^\circ)$

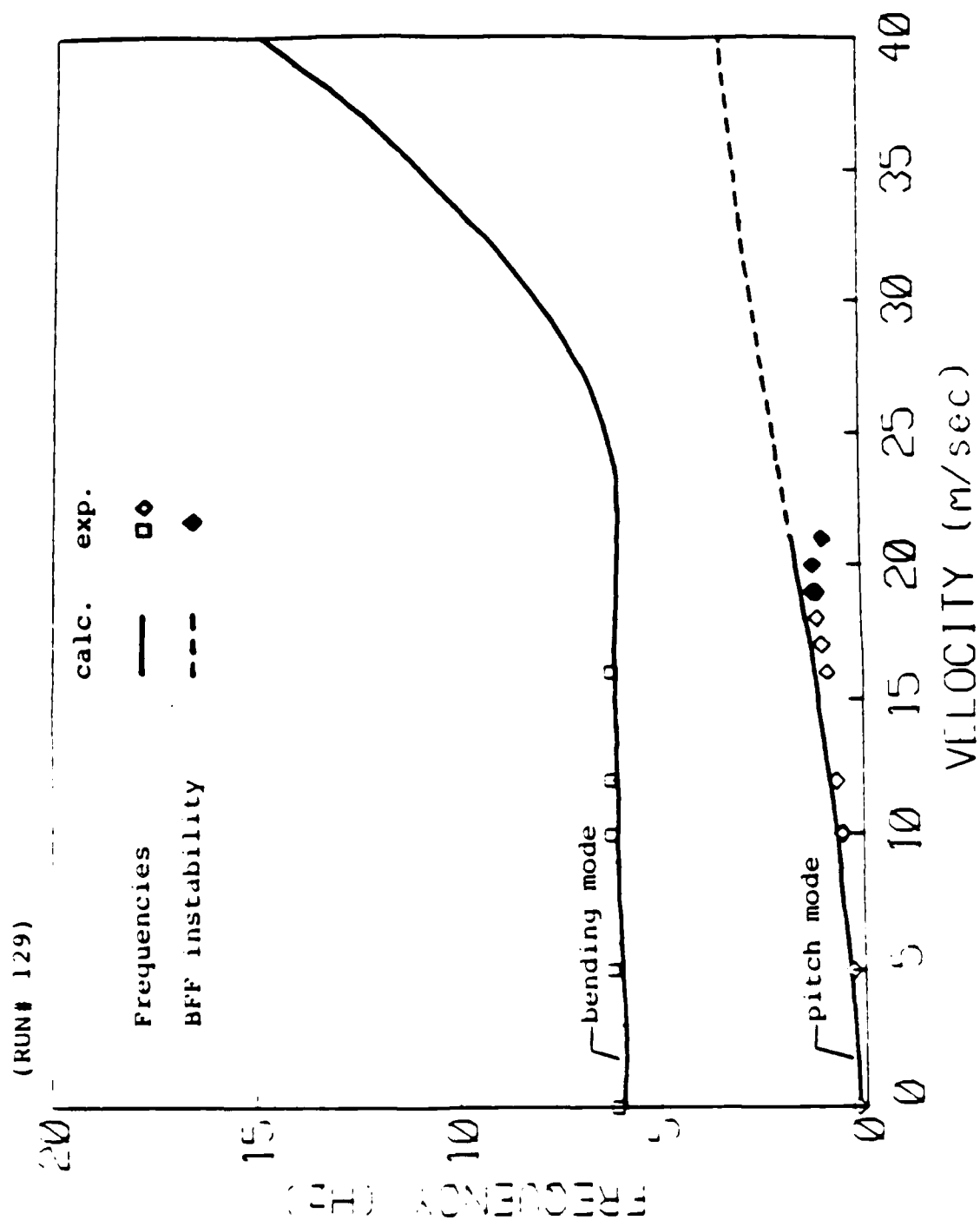


Fig. C.13 ω -V plot, Model Free in Pitch Only, $[30_2/0]_s$ Wing
($\delta_c = 0^\circ$)

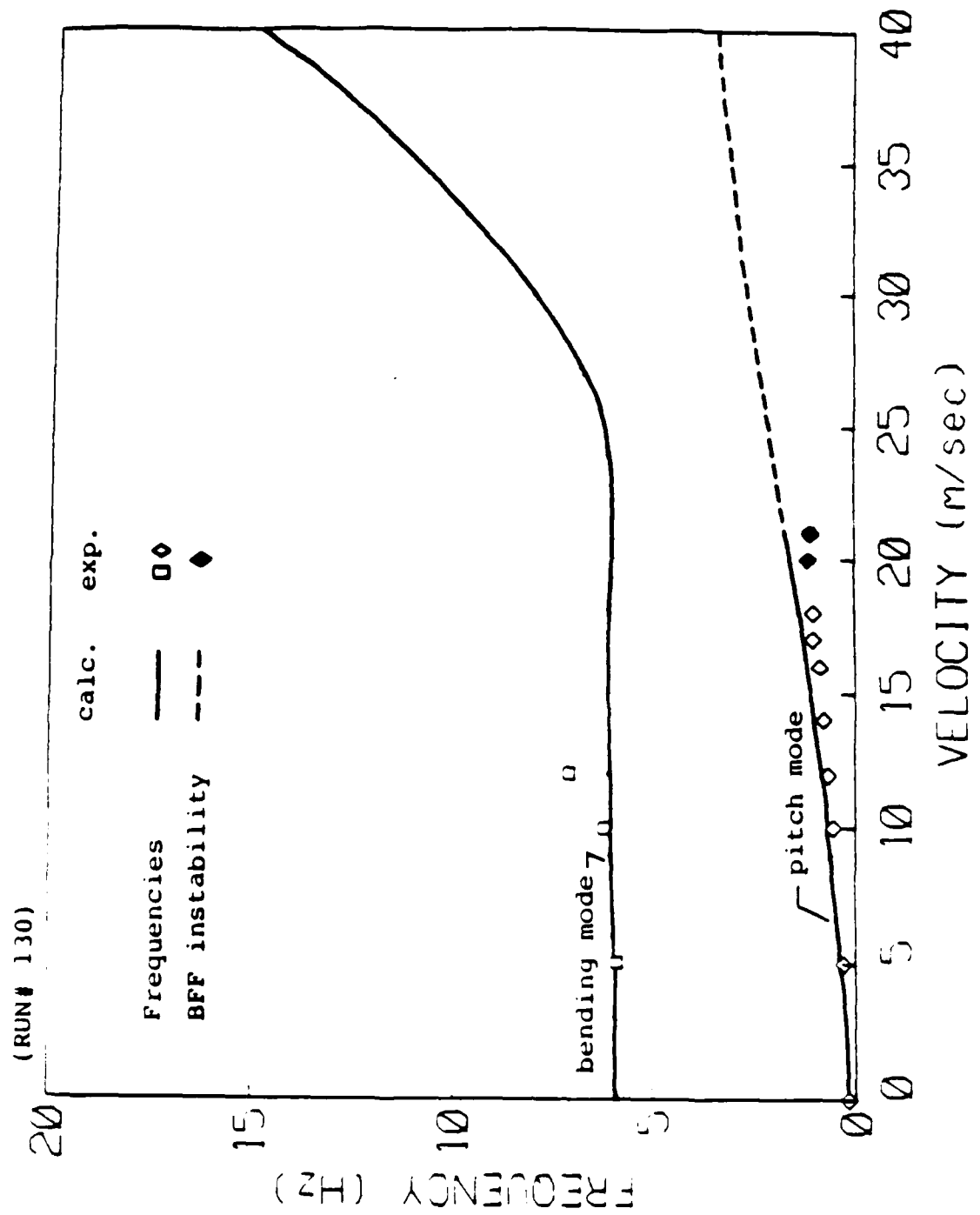


Fig. C.14 ω -V plot, Model Free in Pitch Only, $[30_2/0]_s$ Wing ($\delta_c = 2.5^\circ$)

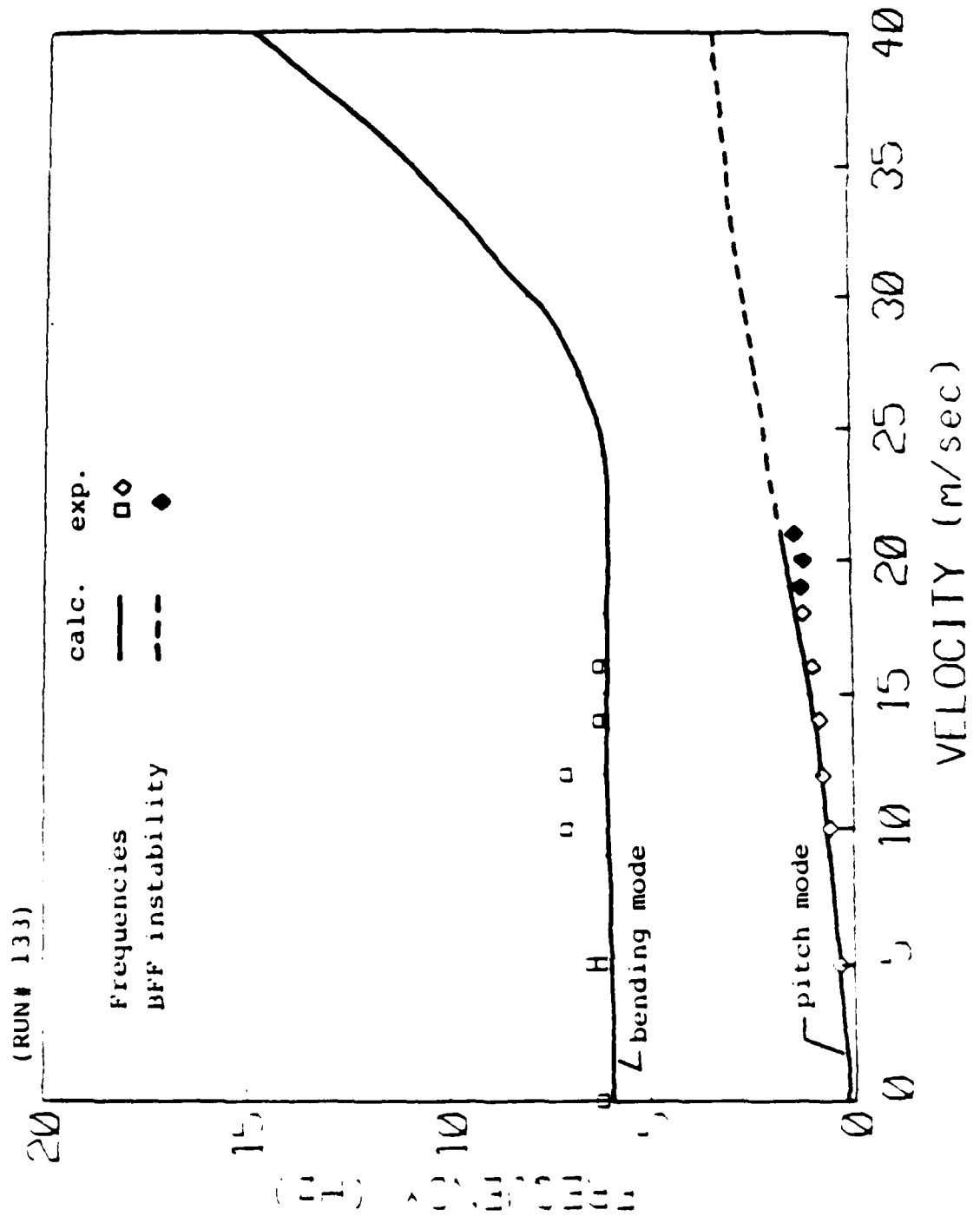


Fig. C.15 ω -V plot, Model Free in Pitch Only, $(30_2/0)_s$ Wing
 $(\delta_c = -2.5^\circ)$

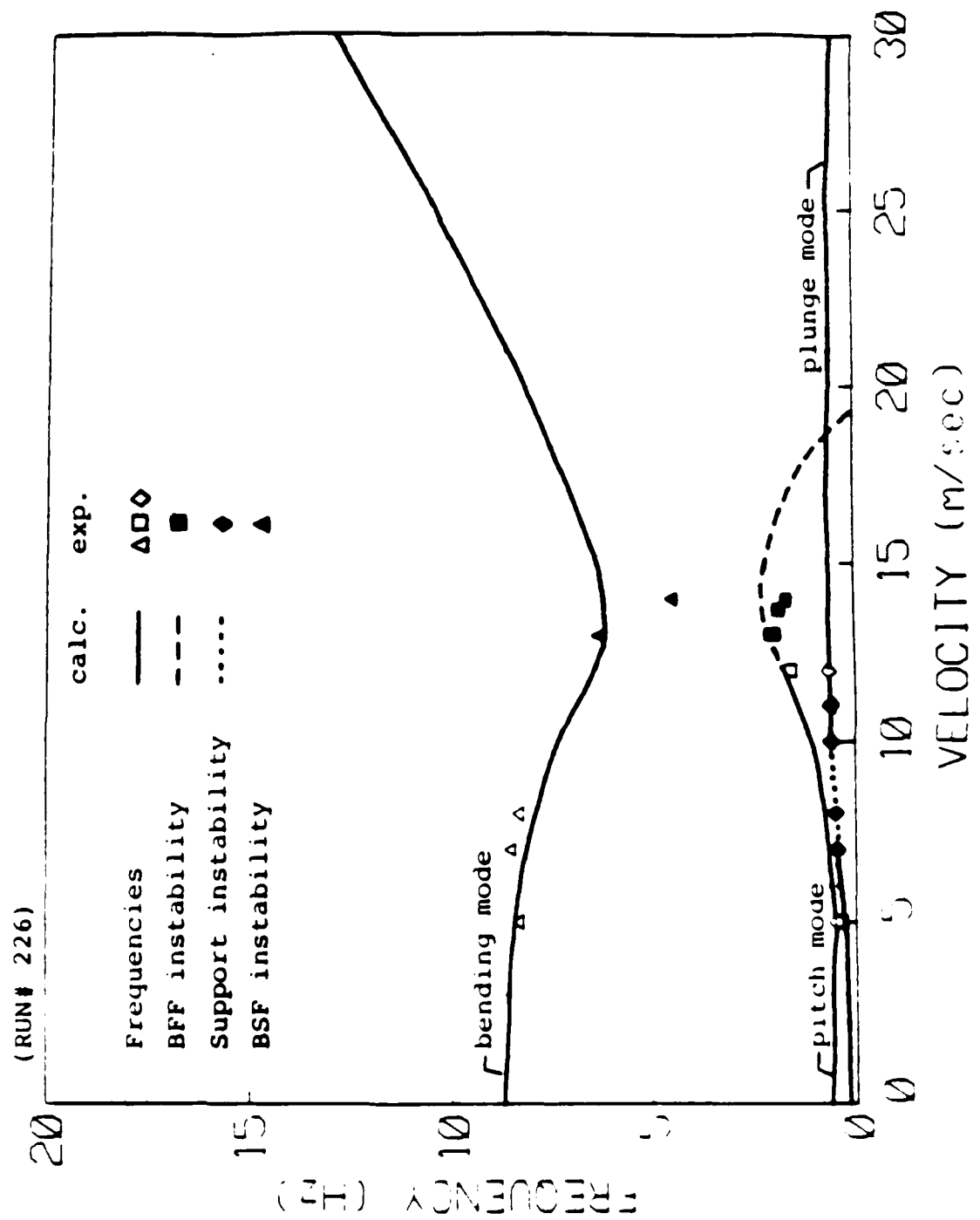


Fig. C.16 ω -V plot, Original Support, $[-15_2/0]_8$ Wing
 $(\delta_c = 0^\circ)$

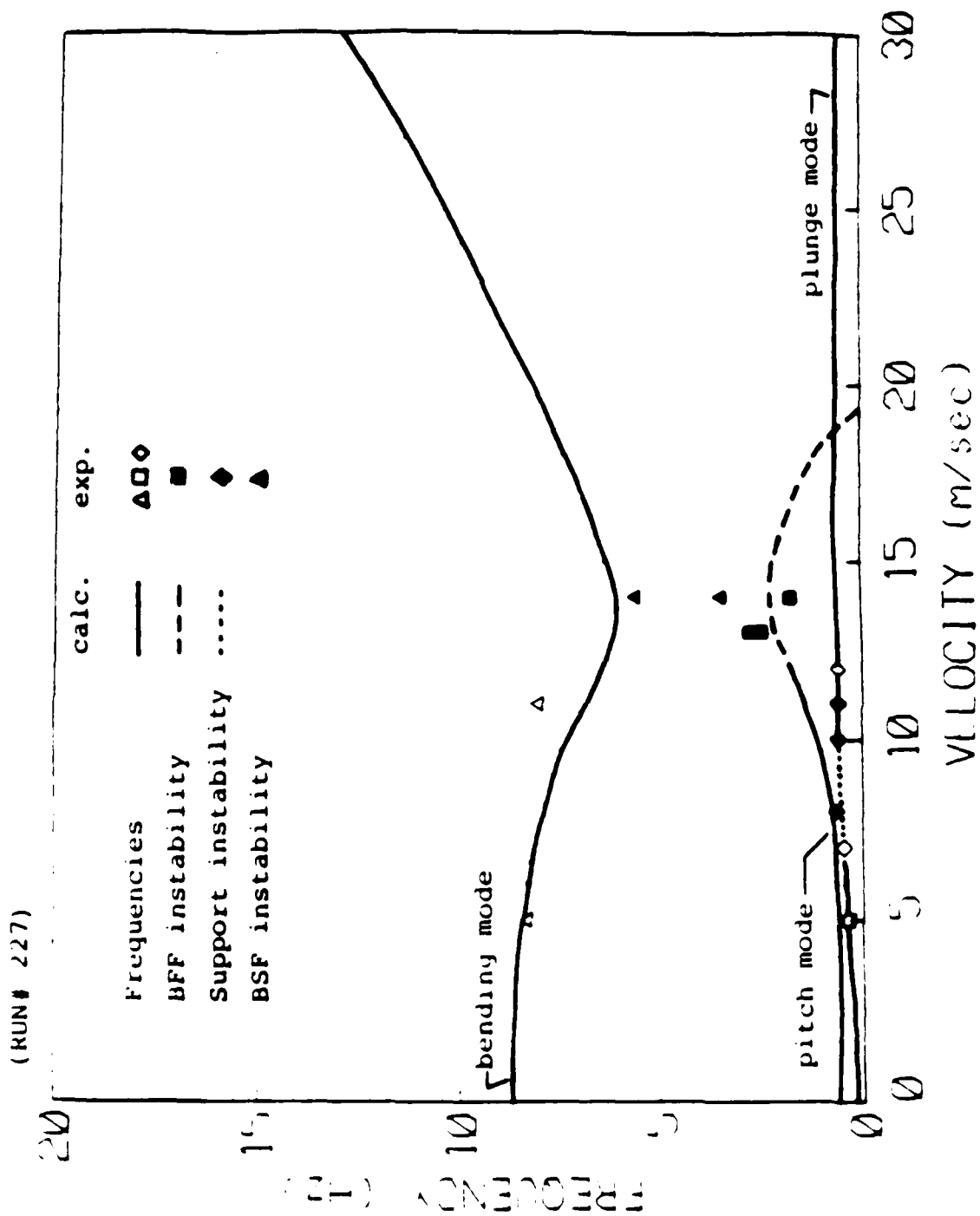


Fig. C.17 ω -V plot, Original Support, $(-15_2/0)$, Wing
 $(\delta_c = 2.5^\circ)$

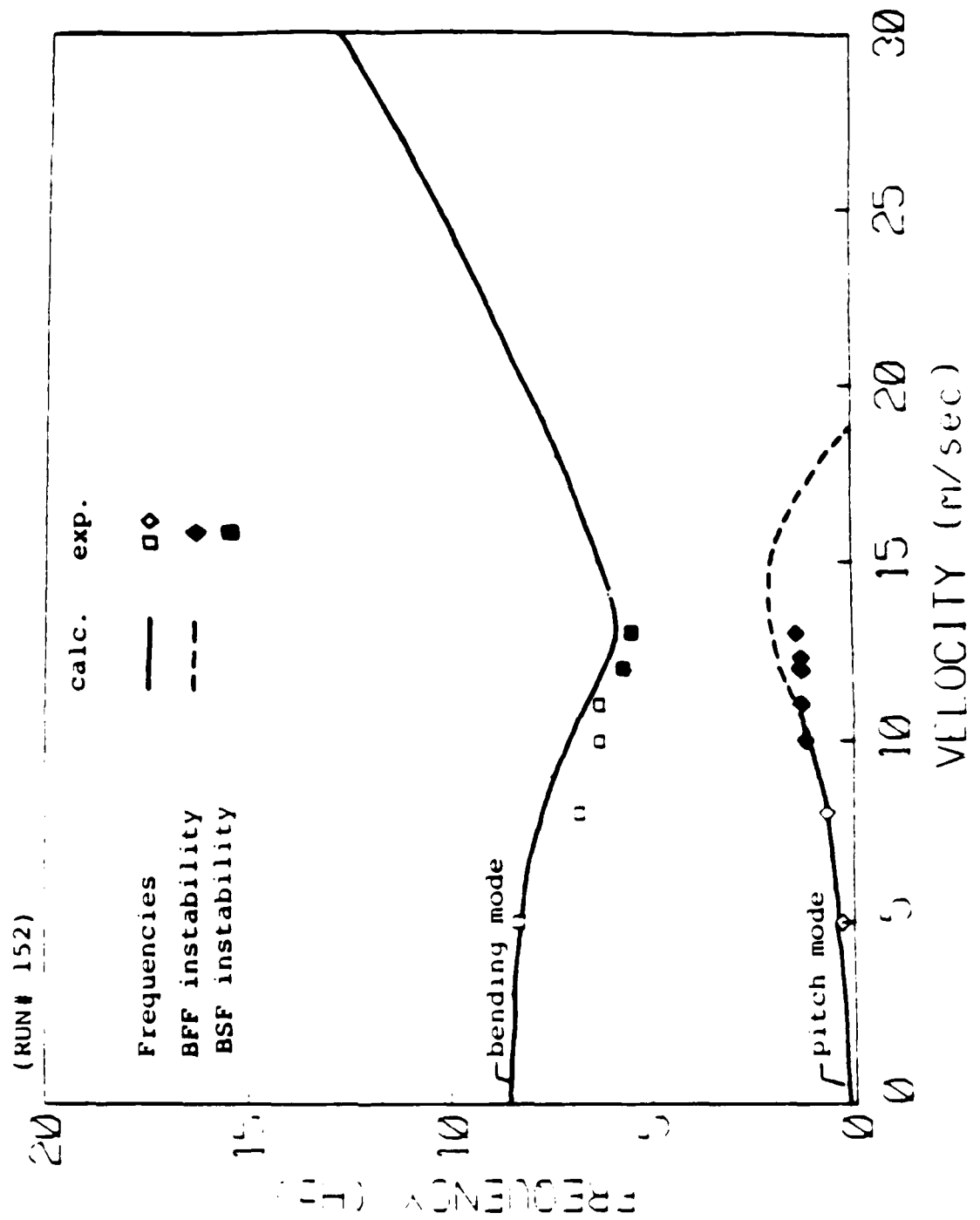


Fig. C.18 ω -V plot, Model Free in Pitch Only, $[-15_2/0]_8$ Wing
 $(\delta_c = 0^\circ)$

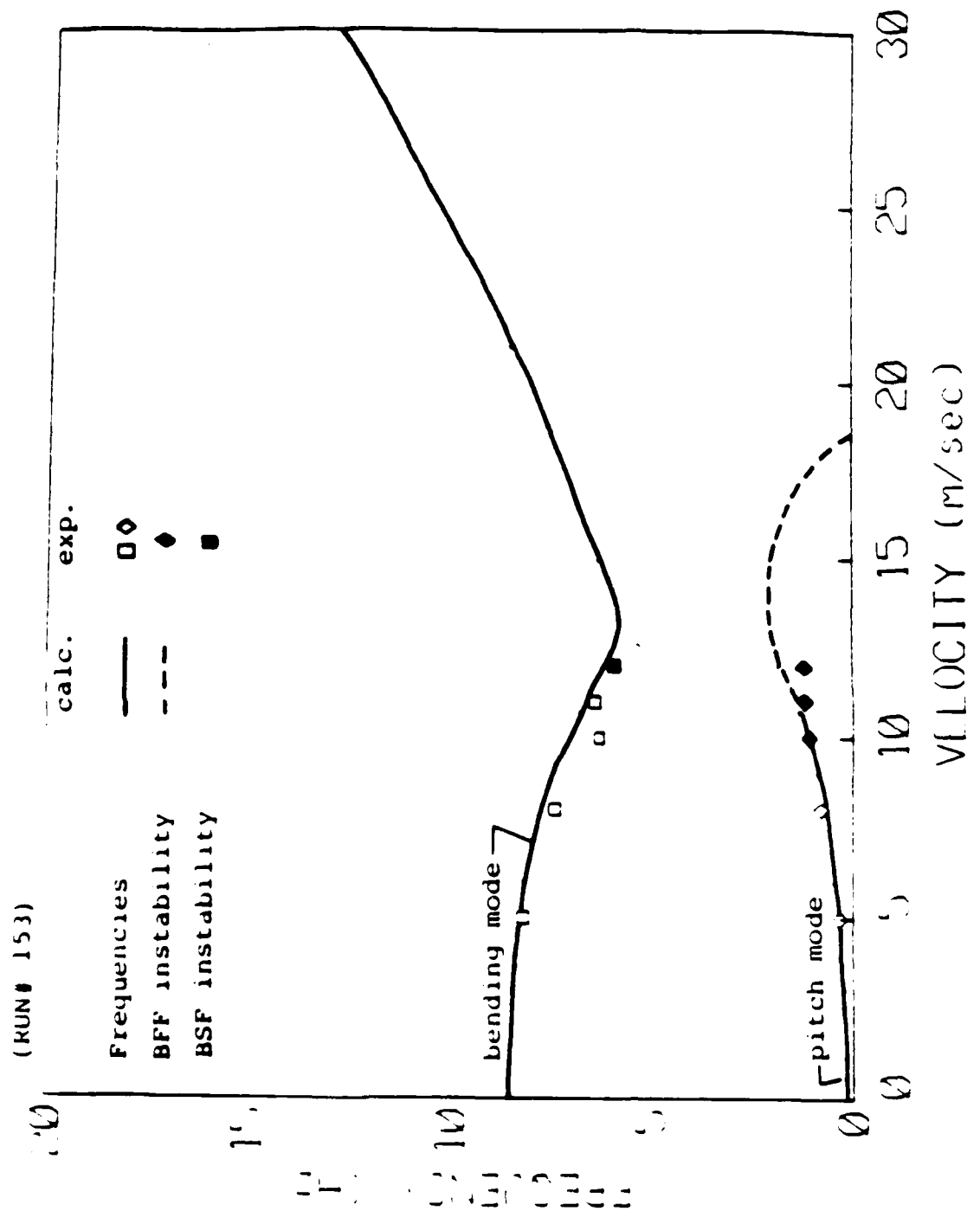


Fig. C.19 ω -V plot, Model Free in Pitch Only, $(-15_2/0)_s$ Wing
($\delta_c = 2.5^\circ$)

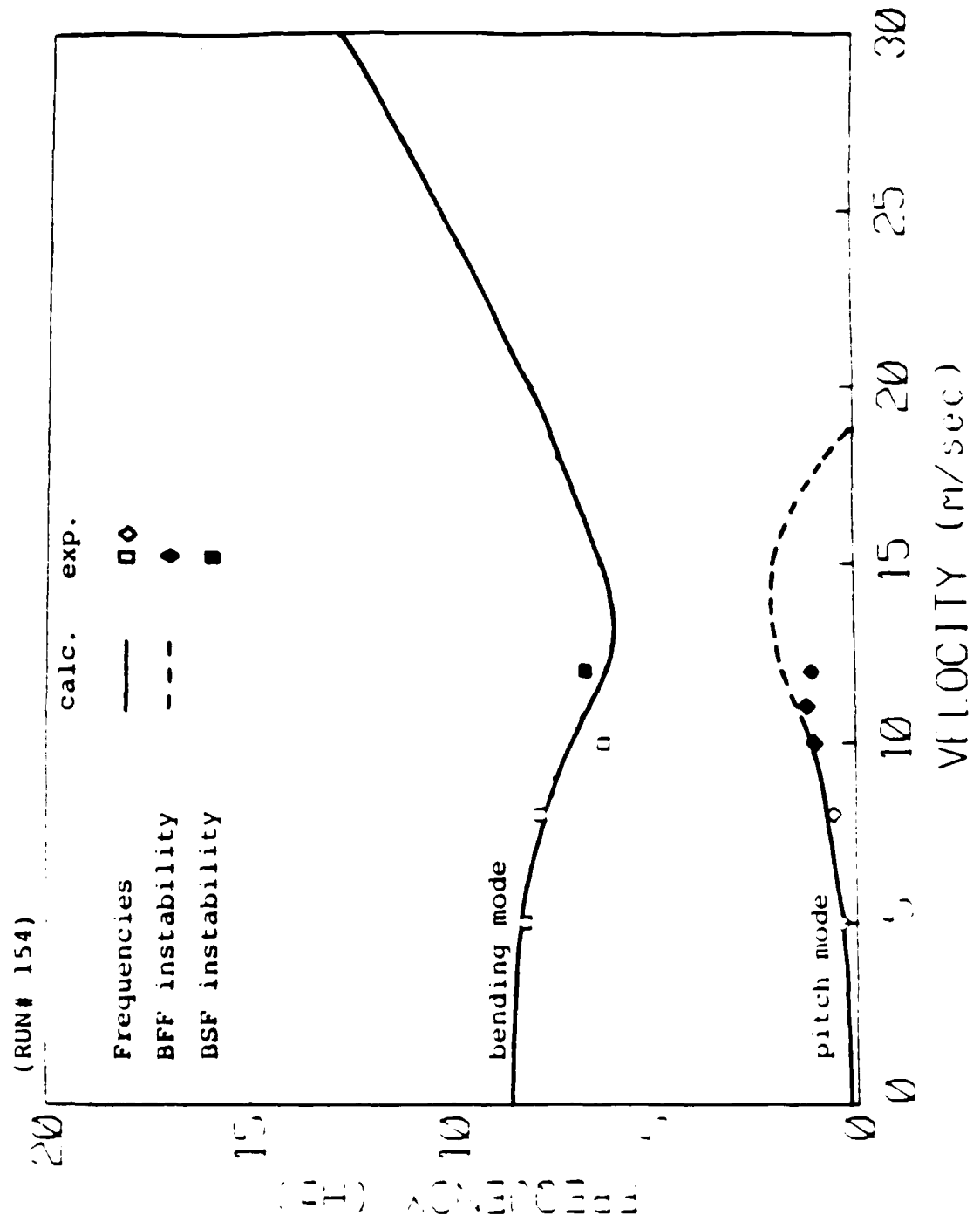


Fig. C.20 ω -V plot, Model Free in Pitch Only, $[-15_2/0]_s$ Wing
 $(\delta_c = -2.5^\circ)$

END

8-87

DTIC